Theoretical investigation of non-invasive methods to identify origins of cardiac arrhythmias

A thesis submitted to
The University of Manchester
for the degree of Doctor of Philosophy
in the Faculty of Engineering and Physical Sciences

2016

Erick Andrés Pérez Alday

School of Physics and Astronomy

Contents

List of Figures

List of Tables

Nomenclature and Abbreviations

$3D$	Three dimensional
λ	Regularization parameter
Ω	Solid angle
AF	Atrial fibrillation
$AFFTr_{2DF}$	Ratio of the area under the PSD between 0-2DF and 2DF-50 HZ
AFL	Atrial flutter
AP	Action potential
AT	Atrial tachycardia
ATP	Adenosine triphosphate
AVN	Atrio-ventricular node
AVR	Atrio-ventricular ring
BB	Bachmanns bundle
BEM	Boundary element method
BSP	Body surface potential
BZ	Border zone
C_m	Membrane capacitance
Ca^{2+}	Calcium ions
CO_2	Carbon dioxide
CT	Cristal terminalis
$CT-scan$	X-ray computed tomography

CZ	Central zone
DF	Dominant frequency
$DT-MRI$	Diffusion tensor MRI
$E_{x,r}$	Nernst potential of ion X
ECG	Electrocardiogram
$ECGi$	Electrocardiography imaging
$ECGs$	Electrocardiogram signals
EIT	Electrical impedance tomography
$ENDO$	Endocardium
EPI	Epicardium
FAA	Fast atrial arrhythmia
FDM	Finite difference method
FEM	Finite element method
FFT	Fast Fourier transformation
FUM	Forward Euler method
g_x	Conductivity of ion X
$GSVD$	Generalized singular value decomposition
I_K	Potassium current
I_x	Current of ion X
I_{ap}	Applied or stimulus current
I_{CaL}	L-type calcium current
I_{K1}	Inward rectifying potassium current
I_{Kr}	Rapid potassium current
I_{Ks}	Slow potassium current
I_{Na}	Sodium current
I_{NCX}	Sodium calcium exchanger current

I_{to}	Transient outward current
IVC	Inferior vena cava
J^i	Applied current density
K^+	Potassium ions
LA	Left atrium
LAA	Left atrial appendage
LPV	Left pulmonary vein
LV	Left ventricle
$MCELL$	Midcardial cell
MCG	Magnetocardiogram
$MCGs$	Magnetocardiogram signals
Mid	Midcardium
MRI	Magnetic resonance imaging
Na^+	Sodium ions
O_2	Oxygen
PF	Purkinje's fiber
PM	Pectinate muscles
PSD	Power spectrum density
PV	Pulmonary vein
PWM	P-wave morphology
Qa	Atrial quadrant
Qt	Torso quadrant
RA	Right atrium
RAA	Right atrial appendage
RPV	Right pulmonary vein
RV	Right ventricle

S_B	Body surface
S_H	Heart surface
SAN	Sino-atrial node
Sp	Mean average of P-wave values in each torso quadrant
$SQUID$	Super quantum interference device
SVC	Superior vena cava
SVD	Singular value decomposition
$TNNP$	Ten Tusscher, Noble, Noble and Panfilov
$TSVD$	Truncated singular value decomposition
V_m	Membrane voltage
VF	Ventricular fibrillation
WCT	Wilson's central terminal

Abstract

The University of Manchester

Abstract of thesis submitted by **Erick Andrés Pérez Alday** for the degree of Doctor of Philosophy and entitled **Theoretical investigation of non-invasive methods to identify origins of cardiac arrhythmias**.

Month and Year of Submission: 23th March, 2016.

Cardiac disease is one of the leading causes of death in the world, with an increase in cardiac arrhythmias in recent years. In addition, myocardial ischemia, which arises from the lack of blood in the cardiac tissue, can lead to cardiac arrhythmias and even sudden cardiac death. Cardiac arrhythmias, such as atrial fibrillation, are characterised by abnormal wave excitation and repolarization patterns in the myocardial tissue. These abnormal patterns are usually diagnosed through non-invasive electrical measurements on the surface of the body, i.e., the electrocardiogram (ECG). However, the most common lead configuration of the ECG, the 12-lead ECG, has its limitations in providing sufficient information to identify and locate the origin of cardiac arrhythmias. Therefore, there is an increasing need to develop novel methods to diagnose and find the origin of arrhythmic excitation, which will increase the efficacy of the treatment and diagnosis of cardiac arrhythmias.

The objective of this research was to develop a family of multi-scale computational models of the human heart and thorax to simulate and investigate the effect of arrhythmic electrical activity in the heart on the electric and magnetic activities on the surface of the body. Based on these simulations, new theoretical algorithms were developed to non-invasively diagnose the origins of cardiac arrhythmias, such as the location of ectopic activities in the atria or ischemic regions within the ventricles, which are challenging to the clinician. These non-invasive diagnose methods were based on the implementation of multi-lead ECG systems, magnetocardiograms (MCGs) and electrocardiographic imaging.

Declaration

No portion of the work referred to in this thesis has been submitted in support of an application for another degree or qualification of this or any other university or other institute of learning.

Copyright and ownership of intellectual property rights

1. The author of this thesis (including any appendices and/or schedules to this thesis) owns certain copyright or related rights in it (the "Copyright") and s/he has given The University of Manchester certain rights to use such Copyright, including for administrative purposes.

2. Copies of this thesis, either in full or in extracts and whether in hard or electronic copy, may be made **only** in accordance with the Copyright, Designs and Patents Act 1988 (as amended) and regulations issued under it or, where appropriate, in accordance with licensing agreements which the University has from time to time. This page must form part of any such copies made.

3. The ownership of certain Copyright, patents, designs, trade marks and other intellectual property (the "Intellectual Property") and any reproductions of copyright works in the thesis, for example graphs and tables ("Reproductions"), which may be described in this thesis, may not be owned by the author and may be owned by third parties. Such Intellectual Property and Reproductions cannot and must not be made available for use without the prior written permission of the owner(s) of the relevant Intellectual Property and/or Reproductions.

4. Further information on the conditions under which disclosure, publication and commercialisation of this thesis, the Copyright and any Intellectual Property and/or Reproductions described in it may take place is available in the University IP Policy (see `http://documents.manchester.ac.uk/DocuInfo.aspx?DocID=487`), in any relevant Thesis restriction declarations deposited in the University Library, The University Library's regulations (see `http://www.manchester.ac.uk/library/aboutus/regulations`) and in The University's policy on Presentation of Theses.

Dedication

A ti.

Acknowledgements

First, I would like to thank my supervisor, prof. Henggui Zhang, for his guidance and support throughout my Ph.D., and for giving me the opportunity to work in this project and to provide all the facilities used. I wish to express my sincere thanks to my colleagues and friends of the Biological Physics Group and Schuster building, in particular, Simon, Gareth, Tim, Jon, Dom, Kun, Roy, Haibo, Petros, Craig, Pete, Cesar, Jimmy and Dave, they can make any topic interesting and worth of discussion, I learnt a lot from you guys, except English. A special thanks is going to my friend and colleague Michael, for his patient, support and advices in different aspects of my work and life. I would also like to thank Rene and Benjamin for making every conversation, meal, football match or any distraction needed enjoyable. I am also grateful to my friends from Manchester for Ayotzinapa, for reminding me the important things in life. I would like to extend my gratitude to my family, mom, dad, sister, grandparents and Juan, their endless support and unceasing encouragement are my reason to carry on. I would like to thank my close friends from Mexico, for providing a different look to things. Special thanks go to Fabiola, her patient, love and companionship gave me the needed encouragement at each stage of this venture. And last but not least, I would like to aknowledge CONACyT for the sponsorship given.

The author

Erick Andres Perez Alday was born in Coatzacoalcos, Veracruz, Mexico in 1986. He graduated in Physics Engineering with laureate distinction in 2009 at the Instituto de Fisica, Universidad de Guanajuato, Mexico. Then in 2011, he completed his Master in Science degree at the Division de Ciencias e Ingenierias, Universidad de Guanajuato, Mexico, the research was performed at the Universitat Politecnica de Catalunya, Spain. In 2012, he joined the Biological Physics Group at the University of Manchester to start his Ph.D.

Supporting Publications

Perez Alday EA*, Colman MA*, Langley P, Butters TD, Higham J, Workman AJ, Hancox JC, Zhang H. A new algorithm to diagnose atrial ectopic origin from multi-lead ECG systems PLoS Comp. Bio. vol 11(1):e1004026. 2015.

Colman MA, Castro SJ, Perez Alday EA, Hancox JC, Garratt C, Zhang H. Recent progress in multi-scale models of the human atria. Drug Discov Today: Dis Models, 2014, (DOI: 10.1016/j.ddmod.2014.04.003).

Perez Alday EA, Zhang C, Colman MA, Ni H, Gan A, Zhang H. Comparison of electric and magnetic cardiograms produced by myocardial Ischemia in models of the human ventricle and torso. In Computing in Cardiology (CinC), 2015 (Conference Proceedings).

Perez Alday EA, Colman MA, Langley P, Zhang H. Spatial Refinement of a New Algorithm to Identify Focus of Atrial Ectopic Activity from 64-lead ECGs In Computing in Cardiology (CinC), 2014 (Conference Proceedings).

Perez Alday EA, Colman MA, Langley P, D Giacopelli, SR Harcge Zhang H. A New Algorithm to Identify Focus of Atrial Ectopic Activity from 64-lead ECGs: insights from 3D virtual human atria and torso In Proceedings of the Physiological Society, The Physiological Society, 2014 (Conference Proceedings).

Perez Alday EA, Colman MA, Butters TD, Higham J, Giacopelli D, Langley P & Zhang H. Diagnosis of atrial ectopic origin from body surface ECG insights from 3D virtual human atria and torso. In Computing in Cardiology (CinC), 2013, pp 1075-1078 (Conference Proceedings).

Perez Alday EA, Colman MA, Langley P, Holden AV & Zhang H (2013). Multi-scale integrative model of the human atria and torso: a platform for the investigation of atrial arrhythmias. Journal of Electrocardiology 46 (4) e17-e18 (Conference Proceedings).

Colman MA, ParraRojas C, Perez Alday EA. From Microscopic Calcium Sparks to the ECG: Model Reduction Approaches for Multiscale Cardiac Simulation. In Computing in Cardiology (CinC), 2015 (Conference Proceedings).

Ni H, Wang W, Perez Alday EA, Zhang H. In Silico Investigation of the Pro-arrhythmogenic Effect of KCNQ1 G269S Mutation in Human Ventricles. In Computing in Cardiology (CinC), 2015 (Conference Proceedings).

Chapter 1

Introduction

Cardiovascular disease affects millions of people worldwide and is one of the leading causes of death in developed countries [1]. Unfortunately, epidemiological studies have shown an increase in the population of patients with cardiac arrhythmias, which has been linked to an ageing society [2, 1]. In addition, myocardial ischemia, which arises from the lack of blood in the cardiac tissue, can also lead to cardiac arrhythmias and in some cases, sudden cardiac death [3, 4]. Cardiac arrhythmias, such as atrial fibrillation, are defined as an irregular beating of the heart or any disordered cardiac rhythm which is associated with abnormal excitation wave and repolarization patterns in the cardiac tissue [5, 6]. These abnormal patterns can be identified by invasive and non-invasive methods, such as electrodes placed on the surface of the heart [7] or on the surface of the body [8]. However, invasive methods can produce further complications during surgery and might require further surgical procedures [9]. Therefore, cardiac arrhythmias are usually diagnosed through non-invasive electrical measurements on the surface of the body, i.e, the electrocardiogram (ECG). Unfortunately, the 12-lead ECG, which has been implemented as a standard clinical diagnostic technique for multiple decades [10], has its limitations in providing sufficient information to identify and locate the origin of cardiac arrhythmias [11, 12, 13]. There is therefore a pressing need to develop effective non-invasive methods to diagnose and determine the origin of arrhythmic excitation.

Previous studies have shown that multi-lead ECG configurations provide more information about irregular cardiac conduction and repolarization patterns than the standard 12-lead ECG [14, 15]. However, it is still an open question whether this information is sufficient for the accurate diagnosis of cardiac arrhythmia [10]. Recent studies have developed algorithms to non-invasively identify the location of focal ectopic sources by using either standard 12-lead [8, 16] or multiple-lead ECG systems [15, 17]. The success rates of these algorithms range from 40% to 90% [8, 16, 17]. It is also important to be able to distinguish the type of arrhythmia, as the underlying

mechanisms in each case can be different and thus different intervention may be required to terminate the arrhythmia.

In addition to the ECG, the magnetic field produced by the electrical activity in the heart has been hypothesized to provide a greater level of detail of cardiac excitation patterns compared to body surface potential measurements. Combined with its high independence to electrical resistivity inhomogeneities inside the tissues of the body [18, 19], magnetocardiograms (MCG) are more sensitive to currents tangential to the surface of the chest than ECGs [19]. In addition to that, due to the high temperature of the MCG sensors, these are placed at a short distance of the body and not on its surface, which makes it a completely non-invasive method. Therefore, the MCG provides a potential practical alternative to the ECG for monitoring certain cardiac conditions, such as ischemia. Unfortunately, the magnetic signals measured from the human heart are around 10^{-9}, while the magnetic earth field is 10^{-4}, therefore, high sensitive sensors and a magnetic shielded room are required which makes MCG technique more expensive than ECG techniques. Therefore, detailed correlation between the presence of cardiac arrhythmias and the characteristic response of the MCG are yet to be established to compare its advantages and disadvantages.

Moreover, the electrocardiographic imaging, the spatio-temporal reconstruction of cardiac electrical activity from multi-lead ECG systems based on inverse problem solutions [20], is a promising method in clinical diagnosis. However, there is a lack of information in the multi-lead ECG measurements that enables one to find a reliable analytical solution of the cardiac electrical activity. Consequently, current algorithms require further information to constrain the solution to achieve a reliable reconstruction of cardiac excitation waves [21]. Furthermore, the minimum number of electrodes needed and the best type of inverse formulation to find a reliable solution during different arrhythmia conditions are still open questions, which are difficult to address in clinical practices.

The aim of this Thesis was to make a computational investigation of non-invasive methods to identify origins of cardiac arrhythmias. Therefore, a family of multi-scale computational models of the human heart and thorax was developed. These computational models allowed simulation of the effect of cardiac arrhythmic excitation patterns on the electric and magnetic activities on the surface of the body. Based on these simulations, new theoretical algorithms were developed to non-invasively diagnose and identify the origins of cardiac arrhythmias, such as the location of focal ectopic activities in the atria or ischemic regions within the ventricles through multi-lead systems. In addition, these simulations allowed the comparison between

non-invasive methods during different heart excitation patterns, such as MCG and ECG signals produced by myocardial ventricular ischemia. Also, these computational models allowed the efficacy of non-invasive methods to be tested, such as spatio-temporal atrial surface reconstruction during atrial fibrillation using electrocardiographic imaging. All these are clinically important challenges [10]

This Thesis is organized following the Alternative Format Thesis allowed by the University of Manchester Thesis submission regulations [22], which allows incorporation of sections based on published peer-reviewed articles or manuscripts in preparation for publication in peer-reviewed journals. Therefore, this Thesis is organized in the following structure: In Chapter 2, a short review of the anatomy and physiology of the heart and thorax is presented, followed by a brief introduction to mathematical models and methods for simulating the electric and magnetic activities of the heart-thorax. In Chapter 3, a more detailed description of the mathematical and numerical methods used to theoretically investigate the non-invasive methods is presented. Chapter 4 details the computational models developed to simulate the various approaches (such as body surface potential mapping, magnetocardiograms and electrocardiogram imaging) used to identify the origins of cardiac arrhythmias. In the subsequent chapters, novel research results on developed algorithms for identifying arrhythmic origins based on 64-lead ECG (Chapter 5 and 6), ECG & MCG (Chapter 7) and electrocardiographic imaging systems (Chapter 8) are presented based on published articles, or manuscripts in preparation for publication. In Chapter 9, a summary and further work based on the Thesis are presented.

The main contribution of this Thesis is presented in the following manuscripts.

Chapter 5.

Perez-Alday EA, Colman MA, Langley P, Butters TD, Higham J, Workman AJ, Hancox JC, Zhang H. A new algorithm to diagnose atrial ectopic origin from multi lead ECG systems - Insights from 3D virtual human atria and torso. PLoS Comput Biol. 2015 Jan 22;11(1):e1004026.

Chapter 6.

Perez-Alday EA, Colman MA, Langley P, Zhang H, Novel non-invasive algorithm to identify the origins of re-entry and ectopic foci in the atria from 64-lead ECGs. A computational study. (Submitted and waiting for revision).

Chapter 7.

Perez Alday EA, Ni H, Zhang C, Coman MA , Gan Z, Zhang H. Comparison of

electric- and magnetic- cardiograms produced by myocardial ischemia in models of the human ventricle and torso. (Submitted and waiting for revision).

Chapter 8.

Perez-Alday EZ, Colman MA, Zhang H. Reconstruction of atrial ectopic focal and re-entrant excitations from body surface potential. Insights from 3D virtual human atria and torso. (Draft version).

In all publications, the author of this Thesis (Perez-Alday) had the main responsibility in designing and writing a first draft of the manuscript, designing and developing the torso tools and as well as analysing the data in each study. Revisions of the writing were incorporated by the co-authors directly or Perez-Alday after discussion with the other authors. The overall contribution of each author is listed bellow:

Prof. Henggui Zhang - *The University of Manchester* - Main supervisor during this research, focusing on the concept and design, providing guidance and support on each study.

Dr. Michael A Colman - *The University of Manchester* - Collaborated on the design; providing advice and support in each study. Further to this, Michael provided the atria model used in this study.

Dr. Philip Langley - *The University of Hull* - Provided the expertise in experimental multi-ECGs and technical discussions needed in the atria studies. Further to this, Philip provided the 64-lead ECG experimental data used to validate the atria-torso model.

Haibo Ni - *The University of Manchester* - Provided the ventricular model, which was used in Chapter 7. Further to this, Haibo provided support on the study of Chapter 7.

Chen Zhang - *Peking University* - Provided the experimental 36-lead ECG and MCG used to validate the ventricular-torso model. Further to this, Chen provided support on the study of Chapter 7.

Dr. Zizhao Gan - *Peking University* - Provided the experimental 36-lead ECG and MCG used to validate the ventricular-torso model. Further to this, Zizhao provided support on the study of Chapter 7.

Dr. John Higham - *University of Manchester* - Provided expertise in heart modelling, along with technical discussion on the study of Chapter 5.

Dr. Timothy Butters - *University of Manchester* - Provided expertise in heart modelling, along with technical discussion on the study of Chapter 5.

Dr. Antony Workman - *University of Glasgow* - Provided clinical perspective, along with technical discussion on the study of Chapter 5.

Dr. Jules Hancox - *University of Manchester* - Provided clinical perspective, along with technical discussion on the study of Chapter 5.

Bibliography

[1] N. J. Pagidipati and T. A. Gaziano, "Estimating deaths from cardiovascular disease: a review of global methodologies of mortality measurement," *Circulation*, vol. 127, no. 6, pp. 749–756, 2013.

[2] F. Rahman, G. F. Kwan, and E. J. Benjamin, "Global epidemiology of atrial fibrillation," *Nature Reviews Cardiology*, vol. 11, no. 11, pp. 639–654, 2014.

[3] A. Ghuran and A. Camm, "Ischaemic heart disease presenting as arrhythmias," *British medical bulletin*, vol. 59, no. 1, pp. 193–210, 2001.

[4] A. M. Katz, *Physiology of the Heart*. Lippincott Williams & Wilkins, 2010.

[5] E. J. Benjamin, P. A. Wolf, R. B. DAgostino, H. Silbershatz, W. B. Kannel, and D. Levy, "Impact of atrial fibrillation on the risk of death the framingham heart study," *Circulation*, vol. 98, no. 10, pp. 946–952, 1998.

[6] E. Anter, M. Jessup, and D. J. Callans, "Atrial fibrillation and heart failure treatment considerations for a dual epidemic," *Circulation*, vol. 119, no. 18, pp. 2516–2525, 2009.

[7] C. Schmitt, G. Ndrepepa, S. Weber, S. Schmieder, S. Weyerbrock, M. Schneider, M. R. Karch, I. Deisenhofer, J. Schreieck, B. Zrenner, *et al.*, "Biatrial multisite mapping of atrial premature complexes triggering onset of atrial fibrillation," *The American journal of cardiology*, vol. 89, no. 12, pp. 1381–1387, 2002.

[8] P. M. Kistler, K. C. Roberts-Thomson, H. M. Haqqani, S. P. Fynn, S. Singarayar, J. K. Vohra, J. B. Morton, P. B. Sparks, and J. M. Kalman, "P-wave

morphology in focal atrial tachycardia: development of an algorithm to predict the anatomic site of origin," *Journal of the American College of Cardiology*, vol. 48, no. 5, pp. 1010–1017, 2006.

[9] W. Anné, H. Van Rensburg, J. Adams, H. Ector, F. Van de Werf, and H. Heidbüchel, "Ablation of post-surgical intra-atrial reentrant tachycardia. predilection target sites and mapping approach," *European heart journal*, vol. 23, no. 20, pp. 1609–1616, 2002.

[10] P. W. Macfarlane, A. van Oosterom, and M. Janse, *Comprehensive electrocardiology*, vol. 4. Springer Science & Business Media, 2010.

[11] W.-S. Lin, C.-T. Tai, M.-H. Hsieh, C.-F. Tsai, Y.-K. Lin, H.-M. Tsao, J.-L. Huang, W.-C. Yu, S.-P. Yang, Y.-A. Ding, *et al.*, "Catheter ablation of paroxysmal atrial fibrillation initiated by non–pulmonary vein ectopy," *Circulation*, vol. 107, no. 25, pp. 3176–3183, 2003.

[12] C. W. Hamm, J.-P. Bassand, S. Agewall, J. Bax, E. Boersma, H. Bueno, P. Caso, D. Dudek, S. Gielen, K. Huber, *et al.*, "Esc guidelines for the management of acute coronary syndromes in patients presenting without persistent st-segment elevation," *European heart journal*, vol. 32, no. 23, pp. 2999–3054, 2011.

[13] D. Giacopelli, J. P. Bourke, A. Murray, and P. Langley, "Spatial pattern of p waves in paroxysmal atrial fibrillation patients in sinus rhythm and controls," *Pacing and Clinical Electrophysiology*, vol. 35, no. 7, pp. 819–826, 2012.

[14] D. Stilli, E. Musso, E. Macchi, C. Manca, L. Dei Cas, P. Vasini, and B. Taccardi, "Body surface potential mapping in ischemic patients with normal resting ecg.," *The Canadian journal of cardiology*, pp. 107A–112A, 1986.

[15] M. Bojarnejad, J. R. Blake, J. Bourke, E. Shepherd, A. Murray, and P. Langley, "Non-invasive estimation of left atrial dominant frequency in atrial fibrillation from different electrode sites: Insight from body surface potential mapping," *JAFIB: Journal of Atrial Fibrillation*, vol. 7, no. 3, 2014.

[16] J.-S. Uhm, J. Shim, J. Wi, H.-S. Mun, H.-N. Pak, M.-H. Lee, and B. Joung, "An electrocardiography algorithm combined with clinical features could localize the origins of focal atrial tachycardias in adjacent structures," *Europace*, vol. 16, no. 7, pp. 1061–1068, 2014.

[17] E. A. P. Alday, M. A. Colman, P. Langley, T. D. Butters, J. Higham, A. J. Workman, J. C. Hancox, and H. Zhang, "A new algorithm to diagnose atrial ectopic origin from multi lead ecg systems-insights from 3D virtual human atria and torso," *PLoS computational biology*, vol. 11, no. 1, 2015.

[18] B. Hailer, I. Chaikovsky, S. Auth-Eisernitz, H. Schäfer, and P. Van Leeuwen, "The value of magnetocardiography in patients with and without relevant stenoses of the coronary arteries using an unshielded system," *Pacing and clinical electrophysiology*, vol. 28, no. 1, pp. 8–16, 2005.

[19] D. B. Geselowitz, "Electric and magnetic field of the heart," *Annual review of biophysics and bioengineering*, vol. 2, no. 1, pp. 37–64, 1973.

[20] C. Ramanathan, R. N. Ghanem, P. Jia, K. Ryu, and Y. Rudy, "Noninvasive electrocardiographic imaging for cardiac electrophysiology and arrhythmia," *Nature medicine*, vol. 10, no. 4, pp. 422–428, 2004.

[21] H. S. Oster and Y. Rudy, "The use of temporal information in the regularization of the inverse problem of electrocardiography," *Biomedical Engineering, IEEE Transactions on*, vol. 39, no. 1, pp. 65–75, 1992.

[22] "documents.manchester.ac.uk/display.aspx?docid=7420." `http://documents.manchester.ac.uk/display.aspx?DocID=7420`.

Chapter 2

Literature Review

The electrical activity of the heart produces an electric and magnetic field surrounding the body. Hence, the human heart can be seen as an electric source inside an inhomogeneous volume conductor (i.e., the human body). Measuring the electric and magnetic field state can give us information about the behaviour of the heart. Unfortunately, the electric and magnetic fields outside or on the surface of the body are extremely weak signals compared to the signals produced in the heart. Thus, it is still a scientific challenge to correlate the state of the heart with the measured electric and magnetic signals on the thorax to a high degree of accuracy. This chapter introduces basic anatomical, physiological, physical and mathematical concepts relevant to this Thesis.

2.1 The heart

The heart is one of the most important organs in the human body. It supplies oxygenated blood to millions of cells throughout the body. In order to achieve this, a normal healthy heart beats approximately 10,000 times a day and pumps more than 14,000 litres of blood in a day.[1]. If the heart stops beating, blood stops flowing to vital organs, which can cause tissue damage and death if it is not treated within minutes [1].

2.1.1 Location of the heart

The healthy human heart is approximately the size of one's fist. It is located inside the thorax, above the diaphragm and surrounded by the lungs and rib cage. From a frontal view, the heart can be seen as a cone pointing to the left, anterior and inferior part of the body; the "peak" is referred to as the apex of the heart, whereas the base of the heart (base of the cone) is in the right, posterior and superior direction (Figure 2.1).

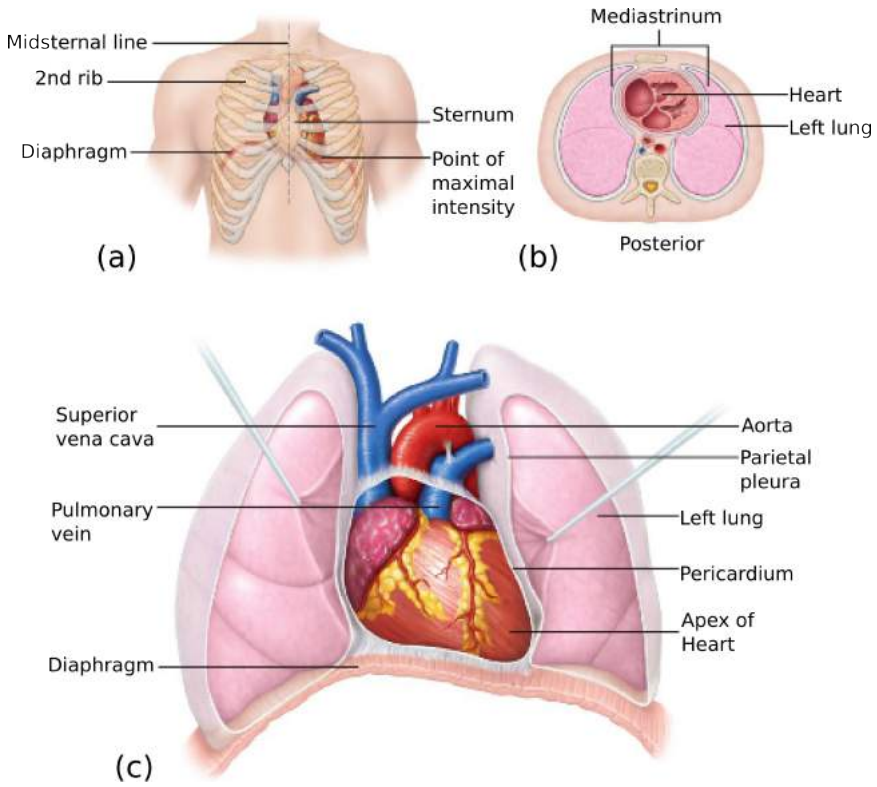

Figure 2.1: Illustrations of the position of the heart inside the body. (a) Location of the heart inside the thorax from a frontal view. (b) Axial cut of the thorax, the position of the lungs and heart can be observed. (c) Coronal cut of the lungs and heart. Figure adapted from [2].

2.1.2 Anatomy of the heart

The heart is composed by four chambers, two upper chambers (the atria) and two lower chambers (the ventricles) (Figure 2.2 a). The atria is comprised of two components, namely left atrium (LA) and right atrium (RA) which are separated by a thin barrier known as the inter-atrial septum. The atria constitutes most of the base of the heart. Similarly, the ventricles are divided into the left ventricle (LV) and right ventricle (RV) which are separated by a narrow barrier called the interventricular septum. The right ventricle constitutes most of the anterior part of the heart, whereas the left ventricle constitutes most of the apex of the heart. Atria and ventricles are electrically and physically isolated by non-conductive fibrous connective tissue rings collectively known as fibrous skeleton [1].

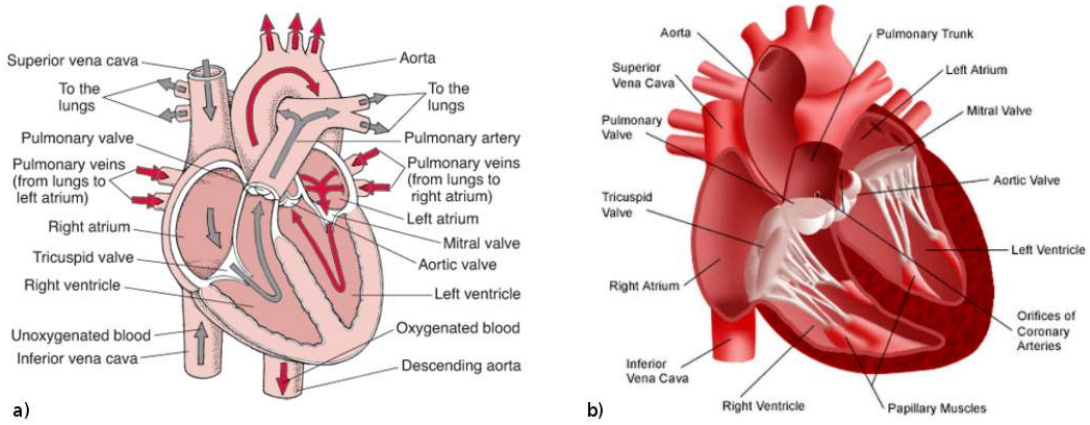

Figure 2.2: Coronal view of the interior of the heart, showing (a) De-oxygenated blood (gray arrows) and oxygenated blood (red arrows) flow through the heart and (b) key anatomical structures of the heart. Figure adapted from [3].

2.1.3 Cardiac working cycle

The RA collects de-oxygenated blood from the body, through the superior vena cava (SVC). Then, it pumps the blood to the RV via the tricuspid valve (Figure 2.2 a). Once the RV is filled with blood, it pumps the blood into the pulmonary arteries, through the pulmonary valve to the lungs, where it loses carbon dioxide (CO_2) and gains oxygen (O_2) (Figure 2.2 (a), gray lines). Subsequently, the LA collects the oxygenated blood from the lungs via the pulmonary veins (PV). Then, it sends the blood to the LV through the mitral atrioventricular valve (Figure 2.2 (a)). Finally, the oxygenated blood inside the LV is pumped through the aortic valve into the aorta and the rest of the body, where the blood loses O_2 and gains CO_2 (Figure 2.2 (a), red lines).

2.1.4 Cardiac electrical conduction system

The action of pumping blood, to either the lungs or the rest of the body, is primarily carried out by the contraction of heart muscle cells, known as cardiac myocytes (described in section 2.1.5). This activity is produced by electrochemical impulses transmitted from one cell to another. Waves of electrical excitation are initiated by auto-rhythmic cells which form the sinoatrial node (SAN), located in the RA (Figure 2.3). Then, the electrical impulse is spread to all cells of the left and right atrium [4, 1].

After propagating through the atria, the fibrous skeleton prevents excitation from the atria to reach the ventricles. However, the atrioventricular node (AVN) provides a conduction pathway from the atria to the start of the Purkinje's fiber (PF) network (Figure 2.3). At the AVN, a time delay, due to slow conduction, is produced to allow

complete contraction of the atria. This delay also allows the ventricles to be filled with blood before the electrical impulse reaches them. In the event of SAN dysfunction, cells in the AVN can act as a subsidiary pacemaker and start the electrical activity in the heart [4, 1].

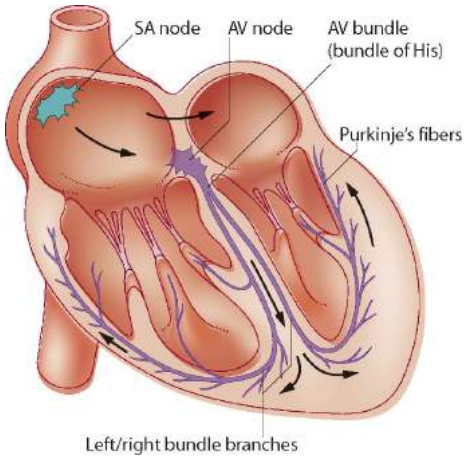

Figure 2.3: Illustration of the conduction system of the heart. The black arrows represent the direction of the electrical wave through the heart. Figure adapted from [5].

The electrical wave propagates to the ventricles through a series of branched tissue structures. First, the AVN transmits the electrical impulse to the bundle of His (Figure 2.3), and then the electrical impulse is spread into the ventricle walls, via the PF network. This activity starts in the apex and then propagates to both left and right ventricles. The outcome is the contraction of the ventricles, and therefore, the pumping of blood to the lungs and the whole body. The PF network ensures synchronous contraction due to the multiple activation sites.

2.1.5 Cardiac electrophysiology

As previously mentioned, myocardiac cells with pacemaking activities form the conduction system of the heart which includes the SAN, the AVN and the PF network as shown in Figure 2.3. The rest of the heart, including the atria and ventricles muscles, consists of mostly contractile cells with the capacity to transmit electrochemical impulses. However, each type of cardiac cell has different electrophysiological and morphological properties which yield to differences in their electrical action potentials. [6, 4].

Membrane potential

All myocytes are surrounded by a phospholipid bilayer which is frequently referred to as the sarcolemma or cell membrane. Across it, there is a resting potential due to the different extra- and intra-cellular ionic concentrations on each side of the membrane. However, there are different proteins that allow and control the flux of specific ions into and out of the cell via elaborated sequences of opening and closing mechanisms of protein-formed ion channels (Figure 2.4 b). These channels can be: passive (ion channels), which allow the flux of ions in the direction of the electrochemical gradient; active (ion pumps), which contribute to the flux of ions against the concentration gradient; and ion exchangers, which move ions in either direction across the membrane. The difference in the transmembrane potential is known as the membrane potential. The resting membrane potential in working myocardial cells is close to -80 mV [7].

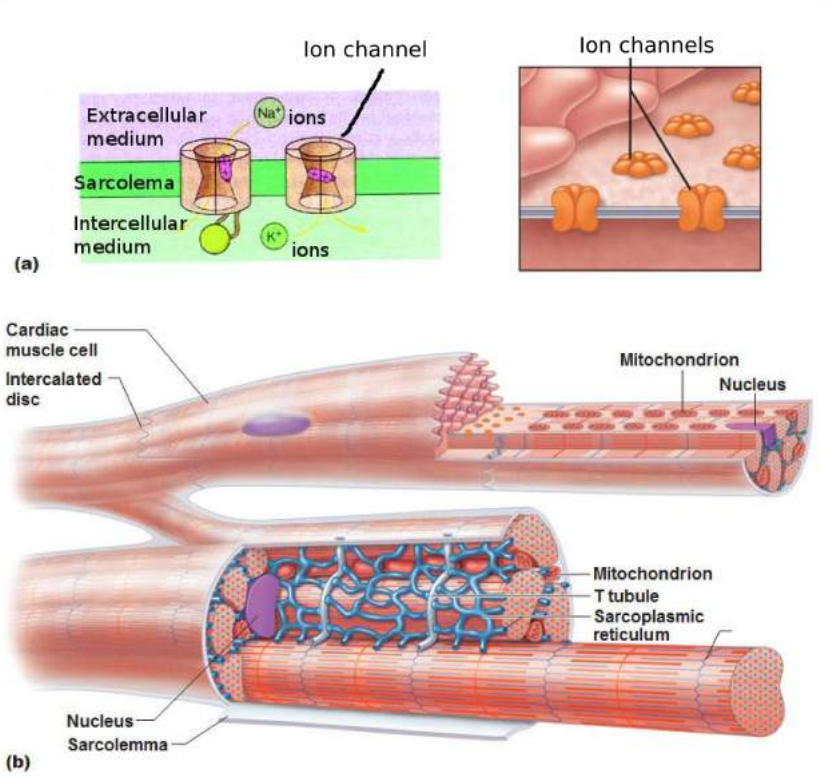

Figure 2.4: Illustration of ion channels (a) and cardiac muscle cells (b), where the extra-, intra-cellular mediums and the sarcolema can be observed. Figure adapted from [2] and [8].

Action potential (AP)

The change that gives rise to a positive membrane potential is known as membrane depolarization. Subsequently, the change that returns the membrane potential to

a negative value is known as membrane repolarization. The change in membrane potential over time is known as action potential (AP) (Figure 2.5). This electrical transient can be propagated through the whole heart, by transferring the impulse from cell to cell, through gap junctions which electrically couple the cells and allow the flux of ions between them (Figure 2.4 a).

The morphological characteristics of an AP, such as shape and duration, is mainly determined by the transmission of ions across the cell membrane. This ion flow produces different types of electrical inward (from outside to inside the cell) or outward (from inside to outside the cell) currents, I, which contribute to the AP. The electrical cycle of a cell can be divided into five phases, one describing the diastolic interval (resting potential) and the other four the evolution of the AP (figure 2.5).

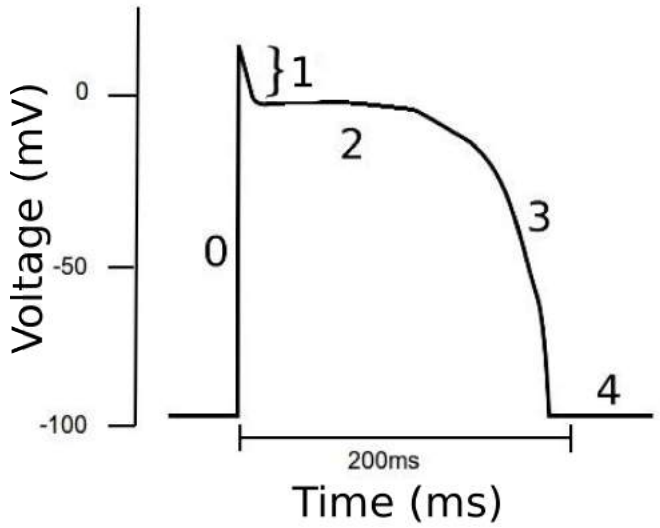

Figure 2.5: Illustration of a generic cell action potential (AP). The 5 phases can be observed in the Figure and are denoted by the numbers: 0 to 4.

Phase 0 is initiated by a rapid depolarization of the membrane (Figure 2.5). It is mainly produced by the activation of sodium (Na) current channels (I_{Na}), which results in an inward flow of Na^+ ions into the cell. At the end of this phase the potassium (K) current (I_K) is activated, this means the depolarization is finished.

Phase 1 is characterised by the rapid repolarization of the membrane, produced by activation of the transient outward K^+ current channels, I_{to}, and the inactivation of I_{Na}. This can be seen as a small downward notch in the action potential, which follows the rapid depolarization (Figure 2.5).

Phase 2, known as the plateau phase, is usually an equilibrated potential produced by the balance of inward and outward currents (Figure 2.5). The inward current is primarily composed by L-type Calcium current I_{CaL}. Meanwhile, the outward current is principally produced by efflux of K^+ to the exterior of the cell, carried by the activation of both rapid (I_{Kr}) and slow (I_{Ks}) components of I_K current channel. Furthermore, the current exchanger of Na^+ and calcium (Ca^{2+}) ions, I_{NCX}, also contributes to the plateau phase.

Phase 3 is usually the last and faster period of re-polarization, which can be seen as the rapid downslope in the AP (Figure 2.5). This is primarily produced by the efflux of K^+ ions to the exterior of the cell, which are carried out by I_{Ks}, I_{Kr} and the inward rectifying potassium current I_{K1}. During this phase, the L-type Ca^{2+} channels close and stop the influx of Ca^{2+} ions into the cell.

Phase 4 is known as the refractory period, during which several channels are inactivated and the cell returns to its resting potential (Figure 2.5). The resting potential (˜80mv) is mainly maintained by the Na^+ and K^+ pump, the I_{NCX} exchanger current, I_{K1} current and background currents.

The shape and duration of the AP vary in each myocardial cell and depend on the different kinetics and current density expressed in each type of cell.

2.1.6 Cardiac arrhythmias

An alteration in the cardiac electrical conduction system can produce cardiac arrhythmias, which are defined as an irregular heartbeat or any period without cardiac rhythm [9, 10]. Cardiac arrhythmias affect about 2-3% of the population worldwide and are one of the principal causes of cardiovascular deaths worldwide [11, 4]. There are different types of cardiac arrhythmias, fast atrial arrhythmias (FAA) being one of the most relevant, which includes atrial tachycardia (AT), atrial fibrillation (AF) and atrial flutter (AFL). An abnormal slow heart rate is called bradycardia or bradyarrythmias and can be caused by a disruption of the electrical conduction signal, which can lead to heart failure and sudden death [11, 4]. In addition, myocardial ischemia, which arises from the lack of blood in the cardiac tissue, can also promote abnormal excitation wave conduction and repolarization patterns, leading to cardiac arrhythmias [12, 4]. All of the above conditions may lead to heart failure and potentially sudden cardiac death.

Unfortunately, the 12-lead ECG (detailed in section 2.4), which has been implemented as a standard evaluation procedure for cardiac arrhythmias diagnosis for

multiple decades [6] has shown to be insensitive or provides insufficient information for satisfactory identification and correct location of the source of FAA or ischemia [13, 14] which are the focus of this project.

Fast atrial arrhythmias

FAA can reduce cardiac output and lead to ventricular arrhythmias and further complications, such as sudden cardiac death and stroke [11, 4]. Such rapid activity may be associated with focal ectopic activity (rapid and irregular spontaneous excitation originating from regions of the heart other than the SAN), re-entrant (self perpetuating) excitation and multiple wavelets [15, 16, 4]. AT is associated with rapid and regular ectopic focal activation of the atria [11, 4]; AFL is associated with re-entrant excitation patterns or self-perpetuating loops across the atria [11, 4], whereas AF is characterized by irregular heartbeats of the atria [11, 4]. Identifying the presence and source of such activity in a non-invasive way may prove vital in diagnosis and treatment of cardiac disorders, such as targeting ablation therapy of which success rate is not entirely satisfactory. This unsatisfactory success rate may lead to repeated operations leaving significant portions of scar tissue which can induce further complications [17]. Invasive methods, such as endosurface mapping has proven to be useful in locating the source of AF, however, they can induce further complications during surgery [18]. Identifying the location of such activities (for example the anatomical location around which leading circuit re-entry occurs) with a non-invasive method presents a greater challenge, due to irregular waves [19]. However, it offers the potential to assist in target catheter therapy, increasing the success rate and reducing the need for repeated operations [6].

Cardiac ischemia

Ischemic heart disease is one of the principal causes of death in developed countries and worldwide [11, 4]. Coronary artery occlusion can cause, within hours, cell death in ischemic myocardium. This results from a lack of blood flow to the heart which decreases, partially or completely, the oxygen supply to the cell, causing irreversible damage to the tissue [4, 14]. Therefore, significant ischemic regions within the heart can reduce the cardiac output, because these cells are unable to contract [4]. Furthermore, the standard diagnosis method, 12-lead ECG (described in section 2.4), has been found to be insensitive in many cases such as silent ischemia, in which ECGs may only differ by 15-30% as compared to normal patients [14, 20]. Other non-invasive techniques, such as magnetic resonance imaging are believed to be far more sensitive to the detection of ischemia [21]. However, they only detect cardiac structures, not electrical conduction patterns. Furthermore, they are highly expensive and time consuming, and therefore not practical for day-to-day, bedside

monitoring and detection of asymptomatic ischemia [22, 23]. Therefore, being able to detect, quantify and locate the site of acute transient ischemic regions in the heart by non-invasive techniques is a clinically important challenge.

2.2 Mathematical models of the heart

Computational modelling can provide a convenient and reliable framework to investigate and predict the relation between cardiac arrhythmias and non-invasive diagnosis methods. In addition, Computer simulations can overcome some of the problems that are faced experimentally/clinically by reproducing the behaviour of a system with different characteristics, dissecting the results in an arbitrary number of ways and re-running simulations an arbitrary number of times with different parameters.

In this section, a brief introduction of the mathematical cardiac models used in this Thesis will be provided for completeness of reviewing the research field, as it is not the aim of this study to develop models for simulating cardiac cells. In the next chapter (Chapter 3) a mathematical description of the electric and magnetic field propagating through a volume conductor will be presented.

Different mathematical formulations of the cell membrane, myocyte function and the propagation of the electric and magnetic field through a volume conductor have been developed over the last decades [24, 6]. Most of the models are based on simple assumptions involving the cellular membrane, ion currents and electrical density in order to reduce computing time [6].

2.2.1 Equivalent electric circuit model of the heart

Generally speaking, the electrical behaviour of a cell can be described by an equivalent circuit model (Figure 2.6), with a capacitance, C_m, representing the membrane and a voltage V_m which is the difference between the potential inside the membrane, ϕ_{in}, and the potential outside the membrane, ϕ_{ex}, i.e.,

$$V_m = \phi_{in} - \phi_{ex}. \tag{2.1}$$

Each ion current, I_X, is associated with a conductivity, g_X, and a potential difference, V_X, which is the driving force of the current across the channel of the respective ion, X, (Na for sodium, Ca for calcium, etc). The sum of all the active ion currents is given by the total current:

$$I_{ion} = I_{Na} + I_K + I_{Ca} + \ldots, \tag{2.2}$$

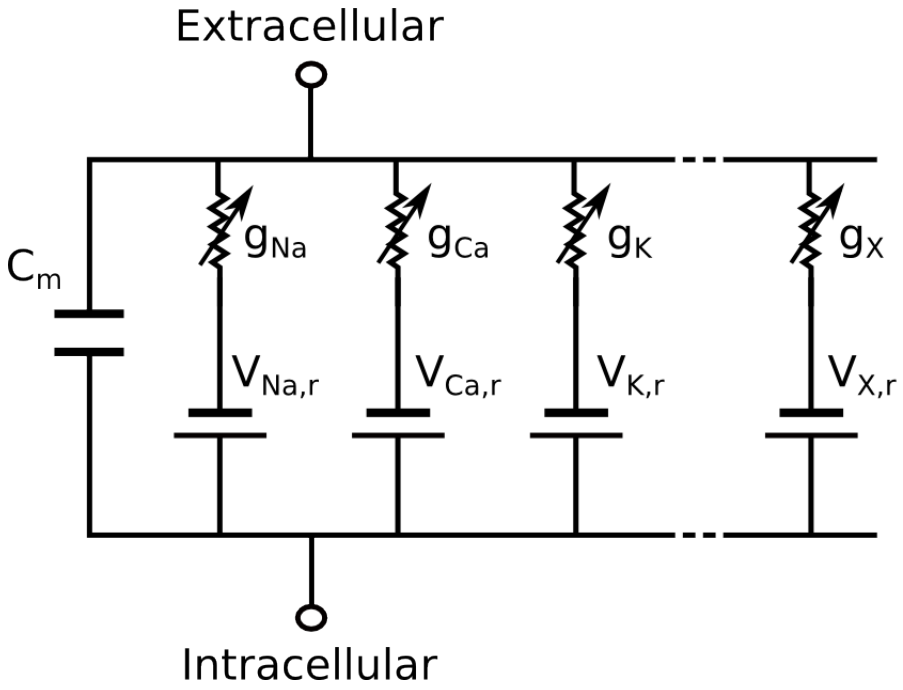

Figure 2.6: Equivalent circuit model of a cardiac cell. C_m is the capacitance of the cell membrane, g_X is the conductivity and V_X the driving force of the ionic currents. Figure adapted from [6]

.

Therefore, from Figure 2.6 and due to conservation of charge (Kirchhoff's circuit laws) [6], the change of the potential with time across the membrane can be described as

$$C_m \frac{dV_m}{dt} + I_{ion} = 0, \tag{2.3}$$

Equation (2.3) relates the total ionic current with the transmembrane potential, and can be used to determine the AP (see section2.2.3). Furthermore, the driving force V_X is related to the Nernst potential described by the Nernst equation (equation 2.4) [6].

2.2.2 Nernst equation

The Nernst equation is a thermodynamic equation which describes the potential difference produced by the ionic concentration, $[X]$, on both sides of a membrane. When the equilibrium is produced between the chemical concentration gradient and the electrical gradient, the potential difference, E_r, is given by [6].

$$E_{X,r} = \frac{RT}{Z_X F} ln \left(\frac{[X]_{ex}}{[X]_{in}} \right), \tag{2.4}$$

where, R is the ideal gas or universal gas constant, T is the absolute temperature,

F is the Faraday constant (magnitude of electric charge per unit of electrons), Z is the charge of ion X, and $[X]_{in}$ and $[X]_{ex}$ denote intracellular and extracellular concentrations of X, respectively. At the Nernst equilibrium potential, E_r, the current across the cell membrane is equal to zero, i.e. the net flow of charge through the ion channel is zero.

2.2.3 Hodgkin-Huxley model

One of the first models to describe the electrical behaviour of a cell membrane, was the Hodgkin-Huxley model, first presented by Alan Lloyd Hodgkin and Andrew Huxley in 1952 [25]. They proposed that the current of a particular ion, I_X, can be determined as the product of voltage difference $V_m - E_{X,r}$ and the channel conductivity, g_X, as follows

$$I_x(V,t) = (V_m - E_{X,r})g_x(V,t). \tag{2.5}$$

Therefore, each ion experiences a net driving force proportional to $V_m - E_{X,r}$, which drives the movement of ions across the membrane.

The Hodgkin and Huxley model is a mathematical model based on an equivalent circuit, formed by three X components: sodium (Na), potassium (K) and a leakage (l) [25] (Figure 2.6).

The model was able to represent the activation and inactivation mechanisms of ion channels by considering the maximal constant conductance of each ion as $\overline{g}_{max}$:

$$g = m^a h^b \overline{g}_{max}. \tag{2.6}$$

Where a and b are numbers specific for each ion and generated empirically, whereas, m and h are the activation and inactivation variables of each conductance. If the value of m (or n) represents the proportion of channels in the activated state (or inactivation states). Hence, the proportion of channels not in the activated state (or not inactivation states) must be $1-m$ (or $1-n$). If α_m is related to the opening of the gate (α_n to the closing gate), then the rate of change of opening will be given by $(\alpha_m(1-m))$ (and the closing $\alpha_n(1-n)$).Therefore if this two variables are time dependent, then the rate change in m and n are given by Rush and Larsen equation [26]:

$$\frac{dm}{dt} = \alpha_m(1-m) - \beta_m m, \tag{2.7a}$$

$$\frac{dh}{dt} = \alpha_h(1-h) - \beta_h h. \tag{2.7b}$$

where, α and β are time independent functions of the potential difference in the membrane. A solution of the equation (2.7), can be given as

$$m(t) = m_\infty - (m_\infty - m_0)e^{\left(-\frac{t}{\tau_m}\right)}, \tag{2.8}$$

where m_0 is the value of m at $t = 0$ and

$$m_\infty = \frac{\alpha_m}{\alpha_m + \beta_m}, \tag{2.9a}$$

$$\tau_m = \frac{1}{\alpha_m + \beta_m}. \tag{2.9b}$$

Here, equation (2.9a) represents the steady-state value of the gate and equation (2.9b) the time constant.

Equation (2.3) is the equation that describes the equivalent circuit in Figure 2.6, and if we consider three ion channels with the assumption given by the Hodgkin-Huxley model (equation (2.5)) and equation (2.6), equation (2.3) becomes:

$$C_m\frac{dV}{dt} = -\overline{g}_K n^4(V - E_{K,r}) - \overline{g}_{Na} m^3 h(V - E_{Na,r}) - \overline{g}_l(V - E_{l,r}) + I_{ap}. \tag{2.10}$$

Here $\overline{g}_i$ is the maximum conductance for each channel i, and $E_{i,r}$ is the equilibrium potential for each channel i. Each channel i, stands for potassium K, sodium Na and the leakage l. The activation and inactivation mechanism are expressed by the gating variables m, n and h. I_{ap} is the applied current, or stimulus current flowing across the membrane. Thus, Hodgkin and Huxley were able to use this model to replicate experimental measurements and received the Nobel prize in recognition for their achievement.

The Hodgkin-Huxley model has been extended to different models which included many different combinations of ion channels, each with their own variations in gating equations. However, there are some processes that can only be described by a Markov Chain model, which is the topic of the subsequent subsection.

2.2.4 Markov chain model

A Markov chain model describes a random process through transitions from one state to another and assume statistical independence. The main characteristic of this model is that the next state only depends on the current states and is independent of any previous states.

The main difference between Hodgkin-Huxley formulation and Markov chain models is that the latter considers the state of each ion channel to be state dependent, and can include many different states, such as open, closed and inactivated.

This formulation allows the description of complex interactions between different states controlled by random processes through stochastic techniques [6]. This behaviour is a more accurate description of some currents, which the Hodgkin-Huxley model may be unable to predict.

In general, the Markov chain formulation also works under the assumption that, the number of ion channels in a certain possible state is depicted as a fraction (between 0 and 1) which changes with time. These channels are expressed by chemical transition formulations, which outline the average behaviour of thousands of individual channels described by multiple differential equations [6]. Therefore, its computational cost is increased considerably due to the large set of differential equations to be solved. However, Markov Chain models are best suited when a more detailed description of the currents is needed and which Hodgkin-Huxley models cannot provide.

Both Markov chain and Hodgkin-Huxley models can describe the AP generation. In this study mostly Hodgkin-Huxley formulation based models were used to produce AP inside the heart.

2.2.5 Action potential propagation

In this section, an overview of modelling AP propagation, based on [6], is presented; further details can be found in [24, 27]. The bidomain equation, first proposed by Miller and Geselowitz in 1978 [28], is one of the main approaches to describe the AP propagation. The process of describing every cell of the heart has around 10 billion sets of parameters at each time instant, thus, computationally speaking, it is not possible to model. Therefore, the bidomain model does not describe every single myocyte inside the heart. Instead, it homogenizes the properties of the myocardiac cells to simplify the modelling of the heart tissue, and thus, the whole heart. In other words, myocytes are considered to be part of a continuum which may be arbitrarily

divided.

The first assumption of the bidomain model is to separate each point of the whole heart into two domains. The two domains are associated with the intracellular and extracellular medium. The two domains exist and overlap in the cardiac muscle, i.e., each point in the myocardium lies in both domains. Therefore, from Ohm's Law, for each point it holds:

$$\vec{J}_n = -\sigma_n \nabla \phi_n, \tag{2.11}$$

where, n represents the intra- or extracellular medium, σ_n, ϕ_n and $\vec{J}_n$ are the conductivity, potential and current density of each medium, respectively. As the two equations hold for the same point and due to conservation of current:

$$\nabla \cdot \vec{J}_{in} = -\nabla \cdot \vec{J}_{ex}. \tag{2.12}$$

Combining equation (2.12) with equation (2.11), it is possible to write

$$\nabla \cdot \sigma_{in} \nabla \phi_{in} = -\nabla \cdot \sigma_{ex} \nabla \phi_{ex}. \tag{2.13}$$

Now, from the previous definition of the transmembrane potential, V_m (equation (2.1)), the equation (2.13) can be rewritten in terms of V_m and the extracellular potential ϕ_{ex}. Then, by subtracting $\nabla \cdot \sigma_{in} \nabla \phi_{ex}$, from both sides, the bidomain equation can be written as

$$\nabla \cdot ((\sigma_{in} + \sigma_{ex}) \nabla \phi_{ex}) = -\nabla \cdot (\sigma_{in} \nabla V_m) \tag{2.14}$$

The last equation relates the extracellular and the transmembrane potentials. Now, as the stimulus current, I_{ap}, crosses the membrane, it follows that:

$$\nabla \cdot \vec{J}_{in} = \nabla \cdot \vec{J}_{ex} = A_m I_{ap}, \tag{2.15}$$

where, A_m represents the membrane surface per volume of tissue. Therefore, by comparing equations (2.14) and (2.15), it is straightforward to arrive to:

$$\vec{J}_{in} = -\sigma_{in} \nabla V_m. \tag{2.16}$$

The last equation is used to compute the intracellular potentials. Now, by introducing equation (2.3) in equation (2.15), it is possible to obtain

$$\nabla \cdot (\sigma_{in} \nabla \phi_{in}) = A_m \left(C_m \frac{\partial V_m}{\partial t} + I_{ion} \right), \tag{2.17}$$

where, as previously defined, C_m is the membrane capacitance and I_{ion} is the

ionic current. Therefore, rewriting equation (2.17) in terms of V_m, and subtracting $\nabla \cdot (\sigma_{in} \nabla \phi_{ex})$ from both sides of the equation, an alternative form of the bidomain equation can be obtained:

$$\nabla \cdot (\sigma_{in} \nabla V_m) + \nabla \cdot (\sigma_{in} \nabla \phi_{ex}) = A_m \left(C_m \frac{\partial V_m}{\partial t} + I_{ion} \right). \tag{2.18}$$

Therefore, from equation (2.14) together with (2.18) the transmembral potential can be computed. As long as the appropriate boundary conditions are included, i.e., there is no intracellular current flowing out of the heart, the body is a passive conductor and the extracellular potential and the body potential, at the surface of the heart, are the same.

However, the computational cost for solving these coupled differential equations is still very high, due to the large scale of the problem and the non-linearity of single cell models. Therefore, another approximation is usually done, and this leads to the monodomain equation, which is another approach to the AP propagation model.

The monodomain model assumes that the two domains are equally anisotropic ($\sigma_{in} = k\sigma_{ex}$). Thus, the set of coupled equations (2.14) and (2.18), can be combined to generate the monodomain equation

$$\nabla \cdot (\sigma \nabla V_m) = A_m \left(C_m \frac{\partial V_m}{\partial t} + I_{ion} \right), \tag{2.19}$$

where, σ is defined as $\sigma^{-1} = \sigma_{ex}^{-1} + \sigma_{in}^{-1}$, it provides the change of the membrane potential, V_m, in an interval of time. Recently, improvements over the monodomain equation have been perform by including different parameters, e.g., Bueno-Orovio et al. [29], which used fractional diffusion models to described structural heterogeneity.

2.2.6 Numerical methods for heart modelling

There are many numerical methods that can be used to solve the mathematical models describing the behaviour of the heart. The models used in this Thesis used the forward Euler method (FUM) together with the finite difference method (FDM), therefore, in this section only these two are described. Furthermore, it was not the aim of this Thesis to develop a new cardiac model.

Forward Euler method

The FUM is an explicit and efficient method to solve integral equations numerically, which can predict the state of a system after a time interval, given the state at the current time. If we consider a certain function $F(y, t)$, with initial variables, (t_0, y_0),

and, under the assumption that the change of F is negligible over some small interval, Δt, then the state of the system at, t, time can be given by

$$y_{t+\Delta t} = y_t + \Delta t F(y, t) \tag{2.20}$$

Therefore, the evolution of the system through time can be predicted with a relatively small time step, Δt, between each successive point. The small time steps are necessary to ensure stability and to ensure an accurate solution is obtained [30]. Although this increases the computational cost, this is compensated by its simplicity (more stable methods are by nature more complicated and introduce more computational cost per iteration) [31]. Due to its simplicity, the Forward Euler Method is the method used for heart modelling in this Thesis.

Finite difference method

The FDM is a numerical technique used to calculate the solution of a spatial partial differential equation, such as the monodomain equation (equation (2.19)), by dividing the space into N discrete nodes. If we consider the spacing between each node as Δx, the left side of the monodomain equation (equation (2.19)) can be approximated in the x direction as

$$D\frac{d^2V}{dx} \approx \frac{D}{\Delta x}(V_{x+\Delta x,t}V_{x-\Delta x,t} - 2V_{x,t}) \tag{2.21}$$

where D is the diffusion tensor which includes the conductivity, the membrane capacity and the membrane surface per volume of tissue terms, $V_{x,t}$, $V_{x+\Delta x,t}$ and $V_{x-\Delta x,t}$ are the value of V at time t and at the nodes x, $x + \Delta x$ and $x - \Delta x$, respectively. Then, rearranging the monodomain equation (2.19) and using equation (2.21), we can write

$$\frac{dV}{dt} \approx \frac{D}{\Delta x}(V_{x+\Delta x,t}V_{x-\Delta x,t} - 2V_{x,t}) - \frac{I_{ion}}{C_m} \tag{2.22}$$

Using Forward Euler method, the value of V at a time $t + \Delta t$, can be written as

$$V_{t+\Delta t} \approx V_t + \frac{D\Delta t}{\Delta x}(V_{x+\Delta x,t}V_{x-\Delta x,t} - 2V_{x,t}) - \frac{\Delta t I_{ion}}{C_m} \tag{2.23}$$

Equation (2.23) can be extended to the three dimensional case by applying the same approximations in each direction. This equation, together with Neumann boundary conditions, which set the $\frac{dV}{dx} = 0$ at the edges of the tissue [32], are the one used in this Thesis to model the heart electrical activity. Other methods can also be used to obtain the AP for cardiac modelling (finite or boundary element method), but FDM provides an easy and efficient way to model the electrical activity in the heart [31].

Numerical stability

Solving the previous integral equations via FUM, and for the specific case of gating variables (equation (2.23)-the Rush-Larsen method [26]), then the second term in equation (2.23), $\frac{D\Delta t}{\Delta x}$, can be related to the numerical stability, and its value for convergence to occur has to be less than 0.5 [33]. Therefore, this constrains the value of the time step (Δt) and spatial step (Δx) used for the integration. To confirm stability, the time step used in this study was range between 0.005 - 0.01 ms, while the spatial step was 0.33 mm, all simulations were run for a period of 10 minutes.

2.3 The thorax

The heart is located inside the thorax, which protects it from the outside. There are different types of tissues and organs inside the thorax, such as lungs, the rib cage, muscles and different internal structures. Therefore, the human thorax can be viewed as an inhomogeneous and anisotropic volume conductor, due to its directionally dependent conductivity and non-linear relations in its electrical parameters. Nevertheless, most modelling studies, related to electrocardiac activity, consider the thorax as a homogeneous and isotropic medium, which may not produce a large difference between theoretical and experimental values [34, 35].

2.3.1 Properties of the thorax

The human thorax is not an infinite medium; instead, it is bounded with skin. In general, the heart is located in the centre of the torso (Figure 2.7). It is surrounded by the rib cage and the intercostal muscles. From an anterior view, the breastbone or sternum and the pectoralis muscles can be observed (Figure 2.8a). From a posterior view (Figure 2.8b), the spinal cord is surrounded by thoracic vertebrae, where the rib cage starts, and the muscles of the back, such as trapezius, rhomboideus and teres major can be found (Figure 2.8b).

From a transverse view of the thorax, the position of the lungs around the heart can be observed (Figure 2.7a). Since the apex of the heart is towards the left, the left lung is smaller compared to the right lung, in order to accommodate the position of the heart. For the respiration process, both lungs fill with air and expand at the same time, and with an isometric movement of the intercostal muscles and ribs, it leads to the expansion of the thorax during inspiration and its contraction during exhalation.

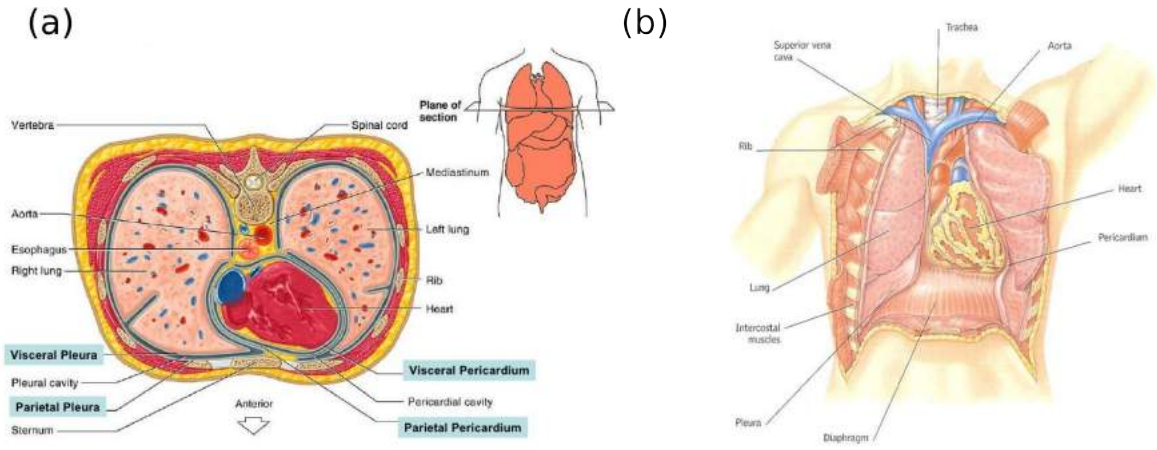

Figure 2.7: Illustration of the location of the human heart inside the body. (a) Cross sectional view. (b) Frontal view. Figure adapted from [36, 37].

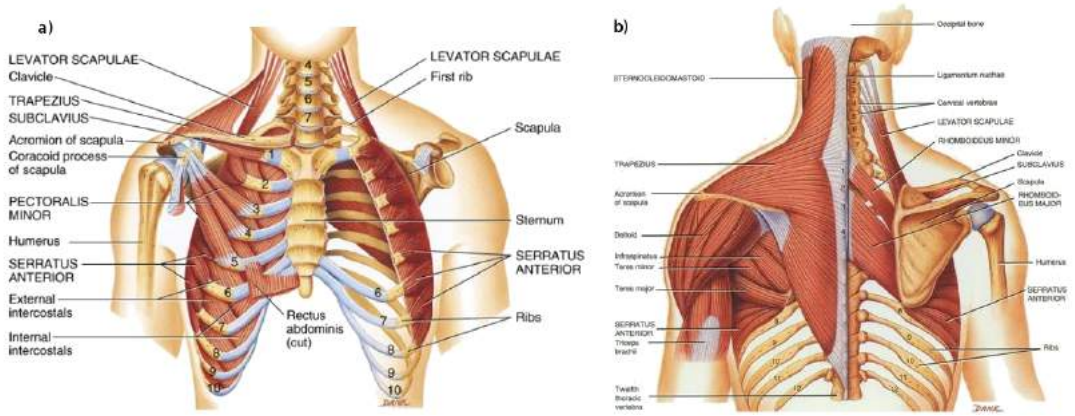

Figure 2.8: Illustration of the upper body musculo-skeletal system. a) Anterior view. b) Posterior view. Figures adapted from [1].

In general, the tissues inside the thorax, in particular the skeletal muscle, are electrically anisotropic, because their cellular structures are composed of parallel long fibres oriented in a specific direction. The electric current at low frequencies cannot flow through the cell membrane [38, 39]. Thus, the conductivity of the tissues strongly depends on the density and distribution of the cells, and on the length of the conductive pathways between them.

Now, taking into account the inhomogeneities already described, and the knowledge that a dipole source declines with the distance r as $\frac{1}{r^2}$ [6, 40], it can be expected that the measurement of the potentials on the body surface is a highly attenuated version of the potentials produced in the heart. However, this potential difference measured with electrodes placed on the surface of the body can be correlated with

the electrical activity in the heart: this process is called electrocardiography and the measurements are known as an electrocardiogram signals (ECGs).

2.4 Electrocardiogram signals (ECGs)

Electrocardiogram signals (ECGs) are measurements of the body surface potential (BSP) produced by the electrical activity in the heart, via electrodes placed on the surface of the thorax. The electrical currents generated inside the heart flow through the heart muscle and the different tissues of the body, depending on its value of conductivity. These currents generate electrical potentials on the surface of the body. Therefore, a potential difference produced between two points on the surface of the thorax where the electrodes are placed generates the ECG.

2.4.1 History of the ECG

It has been more than 120 years since Augustus D. Waller measured the voltage differences between two electrodes placed on the body surface [41]. He found that the frequency of the signals measured was related to the heart rate [6].

As in any research area, several previous studies on measuring the BSP were performed. However, it was in 1903 when Einthoven and co-workers published their results about the ECGs measurement [42], and in several, now "classic", papers [43, 42] the lead theory was introduced, which is the basis of electrocardiography in the modern era.

Einthoven measured the BSP produced by the electrical activity in the heart with a string galvanometer. He placed three electrodes in a triangular configuration; one on each arm and the third one on the left leg. He postulated each electrode measured a potential generated at each vertex of an equilateral triangle, and he assumed the heart, located at the triangle's centroid, was a single, time-dependent, fixed dipole source inside an infinite and homogeneous conductor, where the body was part of it [6].

Due to this landmark in medicine, Einthoven was awarded the Nobel Prize in 1924 [44]. The quality of the ECG signals have gradually improved, as the available equipment and the physical knowledge of the underlying physiological phenomenon have improved. Therefore, different configurations and methods of measuring the ECGs and BSP have been developed.

Lead theory, based on the Einthoven's triangle, was formally introduced around the 1940s and 1950s. It considers the cardiac sources as distributed dipole sources placed inside a three dimensional, finite, irregularly shaped and inhomogeneous medium, i.e., the human body. Both assumptions were first introduced by McFee and Johnston [45], and Burger and van Milan [46].

2.4.2 Lead theory

A lead does not refer to the wires from which the voltage difference is physically measured (these are the electrodes); rather, a lead is the direction from which the electrical activity in the heart is observed. A lead can be interpreted as the measurement produced by the voltage difference of a specific configuration; it can be the difference between two real or artificial terminals. The artificial configurations can be produced using a linear combination of the voltages measured by real electrodes [6].

In order to generate an artificial configuration, the lead theory is based on Helmholtz fundamental principles of field theory. However, an important assumption has to be made, which is to consider the human thorax as a linear volume conductor [6, 39]. This assumption yields two main principles. The first is the superposition principle, which states that the electric field produced from several sources is the same as the arithmetic sum of the electric fields produced by each source separately [6, 39]. The second is the reciprocity principle, which states that the current flowing from a source to a pair of measured points, i.e. electrodes, is the same as if the position between the source and the measured points are interchanged, in other words, the current does not depend on which direction it flows. Another important issue, regarding the lead definition, is the polarity convention. It implies that the "positive" terminal, selected arbitrarily, is seen as having a higher potential in magnitude compared to the "negative" one, which is not always the case.

The gold standard to test and diagnose heart failure is the 12-lead electrocardiogram (12-lead ECG), where, each lead looks at the electrical activity in the heart from a different point, through the position of the electrodes on the surface of the body (Figures 2.10, 2.11). The 12-lead ECG can be constructed using one electrode placed on each limb, and six electrodes placed on the chest (Figure 2.9).

According to Figure 2.9 (a), the electrodes will be labelled in agreement with their location. The right electrode, RA, is located on the right shoulder, and the potential measured on it is ϕ_{RA}. The left electrode, LA, is located on the left shoulder, with a measured potential, ϕ_{LA}. Similarly, the electrode located on the left leg, LF, is

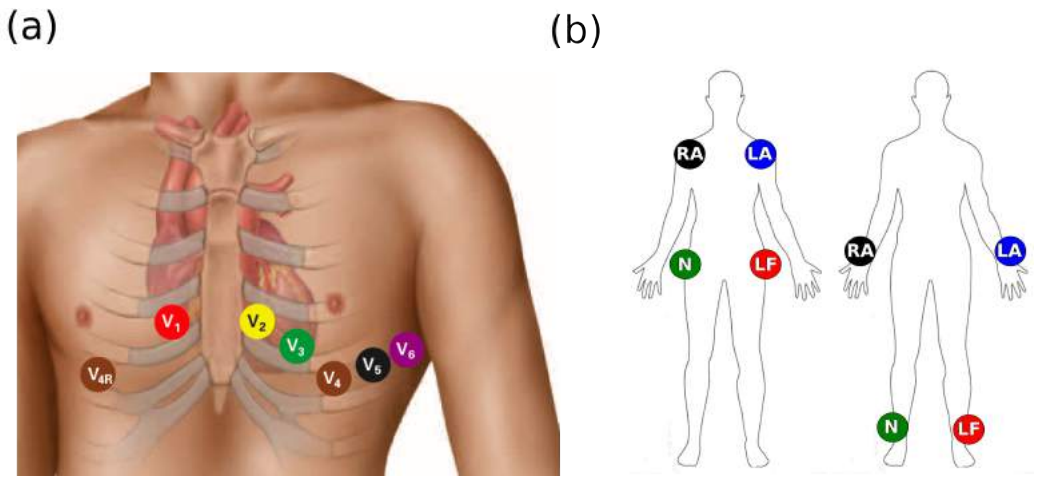

Figure 2.9: Anatomical position of the electrodes for 12-lead ECG recording. a) The locations of the six chest electrodes. b) Two possible configurations for the limb electrodes. The figures were adapted from [47].

called the foot electrode, and its potential measured, ϕ_{LF}. Typically, the electrode located on the right leg, N, is the ground electrode. Therefore, the voltage of the first three leads can be determined by the following equations:

$$V_{Lead\ I} = \phi_{LA} - \phi_{RA}, \tag{2.24a}$$

$$V_{Lead\ II} = \phi_{RA} - \phi_{LF}, \tag{2.24b}$$

$$V_{Lead\ III} = \phi_{LA} - \phi_{LF}, \tag{2.24c}$$

$$\tag{2.24d}$$

From equations (2.24), it is possible to define the first three leads: *Lead I*, equation (2.24a), is the difference of electric potential measured between RA and LA, using RA as the negative terminal. *Lead II*, equation (2.24b), is the difference of electric potential measured between RA and LF, using also RA as the negative terminal. *Lead III*, equation (2.24c), is the difference of electric potential measured between LA and LF, using LA as the negative terminal.

For the remaining leads of the 12-lead ECG, an artificial terminal, the Wilson's central terminal (WCT) is used (equation (2.25):

$$V_{WCT} = \frac{\phi_{LA} + \phi_{RA} + \phi_{LF}}{3}. \tag{2.25}$$

Subsequently, the next three leads are known as the augmented leads. They are formed by one of the electrodes mentioned before, RA, LA or LF, as the positive terminal, and the WCT as the negative terminal. However, as the potential measured

was very small, a consequence of having one electrode on each side of the equation, the convention changed to not include the positive terminal in the WCT calculation [6]. Therefore, the equations for the augmented limb leads are

$$V_{aVL} = \phi_{LA} - \left(\frac{\phi_{RA} + \phi_{LF}}{2}\right), \tag{2.26a}$$

$$V_{aVR} = \phi_{RA} - \left(\frac{\phi_{LA} + \phi_{LF}}{2}\right), \tag{2.26b}$$

$$V_{aVF} = \phi_{LF} - \left(\frac{\phi_{RA} + \phi_{LF}}{2}\right). \tag{2.26c}$$

Lead aVL, equation (2.26a), is formed by electrode LA as the positive terminal and the WCT as the negative terminal, but without taking into account the electrode LA in its computation. In a similar way, Lead aVR (equation (2.26b)) and Lead aVF (equation (2.26c)) are formed with RA and LF electrodes as positive terminals, respectively, and electrode WCT as negative, but without including the positive terminal in its computation.

From the electrode positions and the specific configurations of each limb lead, previously described, it can be observed that each lead "looks" at the heart from a different angle in a coronal plane (Figure 2.10). Starting from *Lead I* at 0^o, and in a clockwise direction: *Lead II* at 60^o, aVF at 90^o, *Lead III* at 120^o, aVR at -150^o and aVL at -30^o

In the same sense, the six electrodes located in the chest area, are denoted as V with a subindex (Figure 2.9). V_1 is located at the right of the breastbone in the fourth intercostal space. V_2 is also placed in the fourth intercostal space but at the left of the breastbone. V_3 is located in the middle of the electrodes V_2 and V_4. V_4 is located in the fifth intercostal space, on the left of the midclavicular line. V_5 is located on the left anterior axillary line, horizontally to the left of V_4. Finally, V_6 is located in the mid-axillary line, horizontally to the left of V_5. Therefore, the voltage potential measured in each electrode, from V_1 to V_6, are named ϕ_1 to ϕ_6, respectively. And so, the chest leads are denoted by

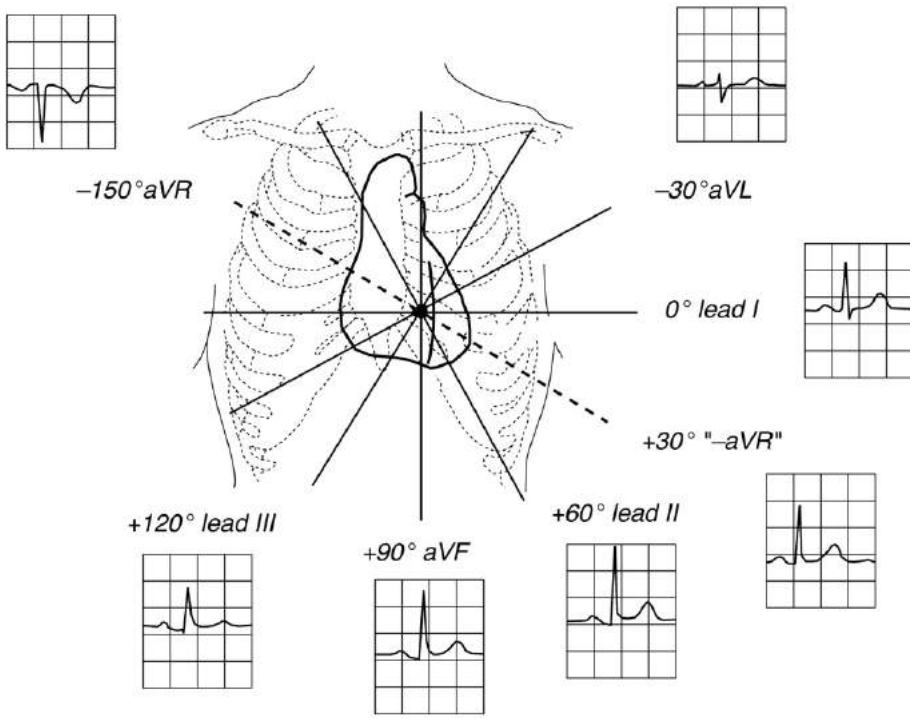

Figure 2.10: Hexaxial reference system. Angular view of each limb lead recording the electrical activity, viewed in the coronal plane. Figure adapted from [48].

$$V_1 = \phi_{V_1} - \phi_{WCT}, \tag{2.27a}$$
$$V_2 = \phi_{V_2} - \phi_{WCT}, \tag{2.27b}$$
$$V_3 = \phi_{V_3} - \phi_{WCT}, \tag{2.27c}$$
$$V_4 = \phi_{V_4} - \phi_{WCT}, \tag{2.27d}$$
$$V_5 = \phi_{V_5} - \phi_{WCT}, \tag{2.27e}$$
$$V_6 = \phi_{V_6} - \phi_{WCT}. \tag{2.27f}$$

Equations (2.27 a to f) are formed by each V_n electrode as the positive terminal, and the WCT as the negative, where $n = 1, \ldots, 6$. Each of them is "looking" at the heart from a different angle in the transversal plane (Figure 2.11).

From each lead's different viewpoint of the heart, the direction of the electrical current propagation in the heart can be determined. If the electrical impulse is flowing towards the positive electrode of a specific lead, it will produce a positive upward deflection in the signal recorded. If it is flowing away from the positive electrode, it will produce a negative downward deflection in the signal recorded. In the same sense, a biphasic deflection will be produced if the direction of the electric

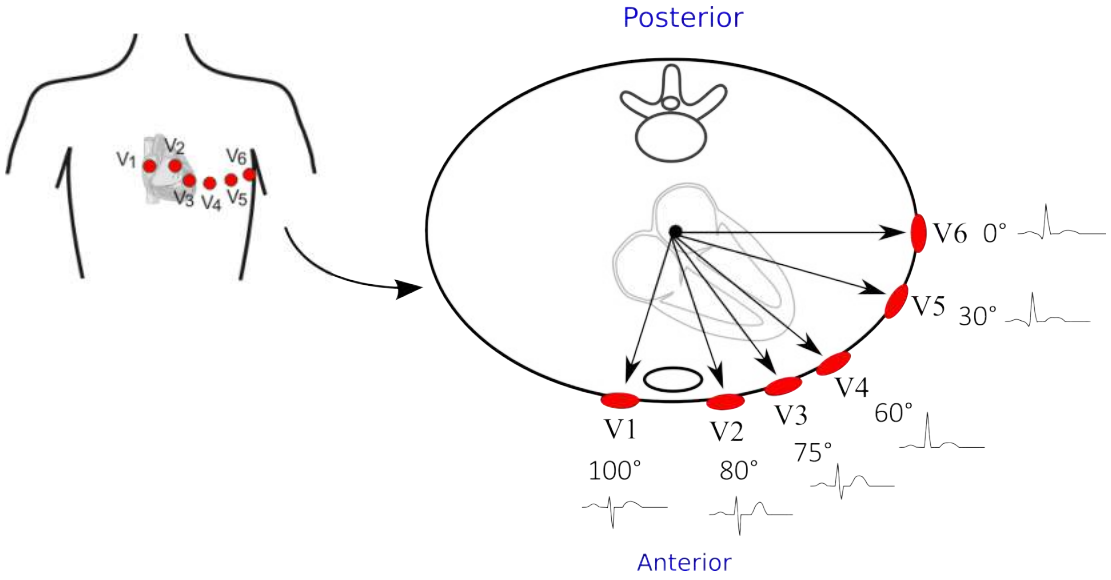

Figure 2.11: Angular view of chest leads (V_1 to V_6), viewed from a cross-section plane. Figure adapted from [49].

propagation vector is perpendicular to the vector between the positive and negative terminals of the lead.

Unfortunately, the 12-lead ECG has its limitations in AF and ischemia diagnosis [14]. Therefore, different multi-lead arrays have been proposed to provide sufficient information to help the diagnosis of these specific cardiac disorders [50].

2.4.3 ECG segments, intervals and waves

An ECG lead is mainly composed of five standard "waves", P, Q, R, S and T (Figure 2.12). Each of them is correlated to the depolarization or repolarization of a specific region in the heart. Therefore, the length of each wave, or complex of waves, provides information about the time duration of each event.

In general, the depolarization of the atria is associated with the P-wave, the QRS complex is produced by ventricular depolarization and the T-wave is produced by ventricular repolarization (Figure 2.12). The convention is that the first upward deflection in the QRS complex is the R-wave, and any downward deflection preceding the R-wave is the Q-wave; thus, any downward deflection after the R-wave is the S-wave [6, 51, 49, 52]. The signals vary in magnitude, depending on which direction of the heart is being considered. Therefore, not all the leads will necessarily have all three Q-, R-, and S-waves in its QRS complex. Although atrial repolarization does occur, it produces a small signal compared with the QRS complex, so it can rarely be measured.

An ECG can be divided into segments and intervals. A segment does not include the wave; it just takes into account the region between the waves [51, 49]. On the contrary, an interval does include the wave and the segment [51, 49]. For example, the PR segment begins at the end of the P-wave until the point where the QRS complex starts, the ST-segment begins at the end of the QRS complex and it finishes at the starting point of the T-wave. Subsequently, the PR interval is the segment from the starting point of the P-wave until the point where the QRS complex begins, and the QT interval includes both the QRS complex and the T-wave (Figure 2.12). The morphology and duration of an ECG of a "healthy patient" can vary significantly.

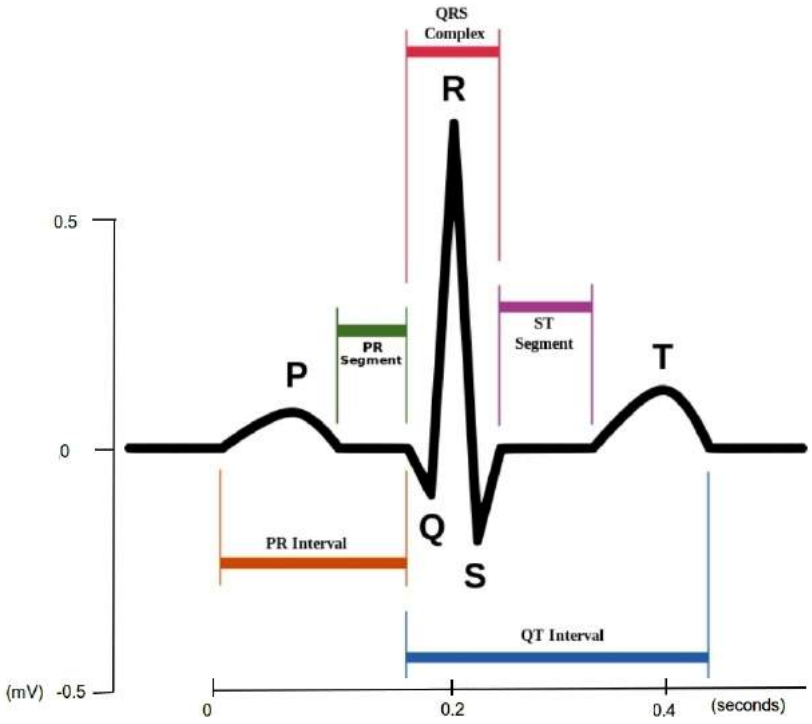

Figure 2.12: Components of an electrocardiography signal, in which all the waves and segments in which it is divided are shown. Figure adapted from [53].

2.4.4 Morphology and duration of ECG

The morphology and duration of the ECG waves, intervals and segments depend on several variables, such as the weight, age, sex, race, physical fitness, body position, etc. [49]. However, most literature tends to agree that a "normal 12-lead ECG" is similarly to Figure 2.13. A summary of the general description made in [6, 51, 49, 52] is described in this section.

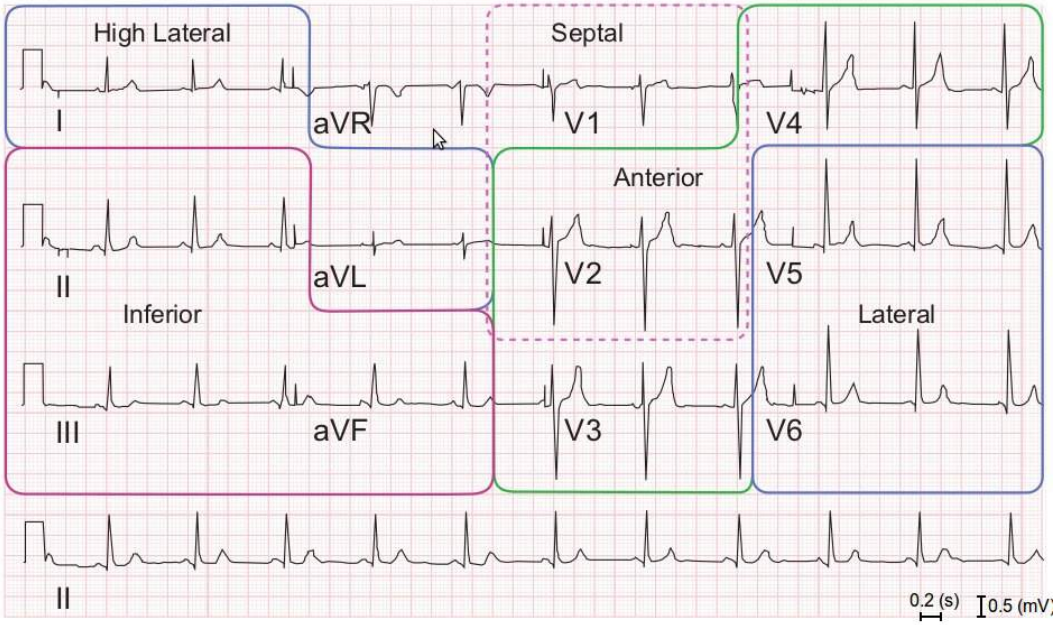

Figure 2.13: 12-lead ECG signal taken from a Caucasian person who does not present any heart disease. Figure adapted from [52].

P-wave and PR interval

In general, the P-wave duration can be interpreted as the time taken by the electrical impulse, which starts in the SAN, to flow through the atria. Meanwhile, the PR interval is the time between atrial and ventricular activation, i.e., the time between atrial and ventricular activation [4]. The P-wave duration is usually around 0.11 seconds. The duration of the PR interval is normally between 0.12 and 0.22 seconds.

The P-wave should be positive in *Lead I*, *Lead II*, aVF and V_4 to V_6, but negative in aVR; it is ofter either positive or biphasic in *Lead III*. There are some discussions about the P-wave profile of aVL [6, 51], but it is generally agreed that it usually has a negative deflection in this lead. V_1 to V_3 are usually positive, but a biphasic wave is acceptable.

QRS complex and ST-segment

The QRS complex duration is the time interval taken for the electrical impulse to flow through the ventricles. The time interval starts from the point at which the first ventricular cells are activated, and ends when both ventricles are excited. There are different QRS complex morphologies among different leads, which is primarily because of the multiple activation points due to the PF network (see section 2.1.4) [4]. The QRS complex duration is usually between 0.08 and 0.12 seconds. The ST-segment duration is normally between 0.08 and 0.12 seconds.

The QRS can vary a lot in the limb leads, whereas it is regularly uniform in the chest leads. There is usually a small negative Q-wave in *Lead I*, aVL, V_5 and V_6, sometimes also presented in *Lead II* and aVF. Then, a positive deflection, R-wave larger than S-wave, can be seen in *Lead I*, *Lead II*, *Lead III* and V_4 to V_6. This is because they are almost entirely determined by the left ventricular depolarization [4]. For the same reason, a large negative deflection (S-wave larger than R-wave) can be seen in leads aVR, V_1 and V_2. Usually, the R-wave gets taller from V_1 to V_6, whereas the S-wave gets smaller in the same direction. However, an S-wave equal or larger than the R-wave in *lead I*, *Lead III*, and *Lead II* is also acceptable in some cases.

The ST-segment is associated with the plateau phase of ventricular AP. It means some leads are constant and usually zero during this segment. Although the ST-segment is completely horizontal in most of the leads, it is also acceptable to have a small elevation in the leads V_2 to V_5 [51].

T-wave and QT interval

The ventricular repolarization is slower than the previously described depolarization process, thus the T-wave is usually broader compared to other waves. In addition, the QT interval can be seen as the duration of ventricular AP, i.e., the total time between depolarization and repolarization of the ventricles. The T-wave duration is usually around 160 ms. The QT interval normally takes less than 0.4 seconds in men, and 0.44 seconds in women.

The T-wave is normally more rounded than asymmetrical. It is positive in leads V_2 to V_6, but inverted in aVR. T-wave of aVF is always positive, however in *Lead III* and V_1, it may be positive or negative. The T-wave has a smaller amplitude than other leads and is usually positive in aVL, but may be negative in some cases. In the case of V_3 a biphasic, inverted or even flat T-wave can be presented depending on the race [49].

Finally, the R-R interval is the time interval of the cardiac cycle and is calculated by taking the difference between two sequential R waves. This is the inverse of the heart rate, which is normally around 60 or 70 bpm, depending on age, complexity, fitness, sex, race, etc [49].

2.4.5 Limitations of the 12-lead ECG

As mentioned before, the 12-lead ECG varies depending on different factors such as anthropometric parameters, sex and race [49]. In addition, cardiac arrhythmias are usually presented as irregular and complex patterns in the different waves and segments, which can be triggered by one or more disorders such as re-entry, multiple wavelets, focal activity or ischemic conditions [15, 16, 4]. Thus, though the 12-lead ECG is the standard tool used to diagnose and monitor cardiac arrhythmias in a clinical environment, it has its limitation in providing detailed information about the origin and location of the disease, which is vital to therapy procedures of such disorders [13, 14]. Therefore, different studies have focused on the prediction, location and treatment of cardiac arrhythmia sources, with invasive [54, 55] and non-invasive methods [56, 50].

Invasive methods, though able to map atrial electrical excitation patterns, can induce further complications during and after the surgery; also they are usually expensive due to the different surgeries that have to be performed [18]. Therefore, recent studies have developed algorithms to non-invasively identify the location of focal sources by using the standard 12-lead ECG [57, 58, 59]. The success rate of these algorithms range from 40% to 70 % [57, 58]. Most are based on the correlation between the location of focal activity and the P-wave morphology or polarity. While they are useful in identifying the origin of focal excitation, current algorithms may not be applicable to identify re-entry or rapid focal activity [57, 58, 59]. Non-invasive methods based on the solution of the inverse problem (see section 2.7) can reconstruct cardiac excitation pattern using the BSP [56, 6], but such reconstructed solutions require further information than the standard 12-lead ECG [56, 6].

Origin and mechanism of ST-segment changes on ECG during ischemia

Abnormal currents flowing through depolarized normal and ischemic regions may results in changes on the ST-segment, either elevation (transmural ischemic regions) or depression (non-transmural ischemic regions).This effects are produced by an increase in the baseline of the AP and a shorter AP duration on the ischemic regions. During non-transmural ischemic conditions, if the depolarizing currents are flowing toward a positive terminal the baseline voltage prior to the QRS complex (normally isoelectric) can be elevated. Then when the ventricles depolarized, all the cardiac muscles depolarized, the ST-segment is recorded as usual and the T-wave may remain positive as well. If this occurs the elevated baseline voltage will give the effect that the ST-segment is depressed relative to the baseline. On the other hand, if

the ventricles are at rest and repolized during transmural ischemic conditions, if the depolarizing current are flowing away from the recording electrode, all the baseline may be depressed except for the ST-segment, therefore it may appeared that the ST-segment is elevated compared to the baseline.

Due to these effects, current diagnosis of cardiac ischemia by the 12-lead ECG has its limitations as some leads are insensitive in many cases and may show unnoticeable differences compared to normal patterns [14, 20]. This suggests that the 12-lead ECG provides insufficient information for satisfactory ischemia diagnosis. Therefore, other non-invasive techniques can be more sensitive to the detection of silent ischemia (i.e. asymptomatic ischemia which does not present as an arrhythmia) [22, 23].

Previous studies have shown that spatially extended recordings of ECG configurations on the torso or BSP maps provide more information for the diagnosis of irregular cardiac conduction and repolarization patterns than the standard 12-lead ECG [20, 23] (see next section - section 2.4.6). This can provide the information needed for the inverse problem solutions and/or the development of multi-lead algorithms. Also, the magnetic field produced by the electrical activity in the heart may provide a greater level of detail of cardiac excitation compared to the body surface potential (see section 2.5), because the magnetocardiograms are more sensitive to currents tangential to the surface of the chest than ECGs [60, 61].

2.4.6 Multi-lead ECG and body surface potential (BSP)

The multi-lead ECG systems are formed by placing additional numbers of electrodes on the body compared to the 12-lead ECG. This can provide further information about the spatio-dynamics of the potential difference in the surface of the body. This technique, which uses many additional leads compared to the 12-lead ECG is known as BSP mapping and allows having a greater spatial coverage of body or torso in order to investigate optimal sites of the heart activity [62]. Several studies have shown that the extra information that body surface ECG measurements produces is useful to generate more accurate non-invasive algorithms and is the basis of the inverse problem solutions [56, 6, 50]. This is because of the strong correlation that has been found between invasive measurements of intracardiac activation rates and multi-lead ECG or BSP [62, 63]. Unfortunately, even though multi-lead body surface ECG can help to improve the diagnosis of cardiac arrhythmias, it is still not practical for day-to-day use and bedside monitoring because of the many electrodes that have to be placed around the torso. Therefore, different studies have focused on finding regions of the BSP with large changes during cardiac diseases compared to normal conditions, in order to reduce the number of electrodes needed and make it more practical for monitoring.

Dipole evolution

Another advantage of the multi-lead body surface ECG is the feasibility to compute the spatial distribution and amplitude evolution of the P-wave dipole [64]. This dipole is obtained with the maximum positive potentials (positive pole) and the minimum negative potentials (negative pole) on the surface of the body at every time step [64]. These poles change in amplitude and spatial distribution across the surface of the body as the atrial activation evolves. Therefore, the atrial dipole can be computed from the maximum positive and minimum negative potentials from the multi-lead ECG P-waves [64].

2.5 Magnetocardiogram signals (MCGs)

A magnetocardiogram (MCG) is the non-invasive measurement of the magnetic field on the surface or outside the body produced by the electrical activity in the heart, the same bioelectrical activity that generates the ECGs. These measurements are more sensitive to currents tangential to the surface of the chest than ECGs and may provide a greater level of detail of cardiac excitation compared to ECG signals [60]. Combined with its high independence to tissue inhomogeneities in electrical resistivity inside the body and on the skin [23, 61], the MCG therefore provides a potential practical alternative to the ECG for monitoring cardiac conditions.

However, it has not been conclusive yet whether or not MCG can provide extra, useful information which increases diagnosis and characterization of cardiac diseases. So far, detailed correlation between the presence of cardiac diseases and the characteristics of the MCG has yet to be established. Direct comparison between ECG and MCG under the same conditions is still a challenge in clinical environments, but can be easily done with mathematical models as described in details in Chapter 3 (in this section a brief introduction was presented).

2.5.1 History of the MCG

The magnetic field produced by the electric activity in the heart was first measured in 1963 by Baule and McFee [65], however the signals were very noisy due to the large magnetic background. David Cohen in 1967 [66] obtained heart measurements inside a magnetic shielded room to avoid the background noise. The noise was significantly reduced, however, due to the measurement system, coil detectors, the signals still had a large level of noise in order to be used in the clinical environment. Therefore, MCG signals remained in a research stage until the 1970 when sensitive superconductor systems (super quantum interference device - SQUID), introduced by Zimmerman

[67], were combined by magnetic shielded room, to produced clearer MCG signals comparable to ECG [68].

Recently, it has started to become a new measurement method in some clinical laboratories due to the introduction of new electronics with multi-channel and high-temperature superconductor systems [6]. Unfortunately, it still has some technical problems such as the use of sensors based on liquid helium/nitrogen and the need of a magnetically shielded room which makes it more expensive [6, 69]. Nevertheless, it has been prove that MCG has improved signal measurements when compared to ECG, such as a multi-channel lead configuration that can be used at the bedside due to its completely non-invasive measurement system. Therefore, different groups have been trying to create databases to standardize the data measurement and analysis and develop compatibility system with ECGs [61, 23].

2.5.2 MCG segments, intervals and waves

The biomagnetic field measured on the surface or outside the body is produced by the electrical activity created by the transmembrane potential of the cardiac cells, i.e., MCGs and ECGs are generated by the same electrical source (the heart). Thus, an MCG has the same general morphology as an ECG (Figure 2.12), for each corresponding segment, interval, P-wave, QRS complex and T-wave [6]. However, they do not necessarily have the same polarity, so, the different information between ECG and MCG is still controversial.

2.6 Forward problem

The forward problem in electrocardiography involves computing the magnetic and/or electric field across the human body or thorax produced by bioelectrical activity in the heart, having previous knowledge of the body shape and electrical properties. These two fields are produced by the same bioelectric source, the human heart, the location and properties of which are also known (Figure 2.14). Going in the opposite direction of the forward problem is called inverse problem, and it is described in the next section (section 2.7) (Figure 2.14).

There have been different approaches to solve the forward problem: experimentally, analytically and numerically. Each of them has its advantages and limitations, nevertheless, in most of the cases two main assumptions are usually used to simplify the description of the problem: considering the human thorax as a linear-homogeneous volume conductor, and a quasi-static approximation [6, 39]. However, before giving a more detailed description of these two assumption (section 2.6.2), a

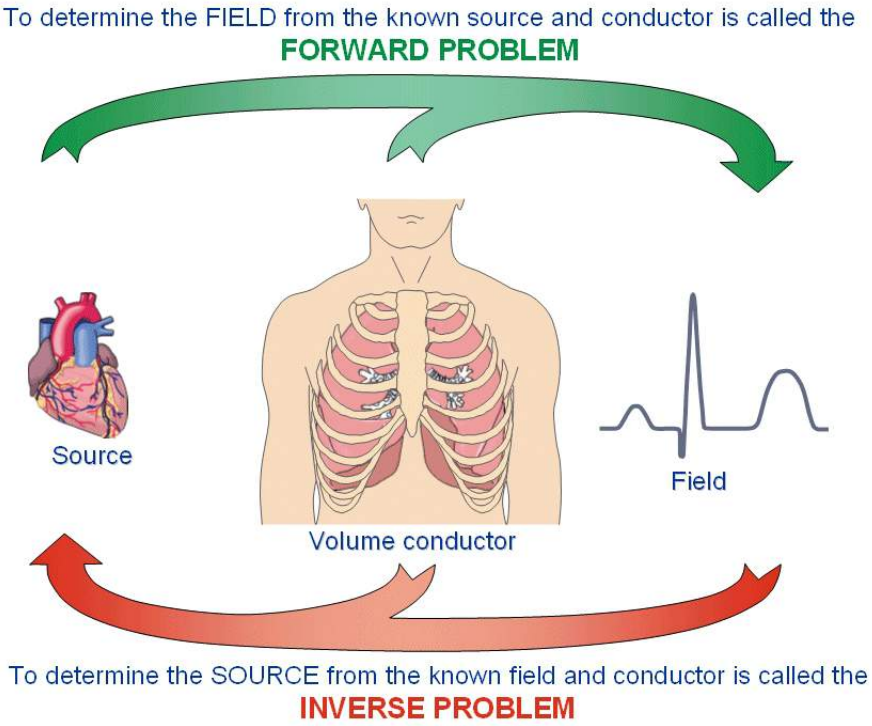

Figure 2.14: Diagram of the forward problem (green line), and the inverse problem (red lines) in electrocardiography. Figure adapted from [39].

brief description of the historical development of the forward problem in cardiology is presented in the next section (section 2.6.1).

2.6.1 History of the forward problem in cardiology

The theory of classical electromagnetism has been well known since Maxwell summarized the electromagnetic theory in four equations in 1873 [40]. This includes the potential propagation through a volume conductor generated by internal current sources, which is the base of the forward problem solution in cardiology.

The history of the forward problem in cardiology is similar to the history of the ECG measurement. In general, simple models which are able to reproduce the measurements, may yield to a better understanding of the problem.

The first approach to forward problem solutions was the construction of physical models. Before the era of computer modelling, the only two options to perform a model experiment were electrolytic tank models and in vivo animal measurements. In 1946, Burger and van Milaan [46] worked with a human torso shaped tank for the first time. They had a dipole representation of the cardiac electrical activity, and used sandbags to model the lungs. This model helped the understanding of

the potential propagation through the body and yielded a more accurate clinical determination of the ECG. For the second approach, canine models with modified intracavity characteristics [70] have been mostly used to model and measure the BSP. Even though a complex set up is needed in order to avoid the human influence in the measurements [71], this physical model is still widely used [72].

Several research groups worked on the improvement of the first model approach. However, in 1971, Rush published the last torso-shaped electrolytic-tank model [71]. This model included several regions of the heart, and some organs and tissues such as lungs, liver, great vessels, skeletal muscle, ribs, and also fat subcutaneous tissue. The cardiac electrical activity was represented by a multiple dipole source.

During the 1980s, as the understanding of the problem increased, so had the complexity of the models, and researchers turned to model specific parts of the heart instead of the whole heart [35]. However, it was in the 1990s, when computational models started to gain more popularity [73], and technology advances and the imaging methods improved in resolution, and the level of detail of computational biophysical models has increased to replace physical models [6].

2.6.2 Numerical approaches

According to experimental evidence [74, 75] and detailed mathematical treatments of bioelectrical systems [76, 77], due to the time it takes the electric wave to propagate through the body, the capacitance, inductive and propagation effects can be neglected to simplify the description of the problem, without important errors arising in the computation of the solution; i.e. it is possible to consider the thorax as a linear conductor and work under quasi-static conditions. Therefore, through conservation of current, and taking into account that the total current, J, flowing into and out of any closed region is zero (the current density is solenoidal), the continuity equation takes the form of:

$$\nabla \cdot \vec{J} = 0. \tag{2.28}$$

Now, taking into account the presence of the electric source inside a known medium conductor, the relation between the electric field, E, and the total current density, J, is given by the Ohm's law:

$$\vec{J} = \sigma \vec{E} + \vec{J^i}, \tag{2.29}$$

where σ is the conductivity and $\vec{J^i}$ is the applied current density, produced by the active source (the heart). This vector is non-zero only in the region where the

source is located. Then, combining equations (2.28) and (2.29), it can be obtained that

$$\nabla \cdot \vec{J^i} = -\nabla \cdot (\sigma \vec{E}). \tag{2.30}$$

From the electrostatic Maxwell equations, which describe the quasi-static electromagnetic behaviour of an electric source inside a linear volume conductor and by conservation of the electric field, the electric field can be associated with the gradient of a scalar potential, ϕ, as

$$\vec{E} = -\nabla \cdot \phi. \tag{2.31}$$

So, introducing equation (2.31) into equation (2.30), and by considering the volume as homogeneous and isotropic, after re-arranging, the Poisson's equation can be written as

$$\nabla^2 \phi = \frac{\nabla \cdot \vec{J^i}}{\sigma}. \tag{2.32}$$

Equation (2.32) describes the relation between the electric potential ϕ, inside a body with conductivity σ, and the active source or its applied current density $\vec{J^i}$.

There are different numerical approaches used to solve equation (2.32). One approach used by the finite element method (FEM) and FDM is to divide the thorax and each region inside it into small volumes with different conductivity, and the potential is computed inside all of these small volumes. However, as the properties and geometry are approximated to real values, the computational cost of this solution becomes very expensive. Another numerical approach splits the body into regions with isotropic and uniform conductivity, and the potential is computed only on the surface of these regions. This method is called the boundary element method (BEM), and is the one used in this study. A more detailed description will be made in the next chapter (Chapter 3).

2.7 Inverse problem

The inverse problem in electrocardiography, or electrocardiographic imaging, can be summarized as finding electrical information about the source, from a set of field measurements produced in a volume conductor, with previous knowledge of the properties of the medium. Therefore, it is going backwards compared with the forward problem previously described (Figure 2.14) (section 2.6).

Generally, the inverse problem can be divided into three types. The first one is

computing the potentials inside the heart or on its surface, from the field measured outside or on the surface of the body. The second one is computing the activation wavefront locations in the heart, also from the BSPs or MCGs. The third one is to reconstruct the intracavity potentials inside the heart from the measured heart surface potentials. This study focused on the first type of inverse problem.

2.7.1 History of the inverse problem in cardiology

Through history, the advantages of solving the inverse problem has been the focus of several studies, almost since the forward problem was first defined. But unfortunately, there is a lack of information on the measured field that enables one to find a reliable analytical solution of the source (further discussion in section 2.7.2), in addition to the difficulty of obtaining simultaneous measurements of the active source and field on the body for validation-comparison purposes. Therefore, it is still a present subject of research interest in different groups. Fortunately, with the development of new imaging techniques, more information about the body or the problem itself can be obtained, compared with the first studies related to this topic, where a lot of information remained unknown, and stronger approximations had to be assumed which did not yield reliable solutions [6].

Early formulations treated the inverse problem as an extension of BSP measurements [6], therefore one of the first studies related to this subject was performed by Burger and van Milaan [46] in 1946. They used a copper disk, as a source inside a tank filled of electrolytes. However, the first attempt to reconstruct the cardiac electrical activity in an animal model using an array of electrodes on its thorax surface and on the heart surface (validation-comparison) was performed by Spach and Barr in 1978 [78]. But, the spatio-temporal resolution of both reconstructed and real measurements were low, and the current theoretical treatment of ECG inverse techniques had not been developed yet. Similar comparative studies have been carried out since, with an increasing understanding of the problem which yields improvements in the measurement techniques. For example, a study made by Nash and co-workers, where they used a pig model, was able to measure the potential on the surface of its body and on the surface of the heart simultaneously, helping to build the current theoretical electrocardiographic imaging techniques [79].

In agreement with the forward problem history, some inverse problem studies were made using electrolytic tanks, but most of them used an animal heart as a source. The study carried out by Taccardi, with a frog's beating heart inside a cylindrical tank [80], was one of the first with a quantitative validation of the reconstructed data. Colli-Franzone et al. [81] used a human-shaped thorax tank, which was the

base of several inverse problem studies which was used to validate the theoretical aspect of the inverse solution [6].

From the theoretical perspective, early formulations were based on reconstructing discrete, equivalent sources, i.e., dipole and multipole heart models [78, 80]. However, the validation of such equivalent sources was sometimes impossible because relating real heart activation times or cardiac electric potentials with dipole or multipole equivalent sources was a difficult task [6].

More recently, as the understanding of the problem improved, so to did the number of mathematical and theoretical approaches which might generate a feasible solution. Unfortunately, a clear quantitative clinical validation of inverse ECG methods remains an elusive challenge [6]. Nevertheless, some research groups have been working intensively for years around different aspects of the inverse problem and have been able to find feasible solutions by limiting the possible solutions in order to make them as physically and physiologically consistent as possible [82, 56], others studies constrained the number of unknowns to be obtained, e.g. reconstruction of the epicardium electrical activity [82, 56]. Another approach uses a numerical solution, which does not explicitly compute an inverse of the matrix, but instead matches the forward problem solution [83]. Others had proposed to include additional information using alternative techniques, e.g. electrical impedance tomography (EIT) [84]. Though each of these different approximations have shown some improvements, such reconstruction might still not give enough information or have even been tested for some clinical procedures and therefore it is still a subject of research due to the lack of clinical validation. As the imaging and computational methods have been increasing in power, the modelling studies represent an important tool to provide additional information which is difficult or impossible to obtain in a clinical procedure, and can also provide a better understanding of the problem.

2.7.2 Challenges of inverse solutions

As mentioned before, the inverse problem in cardiology does not have a mathematically complete solution, because, in agreement with Hadamard axioms [85], it is an ill-posed problem. The characteristics which make it an ill-posed problem are:

• The problem does not have a mathematically unique solution. This means that one set of BSP measurements can be produced by multiple and different configurations of the electric source inside the body.

• The solution does not depend continuously on the data. Slight variations in the measured BSP can lead to a large variation in the solution. This is because the

BSP is a highly attenuated and smoothed signal, due to the resistivity properties of the volume conductor.

However, a set of constraints can be applied to the solution in order to find a more reasonable, physical and physiological solution. These constraints usually mean introducing prior information about the solution. One way is via regularization techniques, and another is to limit the solution to the electrical activity only on the epicardium [56].

2.7.3 Approaches to the inverse problem

There are different approaches found in the literature for solving the inverse problem. However, they can be summarized into analytical and numerical solutions.

An analytical solution, usually based on concentric and eccentric spheres [82], has shown to be sensitive to the geometry proposed, i.e., the position of the heart, concluding that such an approach cannot easily be applied to realistic anatomical solutions. Though, this can still provide some fundamental comprehension of some aspects of the inverse solution behaviour[6].

The numerical approaches can be divided into iterative methods and regularization methods. The iterative methods do not explicitly compute an inverse solution, but instead, match the forward problem solution. The regularization methods add extra information to constrain the solution. But either have their main limitation in the need of a realistic, geometrical and physiological accurate forward problem model [6]. A more complete description of the numerical solution used in the present study is in the next chapter (Chapter 3).

Truncated iterative approaches

The truncated iterative method can approach the solution of the inverse problem by evaluating it according to a 'goodness' criterion: the solution is tested at every time-step until it meets some threshold of accuracy [6]. However, the problem with this type of method is that, as it does not have any constraint, the solution will converge to an unreliable one, given by the ill-posedness of the problem. So, the main issue is when to truncate the iteration, before the ill-posedness affects the solution. The most used method of this type is the Generalized Minimum Residual (GMRes) method. However, it only works if the numbers of measurements and unknowns are the same [86], which is not usually the case.

Regularization method

The regularization method limits the solution in order to find a more reliable physical and physiological one [87]. The most common method in electrocardiography inverse problem imaging is the Tikhonov regularization [6]. In this method one or a set of constraints acts directly on the matrix as a penalty function. Then, the weighted norm of this function plus the residual norm are minimized. This is the method used in this study and is further detailed is in section 3.2.4.

2.7.4 Validation of the inverse problem

The validation of an inverse solution method can be as difficult as solving the problem per-se, due to the need of electrical measurements on two different surfaces at the same time of a patient with a developed cardiac arrhythmia. Mainly, there are two principal validation methods. One is through experimental studies and the other via simulation studies [6]. The simulation studies, which are based on computational algorithms to solve the inverse problems, can also be divided into two types: analytical solutions and numerical solutions [6].

In the case of experimental validation, the main problem is controlling all the physiological variables, which are easier to control in the simulation studies. Most of the experimental studies are based on animal, not human, models [6]. With some exceptions, the majority only have a partial forward solution to validate the problem. In some cases, they may only be able to validate the solution with clinical information that can be found in the literature, which is usually based on indirect evidence [6].

Due to the fact that the inverse problem is ill-posed, an analytical solution would need a high degree of constraints. This would mean that the conclusions cannot be applied to physiological situations. In the case of the numerical solutions, the inverse solution is usually influenced by the assumptions used to compute the forward solution. Most numerical studies used the same matrix to compute the forward and the inverse solution [6]. Therefore, additional information has to be included, such as adding numerical noise in order to validate the solution.

Bibliography

[1] G. J. Tortora and S. R. Grabowski, *Principles of anatomy and physiology*. New York: Harper Collins College Publishers, 1993, 1993.

[2] E. N. Marieb and K. Hoehn, *Human anatomy & physiology*. Pearson Education, 2007.

[3] J. Khuzama, "how the heart works: text, images, music, video — glogster edu - 21st century multimedia tool for educators, teachers and students." `http://khuzama.edu.glogster.com/how-the-heart-works`.

[4] A. M. Katz, *Physiology of the Heart*. Lippincott Williams & Wilkins, 2010.

[5] B. G. Klein, *Cunningham's textbook of veterinary physiology*. Elsevier Health Sciences, 2013.

[6] P. W. Macfarlane, A. van Oosterom, and M. Janse, *Comprehensive electrocardiology*, vol. 4. Springer Science & Business Media, 2010.

[7] M. Courtemanche, R. J. Ramirez, and S. Nattel, "Ionic mechanisms underlying human atrial action potential properties: insights from a mathematical model," *American Journal of Physiology-Heart and Circulatory Physiology*, vol. 275, no. 1, pp. H301–H321, 1998.

[8] L. Pinello, "The movement of substance across cell membranes." `http://jpkc.scu.edu.cn/ywwy/zbsw%28E%29/edetail5.htm`.

[9] E. J. Benjamin, P. A. Wolf, R. B. DAgostino, H. Silbershatz, W. B. Kannel, and D. Levy, "Impact of atrial fibrillation on the risk of death the framingham heart study," *Circulation*, vol. 98, no. 10, pp. 946–952, 1998.

[10] E. Anter, M. Jessup, and D. J. Callans, "Atrial fibrillation and heart failure treatment considerations for a dual epidemic," *Circulation*, vol. 119, no. 18, pp. 2516–2525, 2009.

[11] N. J. Pagidipati and T. A. Gaziano, "Estimating deaths from cardiovascular disease: a review of global methodologies of mortality measurement," *Circulation*, vol. 127, no. 6, pp. 749–756, 2013.

[12] A. Ghuran and A. Camm, "Ischaemic heart disease presenting as arrhythmias," *British medical bulletin*, vol. 59, no. 1, pp. 193–210, 2001.

[13] W. S. Lin, C. T. Tai, M. H. Hsieh, C. F. Tsai, Y. K. Lin, H. M. Tsao, J. L. Huang, W. C. Yu, S. P. Yang, Y. A. Ding, *et al.*, "Catheter ablation of paroxysmal atrial fibrillation initiated by non–pulmonary vein ectopy," *Circulation*, vol. 107, no. 25, pp. 3176–3183, 2003.

[14] C. W. Hamm, J.-P. Bassand, S. Agewall, J. Bax, E. Boersma, H. Bueno, P. Caso, D. Dudek, S. Gielen, K. Huber, *et al.*, "Esc guidelines for the management of

acute coronary syndromes in patients presenting without persistent st-segment elevation," *European heart journal*, vol. 32, no. 23, pp. 2999–3054, 2011.

[15] S. M. Narayan, D. E. Krummen, and W. J. Rappel, "Clinical mapping approach to diagnose electrical rotors and focal impulse sources for human atrial fibrillation," *Journal of cardiovascular electrophysiology*, vol. 23, no. 5, pp. 447–454, 2012.

[16] J. Jalife, O. Berenfeld, A. Skanes, and R. Mandapati, "Mechanisms of atrial fibrillation: mother rotors or multiple daughter wavelets, or both?," *Journal of cardiovascular electrophysiology*, vol. 9, no. 8 Suppl, pp. S2–12, 1998.

[17] A. N. Ganesan, N. J. Shipp, A. G. Brooks, P. Kuklik, D. H. Lau, H. S. Lim, T. Sullivan, K. C. Roberts-Thomson, and P. Sanders, "Long-term outcomes of catheter ablation of atrial fibrillation: A systematic review and meta-analysis," *Journal of the American Heart Association*, vol. 2, no. 2, p. e004549, 2013.

[18] W. Anne, H. Van Rensburg, J. Adams, H. Ector, F. Van de Werf, and H. Heidbuchel, "Ablation of post-surgical intra-atrial reentrant tachycardia," *Eur. Heart J*, vol. 23, pp. 1609–1616, 2002.

[19] J. R. Ehrlich and S. Nattel, "Novel approaches for pharmacological management of atrial fibrillation," *Drugs*, vol. 69, no. 7, pp. 757–774, 2009.

[20] D. Stilli, E. Musso, E. Macchi, C. Manca, L. Dei Cas, P. Vasini, and B. Taccardi, "Body surface potential mapping in ischemic patients with normal resting ecg.," *The Canadian journal of cardiology*, pp. 107A–112A, 1986.

[21] C. Hamilton-Craig, W. E. Strugnell, O. C. Raffel, I. Porto, D. L. Walters, and R. E. Slaughter, "Ct angiography with cardiac mri: non-invasive functional and anatomical assessment for the etiology in newly diagnosed heart failure," *The international journal of cardiovascular imaging*, vol. 28, no. 5, pp. 1111–1122, 2012.

[22] K. Tolstrup, B. E. Madsen, J. A. Ruiz, S. D. Greenwood, J. Camacho, R. J. Siegel, H. C. Gertzen, J.-W. Park, and P. A. Smars, "Non-invasive resting magnetocardiographic imaging for the rapid detection of ischemia in subjects presenting with chest pain," *Cardiology*, vol. 106, no. 4, pp. 270–276, 2006.

[23] B. Hailer, I. Chaikovsky, S. Auth Eisernitz, H. Schäfer, and P. Van Leeuwen, "The value of magnetocardiography in patients with and without relevant stenoses of the coronary arteries using an unshielded system," *Pacing and clinical electrophysiology*, vol. 28, no. 1, pp. 8–16, 2005.

[24] R. Clayton, O. Bernus, E. Cherry, H. Dierckx, F. Fenton, L. Mirabella, A. Panfilov, F. Sachse, G. Seemann, and H. Zhang, "Models of cardiac tissue electrophysiology: progress, challenges and open questions," *Progress in biophysics and molecular biology*, vol. 104, no. 1, pp. 22–48, 2011.

[25] A. L. Hodgkin and A. F. Huxley, "A quantitative description of membrane current and its application to conduction and excitation in nerve," *The Journal of physiology*, vol. 117, no. 4, pp. 500–544, 1952.

[26] S. Rush and H. Larsen, "A practical algorithm for solving dynamic membrane equations," *Biomedical Engineering, IEEE Transactions on*, no. 4, pp. 389–392, 1978.

[27] C. S. Henriquez, "Simulating the electrical behavior of cardiac tissue using the bidomain model.," *Critical reviews in biomedical engineering*, vol. 21, no. 1, pp. 1–77, 1992.

[28] W. T. Miller and D. B. Geselowitz, "Simulation studies of the electrocardiogram. i. the normal heart.," *Circulation Research*, vol. 43, no. 2, pp. 301–315, 1978.

[29] A. Bueno-Orovio, D. Kay, V. Grau, B. Rodriguez, and K. Burrage, "Fractional diffusion models of cardiac electrical propagation: role of structural heterogeneity in dispersion of repolarization," *Journal of The Royal Society Interface*, vol. 11, no. 97, p. 20140352, 2014.

[30] J. W. Moore and F. Ramon, "On numerical integration of the hodgkin and huxley equations for a membrane action potential," *Journal of theoretical Biology*, vol. 45, no. 1, pp. 249–273, 1974.

[31] J. D. Stott, *Developing realistic models of the atrium and the p-wave*. PhD thesis, The University of Manchester, 2009.

[32] D. A. Hooks, K. A. Tomlinson, S. G. Marsden, I. J. LeGrice, B. H. Smaill, A. J. Pullan, and P. J. Hunter, "Cardiac microstructure implications for electrical propagation and defibrillation in the heart," *Circulation Research*, vol. 91, no. 4, pp. 331–338, 2002.

[33] I. Arieh, *A First Course in the Numerical Analysis of Differential Equations*. Cambridge University Press, 1996.

[34] R. Barr, T. Pilkington, J. Boineau, and M. Spach, "Determining surface potentials from current dipoles, with application to electrocardiography," *IEEE Transactions on Biomedical Engineering*, vol. 2, no. BME-13, pp. 88–92, 1966.

[35] R. M. Gulrajani and G. E. Mailloux, "A simulation study of the effects of torso inhomogeneities on electrocardiographic potentials, using realistic heart and torso models.," *Circulation research*, vol. 52, no. 1, pp. 45–56, 1983.

[36] D. Shier, J. Butler, and R. Lewis, *Hole's essentials of human anatomy and physiology*. McGraw-Hill New York, 2006.

[37] D. Darling, "The internet encyclopedia of science," *Heart Valve Disease Retrieved April*, vol. 11, 2009.

[38] O. G. Martinsen and S. Grimnes, *Bioimpedance and bioelectricity basics*. Academic press, 2011.

[39] J. Malmivuo and R. Plonsey, *Bioelectromagnetism: principles and applications of bioelectric and biomagnetic fields*. Oxford university press, 1995.

[40] J. D. Jackson and J. D. Jackson, *Classical electrodynamics*, vol. 3. Wiley New York etc., 1962.

[41] A. D. Waller, "A demonstration on man of electromotive changes accompanying the heart's beat," *The Journal of physiology*, vol. 8, no. 5, pp. 229–234, 1887.

[42] W. Einthoven, "Die galvanometrische registrirung des menschlichen elektrokardiogramms, zugleich eine beurtheilung der anwendung des capillar-elektrometers in der physiologie," *Pflügers Archiv European Journal of Physiology*, vol. 99, no. 9, pp. 472–480, 1903.

[43] W. Einthoven, "Weiteres über das elektrokardiogramm," *Pflügers Archiv European Journal of Physiology*, vol. 122, no. 12, pp. 517–584, 1908.

[44] P. Kligfield, "The centennial of the einthoven electrocardiogram," *Journal of electrocardiology*, vol. 35, no. 4, pp. 123–129, 2002.

[45] R. Mcfee and F. D. Johnston, "Electrocardiographic leads ii. analysis," *Circulation*, vol. 9, no. 2, pp. 255–266, 1954.

[46] H. Burger and J. Van Milaan, "Heart-vector and leads," *British heart journal*, vol. 8, no. 3, p. 157, 1946.

[47] T. B. Garcia *et al.*, *12-lead ECG: The art of interpretation*. Jones & Bartlett Publishers, 2013.

[48] I. Menown and A. Adgey, "Improving the ecg classification of inferior and lateral myocardial infarction by inversion of lead avr," *Heart*, vol. 83, no. 6, pp. 657–660, 2000.

[49] J. R. Hampton, *The ECG made easy*. Elsevier Health Sciences, 2013.

[50] E. A. P. Alday, M. A. Colman, P. Langley, T. D. Butters, J. Higham, A. J. Workman, J. C. Hancox, and H. Zhang, "A new algorithm to diagnose atrial ectopic origin from multi lead ecg systems-insights from 3D virtual human atria and torso," *PLoS computational biology*, vol. 11, no. 1, 2015.

[51] M. Gertsch, *The ECG: a two-step approach to diagnosis*. Springer Science & Business Media, 2003.

[52] M. James, "Sinus rhythm - normal function of the heart - cardiology teaching package - practice learning - division of nursing - the university of nottingham," 2015.

[53] "Electrocardiography - wikipedia, the free encyclopedia, https://en.wikipedia.org/wiki/electrocardiography."

[54] C. Schmitt, G. Ndrepepa, S. Weber, S. Schmieder, S. Weyerbrock, M. Schneider, M. R. Karch, I. Deisenhofer, J. Schreieck, B. Zrenner, *et al.*, "Biatrial multisite mapping of atrial premature complexes triggering onset of atrial fibrillation," *The American journal of cardiology*, vol. 89, no. 12, pp. 1381–1387, 2002.

[55] D. Scherr, D. Dalal, A. Cheema, A. Cheng, C. A. Henrikson, D. Spragg, J. E. Marine, R. D. Berger, H. Calkins, and J. Dong, "Automated detection and characterization of complex fractionated atrial electrograms in human left atrium during atrial fibrillation," *Heart Rhythm*, vol. 4, no. 8, pp. 1013–1020, 2007.

[56] C. Ramanathan, R. N. Ghanem, P. Jia, K. Ryu, and Y. Rudy, "Noninvasive electrocardiographic imaging for cardiac electrophysiology and arrhythmia," *Nature medicine*, vol. 10, no. 4, pp. 422–428, 2004.

[57] Z. Y. Qian, X. F. Hou, D. J. Xu, B. Yang, M. L. Chen, C. Chen, F. X. Zhang, Q. J. Shan, K. J. Cao, and J. G. Zou, "An algorithm to predict the site of origin of focal atrial tachycardia," *Pacing and Clinical Electrophysiology*, vol. 34, no. 4, pp. 414–421, 2011.

[58] J. S. Uhm, J. Shim, J. Wi, H. S. Mun, H. N. Pak, M. H. Lee, and B. Joung, "An electrocardiography algorithm combined with clinical features could localize the origins of focal atrial tachycardias in adjacent structures," *Europace*, vol. 16, no. 7, pp. 1061–1068, 2014.

[59] P. M. Kistler, K. C. Roberts-Thomson, H. M. Haqqani, S. P. Fynn, S. Singarayar, J. K. Vohra, J. B. Morton, P. B. Sparks, and J. M. Kalman, "P-wave morphology in focal atrial tachycardia: development of an algorithm to predict

the anatomic site of origin," *Journal of the American College of Cardiology*, vol. 48, no. 5, pp. 1010–1017, 2006.

[60] D. B. Geselowitz, "Electric and magnetic field of the heart," *Annual review of biophysics and bioengineering*, vol. 2, no. 1, pp. 37–64, 1973.

[61] J. S. Kwong, B. Leithäuser, J.-W. Park, and C.-M. Yu, "Diagnostic value of magnetocardiography in coronary artery disease and cardiac arrhythmias: A review of clinical data," *International journal of cardiology*, vol. 167, no. 5, pp. 1835–1842, 2013.

[62] M. Bojarnejad, J. R. Blake, J. Bourke, E. Shepherd, A. Murray, and P. Langley, "Non-invasive estimation of left atrial dominant frequency in atrial fibrillation from different electrode sites: Insight from body surface potential mapping," *JAFIB: Journal of Atrial Fibrillation*, vol. 7, no. 3, 2014.

[63] M. H. Raitt and W. Kusumoto, "Correlations among the frequencies of atrial activity on the surface electrocardiogram, intracardiac atrial electrograms, and the atrial effective refractory period in patients with atrial fibrillation," *Journal of electrocardiology*, vol. 45, no. 3, pp. 296–303, 2012.

[64] D. Giacopelli, J. P. Bourke, A. Murray, and P. Langley, "Spatial pattern of p waves in paroxysmal atrial fibrillation patients in sinus rhythm and controls," *Pacing and Clinical Electrophysiology*, vol. 35, no. 7, pp. 819–826, 2012.

[65] G. Baule and R. McFee, "Theory of magnetic detection of the heart's electrical activity," *Journal of Applied Physics*, vol. 36, no. 6, pp. 2066–2073, 1965.

[66] D. Cohen, "Magnetic fields around the torso: production by electrical activity of the human heart," *Science*, vol. 156, no. 3775, pp. 652–654, 1967.

[67] J. Zimmerman, P. Thiene, and J. Harding, "Design and operation of stable rf-biased superconducting point-contact quantum devices, and a note on the properties of perfectly clean metal contacts," *Journal of Applied Physics*, vol. 41, no. 4, pp. 1572–1580, 1970.

[68] D. Cohen, E. A. Edelsack, and J. E. Zimmerman, "Magnetocardiograms taken inside a shielded room with a superconducting point-contact magnetometer," *Applied Physics Letters*, vol. 16, no. 7, pp. 278–280, 1970.

[69] S. Mukhopadhyay, K. Jayasundera, and A. Fuchs, *Advancement in Sensing Technology: New Developments and Practical Applications*, vol. 1. Springer Science & Business Media, 2012.

[70] L. N. Katz, E. Sigman, G. I, and F. H. Ocko, "The effect of good electrical conductors introduced near the heart on the electrocardiogram," *Am J physiol*, vol. 125, pp. 343–348, 1936.

[71] C. Nelson and D. Geselowitz, *The theoretical basis of electrocardiography*. Oxford Univ. Press, London, 1976.

[72] R. S. MacLeod, S. Shome, J. Stinstra, B. B. Punske, and B. Hopenfeld, "Mechanisms of ischemia-induced st-segment changes," *Journal of electrocardiology*, vol. 38, no. 4, pp. 8–13, 2005.

[73] L. Weixue, X. Zhengyao, and F. Yingjie, "Microcomputer-based cardiac field simulation model," *Medical and Biological Engineering and Computing*, vol. 31, no. 4, pp. 384–387, 1993.

[74] L. Wei, S. Jingjing, and W. Jianqing, "An approach to evaluate electromagnetic interference with a wearable ecg at frequencies below 1mhz," *IEICE Transactions on Communications*, vol. 98, no. 8, pp. 1606–1613, 2015.

[75] H. Schwan and C. Kay, "The conductivity of living tissues," *Annals of the New York Academy of Sciences*, vol. 65, no. 6, pp. 1007–1013, 1957.

[76] D. B. Geselowitz, "The concept of an equivalent cardiac generator," *Biomedical sciences instrumentation*, vol. 1, pp. 325–330, 1962.

[77] R. Plonsey and D. B. Heppner, "Considerations of quasi-stationarity in electrophysiological systems," *The Bulletin of mathematical biophysics*, vol. 29, no. 4, pp. 657–664, 1967.

[78] R. C. Barr and M. Spach, "Inverse calculation of qrs-t epicardial potentials from body surface potential distributions for normal and ectopic beats in the intact dog," *Circulation research*, vol. 42, no. 5, pp. 661–675, 1978.

[79] M. Nash, C. Bradley, L. Cheng, A. Pullan, and D. Paterson, "Electrocardiographic inverse validation study: in-vivo mapping and analysis," *FASEB J*, vol. 14, no. 4, p. A442, 2000.

[80] B. Taccardi and G. Marchetti, "Distribution of heart potentials on the body surface and in artificial conducting media," in *Electrophysiology of the Heart*, p. 257, Pergamon Press Ltd., 1965.

[81] P. C. Franzone, L. Guerri, B. Taccardi, and C. Viganotti, "The direct and inverse problems in electrocardiology. numerical aspects of some regularization methods and applications to data collected in isolated dog heart experiments," *Lab. Anal. Numerica CNR*, p. 222, 1979.

[82] Y. Rudy and R. Plonsey, "A comparison of volume conductor and source geometry effects on body surface and epicardial potentials," *Circulation research*, vol. 46, no. 2, pp. 283–291, 1980.

[83] B. Messnarz, M. Seger, R. Modre, G. Fischer, F. Hanser, and B. Tilg, "A comparison of noninvasive reconstruction of epicardial versus transmembrane potentials in consideration of the null space," *Biomedical Engineering, IEEE Transactions on*, vol. 51, no. 9, pp. 1609–1618, 2004.

[84] S. Babaeizadeh, D. H. Brooks, D. Isaacson, and J. C. Newell, "Electrode boundary conditions and experimental validation for bem-based eit forward and inverse solutions," *Medical Imaging, IEEE Transactions on*, vol. 25, no. 9, pp. 1180–1188, 2006.

[85] J. Hadamard, *Lectures on Cauchy's problem in linear partial differential equations*. Courier Corporation, 2014.

[86] Y. Saad, *Iterative methods for sparse linear systems*. Siam, 2003.

[87] P. C. Hansen, *Rank-deficient and discrete ill-posed problems: numerical aspects of linear inversion*, vol. 4. Siam, 1998.

Chapter 3

Derivation of Mathematical and Numerical Methods

This chapter contains a description of the mathematical models used to develop, solve and implement the forward and inverse problem in order to conduct a theoretical investigation of non-invasive methods to identify cardiac arrhythmias.

3.1 Forward problem in electrocardiography

The forward problem in electrocardiography consists of computing the fields (electric or magnetic) propagating through the body (or thorax) that are generated by the heart (electrical source) inside the volume, whose properties are well known.

3.1.1 Introduction

The forward problem in electrocardiography is still a very important research subject in several groups, because it can be undertaken experimentally, analytically or numerically to provide correlated information about the dynamics of the fields and the bioelectrical source (i.e. the heart) during specific conditions that is difficult or impossible to obtain in a clinical environment. Although these three approaches (experimental, analytical, and numerical), have contributed over time to the knowledge of electrocardiography theory, the main approach used more recently by most research groups is the numerical computational simulation with experimental results used as validation [1]. Even though the main limitation of computer modelling is the current computer's power and capacity, it is a more flexible approach because it does not have geometrical limitations and can represent any source configuration and activation, which is difficult or impossible to implement by the other two scenarios. Also, as technology advances, more complexity can be included in the problem description and more accurate solutions can be obtained.

In the present study, a numerical approach was used to solve the forward problem, and with a Boundary Element Method (BEM), based on Green's second Theorem, the fields produced by the heart inside the thorax were computed to investigate cardiac arrhythmias.

3.1.2 Body electric field produced by the heart

In order to compute the electric field, E, inside an homogeneous and isotropic volume V, with conductivity σ, produced by a bioelectric source J^i (impressed current previously described, equation (2.30)), Maxwell's electrostatic equations together with Poisson's equation (equation (2.32)) and Ohm's law (equation (2.29)) are the starting point

$$\nabla^2\phi = \frac{\nabla \cdot \vec{J^i}}{\sigma}, \tag{3.1a}$$

$$\vec{J} = \sigma\vec{E} + \vec{J^i}, \tag{3.1b}$$

where ϕ is the electric potential (previously define equation (2.31)) and J is the total current density which is solenoidal, $\nabla \cdot \vec{J} = 0$.

Electric field in an infinite homogeneous medium

In the case where the volume is infinite with a conductivity, σ, the solution for Poisson's equation (equation (3.1a)) is given by

$$\phi(r) = -\frac{1}{4\pi\sigma}\int \frac{\nabla \cdot \vec{J^i}(r')}{|\vec{r} - \vec{r'}|}dv, \tag{3.2}$$

where, $|\vec{r}-\vec{r'}|$ is the distance from an element of the integration (dv) to an observation point inside the volume, where the field is evaluated (Figure 3.1). Now, by using the vector identity $\nabla\cdot(\vec{C}(r)B(r)) = B(r)\nabla\cdot\vec{C}(r)+\vec{C}\cdot\nabla B(r)$ with $\nabla(|\vec{C}|^{-1}) = \vec{C}|\vec{C}|^{-3}$ together with Gauss theorem, and $J^i = 0$ on the boundary, equation (3.3) can be written as

$$\phi(r) = -\frac{1}{4\pi\sigma}\int \vec{J^i}(r') \cdot \frac{\vec{r} - \vec{r'}}{|\vec{r} - \vec{r'}|^3}dv, \tag{3.3}$$

Electric field in a bounded inhomogeneous medium

The Green's second identity, for a volume, V, delimited by a surface S, reads that for any two scalar functions ϕ and ψ, it holds that

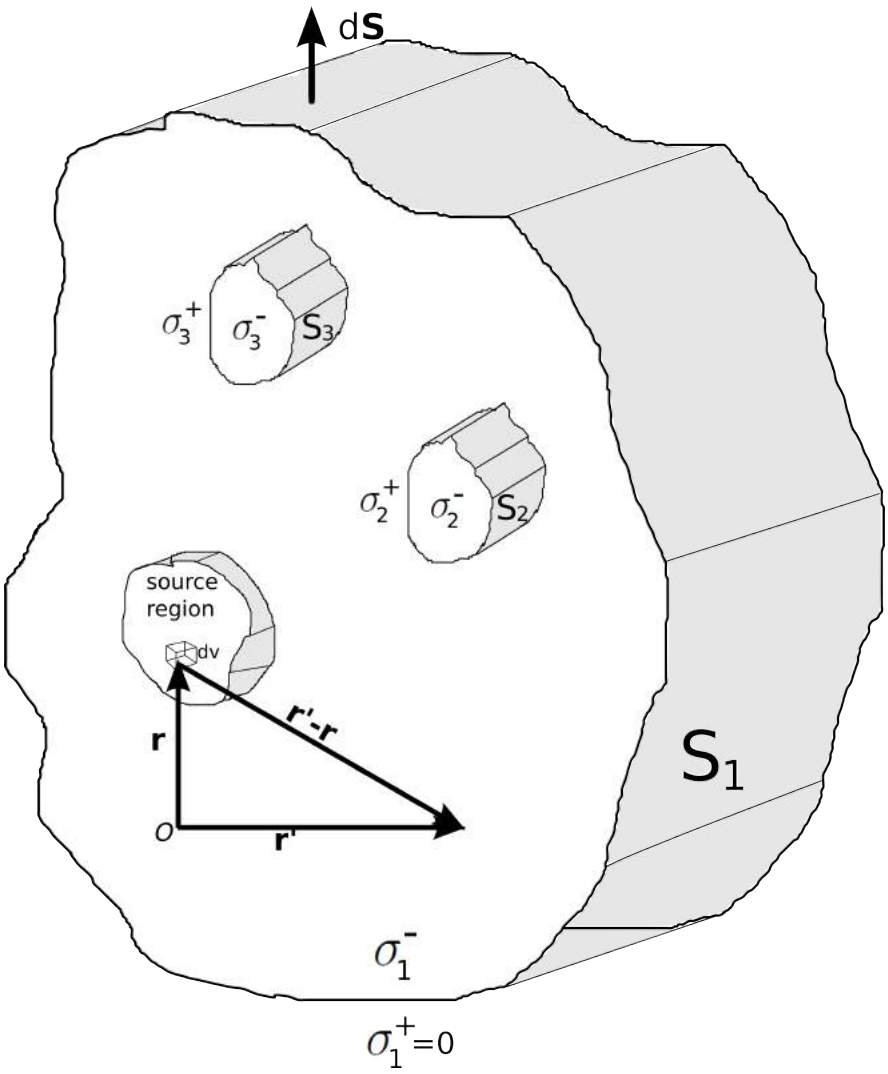

Figure 3.1: Solution components of the forward problem description, i.e., the boundary element method. Where O represents the origin, $\vec{r}$ is the vector to a volume element dv, and $\vec{r'}$ the vector to an arbitrary point within the volume. S_i are the surface involve, with internal conductivity σ_i^- and external conductivity σ_i^+.

$$\int_V (\phi \nabla^2 \psi - \psi \nabla^2 \phi) dv = \int_S (\phi \nabla \psi - \psi \nabla \phi) \cdot dS. \tag{3.4}$$

By taking ϕ as the scalar electrical potential and ψ as $1/r$, where $r = |\vec{r} - \vec{r'}|$ as previously defined, and substituting Poisson's equation (equation (3.1a)), into the equation (3.4), it is possible to arrive at

$$\int_V \left(\phi \nabla^2 \left(\frac{1}{r} \right) - \frac{1}{r} \frac{(\nabla \cdot \vec{J^i})}{\sigma} \right) dv = \int_S \left(\phi \nabla \left(\frac{1}{r} \right) - \left(\frac{1}{r} \right) \nabla \phi \right) \cdot dS. \tag{3.5}$$

Then, taking into account that the nabla operator, ∇, works on the source coordi-

nates (unprimed coordinates). It is possible to rewrite the first term of the equation (3.5) in terms of the Dirac delta function, as

$$\nabla^2 \left(\frac{1}{r}\right) = \nabla^2 \left(\frac{1}{|\vec{r'} - \vec{r}|}\right) = -4\pi\delta(\vec{r'} - r). \tag{3.6}$$

After that, on the surface of the body, the following boundary condition can be assumed, $\nabla\phi \cdot dS = 0$, which means that the air surrounding the body has zero conductivity. Therefore, equation (3.5) can be rewritten as

$$\phi(\vec{r'}) = \frac{1}{4\pi\sigma} \int_V \frac{-\nabla \cdot \vec{J^i}}{r} dv - \frac{1}{4\pi} \int_S \phi(\vec{r}) \nabla \left(\frac{1}{r}\right) \cdot dS. \tag{3.7}$$

From the last equation, it is possible to identify a differential element of solid angle, $d\Omega$, from

$$\nabla \left(\frac{1}{r}\right) \cdot dS = \frac{(\vec{r'} - \vec{r})}{|\vec{r'} - \vec{r}|^3} \cdot dS = d\Omega, \tag{3.8}$$

where, the solid angle, Ω can be seen as the measurement that an object subtends, for the two dimensional angle, at a point in a three dimensional space. Therefore, equation (3.7) takes the form of

$$\phi(\vec{r'}) = \frac{1}{4\pi\sigma} \int_V \frac{-\nabla \cdot \vec{J^i}}{r} dv - \frac{1}{4\pi} \int_S \phi(\vec{r}) d\Omega. \tag{3.9}$$

From equation (3.9), it is possible to notice that the first term in the right hand is the potential in the infinite homogeneous medium, equation (3.3). Therefore, the last term in equation (3.9) is due to the delimited torso. Thus, the next step is to discretize equation (3.9), i.e., dividing the surface, S, into n triangles:

$$\phi(\vec{r'}) \approx \frac{1}{4\pi\sigma} \int_V \frac{-\nabla \cdot \vec{J^i}}{r} dv - \frac{1}{4\pi} \sum_{j=1}^{n} \phi_j \Delta\Omega_j, \tag{3.10}$$

where, each j^{th} surface element has a potential ϕ_j, with an increment of the solid angle $\delta\Omega_j$ taken from $\vec{r'}$. Then, the potential $\phi(\vec{r'})$ is evaluated at an arbitrary point inside the volume. But, if the point is chosen to be at the centre of the triangle, on the surface S, where $\nabla\phi \cdot dS = 0$, the expression to find the potential on the i^{th} triangle, ϕ, takes the form of

$$\phi_i = \frac{1}{4\pi\sigma} \int_V \frac{-\nabla \cdot \vec{J^i}}{r} dv - \frac{1}{4\pi} \sum_{j=1}^{n} \phi_j \Delta\Omega_{ij}. \tag{3.11}$$

Here, $\Delta\Omega_{ij}$ represents the solid angle of the j^{th} triangle taken from the i^{th} triangle. For the special case where $i = j$, then $\Delta\Omega_{ii} = -2\pi$, due to the definition of the solid angle [1]. Therefore, the equation (3.11) can be rewritten as

$$\frac{\phi_i}{2} + \sum_{j=1, j\neq i}^{n} \left(\frac{\Delta\Omega_{ij}}{4\pi} \right) \phi_j = \frac{1}{4\pi\sigma} \int_V \frac{-\nabla \cdot \vec{J^i}}{r} dv, \tag{3.12}$$

which is a system of n equations, that computes the potentials in the surface elements of the volume.

By assuming multiple surfaces, the generalization of the Green's theorem, equation (3.4), for multiple surfaces can be used. Therefore, following the previous derivation, but including multiple inhomogeneities, corresponding to m surfaces, the equation (3.12), becomes

$$\phi_i + \sum_{s=1}^{m} \left(\frac{\sigma_s^- - \sigma_s^s}{\sigma_q^- + \sigma_q^+} \right) \sum_{j=1, j\neq i}^{n} \left(\frac{\Delta\Omega_{ij}}{2\pi} \right) \phi_j = \frac{1}{2\pi(\sigma_q^- + \sigma_q^+)} \int_V \frac{-\nabla \cdot \vec{J^i}}{r} dv, \tag{3.13}$$

where, q correspond to the surface of the i^{th} element. Whereas s is the surface of the j^{th} element. A more complete derivation of equation (3.13) can be found in [2, 3].

Mathematical implementation of the electric field

If we consider an equivalent formulation, where $\vec{J^i}$ is seen as a dipole density [4], we can define the potential in the centre of the triangles at the surface as

$$D_i = \frac{1}{4\pi\sigma} \int_V \frac{\vec{J^i} \cdot (\vec{r'} - \vec{r})}{r^3} dv. \tag{3.14}$$

And, if we defined a matrix $\boldsymbol{A}$, depending only on the geometry of the volume conductor, for the case of the equation (3.12), as

$$A_{ij} = -\frac{\Delta\Omega_{ij}}{4\pi} \qquad with \qquad A_{ii} = 0.5. \tag{3.15}$$

The equation (3.12), can be written in the matrix form

$$\boldsymbol{A}\phi = \boldsymbol{D}, \tag{3.16}$$

with $\boldsymbol{D}$ can be seen as a vector, in which elements are given by equation (3.14), and ϕ is the potential of the n triangles in a column vector form. The same argument can be used to rewrite equation (3.13) in a matrix form, similar to equation (3.16). This last equation is the one used to solve the forward problem, with BEM. Unfortunately, the matrix $\boldsymbol{A}$, is singular, so, in this work, a formulation proposed by Salu in [5], was used.

As mentioned before, the matrix $\boldsymbol{A}$ in equation (3.16) is singular, because the solution for this equation can be found only up to an additive constant C. It means that, if ϕ is a solution, so it is $\phi + C$. Therefore, the matrix $\boldsymbol{A}$ is singular.

Salu proposed a method in 1980 [5], used in [6], to solve the problem of the singularity of matrix $\boldsymbol{A}$. In it, he divided equation (3.16) into a system of equations. First, he imposed the condition that $\phi_1 = 0$. This assumption does not affect the solution; it just sets a reference point. So, the other potentials are determined by a set of n equations with $n-1$ unknowns, i.e., it turned equation (3.16) into

$$\sum_{j=2}^{n} A_{ij}\phi_j = D_i \qquad i = 1, \cdots, n \tag{3.17}$$

Now, the system is complete and it should have only one solution. However, as the rank of the submatrix A_{ij} is $n-1$, because $i = 2, \cdots, n$ and $j = 2, \cdots, n$, there exist n non-trivial $\lambda_i's$, so that the rows of $\boldsymbol{A}$ satisfy

$$\sum_{i=1}^{n} \lambda_i A_{ij} = 0 \qquad j = 2, \cdots, n. \tag{3.18}$$

Where, the $\lambda' s$ can be specified only until a proportionality factor. Also, for consistency with equation (3.17), we have to impose that

$$\sum_{i=1}^{n} \lambda_i D_i = 0. \tag{3.19}$$

Then, for equation (3.19), Salu realized that this may not hold for several reasons, such as numerical inaccuracies in the segmentation of the surface, or in the computation of $\lambda_i's$ or the $D_i's$. Therefore, the solution computed would only be an approximation, meaning that there would be significant differences between the real and the calculated vector ϕ. In the same direction, Salu noted that the electrostatic potential, D_i, can be determined only until an additive constant α, therefore, the equation (3.19) becomes

$$\sum_{i=1}^{n} \lambda_i (D_i + \alpha_i) = 0. \tag{3.20}$$

So, combining this equation with equation (3.17), we can write

$$\sum_{j=2}^{n} A_{ij}\phi_j = D_i + \alpha_i \qquad i = 1, \cdots, n, \tag{3.21}$$

which is now numerically consistent and also physically equivalent to equation (3.16). The α term ensures that equation (3.21) has a consistent solution, which does

not mean that the solution is accurate or correct; it only ensures that the solution exists for the discretized physical problem.

Now, in order to find the value of α, Salu proposed a set of equations. The first was to defined $\phi_j^*(j = 2, \cdots, n)$ as a potential solution of the $n-1$ equations

$$\sum_{j=2}^{n} A_{ij}\phi_j^* = D_i \qquad i = 2, \cdots, n. \tag{3.22}$$

Meanwhile, $\phi_j^1(j = 2, \cdots, n)$ was defined as the solution for the $n-1$ equations

$$\sum_{j=2}^{n} A_{ij}\phi_j^1 = 1_i \qquad i = 2, \cdots, n. \tag{3.23}$$

Where the right side of equation (3.23), represents a column vector of ones. As the same matrix, $\boldsymbol{A}$, multiplies both vectors ϕ_j^* and ϕ_j^1, this matrix only needs to be inverted once, to solve both equations (3.22) and (3.23). Now, if we take $\phi_j(j = 2, \cdots, n)$ as a potential solution of the $n-1$ equations

$$\sum_{j=2}^{n} A_{ij}\phi_j = D_i + \alpha_i \qquad i = 2, \cdots, n, \tag{3.24}$$

where α is the consistency factor, introduced in the equation (3.20). Then, we will get a system of equations (3.22) to (3.24), of which the solution is given by

$$\begin{aligned} \phi_j = \phi_j^* + \alpha\phi_j^1 \qquad & j = 2, \cdots, n \\ \phi_1 = 0. \qquad & \end{aligned} \tag{3.25}$$

Now, substituting equation (3.25) into (3.21), we get

$$\sum_{j=2}^{n} A_{1j}(\phi_j^* + \alpha_i\phi_j^1) = D_i + \alpha_i. \tag{3.26}$$

And finally, solving for α, it gives

$$\alpha_i = \frac{\left(\sum_{j=2}^{n} A_{1j}\phi_j^*\right) - D_i}{1 - \left(\sum_{j=2}^{2} A_{1j}\phi_j^1\right)}. \tag{3.27}$$

The last equation (equation (3.27)), together with equations (3.22) to (3.24), are the ones used to compute the Body Surface Potential in a discretized surface, in the present work.

3.1.3 Body magnetic field produced by the heart

In order to compute the magnetic field, B, inside an homogeneous and isotropic volume V with conductivity σ and magnetic permeability μ_0, produced by a bioelectric source J^i (impressed current previously described, equation (2.30)), Maxwell's magnetostatic equations together with Poisson's equation (equation (3.1a)) and Ohm's law (equation (3.1b)) are the starting point

$$\nabla \cdot \vec{B} = 0, \tag{3.28a}$$

$$\nabla \times \vec{B} = \mu_0 \vec{J} \tag{3.28b}$$

where J is again the total current density which is solenoidal, $\nabla \cdot \vec{J} = 0$, (equation (2.28)), which can also be obtained from equation (3.28b) and the vector identity $\nabla \cdot \times \vec{B} = 0$ [7].

Magnetic field in an infinite homogeneous medium

The solution for the magnetic field, B, due to equations (3.28) is given by the Biot-Savart law [7]:

$$\vec{B}(r) = \frac{\mu_0}{4\pi} \int \vec{J}(r') \times \frac{\vec{r} - \vec{r'}}{|\vec{r} - \vec{r'}|^3} dv, \tag{3.29}$$

by using the vector identities $\nabla \times (\vec{C}(r)D(r)) = D(r)\nabla \times \vec{C}(r) + \nabla(D(r) \times \vec{C}(r)$ with $\nabla(|\vec{C}|^{-1}) = \vec{C}|\vec{C}|^{-3}$, it is possible to write

$$\int_V \vec{J} \times \frac{\vec{r} - \vec{r'}}{|\vec{r} - \vec{r'}|^3} dv = \int_V \vec{J} \times \nabla \frac{1}{|\vec{r} - \vec{r'}|} dv = \int_V \frac{\nabla \times \vec{J}}{|\vec{r} - \vec{r'}|} dv - \int_V \nabla \times \frac{\vec{J}}{|\vec{r} - \vec{r'}|} dv \tag{3.30}$$

By using equation (3.1b), Stoke's theorem and since $J^i = 0$ on the boundary and the curl of a gradient vanishes ($\nabla \times \nabla V = 0$), the last term in the right hand of equation (3.30) vanishes, and going backwards it is possible to write

$$\vec{B}(r) = \frac{\mu_0}{4\pi} \int \vec{J}(r') \times \frac{\vec{r} - \vec{r'}}{|\vec{r} - \vec{r'}|^3} dv = \frac{\mu_0}{4\pi} \int \vec{J^i}(r') \times \frac{\vec{r} - \vec{r'}}{|\vec{r} - \vec{r'}|^3} dv \tag{3.31}$$

For the case of an homogeneous medium there is no contribution of $\sigma \vec{E}$, therefore the total current can be replaced by the impressed current $\vec{J^i}$.

Magnetic field in a bounded inhomogeneous medium

Following a similar derivation of the electric field, it is possible to obtain the magnetic field of an inhomogeneous volume V, delimited by a surface S, divided into subregions of m surfaces. Therefore, from the Biot-savart solution (equation (3.29)) with Ohm's law (equation (3.1b)), it is possible to write

$$\vec{B}(r) = \frac{\mu_0}{4\pi}\int_V [\vec{J^i}(r') - \sigma(r)\nabla\phi(r)] \times \frac{\vec{r}-\vec{r'}}{|\vec{r}-\vec{r'}|^3}dv \tag{3.32a}$$

$$= \vec{B_0} + \frac{\mu_0}{4\pi}\sum_{s=1}^{m}\sigma_j \int_{V_j} [\nabla\phi(r)] \times \frac{\vec{r}-\vec{r'}}{|\vec{r}-\vec{r'}|^3}dv \tag{3.32b}$$

where $\vec{B_0}$ is the magnetic field produced by the current source $\vec{J^i}$ in an homogeneous space. Now, by using the vector identity $\nabla \times (D\vec{C}) = \nabla D \times \nabla \vec{C}$ and Stoke's theorem, is easy to obtain

$$\int_{V_j} \nabla\phi(r) \times \frac{\vec{r}-\vec{r'}}{|\vec{r}-\vec{r'}|^3}dv = \int_{\partial V_j} \phi(r)\vec{n}(r) \times \frac{\vec{r}-\vec{r'}}{|\vec{r}-\vec{r'}|^3}dS_j, \tag{3.33}$$

where $\vec{n}$ is the outer unit vector normal to the surface S_j. Therefore, the magnetic field for all $\vec{r}$ not on any surface S_j, is given by the Geselowitz formula

$$\vec{B}(r) = \vec{B_0} - \frac{\mu_0}{4\pi}\sum_{j=1}^{m}(\sigma_j^- - \sigma_j^+)\int_{S_j} \phi(r)\vec{n}(r) \times \frac{\vec{r}-\vec{r'}}{|\vec{r}-\vec{r'}|^3}dS_j \tag{3.34}$$

where, again, σ_j^- and σ_j^+ are the inner and outer conductivities of the surface S_j, respectively.

Mathematical implementation of the magnetic field

A similar equivalent formulation to the electric field, equation (3.16), can be obtained in order to compute the magnetic field, where $\vec{J^i}$ is seen as a dipole density, therefore, the magnetic field produced in an infinite homogeneous medium can be written as [8]

$$\vec{B}(r) = \frac{\mu_0}{4\pi}\int \vec{J^i}(r') \times \frac{\vec{r}-\vec{r'}}{|\vec{r}-\vec{r'}|^3}dv \tag{3.35}$$

If the electric surface potential is known, the magnetic field can be calculated by discretizing equation (7.4), where each surface S_j is tesselated in k triangular elements and the total number of triangular elements on each surface S_j is $N_{j,k}$,

$$\int_{S_j} \phi_j(r)\vec{n_j}(r) \times \frac{\vec{r}-\vec{r'}}{|\vec{r}-\vec{r'}|^3} dS_j = \sum_{k=1}^{N_{j,k}} \phi_j^k a^k \vec{n_j^k} \times \frac{\vec{r}-\vec{c^k}}{|\vec{r}-\vec{c^k}|^3} \tag{3.36}$$

where a^k is the surface area, $\vec{n_j^k}$ the outward unit normal vector, and $\vec{c^k}$ the centre coordinates of the triangle element k. Therefore, the magnetic field produced by the current source can be obtained in a discretized surface with equations (3.35) and (3.36). Similar to the electric field, the magnetic field can also be written in a matrix form:

$$\boldsymbol{B} = \boldsymbol{B_0} + \boldsymbol{G}\phi \tag{3.37}$$

where ϕ is the electric potential obtained from equation (3.16) and $\boldsymbol{G}$ can be seen as the matrix composed by the last terms in equation (3.36), which is the equation used in this study to compute the magnetic field.

3.2 The inverse problem in electrocardiography

The inverse problem in electrocardiography has been seen as a non-invasive, painless and ideally cheap method to diagnose heart failure, which is a clear advantage over the prevailing imaging methods, which are usually invasive or expensive. However, as mentioned before, it is still an important research subject due to its nature, i.e., its ill-posed behaviour [9]. The ill-posed behaviour leads to a lack of a unique reliable analytical solution which can be used in clinical procedures, because the measured field on the surface of the body is a highly blurred and attenuated sum of the electrical activity of millions of cells that contribute to the cardiac cycle. These properties have been previously discussed in Chapter 2

In this section, the inverse solution and the numerical approach are formalised mathematically. The computational implementation of the selected approach, as used in the studies in this Thesis, is discussed in Chapter 4.

3.2.1 Potential between the heart surface and the body surface

As the reconstruction of the electrical activity in the heart is an ill-posed problem, several assumptions and constraints have to be made in order to have a reliable solution. One important constraint is to limit the solution only to the surface of the heart. Therefore, an alternative formulation compared to the one developed in the previous section (section 3.1) was performed.

With the use of Green's second identity (equation (3.3)), the definition for solid angles (equation (3.8)) and dividing the volume into an inner, S_H (heart), and outer, S_B (body), surfaces, equation (3.9) can be written as [10]

$$\phi^o(\vec{r'}) = -\frac{1}{4\pi}\int_{S_H}\phi_H(\vec{r})d\Omega - \frac{1}{4\pi}\int_{S_H}\frac{\nabla\phi_H(\vec{r})}{r}dS_H - \frac{1}{4\pi}\int_{S_B}\phi_B(\vec{r})d\Omega \tag{3.38}$$

where ϕ^o is the potential at the observer's point. The observer can be located anywhere in the volume, therefore a particular case can be produced when the observer is located very close to S_H or S_B, and the potential is equal to ϕ_H or ϕ_B, this approach was first suggested by [11], which led to the derivation of a set of equations

$$\phi_H(\vec{r'}) - \frac{1}{4\pi}\int_{S_H}\phi_H(\vec{r})d\Omega_{HH} - \frac{1}{4\pi}\int_{S_H}\frac{\nabla\phi_H(\vec{r})}{r}dS_H - \frac{1}{4\pi}\int_{S_B}\phi_B(\vec{r})d\Omega_{HB} = 0. \tag{3.39a}$$

$$\phi_B(\vec{r'}) - \frac{1}{4\pi}\int_{S_H}\phi_H(\vec{r})d\Omega_{HB} - \frac{1}{4\pi}\int_{S_H}\frac{\nabla\phi_H(\vec{r})}{r}dS_H - \frac{1}{4\pi}\int_{S_B}\phi_B(\vec{r})d\Omega_{BB}. \tag{3.39b}$$

Equations (3.39), can be discretized and rewritten in an operators formulation similar to equations (3.10) and (3.15),using

$$P_{HH} = -\frac{1}{4\pi}\int_{S_H} d\Omega_{HH} \tag{3.40a}$$

$$P_{HB} = -\frac{1}{4\pi}\int_{S_B} d\Omega_{HB} \tag{3.40b}$$

$$G_{HH} = -\frac{1}{4\pi}\int_{S_H}\frac{\nabla}{r}dS_H = 0 \tag{3.40c}$$

$$P_{BB} = -\frac{1}{4\pi}\int_{S_B} d\Omega_{BB} \tag{3.40d}$$

$$P_{HB} = -\frac{1}{4\pi}\int_{S_H} d\Omega_{HB} \tag{3.40e}$$

$$G_{BH} = -\frac{1}{4\pi}\int_{S_H}\frac{\nabla}{r}dS_H. \tag{3.40f}$$

Therefore equation (3.39a) becomes

$$P_{HB}\Phi_B + P_{HH}\Phi_H + G_{HH}\Gamma_H = 0 \tag{3.41}$$

and equation (3.39b) becomes

$$P_{BB}\Phi_B + P_{BH}\Phi_H + G_{BH}\Gamma_H = 0 \tag{3.42}$$

and Γ_H contains the normal components of the gradients on S_H from equations (3.39). Then, from equation (3.41), the Γ_H term can be obtained

$$\Gamma_H = -(G_{HH})^{-1}(P_{HB}\Phi_B + P_{HH}\Phi_H) \tag{3.43}$$

Then, substituting equation (3.43) into equation (3.42), an equation that relates Φ_B and Φ_H can be found

$$(P_{BB} - G_{BH}(G_{HH})^{-1}P_{HB})\Phi_B = (G_{BH}(G_{HH})^{-1}P_{HH} - P_{BH})\Phi_H \tag{3.44}$$

Equation (3.44) can be written as

$$\Phi_B = Z_{BH}\Phi_H \tag{3.45}$$

where Z_{BH} is given by

$$Z_{BH} = (P_{BB} - G_{BH}(G_{HH})^{-1}P_{HB})^{-1}(G_{BH}(G_{HH})^{-1}P_{HH} - P_{BH}) \tag{3.46}$$

which is the equation used in this study to relate the potentials on both surfaces.

3.2.2 Inverse problem formulation

In this theoretical investigation only the surface potential of heart will be reconstructed from the electric field measured on the surface of the body by a numerical approximation. Therefore, the inverse problem formulation starts from the forward problem formulation described from equation (3.45), but for simplicity of notation, equation (3.45) is written as

$$\boldsymbol{y} = \boldsymbol{Z}\boldsymbol{x} \tag{3.47}$$

where $\boldsymbol{y}$ represents the measured potentials Φ_B on the surface of the body, $\boldsymbol{Z}$ is the matrix Z_{BH} with only geometrical information, as described in the forward problem section and $\boldsymbol{x}$ is the solution of the cardiac sources, in our case the epicardial potentials Φ_H .

An important property of the matrix $\boldsymbol{Z}$ is that it is independent of time, because it was defined using only the geometrical properties of the volume conductor in a quasi-static formulation without considering the dynamic variation of the geometry (heart motion or other tissue motion due to respiration). This can be justified because of the time delay between the electric excitation and the contraction in

cardiac myocytes, except during the QRS complex. Also, the respiration process and the cardiac rhythm have different main frequencies. Though, this may yield to important sources of error, it is difficult enough to get high resolution static images of the body, with current imaging techniques (such as MRI or CT-scan), to try to create high resolution meshes of the heart and torso at a specific instant in time for each patient.

3.2.3 Ill-posed cardiac inverse problem

Therefore, from equation (3.47), the inverse problem can be seen as finding a solution $\boldsymbol{x}$, given a set of measurements $\boldsymbol{y}$ produced from a model given by $\boldsymbol{Z}$. The solution $\boldsymbol{x}$ must be physically and physiologically consistent. Unfortunately, the mathematical solution cannot be obtained by a simple inversion of the geometry matrix $\boldsymbol{Z}$, and as mentioned before, as $\boldsymbol{x}$ represents the potentials of the million of heart cells Φ_H, the inverse problem becomes ill-posed.

One of the main reasons that the inverse problem is ill-posed, is that different configurations of the electric source can rise to exactly the same set of measurements on the surface of the body; therefore, the solution is not unique. One way to overcome the problem is to limit or constrain the set of possible solutions, i.e., finding the potentials only on the epicardium. Though, it is still not possible to obtain a mathematically unique solution, so, the problem is still ill-posed. Another issue is that the solution does not depend continuously on the measurements, which means small perturbations on the body surface potential measured can produce large changes in the calculated solution. In Figure 3.2, it can be seen that a normal least squares solution makes non sense without previous constraints.

3.2.4 Mathematical model and inverse problem solution

If $\boldsymbol{Z}$ is non square, the typical way to solve equation (3.47) is via least squares method. As long as the non-square condition was due to the number of measurements being larger than the number of unknowns to be computed. The least squares method finds a pseudo-inverse solution, by minimizing the (Euclidean) norm of the residual error.

$$\boldsymbol{x} = \min_{x} ||\boldsymbol{Z}\boldsymbol{x} - \boldsymbol{y}||^2, \tag{3.48}$$

The solution of the equation (3.48), also solves the matrix equation

$$\boldsymbol{x} = (\boldsymbol{Z}^T\boldsymbol{Z})^{-1}\boldsymbol{A}^T\boldsymbol{y}. \tag{3.49}$$

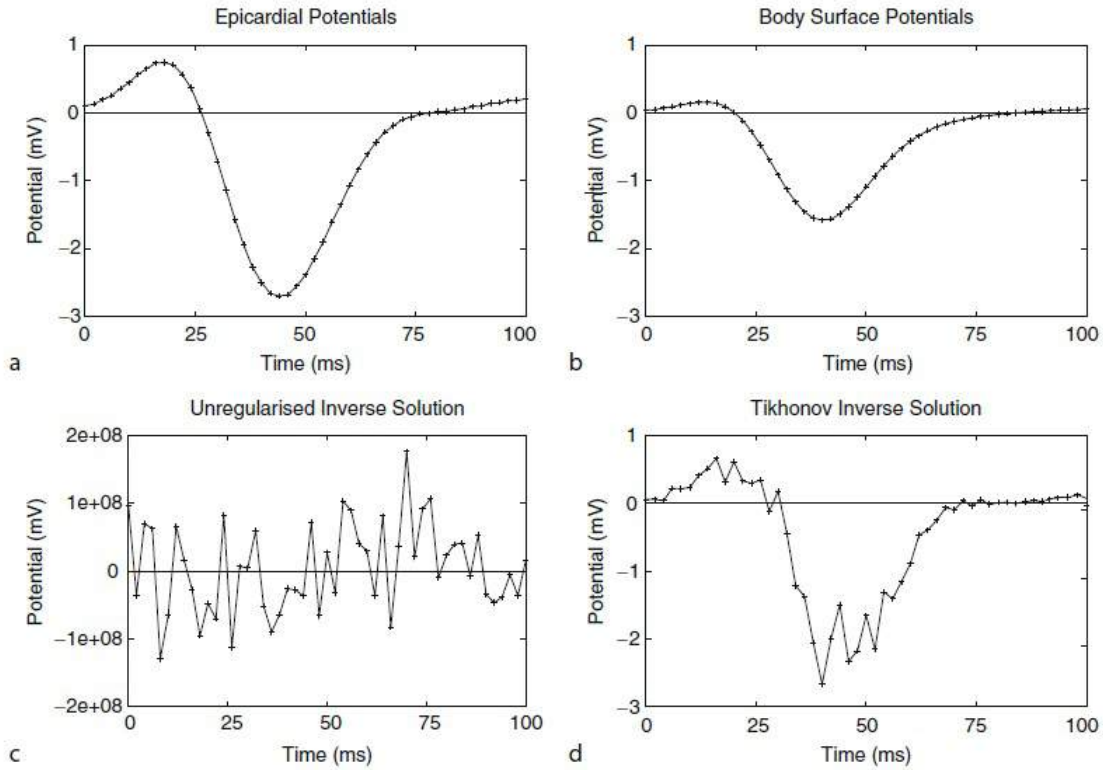

Figure 3.2: Example of a regularized and non-regularized ill-posed signal. a) Epicardial potential in one point. b) Body surface signal obtained by a forward solution. c) Inverse problem solution for the epicardial, from the BSP measured using least square without regularization. d) Inverse solution using Tikhonov regularization. Image taken from [1].

However, this solution not only is not unique, but also can lead to unrealistic solutions, such as the one observe in the Figure 3.2. So, one way to avoid this problem is to add extra information about the solution. This is usually done by constraining the solution, through regularization methods. For example, high spatial frequencies are usually more attenuated in the volume conductor than low frequencies, so, one way is to limit the solution to only low spatial frequencies. The most common method used to reconstruct the epicardial potentials is called Tikhonov Regularization [12], and it is the one used in this Thesis.

Tikhonov regularization method

The Tikhonov regularization method limits the solution in order to find a more reliable physical and physiologically one. In this method one or a set of constraints acts directly on the matrix as a penalty function. Then, the weighted norm of this function plus the residual norm are minimized. Therefore, the equation (3.48), takes the form of

$$\boldsymbol{x} = \min_{x}\{||\boldsymbol{Z}\boldsymbol{x} - \boldsymbol{y}||^2 + \lambda^2||\boldsymbol{R}\boldsymbol{x}||^2\}, \tag{3.50}$$

where λ is the "regularization parameter" or weighted function that controls the degree of regularization. Meanwhile, the matrix $\boldsymbol{R}$ is the "regularization operator", which constrains the solution in the spatial domain.

If $\boldsymbol{R} = \boldsymbol{I}$ (the identity matrix) the amplitude of the solution is limited, this is known as *Zero order Tikhonov regularization*. If $\boldsymbol{R} = \nabla$ (the gradient operator) the amplitude of the first derivative of the solution is limited, this is known as *First order Tikhonov regularization*. Finally, if $\boldsymbol{R} = \Delta = \nabla^2$ (the Laplace differential operator) the amplitude of the second derivative of the solution is restricted, this is known as *second order Tikhonov regularization*.

Therefore, the solution of the equation (3.50) also solves the next matrix equation

$$\boldsymbol{x} = (\boldsymbol{Z}^T\boldsymbol{Z} + \lambda\boldsymbol{R}^T\boldsymbol{R})^{-1}\boldsymbol{Z}^T\boldsymbol{y} \tag{3.51}$$

Thus, the final solution is a match among the unconstrained least squares solution and the set of constraints with prior information, this yields a more physical and physiological solution.

There are other methods to constrain the solution of the inverse problem, such as the singular value decomposition (SVD), which can be truncated (TSVD) or generalize (GSVD) [12], many others have been proposed but not tested yet [1].

L-curve and regularization parameter

The L-curve is a plot of the square norm of the residual vector against the norm of the estimated regularized solution (Figure 3.3), and it is used to find the best regularization parameter which fits the ill-posed problem best [13]. The graph is usually plotted on a log-log scale; however a normal scale can also be used. The best regularization parameter is found by selecting the corner value in the L-curve plot. The corner of the L-curve plot gives the solution which equilibrates best the regularization and the error produced by it. The corner can be found in an automated way by triangulation algorithms [14].

The specific details of the implementation of the methods described in this chapter is given in each result chapter (Chapters 5 to 8). However, in the next chapter (Chapter 4), a description of the computational models (geometries, model development and validation) is presented.

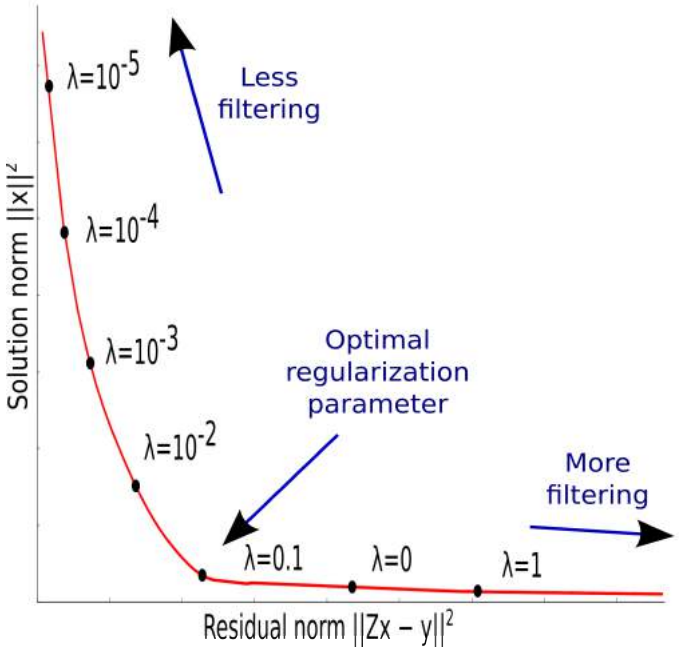

Figure 3.3: L-curve method. Plot of the square norm of the residual vector against the norm of the estimated regularized solution. The corner of the curve corresponds to optimum regularization.

Bibliography

[1] P. W. Macfarlane, A. van Oosterom, and M. Janse, *Comprehensive electrocardiology*, vol. 4. Springer Science & Business Media, 2010.

[2] R. Barr, T. Pilkington, J. Boineau, and M. Spach, "Determining surface potentials from current dipoles, with application to electrocardiography," *IEEE Transactions on Biomedical Engineering*, vol. 2, no. BME-13, pp. 88–92, 1966.

[3] R. M. Gulrajani and G. E. Mailloux, "A simulation study of the effects of torso inhomogeneities on electrocardiographic potentials, using realistic heart and torso models.," *Circulation research*, vol. 52, no. 1, pp. 45–56, 1983.

[4] J. D. Jackson and J. D. Jackson, *Classical electrodynamics*, vol. 3. Wiley New York etc., 1962.

[5] Y. Salu, "Implementing a consistency criterion in numerical solution of the bioelectric forward problem," *Biomedical Engineering, IEEE Transactions on*, no. 6, pp. 338–341, 1980.

[6] J. D. Stott, *Developing realistic models of the atrium and the p-wave*. PhD thesis, The University of Manchester, 2009.

[7] J. Sarvas, "Basic mathematical and electromagnetic concepts of the biomagnetic inverse problem," *Physics in medicine and biology*, vol. 32, no. 1, p. 11, 1987.

[8] J. Nenonen, C. J. Purcell, B. M. Horacek, G. Stroink, and T. Katila, "Magnetocardiographic functional localization using a current dipole in a realistic torso," *Biomedical Engineering, IEEE Transactions on*, vol. 38, no. 7, pp. 658–664, 1991.

[9] J. Hadamard, *Lectures on Cauchy's problem in linear partial differential equations*. Courier Corporation, 2014.

[10] R. C. Barr, M. Ramsey III, and M. S. Spach, "Relating epicardial to body surface potential distributions by means of transfer coefficients based on geometry measurements," *Biomedical Engineering, IEEE Transactions on*, no. 1, pp. 1–11, 1977.

[11] T. Pilkington, R. Barr, and C. Rogers, "Effect of conductivity interfaces in electrocardiography," *The Bulletin of mathematical biophysics*, vol. 30, no. 4, pp. 637–643, 1968.

[12] P. C. Hansen, *Rank-deficient and discrete ill-posed problems: numerical aspects of linear inversion*, vol. 4. Siam, 1998.

[13] P. C. Hansen, "Analysis of discrete ill-posed problems by means of the l-curve," *SIAM review*, vol. 34, no. 4, pp. 561–580, 1992.

[14] J. L. Castellanos, S. Gómez, and V. Guerra, "The triangle method for finding the corner of the l-curve," *Applied Numerical Mathematics*, vol. 43, no. 4, pp. 359–373, 2002.

Chapter 4

Computational Models of the Human Heart and Torso

This chapter outlines the development of human heart and torso models in respect to their constituent geometries, electrophysiological cellular and tissue models. Validation of these models is also discussed.

4.1 Mesh and model development

A brief description of the heart model is presented in this section. However, more details of the heart model and cardiac electrophysiology used in this Thesis are discussed in each result chapter (Chapters 5-8), as it was not the aim of this project to develop a new heart model. A Detailed description of the torso model is presented in this chapter, as development of this model was one the objectives of this Thesis. Therefore, some information presented in this chapter is necessarily repeated in some result chapters (Chapter 5-8).

4.1.1 3D anatomically-accurate cardiac model

The heart anatomical models implemented in this Thesis were based on three-dimensional (3D) detailed structural models of human atria (Figure 4.1A) and ventricles (Figure 4.1B) that were developed in previous studies [1, 2, 3]. In both atrial and ventricular anatomical models, cardiac tissues were segmented into variant structural regions with distinctive electrophysiological properties (Figure 4.1) [1, 2, 3]. Such anatomically accurate and electrophysiologically detailed 3D atrial and ventricular models have been shown to be suitable for studying mechanisms underlying AF [1, 4, 2] and ventricular fibrillation (VF) genesis [3]. Details of the atrial cellular and whole organ models can be found in Colman et al [4]. Details of cellular models of ventricular electrophysiology and its spatial heterogeneity can be found in the study

of Ten Tusscher et al [5].

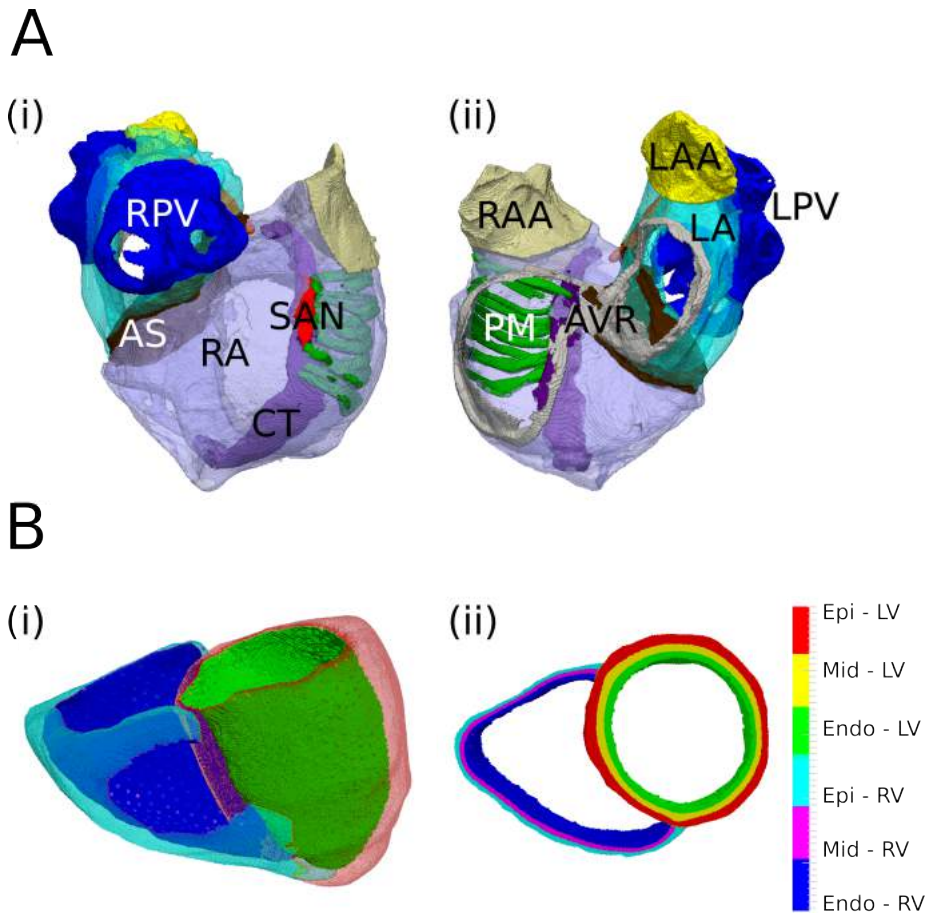

Figure 4.1: 3D atria and ventricular models of the human heart with segmented regions. Frontal (A-i) and posterior (A-ii) atria views are presented. (A) Atria: right atrium (RA, transparent purple), right atrial appendage (RAA, beige), pectinate muscles (PM, green), cristal terminalis (CT, solid purple), sinoatrial node (SAN, red), superior vena cava (SVC), atrio-ventricular ring (AVR, grey), right pulmonary vein (RPV, blue), Bachmanns bundle (BB, orange), left atrium (LA, light blue), left atrial appendage (LAA, yellow), inferior vena cava (IVC) and left pulmonary veins (LPV, blue). Lateral (B-i) and horizontal (B-ii) ventricular views are presented. (B) Ventricles: Left ventricle epicardium (EPI-LV, red), left ventricle midcardium (Mid-LV, yellow), left ventricle endocardium (Endo-LV, green), right ventricle epicardium (Epi-RV, light blue), right ventricle midcardium (Mid-RV, purple), right ventricle endocardium (Endo-RV, dark blue). Figure adapted from [4]

.

4.1.2 3D anatomically-accurate human thorax model

The torso model was based on the semi-automatic segmentation of MRI images taken from the visible human dataset [6] using the software ITK-Snap [7] and MATLAB [8]. Two torso models have been used, including one male and one female, each considers the inner organ structures of lungs, liver, spinal cord, ribs, stomach and kidneys with different electrical conductivities (Figure 4.2). The electrical conductivity of the inner organs was added using values derived from the literature and can be found in [9, 10, 11, 12, 13] and in Table 4.1.

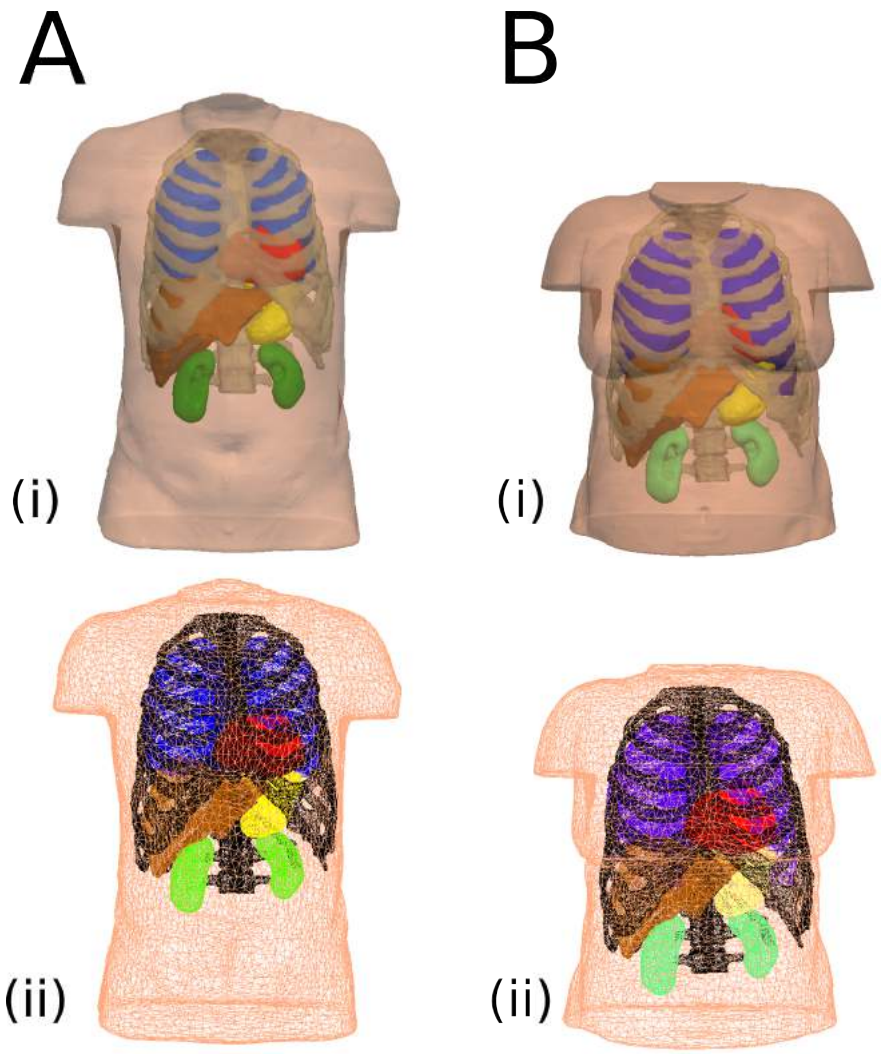

Figure 4.2: (A) Male and (B) female torso models reconstructed from the visible human dataset [6]. Different internal tissues included in the model are illustrated using (i) transparency and (ii) meshes. Blue-lungs, brown-liver, yellow-stomach, black-spinal cord and ribs, green-kidneys, red-ventricles, pink-torso. The position of the ventricles inside the body can also be observed.

The male (Figure 4.2A) and female (Figure 4.2B) geometries were discretised at a spatial resolution of 0.66 x 0.66 x 0.66 mm^3 and 0.66 x 0.66 x 0.1 mm^3, respectively. The inhomogeneous regions (lungs, liver, spinal cord, ribs, stomach, kidneys -

Tissue type	Conductivity (Sm^{-1})
Thorax	0.2
Lungs	0.08
Liver	0.15
Stomach	0.12
Kidneys	0.07
Bone	0.005
Blood	0.6
Fat	0.05
Myocardium	0.25

Table 4.1: Table of tissue conductivities [9, 10, 11, 12, 13].

Figure 4.2-i), were discretised at varying, lower resolutions (1 x 1 x 1 mm^3, 1.5 x 1.5 x 1.5 mm^3 and 2 x 2 x 2 mm^3) in order to improve the performance of the numerical solution. All surfaces were meshes created by triangular elements connected through nodes (Figure 4.2-ii).

The atria and ventricles models were placed inside the thorax models, with location and orientation set based on the description made by Ho and Sanchez-Quintana (Figure 4.3-i) [14] and Adeniran et al [3] (Figure 4.2), respectively. The position of the heart was also aligned with the segmented heart surfaces in the torso (Figure 4.3-ii) as an additional guidance. In simulations, the two positions of the atria used varied by a rotation of (315, 45, 40) in each direction, using a z-x-y Euler angles convention, acting in the coordinate system of the heart, and a translation of (0.055, -0.177, -0.217) mm in the x-y-z coordinate system (Figure 4.3).

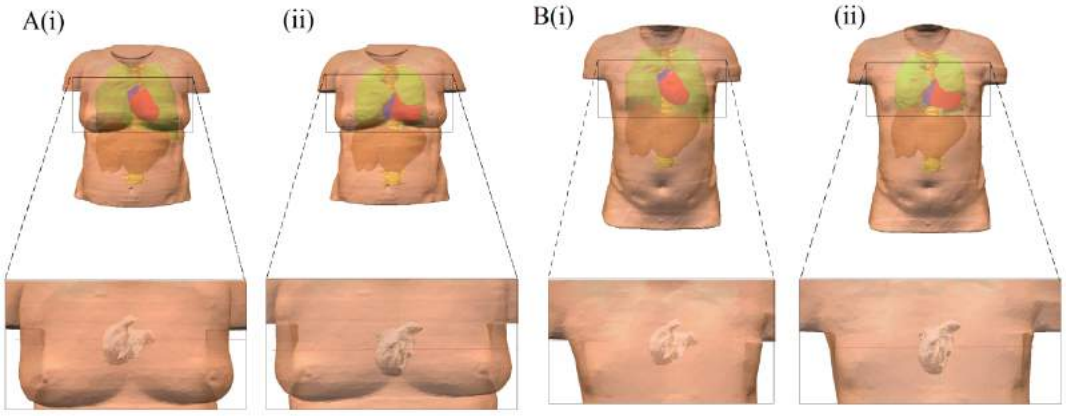

Figure 4.3: (A) Female and (B) Male torso models reconstructed from the visible human dataset [6]. (i) Position of the atria as described by Ho and Sanchez-Quintana [14]. (ii) Position of the atria based on the segmentation of the original MRI images. Figure adapted from [15]. Green-lungs, brown-liver, yellow-spinal cord, blue/white-atria, red-ventricles, pink-torso.

.

4.2 Simulation of electric and magnetic fields

A computational program, written in the C language, was developed to calculate the electric potential and the magnetic field on the body surface, as described in Chapter 3. The fields were simulated at each element of the geometries described in the previous section (section 4.1). These BSPs were used to find an inverse problem solution with Tikhonov regularization method [16] on the surface of the atria (as described in Chapter 3). Using equations (3.27) and (3.22) to (3.24), described in Chapter 3, the electric potentials on the body surfaces were computed, based on the method described by Salu [17, 18]. The magnetic field was calculated using equations (3.35) and (3.36), based on a method described by Nenonen et al [19, 20]. The transfer matrices from equations (3.16), (3.47) and (3.37), were constructed by computing the solid angle subtended by every triangular element, based on the method proposed by van Oosterom and Strackee [21].

A subroutine was developed to read the pre-calculated cardiac membrane potentials from a specific cardiac geometrical model (either atria or ventricles) as input. The input file consists of a series of data representing membrane potentials of each node in the heart model, with a time interval of 1 ms. In the geometry of the heart model, there are cell nodes (active nodes) and empty space (passive nodes). For each active node of the heart tissue, the current density was computed from equation (2.16). In order to reduce computational time, the atrial or ventricular model was divided into 5x5x5 node blocks. From the active nodes, dipoles were generated at the centroid of each block; the centroid was calculated from the distribution of active nodes among the blocks. The constructed dipoles were then used as the source terms in equations (3.3), (3.38) and (3.29). From these dipoles, the transfer matrices (equations (3.16), (3.47) and (3.37)) were computed.

The Intel-LAPACK library [22], was used to solve the system of equations (3.16) to (3.18). First, the SGETRF subroutine was used to factorize the transfer matrix $\boldsymbol{A}$ (equation (3.16)). As a static torso was considered, this factorization had to be performed only once. Then, the SGETRS subroutine was used to solve the equations (3.17) and (3.18), for each instant of time, and using the factored transfer matrix $\boldsymbol{A}$. The first element of the mesh was chosen to be the zero potential, as required by Salu's method [17]. This element is part of the neck location of the torso mesh. Once the BSP was calculated, the magnetic field was obtained with similar subroutines.

The discretized transfer matrix $\boldsymbol{Z}$ (equation (3.47)) was also computed using the SGETRF and SGETRS subroutines to factorize each matrix from equation (3.46). Then, equations (3.48) and (3.50) were calculated using the SGELS subroutine. In

order to find the regularization parameters for each Tikhonov order, the identity (Zero order), gradient (First order) and Laplace (Second order) operator were computed and introduced on the regularized solution (equation (3.50)) [23]. The L-curve method (section 3.2.4) together with the triangulation method [24] were also used to find the best regularization parameter. Then, the best inverse solution was obtained using equation (3.51) with the best regularization parameter and the SGETRF and SGETRS subroutines.

4.2.1 Simulated ECG and MCG systems

After calculating the electrical potential and the magnetic field in all elements of the body surface, the 12-, 36- and 64-lead ECG and MCG signals were derived from selected elements of the torso mesh, corresponding to the locations of electrodes/sensors for 12-, 36-, and 64-lead ECGs and 36-lead MCG sytems (Figure 4.4).

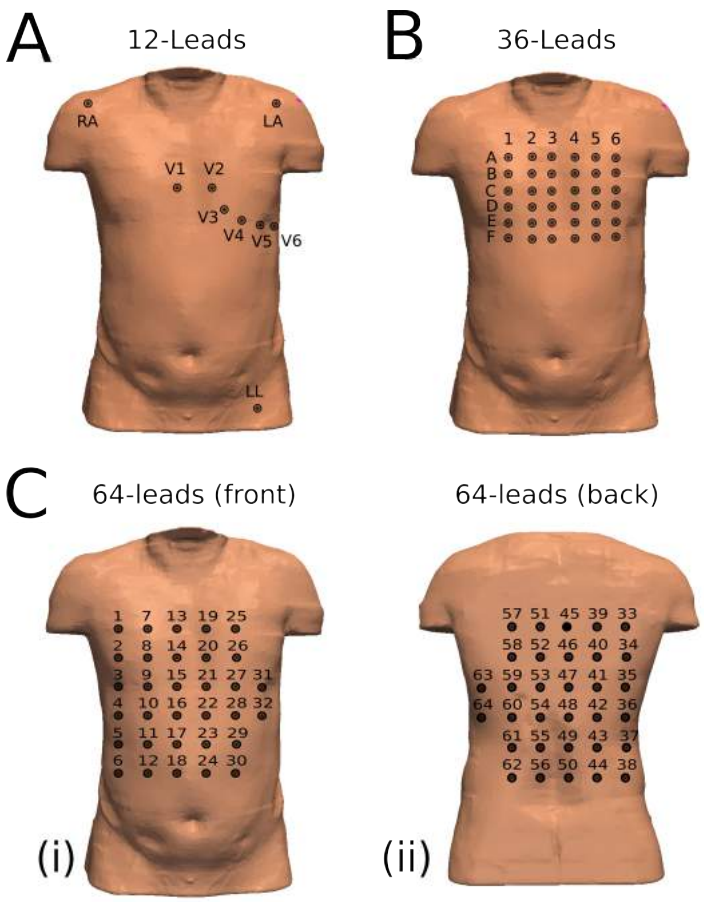

Figure 4.4: Positions of the electrode placement in the torso mesh for (A) 12-lead, (B) 36-lead and (C) 64-lead systems, from the front (i) and from the back (ii).

4.3 Validation of the model

An agreement between experimental and simulated data is not guarantee that the model is well validated [25]. In principle, the validation of a multi-scale model needs to include the agreement of many physical and physiological parameters, however, taking into account all the variabilities in geometry and model parameter between individual patients can be a difficult or impossible task. Therefore, most validation process are preformed through comparison of the simulated and experimental data during different conditions [25]. In this study, the models were validated by comparing simulations with experimental data during normal (sinus rhythm) conditions at different scales.

Validation of atrial and ventricular activation sequence during healthy/normal conditions has been previously discussed and can be found in [1, 2, 4] and [3, 26], respectively. The models have been previously used and determined suitable for studying cardiac arrhythmia mechanisms [1, 2, 4, 3, 26].

4.3.1 BSP and ECG data

Atria

The simulated 12- and 64-lead ECG P-waves for healthy/control conditions (no cardiac disease presented) matched well with those of the experimental data of multiple patients [27]. The simulated P-wave (morphology and duration) of the 12-lead ECGs during normal conditions (Figure 4.5) were within the normal range (section 2.4.4) [25, 28, 29, 30]. In simulations, an upright P-wave was seen in *Lead I*, *Lead II*, aVF and V_3 to V_6, with some degree of bifidity in V_1 and V_2. An inverted P-wave was seen in aVR and aVL, with a biphasic almost flat P-wave in *Lead III*. The simulated P-wave duration was 120 ms.

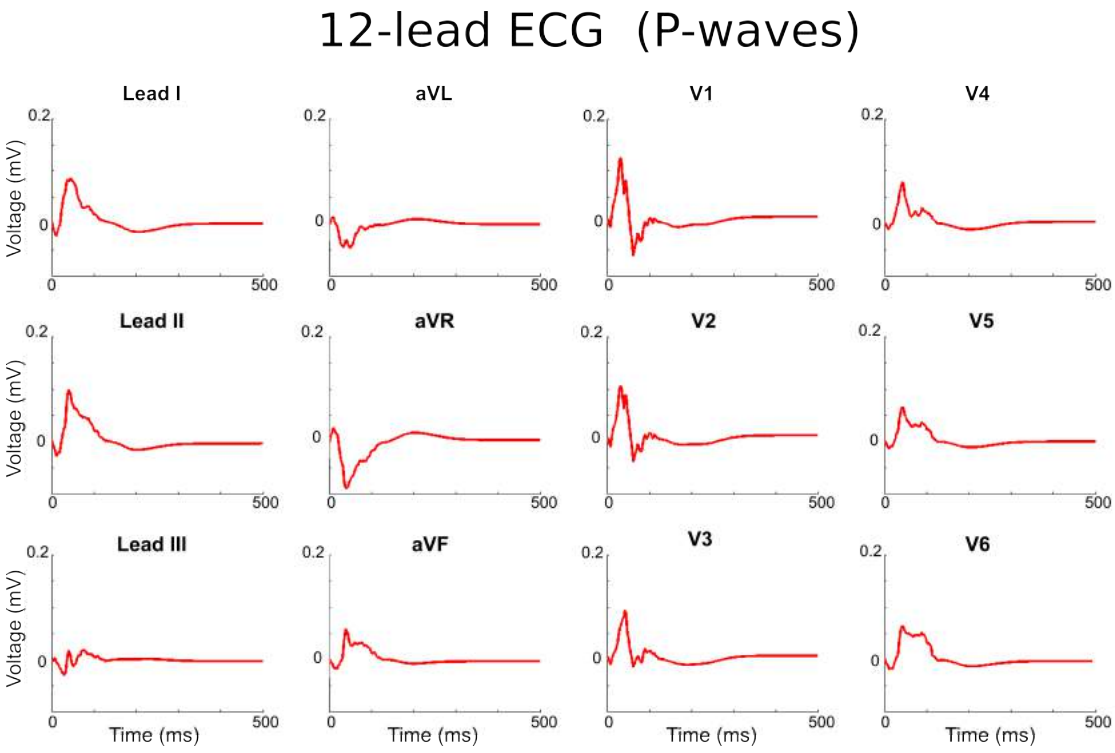

Figure 4.5: Simulated P-waves of 12-lead ECGs during healthy/normal conditions.

The polarity in simulated and experimental P-waves in the 64-lead ECG was mainly positive in the left-superior part of the body, negative in the right, inferior part of the body, and biphasic or flat in intermediary locations (Figure 4.6 A and B) [15]. To quantify this agreement, polarity maps were also compared. In this map, the polarity of the P-wave (positive/negative/biphasic) is noted at each electrode location. A biphasic P-wave was defined as one in which the second largest peak (positive or negative) was at least half of the amplitude of the largest peak (negative or positive). Simulated data shows an agreement of 90.1 $\pm$ 3.2% in polarity distribution with experimental data (Figure 4.6) [15].

The spatial distribution and amplitude evolution of the P-wave dipole was also computed, replicating the experimental data [27]. Therefore, the atrial dipole was computed from the maximum positive and minimum negative potentials from the 64-lead ECG P-waves [27]. The temporal evolution of the dipole location (Figure 4.7C-i) and amplitude (Figure 4.7C-ii) agreed with experimental data [27, 15]. Hence, the model is validated for control and suitable for the investigation of ectopic atrial activity. Further discussion of the P-wave dipole evolution can be found in Chapter 5.

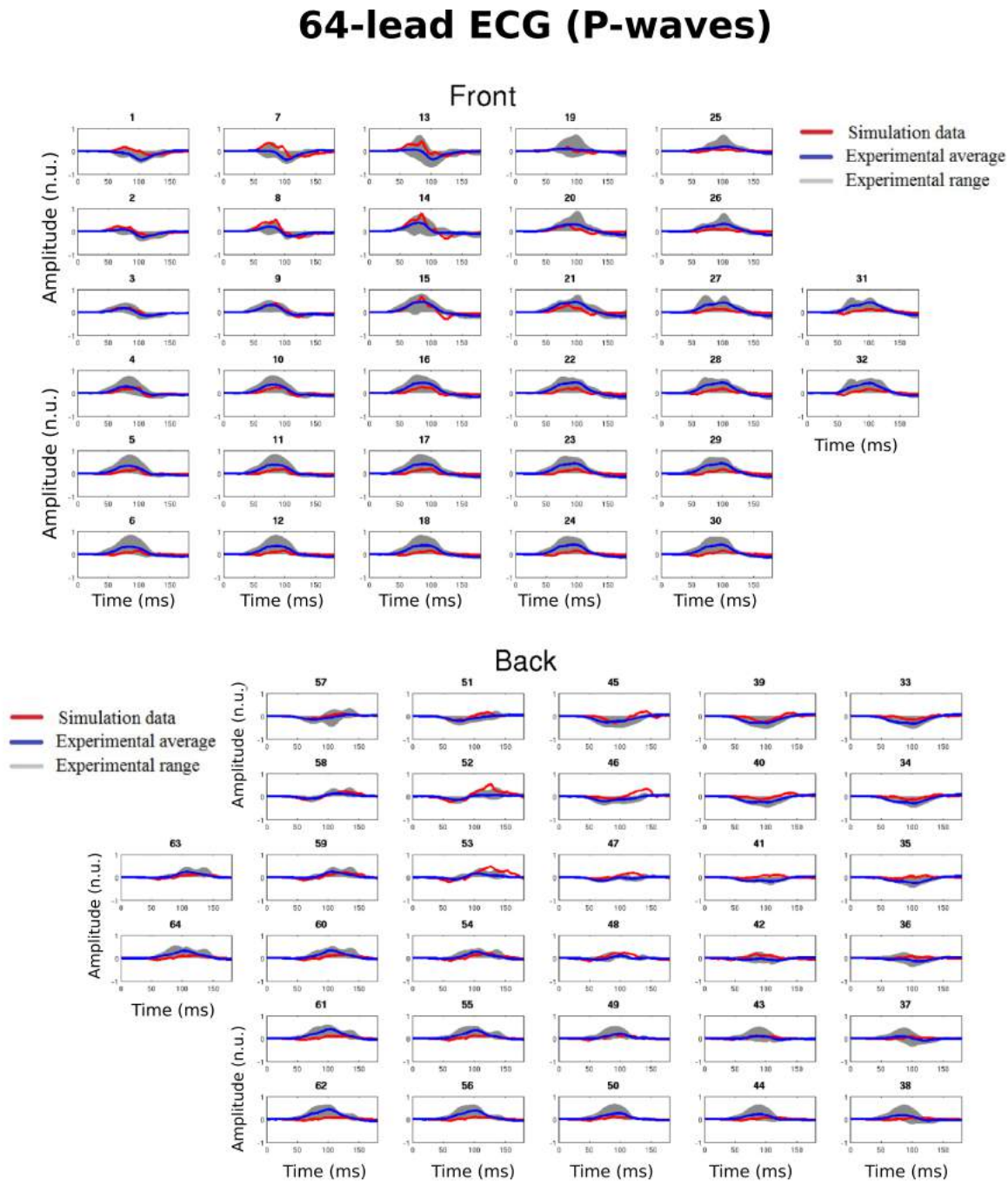

Figure 4.6: P-waves obtained from experimental data (blue line and grey shadow) and simulated (red line) data. The experimental average is the average data of 8 healthy people (blue line), and the experimental range corresponds to the maximum and minimum values of these signals (grey shadow). These measurements used the same protocol as described in [15]. Both experimental and simulated P-waves were normalized for comparison. Figure adapted from [15]

.

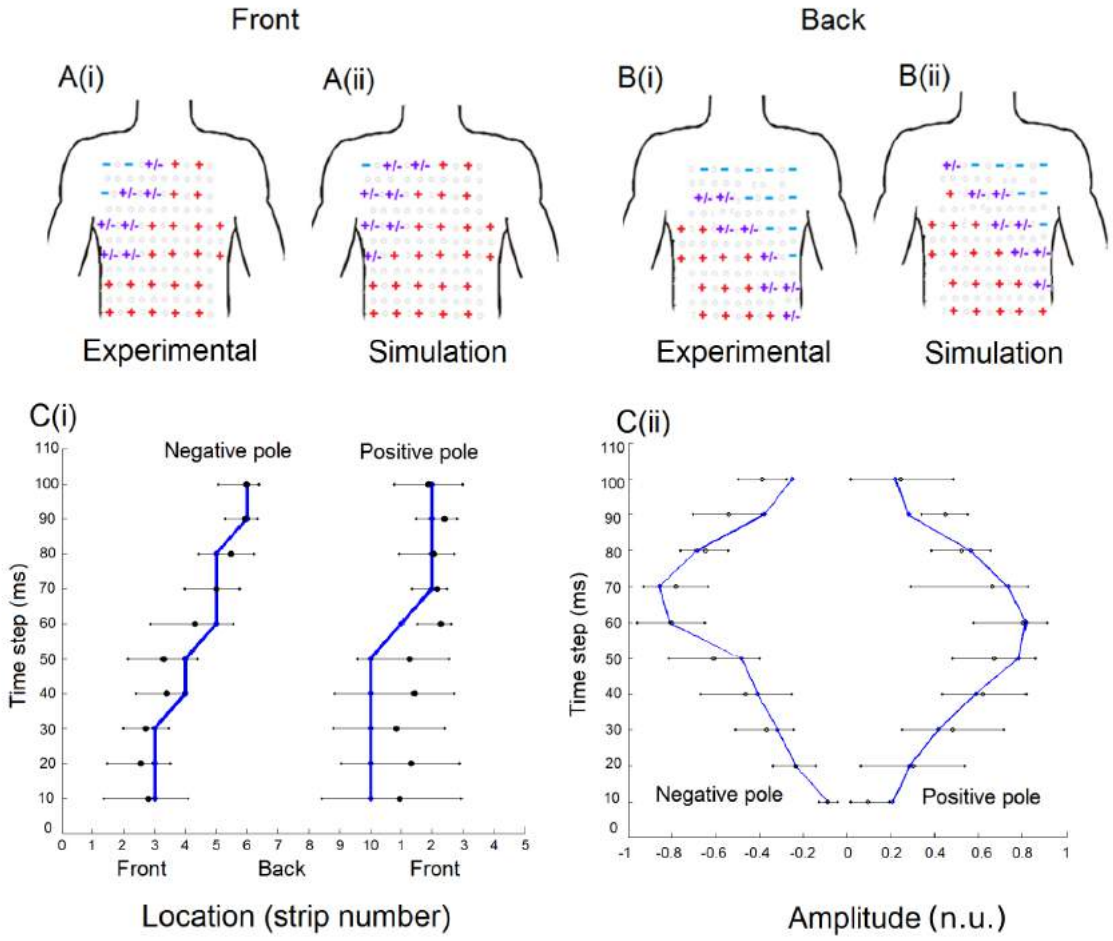

Figure 4.7: Polarity maps and dipole validation. (A) and (B) Comparison of the simulated 64-lead ECG P-waves polarity (ii) to experimental data (i). In this figure, the arrangement of the P-waves is set out to match electrode placement (Figure 4.4). We observed the polarity pattern of the P-waves of the experimental and simulation, in the front (A) and back (B) part of the body. The red positive sign signifies an upright P-wave, the blue negative sign represents an inverted P-wave, and the purple positive/negative sign represents a biphasic P-wave. (C) Spatial (i) and amplitude (ii) temporal evolution of the dipole. The black dots and lines are the experimental data and error bar taken from [27], and the blue lines and dots are obtained from our simulation during a stimuli applied to the superior part of the sino-atrial node region. In (i) the horizontal axis is a continuous scale from the first vertical line electrodes (1 to 6) to the last line of electrodes (33 to 38), without taking in to account 31, 32, 63 and 64. Figure adapted from [15]

Ventricles

The simulated QRS complex and T-wave of the 12-lead ECGs during normal conditions were within the normal range (section 2.4.4) [25, 28, 29, 30] (Figure 4.8). An upright QRS complex was seen in *Lead I* and aVL. An inverted QRS complex was seen in *Lead II*, aVR and aVF, with some degree of bifidity. A biphasic QRS complex was seen in *Lead II*. The transient zone was seen in the chest leads, with a negative to positive transition from V_1 to V_6. The simulated QRS complex duration was 80 ms. A positive T-wave was seen in all the leads except for aVR, with an observed duration of 120 ms.

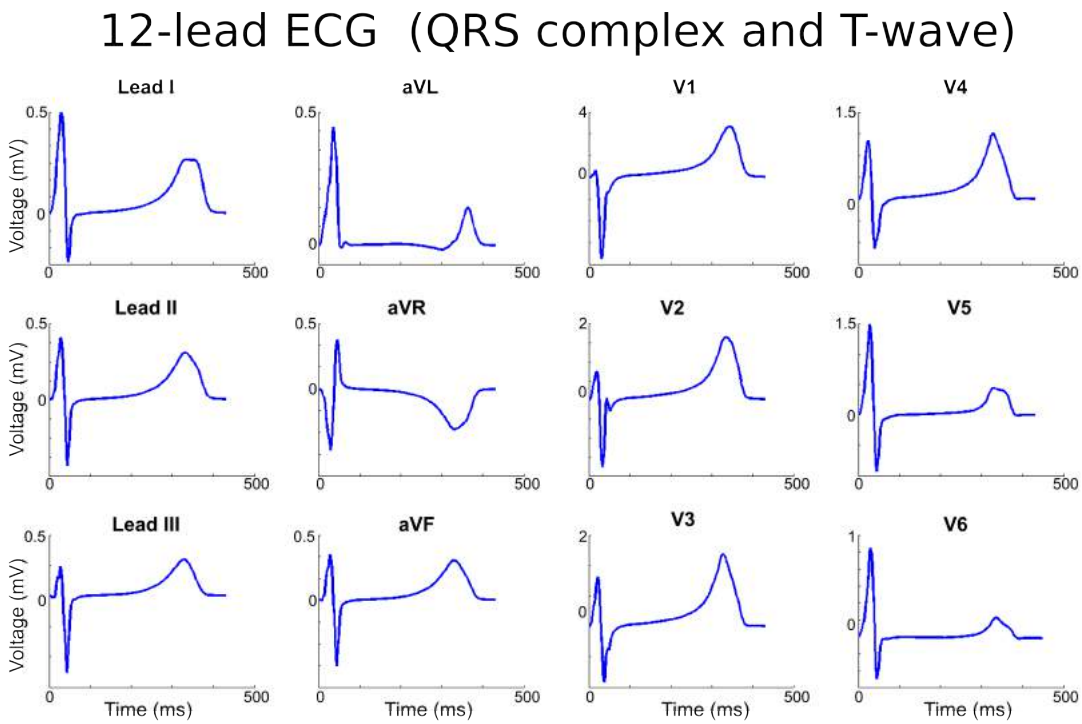

Figure 4.8: Simulated QRS complex and T-wave in 12-lead ECG during healthy/normal conditions.

During normal conditions, in both experimental and simulated data, the polarity of the QRS and T-wave of 36-lead ECG signals showed similar spatial distribution patterns (Figure 4.9). The polarity of the QRS complex was mainly positive in the left-inferior part of the body, negative in the superior right part of the body, and biphasic or flat in intermediary locations (Figure 4.9). The T-wave was positive in most of the leads, except for the superior right part of the body. These simulated spatial distribution patterns of QRS and T-wave of ECG matched experimental data [31]. Further discussion of simulated and experimental 36-lead ECG can be found in Chapter 7.

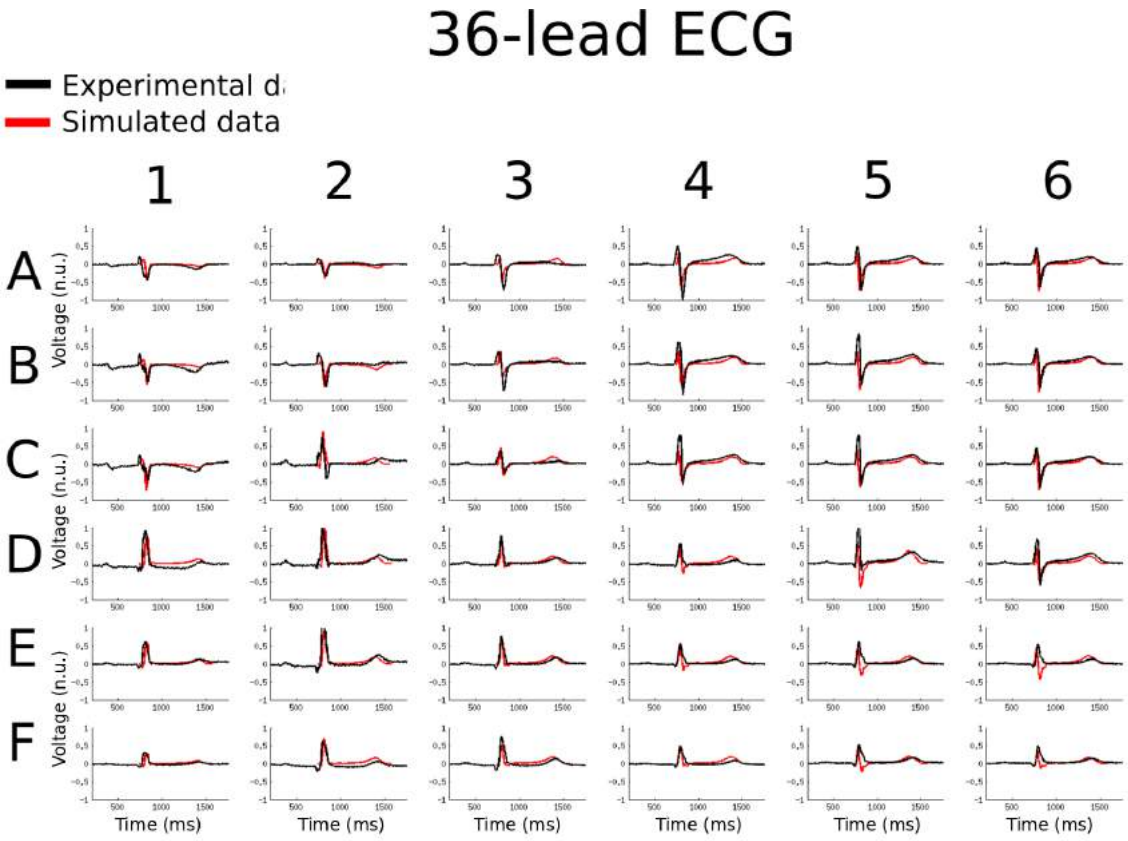

Figure 4.9: Comparison of 36-lead ECG between experimental data (black line) and simulated data (red line) during control conditions. The numbers and letters represent the electrode/sensor position (Figure 4.4).

4.3.2 Magnetic field data

Ventricles

During normal conditions, in both experimental and simulated data, the polarity of the QRS and T-wave of MCG signals showed similar spatial distribution patterns. For MCG, the polarity of the QRS complex was mainly positive in the right-inferior part of the body, negative in the superior left part of the body, and biphasic or flat in intermediary locations (Figure 4.10). The T-wave was positive in most of the leads, except for the superior left part of the body. These simulated spatial distributions patterns of QRS and T-wave of MCG matched to experimental data [31]. Further discussion of simulated and experimental 36-lead MCG can be found in Chapter 7.

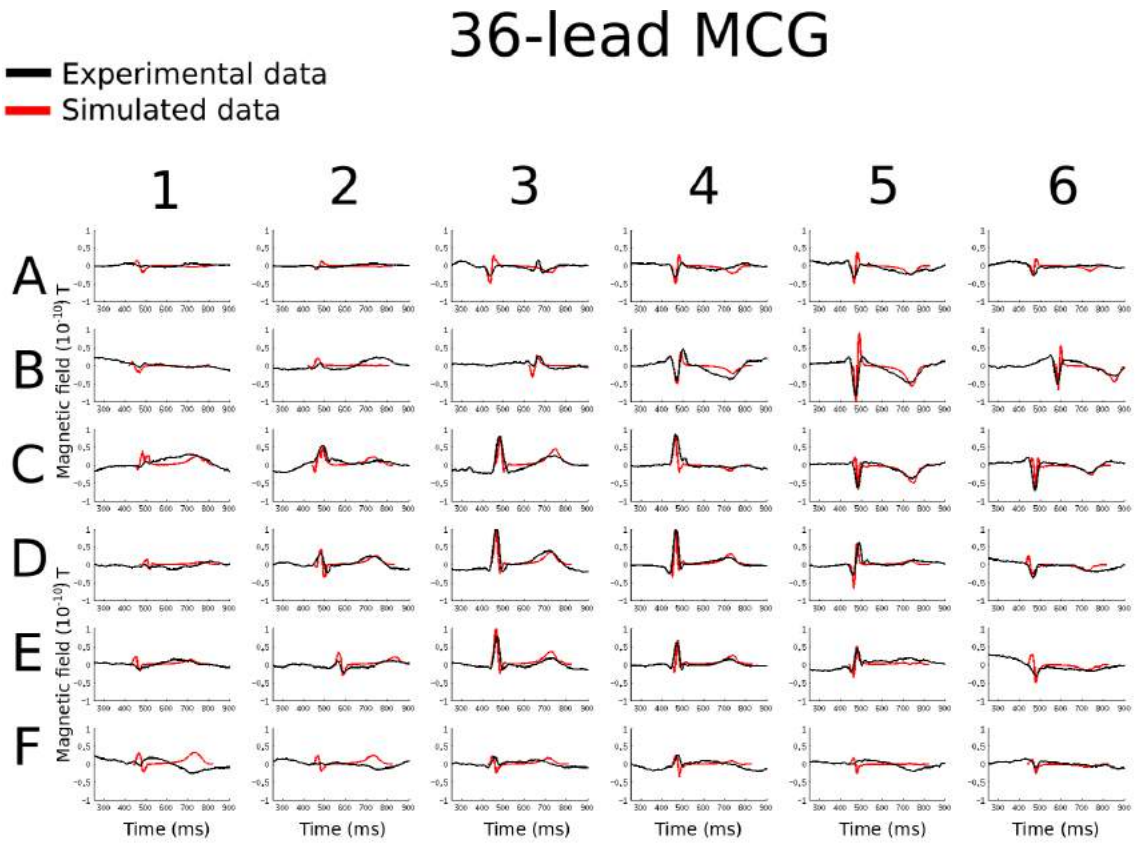

Figure 4.10: Comparison of 36-lead MCG between experimental data (black line) and simulated data (red line) during control conditions. The numbers and letters represent the electrode/sensor position (Figure 4.10).

4.3.3 Inverse problem data

Validation of the inverse problem solution in this Thesis was performed by quantitatively comparing the reconstructed activation maps and activation timings at each node of the cardiac surface to the original data, from which the inverse-problem solutions were based by solving equation (3.51). In order to investigate the effects of the spatial resolution of electrode placement on the accuracy of the reconstruction, different lead densities, i.e. numbers of electrodes, were used together with triangular atrial surface meshes with different number of nodes 4.11.

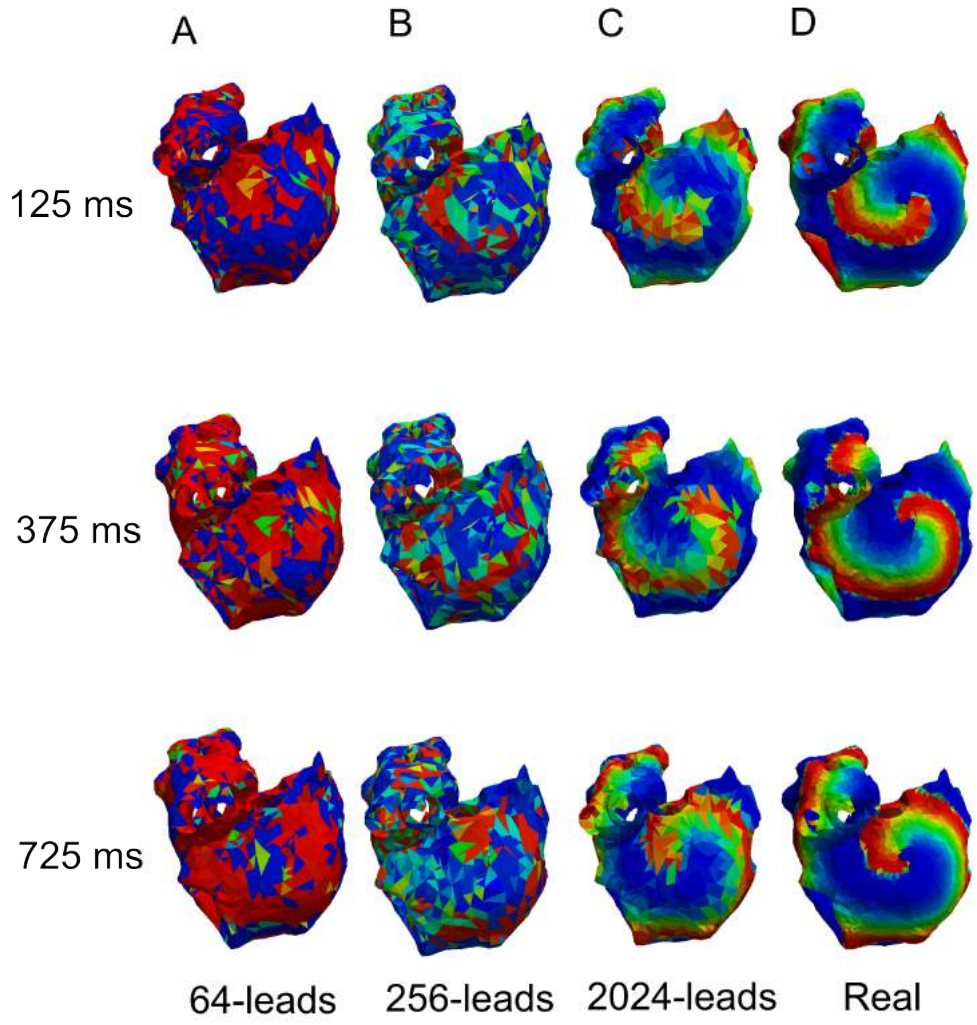

Figure 4.11: Snapshot of reconstructed epicardial surface activity during the time course of a rotor wave, which were compared with its original data at different timings (125, 375 and 725 ms). Reconstructed pattern with variant numbers of electrodes of 64 (A), 256 (B) and 2024 (C) were compared to the real activation pattern (D).

4.4 Limitations

The ECGs and MCGs simulated in this work are the cumulation of a series of processes involving the electric potential and magnetic field distribution inside the body, originating from the electrical activation sequence of the heart. As previously mentioned, simulating the electrical activation sequence of the heart was not the aim of this project. Therefore, changes in the activation of the heart, or differences in the propagation velocities through the fibres could influence the simulated fields.

While the described models, torso and heart geometries provide a good reproduction of the characteristics of the BSP distribution and simulated ECGs and MCGs, there are existing limitations which are worthwhile discussing. For example, the "assembled" nature of the model, i.e. a different atria or ventricles orientation inside the torso could produce better and different results. However, there were some anatomical landmarks present inside each torso geometry, which limited its placement, e.g. the addition of the inhomogeneous regions (lungs, liver, ribs, etc) produced a change in the orientation of the atria and ventricles inside each torso geometry.

Inhomogeneous regions which were not considered in the torso model used in this Thesis, such as skeletal muscle and subcutaneous fat layers, can produce some influence on the measured electric and magnetic fields. Previous studies suggest that the influence of these layers may affect the amplitude of surface potentials [32]. Nevertheless, the absence of these tissues does not have a large effect on the polarity of the ECG [33], MCG [34] waves and in the surface reconstruction process [35].

Another important limitation is the anisotropy in the cardiac muscle, which was not considered during the estimation of the dipole sources of the heart. Unfortunately, the effects of this are unknown due to the lack of studies considering this behaviour [25]. In addition, the anisotropic electric conductivity of the tissue inside any organ of the body was not considered. All the calculations in this Thesis were perform using BEM, which discretizes the volume into meshes with isotropic and homogeneous conductivity. FEM may prove to be an important tool with which to include this effects; however, the computational time needed could increase significantly.

Another limitation is that the presented model is static, meaning the effects of myocardium contraction are neglected. Including this would introduce variations in the position and shape of the sources and therefore may affect the computation of the resultant BSP. Unfortunately, the effects of this are also unknown due to the lack of studies considering this behaviour [25]. In addition, this could significantly

increase the computational power required to solved the problem.

As previously mentioned, the inverse problem solution was only compared with results obtained by cardiac simulations; this may have important differences in a clinical study due to the non-static nature of the problem. In addition, in simulation studies the inverse problem solution may be dependent on the forward problem calculation and the assumptions used to obtain a forward solution. To overcome these limitations the forward problem was calculated using equation (3.16), meanwhile the inverse problem calculation used equation (3.47) to obtain the matrix equations. Equation (3.16) considered different inhomogeneities inside the body and a dipoles source model, whereas, equation (3.47) considered an homogeneous torso and epicardial surface potentials as source.

Last but not least is the absence of noise in the present models, which may affect the results obtained in this Thesis. However, most of the signals used in ECG are highly filtered signals, i.e., there are algorithms designed to remove or reduce the noise, whereas cardiac signals with large degrees of noise would be unsuitable for use in any detailed clinical diagnosis.

Bibliography

[1] O. V. Aslanidi, M. A. Colman, J. Stott, H. Dobrzynski, M. R. Boyett, A. V. Holden, and H. Zhang, "3D virtual human atria: a computational platform for studying clinical atrial fibrillation," *Progress in biophysics and molecular biology*, vol. 107, no. 1, pp. 156–168, 2011.

[2] M. A. Colman, *Development of a biophysically detailed model of the human atria for the investigation of the mechanisms of atrial arrhythmias*. PhD thesis, University of Manchester, 2013.

[3] I. Adeniran, M. J. McPate, H. J. Witchel, J. C. Hancox, and H. Zhang, "Increased vulnerability of human ventricle to re-entrant excitation in herg-linked variant 1 short qt syndrome," *PLoS Comput Biol*, vol. 7, no. 12, pp. e1002313–e1002313, 2011.

[4] M. A. Colman, O. V. Aslanidi, S. Kharche, M. R. Boyett, C. Garratt, J. C. Hancox, and H. Zhang, "Pro-arrhythmogenic effects of atrial fibrillation-induced electrical remodelling: insights from the three-dimensional virtual human atria," *The Journal of physiology*, vol. 591, no. 17, pp. 4249–4272, 2013.

[5] K. Ten Tusscher, D. Noble, P. Noble, and A. Panfilov, "A model for human ventricular tissue," *American Journal of Physiology-Heart and Circulatory Physiology*, vol. 286, no. 4, pp. H1573–H1589, 2004.

[6] M. J. Ackerman, "The visible human project," *Proceedings of the IEEE*, vol. 86, no. 3, pp. 504–511, 1998.

[7] P. A. Yushkevich, J. Piven, H. C. Hazlett, R. G. Smith, S. Ho, J. C. Gee, and G. Gerig, "User-guided 3D active contour segmentation of anatomical structures: significantly improved efficiency and reliability," *Neuroimage*, vol. 31, no. 3, pp. 1116–1128, 2006.

[8] H.-Y. Lee, N. C. Codella, M. D. Cham, J. W. Weinsaft, and Y. Wang, "Automatic left ventricle segmentation using iterative thresholding and an active contour model with adaptation on short-axis cardiac mri," *Biomedical Engineering, IEEE Transactions on*, vol. 57, no. 4, pp. 905–913, 2010.

[9] M. Jolley, J. Stinstra, S. Pieper, R. MacLeod, D. H. Brooks, F. Cecchin, and J. K. Triedman, "A computer modeling tool for comparing novel icd electrode orientations in children and adults," *Heart Rhythm*, vol. 5, no. 4, pp. 565–572, 2008.

[10] L. Geddes and L. Baker, "The specific resistance of biological materiala compendium of data for the biomedical engineer and physiologist," *Medical and biological engineering*, vol. 5, no. 3, pp. 271–293, 1967.

[11] S. Rush, J. A. Abildskov, and R. McFee, "Resistivity of body tissues at low frequencies," *Circulation research*, vol. 12, no. 1, pp. 40–50, 1963.

[12] S. Gabriel, R. Lau, and C. Gabriel, "The dielectric properties of biological tissues.," *Physics in medicine and biology*, vol. 41, no. 11, p. 2251, 1996.

[13] O. G. Martinsen and S. Grimnes, *Bioimpedance and bioelectricity basics*. Academic press, 2011.

[14] S. Ho and D. Sanchez-Quintana, "The importance of atrial structure and fibers," *Clin Anat*, vol. 22, no. 1, pp. 52–63, 2009.

[15] E. A. P. Alday, M. A. Colman, P. Langley, T. D. Butters, J. Higham, A. J. Workman, J. C. Hancox, and H. Zhang, "A new algorithm to diagnose atrial ectopic origin from multi lead ecg systems-insights from 3D virtual human atria and torso," *PLoS computational biology*, vol. 11, no. 1, 2015.

[16] P. C. Hansen, *Rank-deficient and discrete ill-posed problems: numerical aspects of linear inversion*, vol. 4. Siam, 1998.

[17] Y. Salu, "Implementing a consistency criterion in numerical solution of the bioelectric forward problem," *Biomedical Engineering, IEEE Transactions on*, no. 6, pp. 338–341, 1980.

[18] J. D. Stott, *Developing realistic models of the atrium and the p-wave*. PhD thesis, The University of Manchester, 2009.

[19] J. Nenonen, C. J. Purcell, B. M. Horacek, G. Stroink, and T. Katila, "Magnetocardiographic functional localization using a current dipole in a realistic torso," *Biomedical Engineering, IEEE Transactions on*, vol. 38, no. 7, pp. 658–664, 1991.

[20] J. Sarvas, "Basic mathematical and electromagnetic concepts of the biomagnetic inverse problem," *Physics in medicine and biology*, vol. 32, no. 1, p. 11, 1987.

[21] A. Van Oosterom and J. Strackee, "The solid angle of a plane triangle," *IEEE Transactions on Biomedical Engineering*, vol. 2, no. BME-30, pp. 125–126, 1983.

[22] E. Anderson, Z. Bai, C. Bischof, S. Blackford, J. Demmel, J. Dongarra, J. Du Croz, A. Greenbaum, S. Hammerling, A. McKenney, *et al.*, *LAPACK Users' guide*, vol. 9. Siam, 1999.

[23] P. C. Hansen, "Analysis of discrete ill-posed problems by means of the l-curve," *SIAM review*, vol. 34, no. 4, pp. 561–580, 1992.

[24] J. L. Castellanos, S. Gómez, and V. Guerra, "The triangle method for finding the corner of the l-curve," *Applied Numerical Mathematics*, vol. 43, no. 4, pp. 359–373, 2002.

[25] P. W. Macfarlane, A. van Oosterom, and M. Janse, *Comprehensive electrocardiology*, vol. 4. Springer Science & Business Media, 2010.

[26] I. Adeniran, J. C. Hancox, H. Zhang, *et al.*, "Effect of cardiac ventricular mechanical contraction on the characteristics of the ecg: a simulation study," *Journal of Biomedical Science and Engineering*, vol. 6, no. 12, p. 47, 2013.

[27] D. Giacopelli, J. P. Bourke, A. Murray, and P. Langley, "Spatial pattern of p waves in paroxysmal atrial fibrillation patients in sinus rhythm and controls," *Pacing and Clinical Electrophysiology*, vol. 35, no. 7, pp. 819–826, 2012.

[28] M. Gertsch, *The ECG: a two-step approach to diagnosis*. Springer Science & Business Media, 2003.

[29] J. R. Hampton and D. Adlam, *The ECG in practice*. Edinburgh, 1992.

[30] M. James, "Sinus rhythm - normal function of the heart - cardiology teaching package - practice learning - division of nursing - the university of nottingham," 2015.

[31] C. Zhang, F. Tang, P. Ma, and Z. Gan, "A simplified htc rf squid to analyze the human cardiac magnetic field," *AIP Advances*, vol. 4, no. 12, p. 127131, 2014.

[32] R. N. Klepfer, C. R. Johnson, and R. S. Macleod, "The effects of inhomogeneities and anisotropies on electrocardiographic fields: a 3-d finite-element study," *Biomedical Engineering, IEEE Transactions on*, vol. 44, no. 8, pp. 706–719, 1997.

[33] C. Bradley, A. Pullan, and P. Hunter, "Effects of material properties and geometry on electrocardiographic forward simulations," *Annals of biomedical engineering*, vol. 28, no. 7, pp. 721–741, 2000.

[34] B. Hailer, I. Chaikovsky, S. Auth Eisenrnitz, H. Schäfer, and P. Van Leeuwen, "The value of magnetocardiography in patients with and without relevant stenoses of the coronary arteries using an unshielded system," *Pacing and clinical electrophysiology*, vol. 28, no. 1, pp. 8–16, 2005.

[35] C. Ramanathan and Y. Rudy, "Electrocardiographic imaging: Ii. effect of torso inhomogeneities on noninvasive reconstruction of epicardial potentials, electrograms, and isochrones," *Journal of cardiovascular electrophysiology*, vol. 12, no. 2, pp. 241–252, 2001.

Chapter 5

First Manuscript

A new algorithm to diagnose atrial ectopic origin from multi-lead ECG systems insights from 3D virtual human atria and torso.

Erick A. Perez Alday[1,*], Michael A. Colman[1*], Philip Langley[2], Timothy D. Butters[1], Jonathan Higham[1], Antony J. Workman[3], Jules C. Hancox[4] Henggui Zhang[1]

1 Biological Physics Group, Department of Physics and Astronomy, University of Manchester, Manchester, United Kingdom
2 School of Engineering, University of Hull, Hull, United Kingdom,
3 Institute of Cardiovascular and Medical Sciences, University of Glasgow, Glasgow, United Kingdom,
4 School of Physiology and Pharmacology, and Cardiovascular Research Laboratories, School of Medical Sciences, University of Bristol, Bristol, United Kingdom.
** These authors contributed equally to this work.*

A new algorithm to diagnose atrial ectopic origin from multi lead ECG systems insights from 3D virtual human atria and torso.

Erick A. Perez Alday[1,*], Michael A. Colman[1*], Philip Langley[2], Timothy D. Butters[1], Jonathan Higham[1], Antony J. Workman[3], Jules C. Hancox[4] Henggui Zhang[1]

1 Biological Physics Group, Department of Physics and Astronomy, University of Manchester, Manchester, United Kingdom
2 School of Engineering, University of Hull, Hull, United Kingdom,
3 Institute of Cardiovascular and Medical Sciences, University of Glasgow, Glasgow, United Kingdom,
4 School of Physiology and Pharmacology, and Cardiovascular Research Laboratories, School of Medical Sciences, University of Bristol, Bristol, United Kingdom.
** These authors contributed equally to this work.*

Abstract

Rapid atrial arrhythmias such as atrial fibrillation (AF) predispose to ventricular arrhythmias, sudden cardiac death and stroke. Identifying the origin of atrial ectopic activity from the electrocardiogram (ECG) can help to diagnose the early onset of AF in a cost-effective manner. The complex and rapid atrial electrical activity during AF makes it difficult to obtain detailed information on atrial activation using the standard 12-lead ECG alone. Compared to conventional 12-lead ECG, more detailed ECG lead configurations may provide further information about spatio-temporal dynamics of the body surface potential (BSP) during atrial excitation. We apply a recently developed 3D human atrial model to simulate electrical activity during normal sinus rhythm and ectopic pacing. The atrial model is placed into a newly developed torso model which considers the presence of the lungs, liver and spinal cord. A boundary element method is used to compute the BSP resulting from atrial excitation. Elements of the torso mesh corresponding to the locations of the placement of the electrodes in the standard 12-lead and a more detailed 64-lead ECG configuration were selected. The ectopic focal activity was simulated at various origins across all the different regions of the atria. Simulated BSP maps during normal atrial excitation (i.e. sinoatrial node excitation) were compared to those observed experimentally (obtained from the 64-lead ECG system), showing a strong agreement between the evolution in time of the simulated and experimental

data in the P-wave morphology of the ECG and dipole evolution. An algorithm to obtain the location of the stimulus from a 64-lead ECG system was developed. The algorithm presented had a success rate of 93%, meaning that it correctly identified the origin of atrial focus in 75/80 simulations, and involved a general approach relevant to any multi-lead ECG system. This represents a significant improvement over previously developed algorithms.

Introduction

Rapid atrial arrhythmias such as atrial tachycardia (AT) and atrial fibrillation (AF) can reduce cardiac output and predispose to ventricular arrhythmias and further complications, such as stroke and even sudden cardiac death [1, 2, 3]. Both AT and AF are associated with ectopic activity - rapid and irregular spontaneous excitation originating from regions of the atria other than the cardiac pacemaker, the sinoatrial node [4]. Such activity can interrupt normal sinus rhythm and mediate the development of the self-perpetuating re-entrant excitation associated with AT/AF [5], therefore implicating an important role for ectopic activity in the initiation and recurrence of both arrhythmias. The pulmonary vein (PV) sleeves in the left atrium (LA) are usually identified as a major source of rapid ectopic activity [6, 7, 8], and catheter ablation therapy targeting the PV sleeves is commonly used as a treatment of AF [4, 7]. However, success rates for catheter ablation therapy are not entirely satisfactory (about 50% in single-procedure ablation [9]). Consequently, repeated operations may be required, resulting in significant scar tissue in the LA. Such scarring may induce further complications, such as contributing towards a reduction in cardiac output as well as providing conduction barriers which may promote the development of re-entry [10]. Furthermore, ectopic activity is not associated with the PVs alone; focal beats have been observed to originate from multiple regions of both the left and right atria [11, 12]. Hence, identifying the presence and location of ectopic activity is important for guiding ablation therapy, which may increase success rates and reduce the need for repeated operations. Moreover, identifying atrial ectopic activity and its origins may help in the diagnosis of early onset AF [13] and lead to timely treatment, inhibiting the development of persistent or chronic AF before the occurrence of permanent electrical and structural remodelling [13]. The electrocardiogram (ECG) is the most common non-invasive method of monitoring cardiac activity. The P-wave of the ECG is associated with atrial activation; irregular ectopic atrial activity may therefore be reflected as an alteration to the P-wave morphology (PWM). Multi-electrode ECG systems, such a 64-lead ECG vest [14], provide spatially detailed mapping of the body-surface potential (BSP). However, it is unclear if such further detail provides significant benefits over the standard 12-

lead ECG in terms of resolving the location of ectopic atrial activity. In this study, we have used a biophysically detailed computational model of the human atria and torso to investigate the correlation between PWM of 64-lead ECGs and the location of atrial ectopic activity, in order to develop a focus-location algorithm.

Methods and Models

3D atria-torso model and simulation of BSP and multi-lead ECG

Previously we have developed a biophysically detailed computational model of the three-dimensional (3D) human atria and torso [15, 16, 17]. The model accounts for atrial anatomy [18] including segmented regions for the major anatomical structures [16] (Figure 5.1Ai) and detailed atrial electrophysiology including regional differences in electrical properties [16]. The model reproduces sinus rhythm depolarisation and repolarisation patterns (Figure 5.1Aii) and has been used to study the mechanisms underlying AF genesis [16, 17]. Implementation of the torso model proved useful in correlating PWM with the origin of atrial ectopic activity in a previous study [15]. However, detailed correlation between the two has not yet been established, and the torso geometry used in the previous study was idealised [15]. For a more comprehensive analysis of the relation between PWM and ectopic activity, a more realistic torso model must be used. In this study, we use our 3D model of the human atria and update the torso model in order to develop an algorithm to identify the location of focal ectopic activity in the atria (Figure 5.1). Details of atrial model development and simulation protocols can be found in Colman et al.[16], and in the Supplementary Material Text S1.

Two torso reconstructions are used in the present study (Figure 5.2), based on segmentation of magnetic resonance imaging (MRI) images taken from the female and male visible human dataset [19], by using the software ITK-SNAP [20]. Note that the atrial model does not account for gender differences in either anatomy or electrophysiology [16] and investigation of gender differences is not the aim of this study; rather, use of multiple torso geometries ensures generality of the developed algorithm. The models account for the structure and different electrical conductivities in the lungs, liver, spinal cord and blood masses [21]. The female torso model was discretised at a spatial resolution of 0.33mm 0.33mm 0.33 mm [19], corresponding to that of the female atrial model [16]. Meanwhile the male torso model was discretised at a spatial resolution of 0.33mm 0.33mm 1 mm[19]. The 3D atrial model (Figure 5.1A) [19] was then integrated into the two torso geometries and the BSP

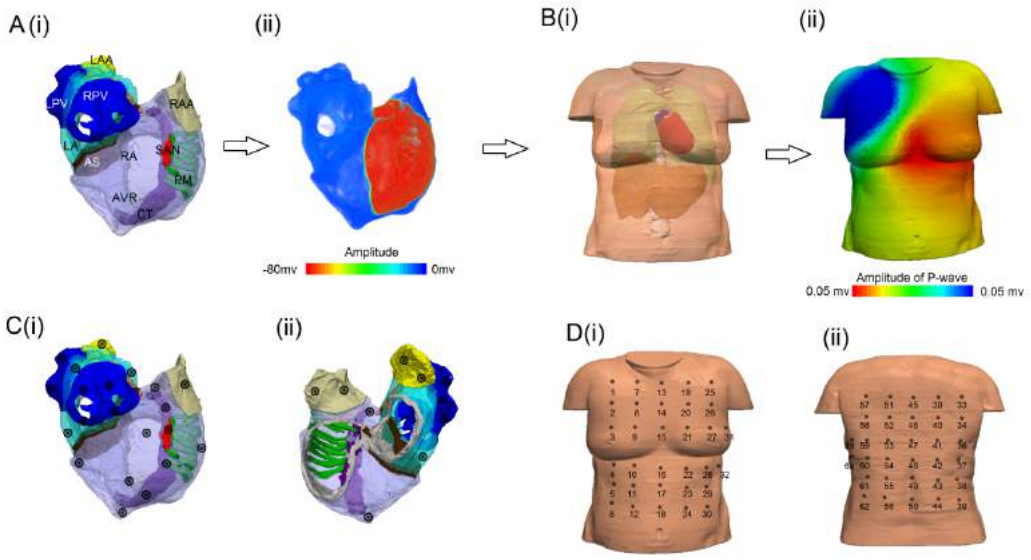

Figure 5.1: Models and procedure used to develop the algorithm. (A(i)) 3D Atrial model with the different regions of the atria included in this simulation: right atrium (RA, transparent purple), right atrial appendage (RAA, beige), pectinate muscles (PM, green), cristalterminalis (CT, solid purple), sinoatrial node (SAN, red), superior vena cava (SVC), atrio-ventricular ring (AVR, grey), right pulmonary vein (RPV, blue), Bachmanns bundle (BB, orange), left atrium (LA, light blue), left atrial appendage (LAA, yellow), inferior vena cava (IVC) and left pulmonary veins (LPV, blue). A(ii) is a snapshot of the activation of the atria at 30ms after initiation. B(i) Torso model with all the considerations used in the simulation, we can observe the position of the atria as well. B(ii) BSP produced in our simulation, corresponding to the atrial snapshot in Aii. C(i) and (ii) indicate the different stimulated points across the surface of the atria, used for focal ectopic pacing. D Positions of the electrodes placement in the torso mesh from the front (i) and from the back (ii), for the 64-lead ECG system.

distribution was calculated through the use of a boundary element method (Figure 5.1B) [22]. Two different positions of the atria inside the torso were used to account for variability between patients; one is based on Ho and Sanchez-Quintana [23] (Figure 5.2Ai,Bi), and the second one is the position of the atria obtained directly from the segmentation of the visible human female dataset (from which the atrial anatomical model was extracted) (Figure 5.2Aii,Bii). From the BSP, ECG signals can be derived by selecting elements of the torso mesh which correspond to the location of electrodes used in ECG systems. Ectopic focal activity was simulated by applying stimuli to various locations across all regions of the atria (Figure 5.1C).In this study, we replicated a 64-lead ECG system which measures the BSP on the front and back of the torso (Figure 5.1D) as well as the standard 12-lead ECG. All leads in the 64-lead system are unipolar: the potential at the electrode is the positive terminal and Wilsons Central Terminal [24] is the negative terminal.

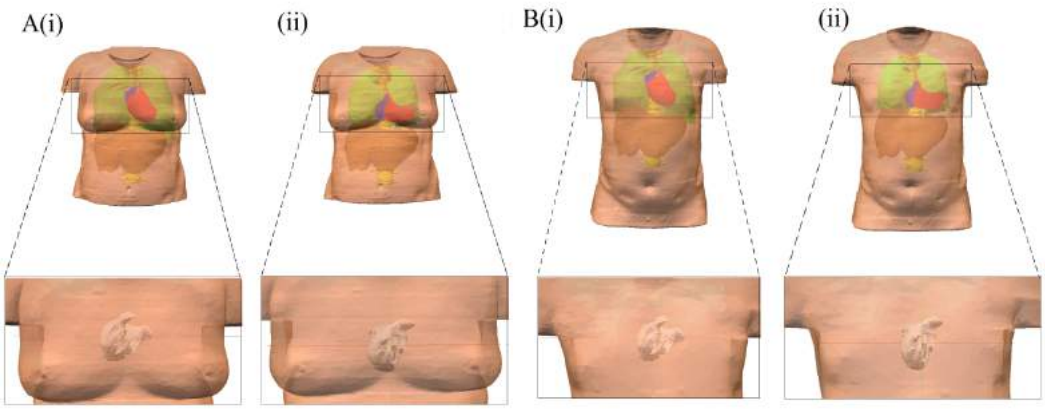

Figure 5.2: Positions of the atria inside the two different torso reconstructions used in this study. A, Female torso taken from the visible human dataset [19]. B, Male torso taken from the visible human dataset [19]. The labels (i) correspond to the position based on Ho and Sanchez-Quintana [23]. The labels (ii) correspond to the position of the atria obtained from the segmentation. The different tissues accounted for in the model are illustrated in (i) and (ii); Green-Lungs, Brown-Liver, Yellow-Spinal cord, red-Ventricles, Blue-Atria, Pink-Torso.

Characterisation of the P-wave

For each lead, the P-wave was characterised by its morphology and polarity. It was indexed as positive if the amplitude of the positive peak was greater than double that of the negative peak (if there was one), and vice-versa for a negative P-wave. A biphasic P-wave is defined as one in which the second peak (positive or negative) was at least half of the amplitude of the largest peak (negative or positive). Such a definition resulted in the best performance of our focus location algorithm (described in the next section), and is not intended as a general definition for other purposes.

Quantification of the atrial dipole evolution

The P-wave dipole pattern was constructed based on the maximum positive potentials (positive pole) and the minimum negative potentials (negative pole) in the body surface at every time step [14]. As the atrial activation evolves, the amplitude and spatial distribution of the poles across the surface of the body change dynamically. Furthermore, we constructed spatial polarity maps based on the polarity (positive/negative/biphasic) of the P-wave at each electrode location.

Simulation of atrial focal activity

To simulate ectopic focal activity the model was stimulated by a sequence of external supra-threshold electrical pulses applied to various locations across all different

regions of the atria (Figure 1C), representing the range of ectopic foci observed experimentally [11, 12]. Stimuli were applied to each location at both slow (cycle length = 700ms) and fast (cycle length = 300ms) rates to ensure that rate dependent changes in PWM are accounted for. In each case, the P-wave resulting from the final of three stimuli was analysed.

Focus location algorithm

Simulated BSP maps and ECG P-waves varied significantly with the location of the ectopic focus (Figure 5.3). The P-wave polarity map offered the most effective method of quantifying such differences, offering more information than the temporal evolution of the dipole peaks while being less affected by noise than the raw P-waves. P-wave polarity maps therefore form the basis of the development of an algorithm to determine the location of an atrial focus from 64-lead ECG measurements.

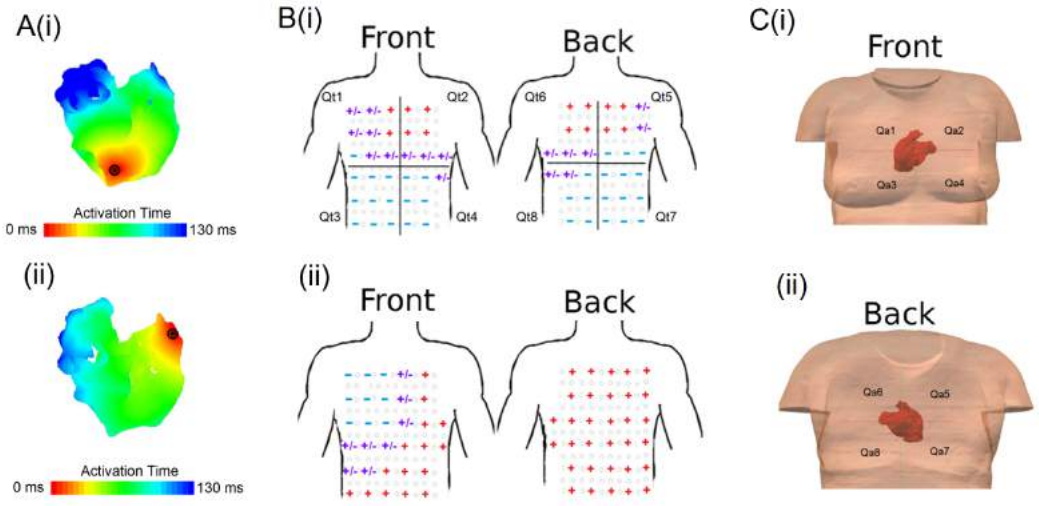

Figure 5.3: Correlation between origin of two ectopic focal atrial activation and the division of quadrants. Correlation between atrial focal origin (A) and the body surface polarity (B), corresponding to ectopic pacing at the inferior vena cava (Ai) right atrial appendage (Aii). In B, both the front (i,ii) and back (ii, iv) of the torso are shown. The quadrants on the torso and the atria are illustrated in B (i),(ii) and C. Qti indexes the quadrants of the torso B(i) and (ii), and the Qai indexes quadrants of the atria C(i) and (ii).

To relate polarity patterns to atrial anatomical sites, both the atria and the torso were divided into two sets of quadrants, four in the anterior part and four in the posterior part of each anatomical model (Figure 5.3B,C). For the torso model, Qt1 to Qt8 were used to label the quadrants (Figure 5.3Bi,ii). In the atria Qa1 to Qa8 were used (Figure 5.3C) where each quadrant contains corresponding anatomical regions

(Table 5.1). Note that the position of the atria within the torso had a significant effect on PWM and the P-wave polarity map (Supplementary Figure S1), and that the atrial anatomical locations associated with each atrial quadrant differ for both orientations considered. As such, patient variability in the orientation of the heart within the torso must be considered, and can be accounted for in this table rather than the algorithm itself, which operates by relating atrial and torso quadrants.

Table 5.1: Regions of the atria included in each quadrant for the two positions inside the torso.

Quadrant	**Position 1 Regions included**	**Position 2 Regions included**
Qa1	Superior-anterior part of RA, right part of RAA, superior part of the PM, superior part CT, superior part of the SAN, anterior part of the SVC	Superior-anterior part of RA, right part of RAA, SAN, PM, Superior part of CT.
Qa2	Left part of RAA	Left part of RAA
Qa3	Inferior-anterior part of the RA, inferior part of the PM, inferior anterior part of the CT, inferior part of the SAN	Inferior-anterior part of the RA, inferior anterior part of the CT, AVR, inferior-anterior part of IVC.
Qa4	inferior-anterior-left part of the RA, anterior part of the AVR	Anterior part of AVR.
Qa5	RPV, superior-right part of LA, superior part of the AS, BB, posterior part of the SVC	RSPV, superior-right part of LA, BB, SVC, superior part of AS
Qa6	LPV, superior-left part of the LA, LAA, posterior part of the AVR	LSPV, superior-left part of LA, LAA, posterior part of AVR.
Qa7	inferior part of the AS, inferior-right part of the LA, inferior-posterior part of the CT, IVC	RIPV, inferior part of AS, inferior-right part of LA, inferior-posterior part of IVC.
Qa8	inferior-left part of the LA	LIPV, inferior-left part of LA

The regions of the atria are: Right atrium (RA), right atrial appendage (RAA), pectinate muscles (PM), cristal terminalis (CT), sinoatrial node (SAN), superior vena cava (SVC), atrio-ventricular ring (AVR), right pulmonary vein (RPV), bundle branch (BB), left atrium (LA), left atrial appendage (LAA), inferior vena cava (IVC) and left pulmonary veins (LPV). Position 1 is taken from [23]. Position 2 is taken from the actual position of the atria inside its torso.

Schematic illustration of the algorithm is shown in Figure 5.4, and details of the algorithm are described below:

1. Construct the spatial polarity map.

2. Assign a numerical value to each electrode position based on the polarity of

the P-wave at that position; 2 for a negative P-wave, 1 for a bi-phasic P-wave and 0 for a positive P-wave.

3. Take the mean average of all the values in each torso quadrant, denoted Sp.

4. Determine the largest value of Sp across all quadrants, denoted Sp_{max}. If there is a single quadrant which contains this value (Qtx, x=1-8), then the location of the atrial focus is in the corresponding atrial quadrant (Qax).

5. If there are multiple quadrants which contain Sp_{max}, then further analysis is required:

   (a) If the value of Sp in two quadrants is equal to Sp_{max}, then two adjacent quadrants must be compared. Then, the quadrant Sp_{max}, adjacent to the larger Sp from the second comparison, will be identified as the origin.

   Note: for example, if both superior-right and superior-left anterior quadrants have the same Sp_{max} value, then the Sp in the inferior-left and inferior-right anterior quadrants are compared, as long as they are different. If the inferior left has a greater Sp, then the atrial focal is in the superior-left region.

   (b) If there are 3 quadrants with the same Sp_{max} value, then the corner quadrant will be identified as the atrial focal origin.

   Note: for example, if the anterior superior-right, the anterior superior-left and the anterior inferior-left quadrants have the same maximal value, then the anterior superior-left quadrant will be the origin.

   (c) If 4 or more quadrants have the same Sp_{max}, the adjacent quadrants with different Sp will be compared, and the quadrant with a larger Sp will be identified as the origin.

   Note: for example, if the four anterior quadrants have the Sp_{max}, a subsequent maximal Sp in the posterior quadrants will be searched. If there is one, say the superior-right posterior one, then the superior-right anterior quadrant will be identified as the origin.

Results

Validation of the simulated 64-lead ECG system

Validation of the atrial activation sequence during control conditions has been discussed in [16, 17]. In order to validate the 3D atria-torso model, we first compared the simulated BSP pattern and 12- and 64-lead ECG P-waves for the control case

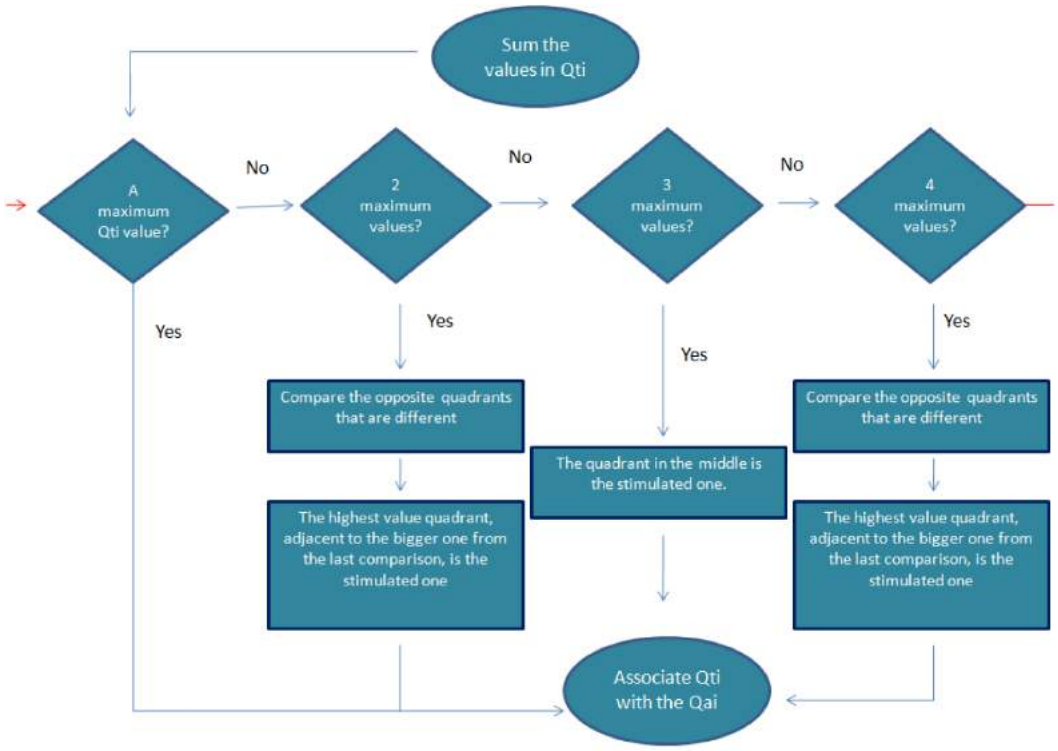

Figure 5.4: Schematic illustration of the algorithm to identify the quadrant of atrial focal origin based on 64-lead ECG P-wave values.

to experimental data obtained from eight healthy subjects. It was demonstrated that the simulated data of the 64-lead ECG (Figure 5.5) as well as the 12-lead ECG and BSP pattern are in fair agreement to the experimental data. Then, we further compared the simulated P-wave polarity to the experimental data. In both simulations and experimental data, the polarity of P-waves was mainly positive in the left-superior part of the body, negative in the right, inferior part of the body, and biphasic or flat in the intermediary locations (Figure 5.6A,B).

To assess quantitatively the agreement between the polarity patterns in simulation and experiment, the polarity of the simulated P-wave at every electrode was compared with each experimental dataset. Inter-patient variability was quantified by also comparing experimental datasets to each-other. The simulation data showed a range of agreement between 87.1% and 94.5% with experimental data, comparable to the range observed within the experimental data of 81.5% and 93.7%. Furthermore, the simulated temporal evolution of the dipole location (Figure 5.6Ci) and amplitude (Figure 5.6Cii) agreed with experimental data [14]. Hence, the model was validated for the control condition, and suitable for investigating the correlation between ectopic atrial activity and P-wave profiles.

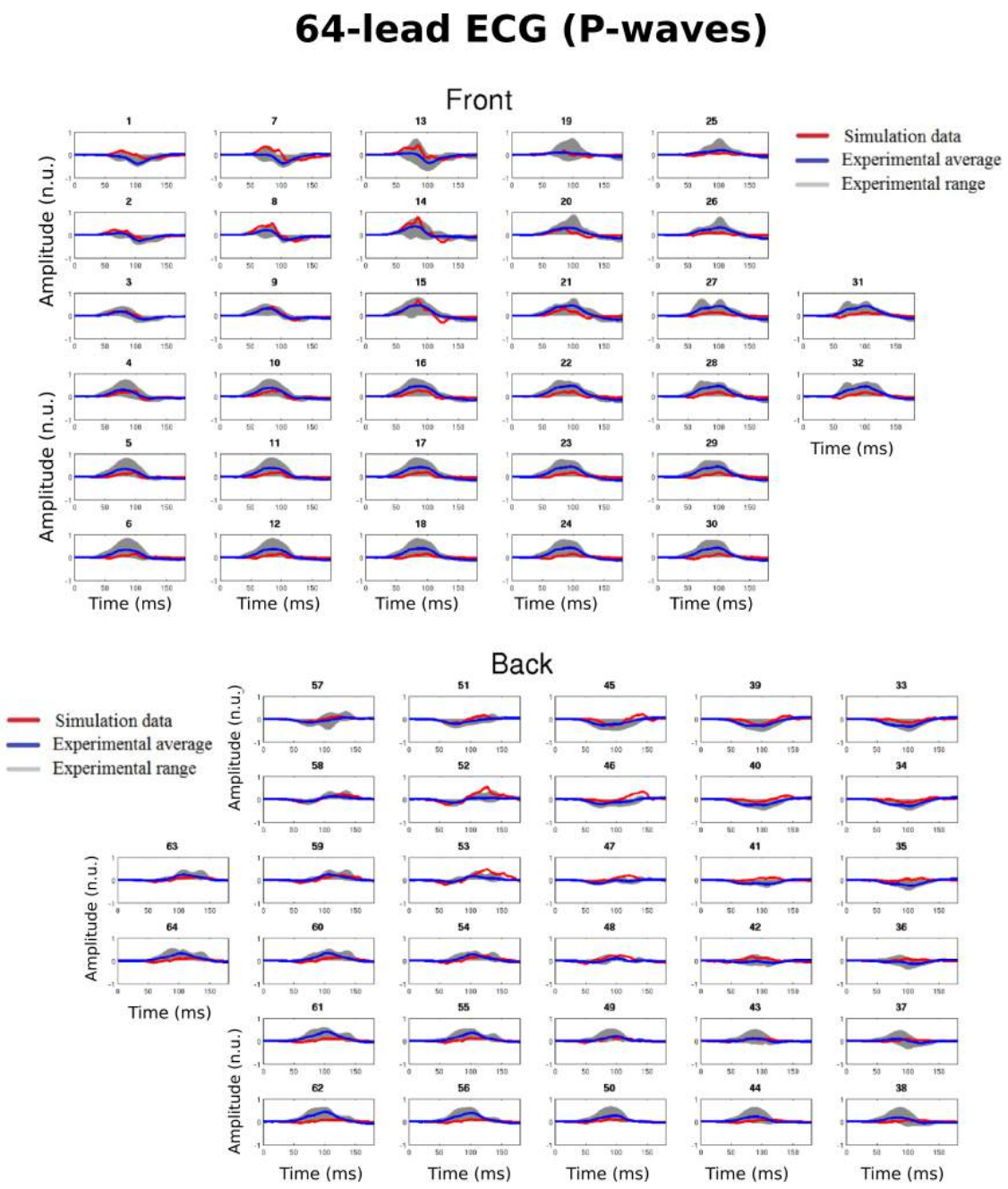

Figure 5.5: P-waves obtained from experimental data (blue line and grey shadow) and simulated (red line) data. The experimental average is the average data of 8 healthy people (blue line), and the experimental range corresponds to the maximum and minimum values of these signals (grey shadow). This measurements used the same protocol as described in [14]. Both, experimental and simulated P-waves were normalized for comparison.

Focus location algorithm results

The algorithm was developed based on results from 30 simulations with different atrial foci. It was then tested with 50 further simulations to determine its success rate (i.e. the proportion of cases in which the algorithm correctly identified the origin

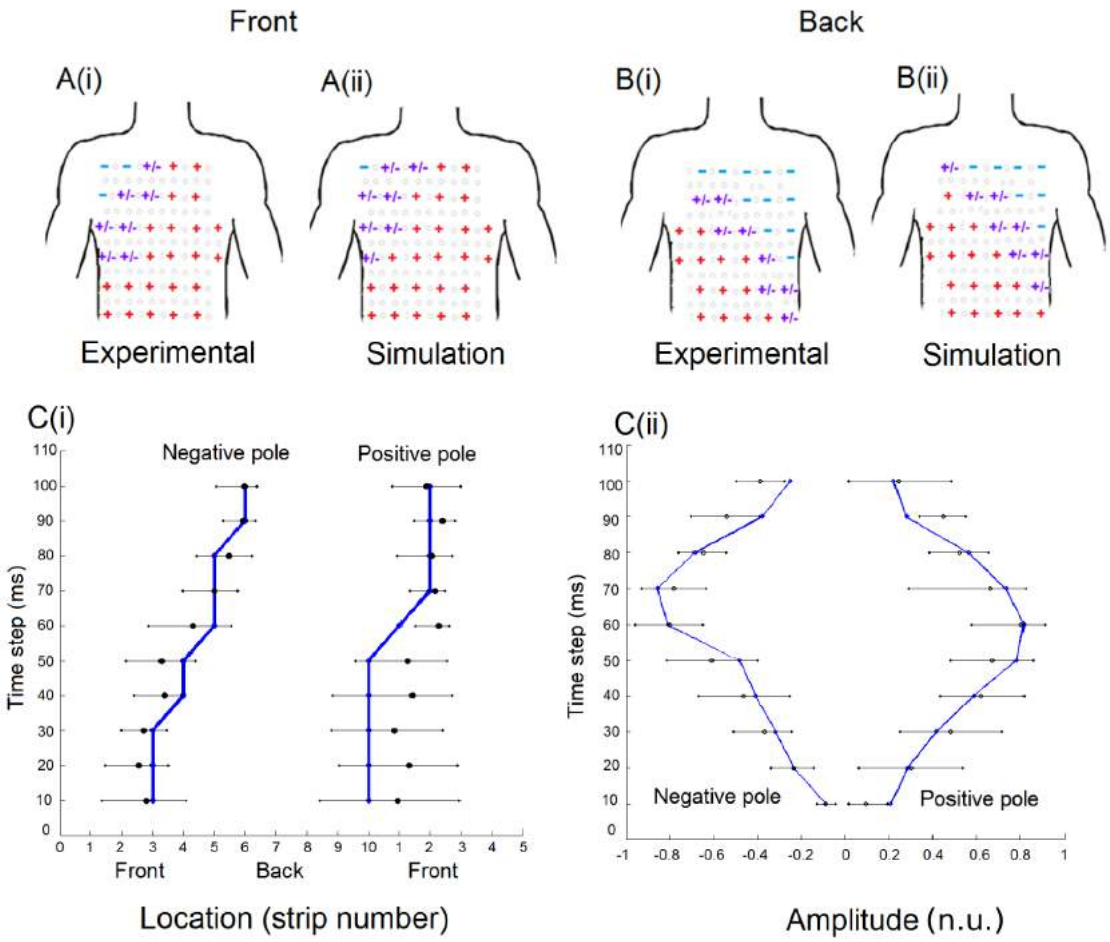

Figure 5.6: Comparison of p-waves and dipole evolution between the simulated and experimental data. (A) and (B) Comparison of the simulated 64-lead ECG P-waves polarity (ii) to experimental data (i). In this figure, the arrangement of the P-waves is set out to match electrode placement (see Figure 1). We observed the polarity pattern of the P-waves of the experimental and simulation, in the front (A) and back (B) part of the body. The red positive sign signifies an upright P-wave, the blue negative sign represents an inverted P-wave, and the purple positive/negative sign represents a biphasic P-wave. (C) Spatial (i) and amplitude (ii) temporal evolution of the dipole. The black dots and lines are the experimental data and error bar taken from [14], and the blue lines and dots are obtained from our simulation during a stimuli applied to the superior part of the sino-atrial node region. In (i) the horizontal axis is a continuous scale from the first vertical line electrodes (1-6) to the last line of electrodes (33-38), without taking in to account 31, 32, 63 and 64.

of atrial focus from the P-wave polarity pattern). In such blind tests, the success rate was 93%. Note that pacing rate affected PWM only to a small degree, and had no effect on the P-wave polarity map (Supplementary Figure S2), hence ensuring the algorithm is appropriate for both fast and slow pacing rates.

There were five cases for which the origin identified by the algorithm did not

match the actual excitation site. In those cases the mismatch was a result of the definition of a biphasic P-wave, when the PWM was highly irregular. These irregularities could impact the value of the average for each quadrant, leading to a mismatch in the location of the ectopic focus, mainly when the focal origin was close to the boundary between two or more quadrants.

Further refinements to the spatial resolution of the quadrants could be performed with the aim to improve the specificity of the algorithm for locating the focal origin site, by dividing each quadrant into sub-quadrants. Accordingly, the algorithm was updated as follows: if a quadrant adjacent to the quadrant with Sp_{max} has an Sp value close to that of the maximum quadrant (i.e. within 0.1 in this case), then the activation focus is determined to be in the sub-quadrant that is close to the boundary between the two quadrants (i.e. within the quadrant of maximum Sp value in close proximity to the neighbouring quadrant considered). Conversely, if the difference in values between the two quadrants is very large (i.e. greater than 0.1) then the focus of the activation is determined to be within the sub-quadrant that is far from the boundary of the two quadrants. Though such a spatial refinement improved the detection accuracy in terms of the spatial resolution, the success rate of detection showed a slight decrease, down to 89%. This could be due to the limitation of the 64-lead ECG to map the BSP.

Discussion

In this study, we have developed a new algorithm for detecting the location of atrial focal activity using a 64-lead ECG system. The algorithm was developed using simulation data, which enabled us to correlate BSP patterns to atrial activation sequences more comprehensively than in an experimental setting.

Computational models:

The computational model implemented for this study was an update of our previous model of the human atria and torso [15, 16, 17]. The updated model has the following advantages compared to the previous model [15, 17]: (i) realistic torso meshes were used for male and female, rather than an idealised one as used in the previous studies [15, 17]; (ii) a greater level of detail was considered within the torso, including the spine and liver as well as blood masses and lungs; (iii) various, experimentally justified orientations of the atria [23] were considered. The developed atria-torso models were validated by their ability to simulate BSP patterns, 12- and 64-lead ECG PWM, 64-lead ECG polarity patterns and the spatio-temporal evolution of the dipole peaks, all of which matched to experimental data from eight healthy

patients. Note that experimental P-waves were filtered and averaged over a time period of 1 minute - this has the effect of smoothing the signals compared to the simulated P-waves, for which averaging would have no smoothing effect due to the model being deterministic and subsequent P-waves being identical. Therefore, the presented models provide a useful platform for simulating atrial excitations and their BSP patterns in variant physiological conditions.

Comparison to other models

Several human atria-torso models have been developed by other groups in previous studies [25, 26, 27, 28, 29], including the one by Krueger et al. [25], in which personalised atrial geometries were implemented for reproducing accurate patient specific P-waves. The model in that study considered fat and muscle tissue, which can affect the P-wave. However, due to the difficulty in segmenting both tissue types, few models include them [25, 30]. That model also considered soft tissues of the bowels, kidneys and spleen, which were absent in the present model. However, the simulated PWM from the present models were similar to those from Kruger et al. [25], suggesting that these soft tissues play only a small role in affecting the polarity of the P-waves, as also suggested in a previous study [30, 31, 32]. Furthermore, agreement of PWM between simulation and experiment were similar in both studies, despite Krueger et al [25]. being patient-specific. Though other atria-torso models have been developed for simulating body surface potential maps and multi-lead ECGs, the focus of those studies were in finding the ideal number of electrodes to obtain more information of the atria as compared to the standard 12-lead ECG system [26, 27], or to create a database for detecting atrial fibrillation [33, 34]. To our knowledge, the present study is the first attempt to establish a detailed correlation between the polarity map of body surface potentials and origins of atrial ectopic focus.

Focus location detection algorithm:

Comparison to previous algorithms

Focus-location algorithms have been developed previously based on the standard 12-lead ECG system [35, 36], including the well-established Kistler et al. algorithm [11]. However, the 12-lead based algorithms have limited effectiveness due to the smaller number of electrodes that provided incomplete information on atrial excitations. In their study, Kistler et al. reported 93% focus detection accuracy. However, subsequent studies have found a lower accuracy [35, 36]. When we applied the Kistler et al. algorithm to simulation data of P-waves, an accuracy of 73% was achieved, which is within the 55-78% range observed in other studies [35, 36].

In this study, we presented an algorithm for identifying atrial focal origins based on simulated 64-lead ECG system. The developed algorithm showed a higher success rate on the same data than the Kistler et al. algorithm (93% vs 73% respectively). Our results suggest that the extra level of detail provided by 64-lead ECG compared to the 12-lead ECG system was useful in accurately locating atrial focal activity.

The developed algorithm has two key strengths compared to previous algorithms: (i) splitting the torso into two sets of quadrants means that the algorithm is not specific to an electrode array set up any array which covers the front and back of the torso (symmetric or asymmetric) may be used, and the algorithm need not be adjusted. Similarly, relation of atrial anatomy to torso quadrants via a correlation table intrinsically accounts for patient variability, also without the need to adjust the algorithm itself; (ii) the algorithm is based on polarity patterns of the P-waves, rather than the detailed PWM. Whereas this does not provide a full level of detail as with PWM, such an approach has the following advantages: (a) inter-patient variations manifest as alterations in PWM but have a much smaller effect on P-wave polarity; (b) similarly, noise will not affect the P-wave polarity pattern but may have a significant effect on PWM, especially regarding bifidity; (c) we did not consider bifidity in our definition of polarity, therefore avoiding the limitations of algorithms which use bifidity, such as ambiguity in the definition of the magnitude of bump necessary to be considered bifid and the effect of noise on accentuating or reducing bifidity. Note that this was one of the primary limitations of the Kistler et al. algorithm [11] responsible for the majority of its errors.

Another possible approach for locating atrial ectopic foci is to implement an inverse solution. However, inverse solutions are computationally intensive and have several limitations as discussed in other studies [37, 28, 38].

Potential application to the clinic

In the current study, torso quadrants are associated with atrial anatomical locations by Table 5.1. For potential use of the algorithm in the clinic, a patient specific atria-torso correlation table could be constructed if necessary. Low resolution MRI image data can provide information of the orientation of the atria in the torso; typical MRI images would be sufficient to construct such patient specific table, and allow correlation between torso quadrants and atrial anatomical sites. As the algorithm itself is generic, it could be applicable to patients without a need for individual adjustment.

Limitations

The torso model lacks considerations of some other tissue types or organs (such as muscles, fat tissue, bowels, kidneys, spleen and skin) that may affect body surface potentials. However, the absence of those tissues does not have a big effect on the polarity of the P-waves [30, 31], which is the characteristic used in the present algorithm. For example, test simulations in which the conductivity of the torso was replaced by an average tissue conductivity accounting for muscle, fat and skin in various configurations demonstrates significant changes to P-wave amplitude but not to the polarity patterns (Supplementary Figure S3).The developed algorithm was based on simulation data, lacking consideration of the measurement noise as seen in real data. However, the use of P-wave polarity in the detecting algorithm can minimise the influence of noise as this may affect the amplitude of P-wave signals, but have less impact on the P-wave polarity. Whereas polarity patterns may be affected by large degrees of noise, such signals would be unsuitable for use in any clinical diagnosis.

In the algorithm, eight quadrants were defined to cover the torso. The spatial resolution of the quadrant may require further refinement. For example, each quadrant can be split into eight sub-quadrants. However, finer spatial resolution of the quadrants may not help to improve the detection success rate as it decreases to 89% when eight sub-quadrants were used for each quadrant. Another potential limitation of the algorithm arises from the definition of a biphasic P-wave as it may lead to a miscalculation of the atrial activation site. Although the use of P-wave polarity overcomes the problems arising from the bifid definition as implemented in the Kistler et al. algorithm [11], the present algorithm requires a well-defined biphasic wave to optimise the performance of the algorithm. This biphasic definition leads to a better performance of the algorithm than the use of the Kistlers bifid wave.

In the present study, we only tested the effectiveness of the algorithm for detecting atrial focal activity. Its use for detecting the organisation centre of rotor activity has not been performed. For that purpose, consideration of combined use of the present algorithm with vectorcardiograms [39], phase relationships [40] and correlation analysis [41] may be necessary, warranting further investigation. Finally, the algorithm was based on simulation data. Though it provides a theoretical basis for detecting atrial focus from multi-lead ECGs, it requires further tests on real ECG data from patients or animal models with known atrial foci. Nevertheless, a test of 50 simulated atrial focus activities, different to those used to develop the algorithm, was performed, which showed a similar success rate in both male and female torso models with varying atrial position.

Conclusion

Using a biophysically detailed computer model of the human atria-torso, we have demonstrated a correlation between atrial focal origin and polarity pattern of the BSP. Based on such correlation, a new algorithm has been developed to identify the atrial origin from the BSP reconstructed from 64-lead ECG. This study provides a theoretical basis for non-invasively detecting atrial focal origins, which is important for designing AF ablation protocol, and demonstrates the advantages of multi-lead ECG systems over the standard 12-lead ECG in detecting the origin of focal activity.

Supporting Information

Supporting Information S1

Figure S1. 64-lead ECG of the two position of the atria

Supporting Information S2

Figure S2. 64-lead ECG and polarity maps of two pacing rates

Supporting Information S3

Figure S3. Lead 2 of the 64-lead ECG system

Supporting Information S4

Text S4. Key features of the models.

Acknowledgments

This work was supported by CONACyT and project grants from Engineering and Physical Science Research Council UK (EP/J00958X/1; EP/ I029826/1), an Engineering and Physical Science Research Council UK Doctoral Prize Fellowship, and the Natural Science Foundation of China (61179009) and the University of Manchester. The funders had no role in study design, data collection and analysis, decision to publish, or preparation of the manuscript.

Bibliography

[1] S. Nattel, A. Shiroshita-Takeshita, B. J. Brundel, and L. Rivard, "Mechanisms of atrial fibrillation: lessons from animal models," *Progress in cardiovascular diseases*, vol. 48, no. 1, pp. 9–28, 2005.

[2] E. J. Benjamin, P. A. Wolf, R. B. DAgostino, H. Silbershatz, W. B. Kannel, and D. Levy, "Impact of atrial fibrillation on the risk of death the framingham heart study," *Circulation*, vol. 98, no. 10, pp. 946–952, 1998.

[3] E. Anter, M. Jessup, and D. J. Callans, "Atrial fibrillation and heart failure treatment considerations for a dual epidemic," *Circulation*, vol. 119, no. 18, pp. 2516–2525, 2009.

[4] W.-S. Lin, C.-T. Tai, M.-H. Hsieh, C.-F. Tsai, Y.-K. Lin, H.-M. Tsao, J.-L. Huang, W.-C. Yu, S.-P. Yang, Y.-A. Ding, *et al.*, "Catheter ablation of paroxysmal atrial fibrillation initiated by non–pulmonary vein ectopy," *Circulation*, vol. 107, no. 25, pp. 3176–3183, 2003.

[5] M. A. Colman, M. Varela, J. C. Hancox, H. Zhang, and O. V. Aslanidi, "Evolution and pharmacological modulation of the arrhythmogenic wave dynamics in canine pulmonary vein model," *Europace*, vol. 16, no. 3, pp. 416–423, 2014.

[6] R. Arora, S. Verheule, L. Scott, A. Navarrete, V. Katari, E. Wilson, D. Vaz, and J. E. Olgin, "Arrhythmogenic substrate of the pulmonary veins assessed by high-resolution optical mapping," *Circulation*, vol. 107, no. 13, pp. 1816–1821, 2003.

[7] K. Kumagai, M. Ogawa, H. Noguchi, T. Yasuda, H. Nakashima, and K. Saku, "Electrophysiologic properties of pulmonary veins assessed using a multielectrode basket catheter," *Journal of the American College of Cardiology*, vol. 43, no. 12, pp. 2281–2289, 2004.

[8] M. Haissaguerre, P. Jaïs, D. C. Shah, A. Takahashi, M. Hocini, G. Quiniou, S. Garrigue, A. Le Mouroux, P. Le Métayer, and J. Clémenty, "Spontaneous initiation of atrial fibrillation by ectopic beats originating in the pulmonary veins," *New England Journal of Medicine*, vol. 339, no. 10, pp. 659–666, 1998.

[9] A. N. Ganesan, N. J. Shipp, A. G. Brooks, P. Kuklik, D. H. Lau, H. S. Lim, T. Sullivan, K. C. Roberts-Thomson, and P. Sanders, "Long-term outcomes of catheter ablation of atrial fibrillation: A systematic review and meta-analysis," *Journal of the American Heart Association*, vol. 2, no. 2, p. e004549, 2013.

[10] W. Anné, H. Van Rensburg, J. Adams, H. Ector, F. Van de Werf, and H. Heidbüchel, "Ablation of post-surgical intra-atrial reentrant tachycardia. predilection target sites and mapping approach," *European heart journal*, vol. 23, no. 20, pp. 1609–1616, 2002.

[11] P. M. Kistler, K. C. Roberts-Thomson, H. M. Haqqani, S. P. Fynn, S. Singarayar, J. K. Vohra, J. B. Morton, P. B. Sparks, and J. M. Kalman, "P-wave morphology in focal atrial tachycardia: development of an algorithm to predict the anatomic site of origin," *Journal of the American College of Cardiology*, vol. 48, no. 5, pp. 1010–1017, 2006.

[12] M. Haissaguerre, M. Hocini, A. Denis, A. J. Shah, Y. Komatsu, S. Yamashita, M. Daly, S. Amraoui, S. Zellerhoff, M.-Q. Picat, *et al.*, "Driver domains in persistent atrial fibrillation," *Circulation*, vol. 130, no. 7, pp. 530–538, 2014.

[13] J. R. Ehrlich and S. Nattel, "Novel approaches for pharmacological management of atrial fibrillation," *Drugs*, vol. 69, no. 7, pp. 757–774, 2009.

[14] D. Giacopelli, J. P. Bourke, A. Murray, and P. Langley, "Spatial pattern of p waves in paroxysmal atrial fibrillation patients in sinus rhythm and controls," *Pacing and Clinical Electrophysiology*, vol. 35, no. 7, pp. 819–826, 2012.

[15] M. A. Colman, O. V. Aslanidi, J. Stott, A. V. Holden, and H. Zhang, "Correlation between p-wave morphology and origin of atrial focal tachycardiainsights from realistic models of the human atria and torso," *Biomedical Engineering, IEEE Transactions on*, vol. 58, no. 10, pp. 2952–2955, 2011.

[16] M. A. Colman, O. V. Aslanidi, S. Kharche, M. R. Boyett, C. Garratt, J. C. Hancox, and H. Zhang, "Pro-arrhythmogenic effects of atrial fibrillation-induced electrical remodelling: insights from the three-dimensional virtual human atria," *The Journal of physiology*, vol. 591, no. 17, pp. 4249–4272, 2013.

[17] O. V. Aslanidi, M. A. Colman, J. Stott, H. Dobrzynski, M. R. Boyett, A. V. Holden, and H. Zhang, "3D virtual human atria: a computational platform for studying clinical atrial fibrillation," *Progress in biophysics and molecular biology*, vol. 107, no. 1, pp. 156–168, 2011.

[18] G. Seemann, C. Höper, F. B. Sachse, O. Dössel, A. V. Holden, and H. Zhang, "Heterogeneous three-dimensional anatomical and electrophysiological model of human atria," *Philosophical Transactions of the Royal Society of London A: Mathematical, Physical and Engineering Sciences*, vol. 364, no. 1843, pp. 1465–1481, 2006.

[19] M. J. Ackerman, "The visible human project," *Proceedings of the IEEE*, vol. 86, no. 3, pp. 504–511, 1998.

[20] P. A. Yushkevich, J. Piven, H. C. Hazlett, R. G. Smith, S. Ho, J. C. Gee, and G. Gerig, "User-guided 3D active contour segmentation of anatomical structures: significantly improved efficiency and reliability," *Neuroimage*, vol. 31, no. 3, pp. 1116–1128, 2006.

[21] O. G. Martinsen and S. Grimnes, *Bioimpedance and bioelectricity basics*. Academic press, 2011.

[22] J. Stott, S. Kharche, P. Law, and H. Zhang, "Simulating the effects of atrial fibrillation in electrically heterogeneous human atria: A computer modelling study," in *Computers in Cardiology, 2008*, pp. 65–68, IEEE, 2008.

[23] S. Ho and D. Sanchez-Quintana, "The importance of atrial structure and fibers," *Clin Anat*, vol. 22, no. 1, pp. 52–63, 2009.

[24] F. N. Wilson, F. D. Johnston, A. G. Macleod, and P. S. Barker, "Electrocardiograms that represent the potential variations of a single electrode," *American Heart Journal*, vol. 9, no. 4, pp. 447–458, 1934.

[25] M. W. Krueger, G. Seemann, K. Rhode, D. U. Keller, C. Schilling, A. Arujuna, J. Gill, M. D. O'Neill, R. Razavi, and O. Dossel, "Personalization of atrial anatomy and electrophysiology as a basis for clinical modeling of radio-frequency ablation of atrial fibrillation," *Medical Imaging, IEEE Transactions on*, vol. 32, no. 1, pp. 73–84, 2013.

[26] R. Llinares, J. Igual, J. Millet, and M. Guillem, "Independent component analysis of body surface potential mapping recordings with atrial fibrillation," in *Neural Networks, 2006. IJCNN'06. International Joint Conference on*, pp. 2287–2294, IEEE, 2006.

[27] A. Liberos, J. Pedrón-Torrecilla, M. Rodrigo, J. Millet, A. M. Climent, and M. S. Guillem, "Body surface potential propagation maps during macroreentrant atrial arrhythmias. a simulation study," in *Computing in Cardiology Conference (CinC), 2013*, pp. 915–918, IEEE, 2013.

[28] A. van Oosterom and V. Jacquemet, "Genesis of the p wave: atrial signals as generated by the equivalent double layer source model," *Europace*, vol. 7, no. s2, pp. S21–S29, 2005.

[29] M. A. Colman, S. J. Castro, E. A. P. Alday, J. C. Hancox, C. Garratt, and H. Zhang, "Recent progress in multi-scale models of the human atria," *Drug Discovery Today: Disease Models*, vol. 14, pp. 23–32, 2015.

[30] C. Bradley, A. Pullan, and P. Hunter, "Effects of material properties and geometry on electrocardiographic forward simulations," *Annals of biomedical engineering*, vol. 28, no. 7, pp. 721–741, 2000.

[31] A. V. Shahidi and P. Savard, "Forward problem of electrocardiography: construction of human torso models and field calculations using finite element method," *Medical and Biological Engineering and Computing*, vol. 32, no. 1, pp. S25–S33, 1994.

[32] D. U. Keller, F. M. Weber, G. Seemann, and O. Doessel, "Ranking the influence of tissue conductivities on forward-calculated ecgs," *Biomedical Engineering, IEEE Transactions on*, vol. 57, no. 7, pp. 1568–1576, 2010.

[33] A. Sippens Groenewegen, A. Natale, N. F. Marrouche, D. Bash, and J. Cheng, "Potential role of body surface ecg mapping for localization of atrial fibrillation trigger sites," *Journal of electrocardiology*, vol. 37, pp. 47–52, 2004.

[34] J. Lian, G. Li, J. Cheng, B. Avitall, and B. He, "Body surface laplacian mapping of atrial depolarization in healthy human subjects," *Medical and Biological Engineering and Computing*, vol. 40, no. 6, pp. 650–659, 2002.

[35] Z. Y. Qian, X. F. Hou, D. J. Xu, B. Yang, M. L. Chen, C. Chen, F. X. Zhang, Q. J. Shan, K. J. Cao, and J. G. Zou, "An algorithm to predict the site of origin of focal atrial tachycardia," *Pacing and Clinical Electrophysiology*, vol. 34, no. 4, pp. 414–421, 2011.

[36] J. S. Uhm, J. Shim, J. Wi, H. S. Mun, H. N. Pak, M. H. Lee, and B. Joung, "An electrocardiography algorithm combined with clinical features could localize the origins of focal atrial tachycardias in adjacent structures," *Europace*, vol. 16, no. 7, pp. 1061–1068, 2014.

[37] Y. Rudy and J. E. Burnes, "Noninvasive electrocardiographic imaging," *Annals of noninvasive electrocardiology*, vol. 4, no. 3, pp. 340–359, 1999.

[38] Y. Rudy and B. Messinger-Rapport, "The inverse problem in electrocardiography: solutions in terms of epicardial potentials.," *Critical reviews in biomedical engineering*, vol. 16, no. 3, pp. 215–268, 1987.

[39] R. Gamboa, P. G. Hugenholtz, and A. S. Nadas, "Comparison of electrocardiograms and vectorcardiograms in congenital aortic stenosis," *British heart journal*, vol. 27, no. 3, p. 344, 1965.

[40] S. M. Narayan and V. Bhargava, "Temporal and spatial phase analyses of the electrocardiogram stratify intra-atrial and intra-ventricular organization,"

Biomedical Engineering, IEEE Transactions on, vol. 51, no. 10, pp. 1749–1764, 2004.

[41] M. R. Homaeinezhad, M. ErfanianMoshiri-Nejad, and H. Naseri, "A correlation analysis-based detection and delineation of ecg characteristic events using template waveforms extracted by ensemble averaging of clustered heart cycles," *Computers in biology and medicine*, vol. 44, pp. 66–75, 2014.

Chapter 6

Second Manuscript

Novel non-invasive algorithm to identify the origins of re-entry and ectopic foci in the atria from 64-lead ECGs. A computational study.

Erick A. Perez Alday[1], Michael A. Colman[1], Philip Langley[2], Henggui Zhang[1]

1 Biological Physics Group, Department of Physics and Astronomy, University of Manchester, Manchester, United Kingdom
2 School of Engineering, University of Hull, Hull, United Kingdom,

Novel non-invasive algorithm to identify the origins of re-entry and ectopic foci in the atria from 64-lead ECGs. A computational study.

Erick A. Perez Alday[1], Michael A. Colman[1], Philip Langley[2], Henggui Zhang[1]

1 Biological Physics Group, Department of Physics and Astronomy, University of Manchester, Manchester, United Kingdom
2 School of Engineering, University of Hull, Hull, United Kingdom,

Abstract

Atrial tachy-arrhythmias, such as atrial fibrillation (AF), are characterised by irregular electrical activity in the atria, generally associated with erratic excitation underlain by re-entrant scroll waves, fibrillatory conduction of multiple wavelets or rapid focal activity. Epidemiological studies have shown an increase in AF prevalence in the developed world associated with an ageing society, highlighting the need for effective treatment options. Catheter ablation therapy, commonly used in the treatment of AF, requires spatial information on atrial electrical excitation. The standard 12-lead electrocardiogram (ECG) provides a method for non-invasive identification of the presence of arrhythmia, due to irregularity in the ECG signal associated with atrial activation compared to sinus rhythm, but has limitations in providing specific spatial information. There is therefore a pressing need to develop novel methods to identify and locate the origin of arrhythmic excitation. Invasive methods provide direct information on atrial activity, but may induce clinical complications. Non-invasive methods avoid such complications, but their development presents a greater challenge due to the non-direct nature of monitoring. Algorithms based on the ECG signals in multiple leads (e.g. a 64-lead vest) may provide a viable approach. In this study, we used a biophysically detailed model of the human atria and torso to investigate the correlation between the morphology of the ECG signals from a 64-lead vest and the location of the origin of rapid atrial excitation arising from rapid focal activity and/or re-entrant scroll waves. A focus-location algorithm was then constructed from this correlation. The algorithm had success rates of 93% and 76% for correctly identifying the origin of focal and re-entrant excitation, respectively. The general approach allows its application to any multi-lead ECG system. This represents a significant extension to previously developed algorithms to predict the AF origins in association with focal activities.

Introduction

Atrial tachy-arrhtyhmias, including atrial fibrillation (AF), atrial tachycardia (AT) and flutter (AFL), are the most common cardiac arrhythmias, predisposing to heart attack, stroke and even possible cardiac death [1, 2]. All three are characterised by rapid and irregular electrical activation of the atria, with AF presenting the greatest complexity. Such rapid and irregular electrical activity of the atria is normally associated with one or more of the following abnormal excitation patterns: focal pacing (spontaneous rapid firing of non-pacemaker cells) [3, 4], fibrillatory conduction of multiple wavelets [5] and re-entrant excitation scroll waves (i.e., rotors) [4, 5].

Epidemiological studies have shown an increase in AF prevalence in the developed world associated with an ageing society, highlighting the need for effective treatment options [6, 7]. Current treatment of AF involves the use of rate control, anticoagulation, cardioversion and ablation [8]. The restoration of sinus rhythm in the atria may improve cardiac function, however several drug treatments have limited efficacy in long term maintenance of sinus rhythm [4, 9]. Developments aiming to reduce the critical mass required to sustain AF, such as catheter-based radio-frequency ablation therapy, have proven to be more effective in suppressing AF substantially [9], although multiple procedures may still be necessary due to high recurrence rates [10].

For a successful AF ablation, it is vital to know the origins (i.e., the driving sources) of AF prior to the procedure, because isolating the driving source from the rest of the atria is the primary goal of such therapy [9]. To identify such origins, both invasive and non-invasive techniques have been developed. These include the low density endo-surface mapping technique of 64-electrode basket catheters [11] and electrocardiography imaging (ECGi) [12]. The main limitation of using an invasive method is that it might produce further complications during the surgery [13]. There is a pressing need to develop effective non-invasive methods to identify AF origins which might provide all of the necessary information prior to the surgery. The ECGi technology, based on the inverse problem solution [12], is a promising method in clinical diagnosis. However, current algorithms require further information to constrain the solution to achieve a reliable reconstruction of cardiac excitation waves due to the ill-posedness of the problem [14].

Recent studies have also developed algorithms to identify non-invasively the location of focal sources by using either the standard 12-lead [15, 16, 17] or multiple-lead (e.g. 64-lead) ECG systems [18, 19]. The success rates of these algorithms range from 40 to 90 %. Most are based on the correlation between the location of focal activity and the P-wave morphology or polarity [16, 17, 18]. Whereas they are useful

in identifying the origin of focal excitation, current algorithms may not be applicable to identify re-entry or very rapid focal activity; at such rapid rates, atrial fibrillatory waves or f-waves are typically observed and thus determination of morphology or polarity of the main activation wave is non-trivial. Confounding the case for re-entry, f-waves are also likely to be less regular and more complex in nature. It is also important to be able to distinguish very rapid focal activity from that of re-entry at a comparable rate, as the underlying maintenance mechanisms in these conditions are different and thus it is possible that different intervention may be required to terminate the arrhythmia.

The aim of this study is to go-beyond our previous studies [17, 18, 19] in identifying the origins of focal-related AF from body surface ECG to develop a novel algorithm based on f-waves in order to identify origins for both rapid focal and re-entrant activity from a multi-lead ECG system. A comparison with an inverse problem reconstruction to investigate the effect of lead density is also presented.

Methods

Atria-torso model

A previously validated biophysically detailed computational model of the three-dimensional (3D) human atria and torso [17, 18, 20] was used to simulate ectopic focal and re-entry conditions (Figure 6.1). The atrial model was segmented into the major anatomical structures and accounts for electrophysiological heterogeneity between these regions (Figure 6.1A) [21]. The model has been previously used and determined suitable for studying atrial arrhythmia mechanisms [21, 22]. The atrial model was placed into a previously developed and validated torso model which accounts for the segmented structure of lungs, liver, blood masses and spinal cord and the respective electrical conductivities (Figure 6.1B) [18, 20]. This model has been used before to develop an algorithm to diagnose atrial ectopic origin from multi lead ECG systems [18]. Details of the atrial cell models and 3D simulation protocols can be found in Colman et al [22]; details of the torso model development, validation and simulation protocols can be found in Perez Alday et al [18].

Simulating atrial rapid ectopic foci and re-entry

Ectopic focal and re-entrant excitations were initiated in different regions of the atria (Figure 6.2 Ai). In order to allow rapid excitation waves with rates at frequencies typical of AF/AT/AFL (i.e. 2.5-8 HZ [22, 23]) to be sustained in the atria, parameters of the Colman et al. model of single human atrial myocytes were modified to

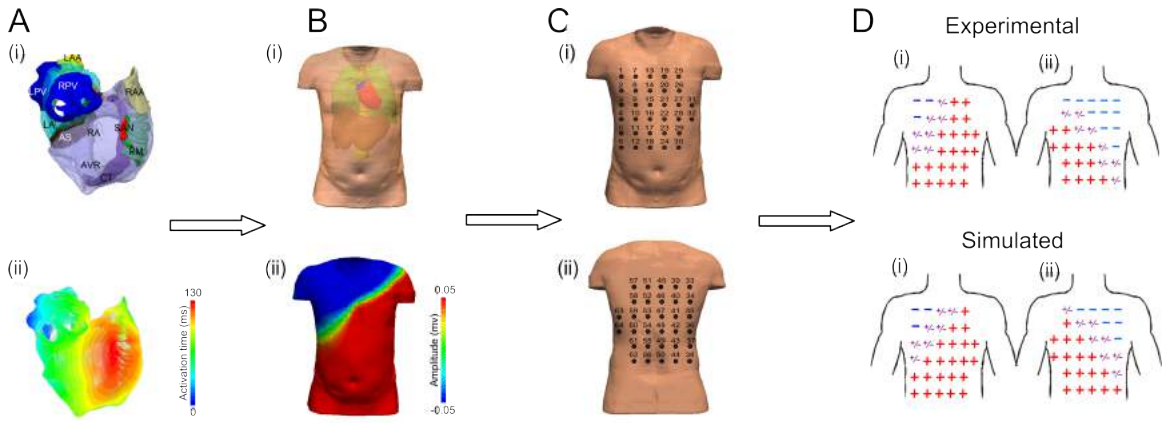

Figure 6.1: Models and procedure used to develop the algorithm. Illustration of atria (A) and torso (B) models used in the study to simulate re-entry and ectopic activity in the atria. (C) Electrode positions used to simulate the 64-lead ECG. (D) Simulated anterior (i) and posterior (ii) polarity map, as compared to experimental data, validating the 3D atria-torso models.

incorporate experimentally observed AF-induced electrical remodelling of ion channels [22], which resulted in shortened AP (Figure 6.2A). To simulate ectopic focal activity, a sequence of external supra-threshold electrical pulses (with amplitude of 2nA and duration of 2-3ms) was applied to various locations across different regions of the atria (Figure 6.2Ai). Re-entrant excitation waves were initiated by a phase distribution method [24, 25]. Although this is an artificial method for initiating re-entrant excitation, it allows the location of the centre of the rotor wave to be easily controlled. To avoid possible effects of the transition period of excitation waves on their kinetics due to the unphysiological initiation procedure, data after 1 second of initiation were analysed. In cases where re-entrant scroll waves were not localised to the initiation point, i.e. there was a degree of meander, a small non-excitation area (0.5 cm in radius) was incorporated around a specific region of the atria, in order to stabilise the rotor centre (Figure 6.2C). This allowed sustained re-entrant activity with its origin (i.e. tip) located in a specific region of the atria to be produced. The inclusion of a small area of non-excitable tissue did not produce a marked change in tissues volume or morphology of the measured potential on the body surface. In simulations, cases when re-entrant excitation waves had a significant degree of meander were used to test the ability of the algorithm to track the tip of the scroll waves spatio-temporally.

To test the algorithms ability to distinguish between focal and re-entrant activities centred on the same spatial locations, a set of focal stimuli simulations were matched in location and excitation rate to re-entrant simulations centre at multiple locations.

Simulating body surface potential

A boundary element method (BEM) was used to calculate the potential on the surface of the torso [26]. From the body surface potential (BSP), 64-lead ECG signals were obtained by selecting elements of the torso mesh corresponding to the position of the electrodes as described in previous studies [18, 20]. The P-wave of the 64-lead ECG during control conditions matched the experimental data of multiple patients [18, 27] (see S1 Fig), validating the development of the heart-torso model.

Measurement of potentials of positive and negative poles

From the measured atrial-waves, the dynamical evolution of the spatial distribution and amplitude of the atrial-wave dipole was computed from the 64-lead ECG, following the same method as used in previous experimental studies [18, 27]. The dipole pattern on the body surface was reconstructed by selecting the maximum positive potential value (positive pole) and the minimum negative potential value (negative pole) of the 64-lead ECG at every time step [27]. The amplitude and the spatial pattern of the atrial-wave dipole based on the 64-lead ECG changed with time as the atrial activation evolved. In the model, both the amplitude and the temporal evolution of the dipole location agreed with the experimental data [18, 27] during control conditions (S1 Fig), further validating the model development.

Algorithm to locate the atrial source

In a previous study, we developed an algorithm to identify the location of atrial ectopic focal activity, using the polarity map on the body surface potential that was produced from a 64-lead ECG system, which was split into two sets of quadrants (anterior/posterior) [18]. The algorithm was based on the fact that a negative polarity P-wave in a certain lead implied an excitation wave propagating away from the positive electrode of that lead. Thus, the quadrant of the 64-lead electrode positions with the largest number of electrodes with negative P-waves would correlate directly to the origin of the focal excitation. The success rate of the algorithm was 93%.

However, the previous algorithm cannot be applied directly to detect the origin of atrial excitation waves due to rapid focal or re-entrant activity because of the complexity of the body surface waveform, which produces f-waves. Determining the polarity of f-waves is not trivial since an f-wave may consist of positive, negative and biphasic waves, depending on the time period investigated (Figure 6.2C(ii), 6.2D(ii)). Furthermore, re-entrant and focal excitation patterns may present different characteristics of f-waves, and the ability to distinguish between these types of excitation could provide valuable information for directing treatment. Thus, in order to apply

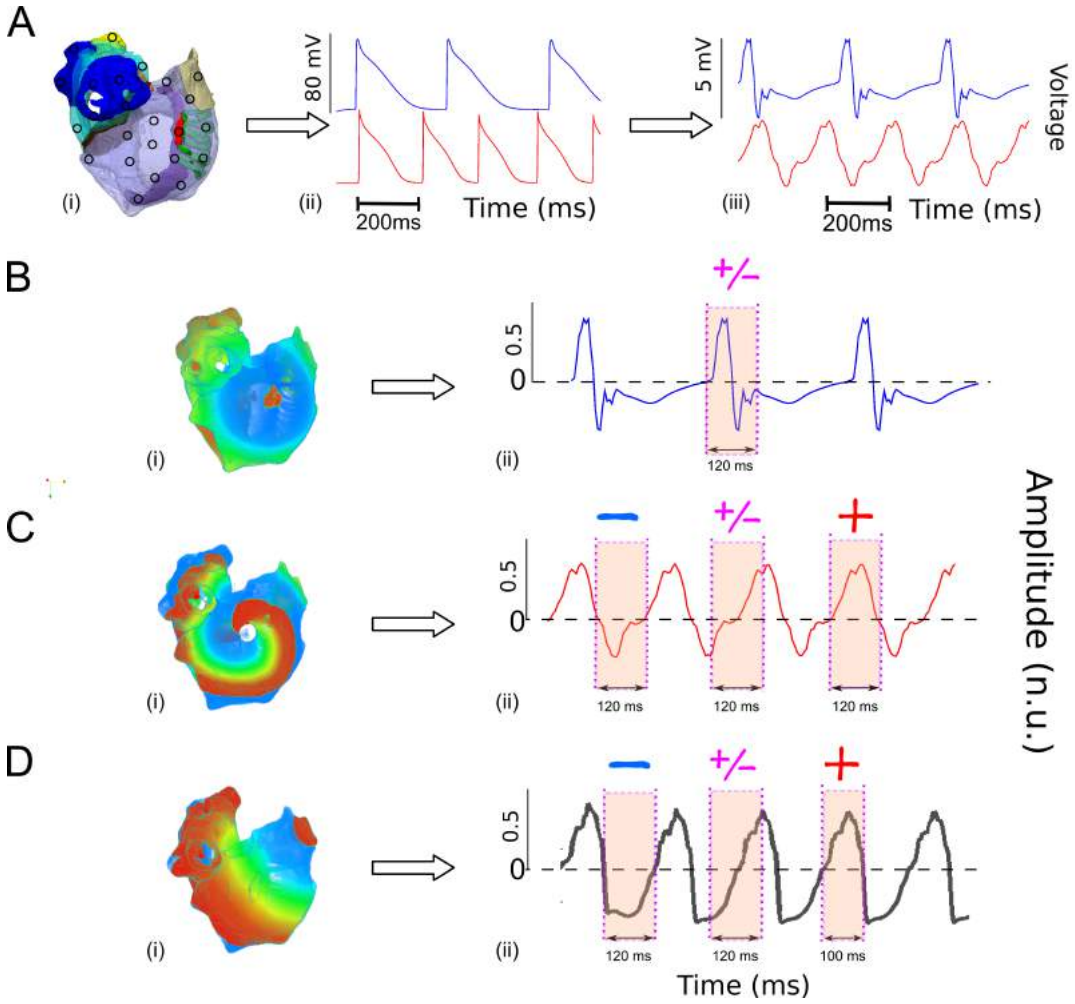

Figure 6.2: Illustration of different atrial activation associated with different body surface atrial waveform morphology. (A) Different stimulated points (circle) and tip of re-entry across the surface of the atria (i), atrial action potentials (ii) and their corresponding body surface atrial-waves at different excitation rates (iii): top 3Hz; bottom 5Hz. (B) Snapshot of atrial activation at control conditions at a fast rate, (i) and its corresponding ECG exhibiting distinct P-wave in lead V1 (ii). (C) Snapshot of atrial activation when the tip of the re-entry is located in the SAN (i), and its corresponding f-waves of lead V1 (ii). (D) Snapshot of atrial activation with the focal ectopic activity located in the right atrial appendage (RAA) (i) and the corresponding f-waves of lead V1 (ii). A red sign represents a positive polarity in the atrial-wave (magenta/shaded area), the blue sign is a negative polarity and a purple sign represents a biphasic atrial-wave (magenta/shaded area).

our previously developed algorithm to both rapid focal and re-entrant excitation, new tools were developed. The first tool was to determine the polarity of the f-wave associated with main atrial activation, in order to identify the location of the source. The second tool was to quantify the differences between focal and re-entrant activity. Further details of these algorithmic developments are provided below.

Determining the polarity of f-waves.

At slow pacing rates, it is straightforward to determine the polarity of individual P-waves: the long period of the diastolic phase means that the ECG signal remains at a baseline during this interval, with a clear deflection from the baseline corresponding to atrial activation during the systolic period (Figure 6.2B). This deflection is the P-wave, and may be positive, negative or biphasic (with both positive and negative portions). The duration (i.e., the time interval) of the P-wave corresponds to the time interval of atrial activation.

The challenge for determining the polarity of the atrial wave at rapid pacing rates is that the diastolic period is absent, leaving the ECG signal absent of a stable baseline. Therefore, there is no clear distinction between successive deflections (Figure 6.2C(ii), 6.2D(ii)). Determination of the polarity of the atrial wave in such case is thus non-trivial; any polarity can be extracted from the same signal, depending on the time interval which is considered (Figure 6.2C(ii), 6.2D(ii)). However, the polarity in the interval during which a large volume of the atrial mass is excited (i.e. main atrial activation) can be determined and is suitable for our algorithm. Thus the time interval corresponding to the main atrial activation must first be determined.

Analysis shows that the dipole signal provides sufficient information to determine the time interval of main atrial excitation (Figure 6.3). Figure 6.3 illustrates results for three different cases of atrial activation originating from the same location but with increasing complexity (i.e. slow focal pacing, rapid focal pacing, and re-entrant excitation).

At the slow rate, determination of the polarity of the P-wave is straightforward and can be seen to be positive in lead V1 (Figure 6.3A black line). Note that the time interval of the P-wave indeed corresponds to the time interval of the atrial activation (Figure 6.3A(i),(ii)). Also, both positive and negative poles of the body surface dipole have one significant deflection, and the time interval of this deflection corresponds directly to the time interval of atrial activation and therefore the P-wave (Figure 6.3 red and blue lines). The positive and negative dipole signals can be combined as a dipole sum (defined as the sum of the modulus of the negative and positive poles), giving a single signal with a significant deflection corresponding to the time interval of atrial activation (Figure 6.3 green line).

At rapid rates where f-waves rather than P-waves are observed, there are no clear markers for the time interval of atrial activation in the ECG f-wave signal (Figure 6.3B and C black line). The dipole sum, however, still presents a signal with one easily identifiable prominent deflection; the time interval of this deflection corresponds to the main atrial activation (Figure 6.3B(i),(ii)), even in the case of more fragmented f-waves resulting from re-entrant activity (Figure 6.3C(i),(ii)). The portion of the f-wave within this time interval therefore gives the polarity associated

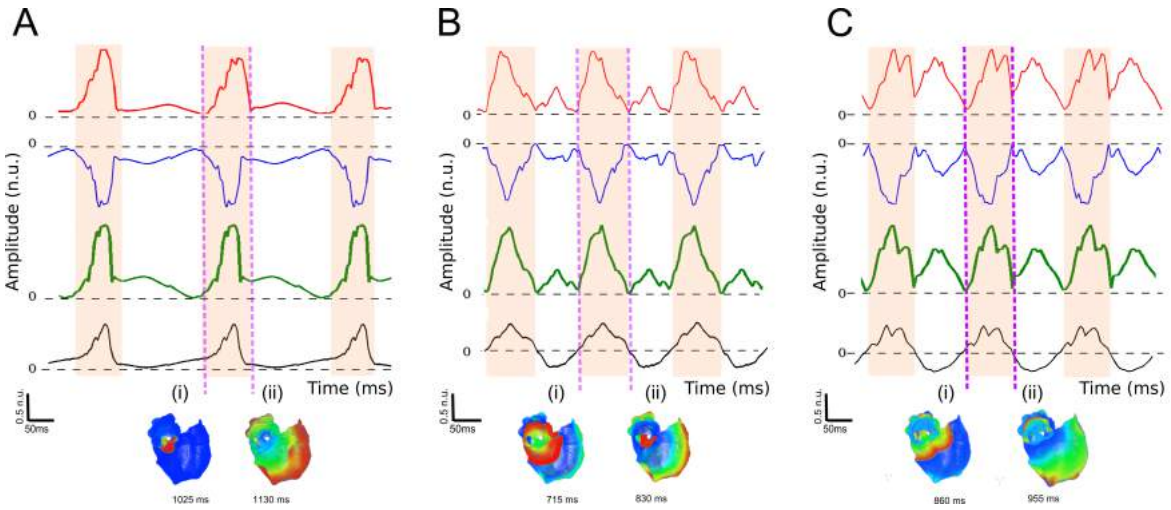

Figure 6.3: Dipole and atrial activation evolution in different atrial activations located in the pulmonary veins (PV). (A) Slow ectopic atrial activation focus in the PV (non f-waves observed). (B) Fast focal activation focus in the PV (f-waves observed). (C) Re-entrant activation around the PV (f-waves observed). Red line: Positive dipole. Blue line: Negative dipole. Green line: Dipole sum. Black line: lead V1 (ECG). The Magenta regions represent the time interval of the main atrial wave, selected from the peaks in the dipole pattern. (i)-(ii) Snapshots of the atria activation at the beginning and end of the time interval selected.

with the main atrial activation. In examples shown in Figure 6.3, the polarity is positive in lead V1 for all cases but the polarity will vary spatially across the body surface according to lead position.

Thus, by selecting the ECG segment corresponding to the main atrial activation (obtained from dipole sum, Figure 6.3 magenta/shaded regions), the polarity (positive, negative or biphasic) of each lead in this segment is determined.

Atrial source location based on the atrial-wave polarity map

Having identified the polarity of the f-waves in each lead, the resulting 64-lead polarity distribution feeds directly into our original atrial source location algorithm [18].

Figure 6.4 shows the implementation of the developed algorithm for determining the origin of non-meandering atrial re-entrant activations, centred on the sino-atrial node (SAN) (left), right atrial appendage (RAA) (middle) and pulmonary veins (PV) (right). In each case, the time interval has been obtained by selecting the largest deflection in the dipole sum evolution pattern (Figure 6.4A- vertical dashed lines) as described in the previous section. Then, an atrial-wave polarity map is created (Figure 6.4B) from the time interval selection. Once the polarity map has been created (Figure 6.4A and 6.4B), the location of the source of the atrial activation

can be found through the Perez Alday et al. algorithm [18] (S2 Fig), which associates the two set of torso quadrants (Qti) (Figure 6.4B) with the two set of atria quadrants (Qai) (Figure 6.4C (i)-(ii)).

Differentiating ectopic focal from the re-entrant activity

Our simulations demonstrate that re-entrant excitation waves are characterised by more fragmented ECGs (Figure 6.3C) compared to focal activity (Figure 6.3A,B). This might be attributable to the fact that the wave propagation through the atria due to focal excitation is more uniform and symmetric (around the origin of excitation) than re-entrant excitation. Performing Fourier Transformation analysis (FFT) of the signal from lead V1, commonly used for AF analysis due to its large atrial signal [28] (closest is lead 15 in the 64-lead configuration), allows the fragmentation of the signal V1 to be quantified, providing a way to distinguish the cases of focal from re-entrant excitation waves, with the same excitation rate and origin (Figure 6.5). From the FFT, as would be expected the dominant frequency (DF) shows no marked difference between the focal and re-entrant cases due to the same activation rates. However, the re-entrant cases exhibited considerably more power at higher frequencies. To quantify this, the ratio of the area under the power spectrum density (PSD) in the ranges 0 (2 x DF) Hz and 0 50 Hz ($AFFTr_{2DF}$) was calculated. The use of the threshold of (2 x DF) was chosen because it is the value at which the distinction between focal and re-entrant excitation was the most significant (S3 Figs). The ratio showed dramatic differences between re-entrant and ectopic activations (Figure 6.5A,B,C). By plotting the $AFFTr_{2DF}$ against its DF for all simulations (Figure 6.5D), it was clear that a ratio of above 0.675 corresponded to focal activity, a ratio below 0.655 corresponded to re-entrant activity and a ratio in the range 0.655 to 0.675 could correspond to either (overlapping area in Figure 6.5D).

Algorithm flow chart

The new tools developed were integrated into a flow chart of the algorithm as illustrated in (Figure 6.6). The first step of the new algorithm was to compute the dipole sum from the body surface potential distribution. Then, by selecting the time interval corresponding to the largest peak in the dipole sum, which is attributable to a large volume of the atrial mass that has been excited, a polarity map can be created. The next step was to implement the previous algorithm we have developed [18] to identify the source of atrial activation based on the body surface potential distribution. The last step was to differentiate focal from re-entrant activities based on the spectral characteristics of the f-waves.

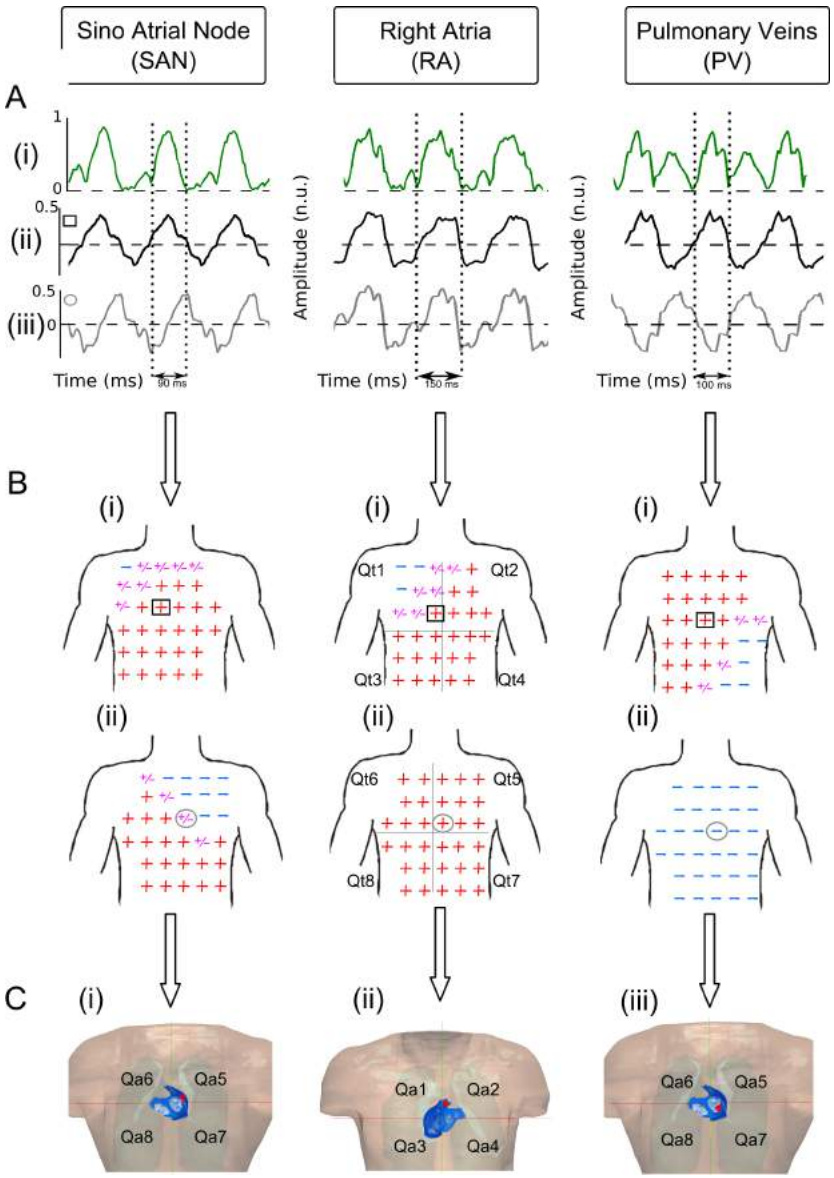

Figure 6.4: Illustration of algorithm implementation for activation from three atrial sites. (A): Dipole sum (green line) (i), lead V1 (black line) (ii) and Lead 47 (Grey line)(iii), (i) were used to identify the time interval (section between dotted lines) of re-entrant patterns where the tip was located in the sino-atrial node (SAN), right atria (RA) and pulmonary veins (PV). The amplitude in all cases has been normalized. (B): Atrial-wave polarity map in the anterior (i) and posterior (ii) part of the torso for atrial activation initiated at different locations of the atria (SAN, RA and PV). A red sign represents a positive polarity in the atrial-wave, the blue sign is a negative polarity and a purple sign represents a biphasic atrial-wave. The black square represents the electrode position of lead V1, and the grey circle represents the electrode position of lead 47. (C): Rotor tip (red dot) identified by the algorithm in each simulation. The anterior (ii) and posterior (i) parts of the atria and torso (B-i,ii) are shown for each case. In each case the algorithm correctly identifies the correct quadrant: SAN the tip is located in the quadrant Qa5 (i), for RA the tip is located in the quadrant Qa2 (ii), and for PV the tip is located in the quadrant Qa7 (iii).

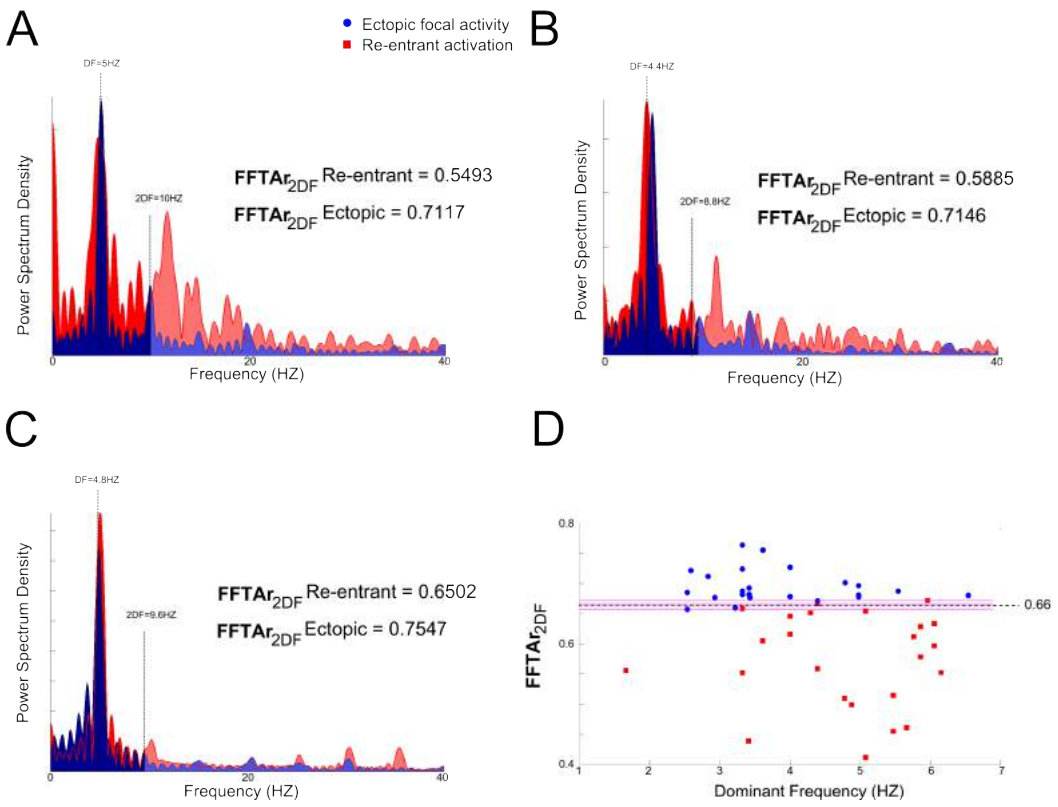

Figure 6.5: Power spectral density for ectopic focal and re-entrant activation. Power spectral density for ectopic focal (blue) and re-entrant (red) activity located in (A) SAN; (B) PV and (C) RAA. The darker shadow corresponds to the area between 0 2 x DF. (D): a scatter plot of ($AFFTr_{2DF}$) against the DF, the magenta area is the overlapping area where both activities can occur. $AFFTr_{2DF}$ is the ratio of the area under the power spectrum density in the ranges 0 (2 x DF) Hz and (2 x DF) 50 Hz: $AFFTr_{2DF} = Area_{(0\text{-}2DF)}/Area_{(0\text{-}50Hz)}$

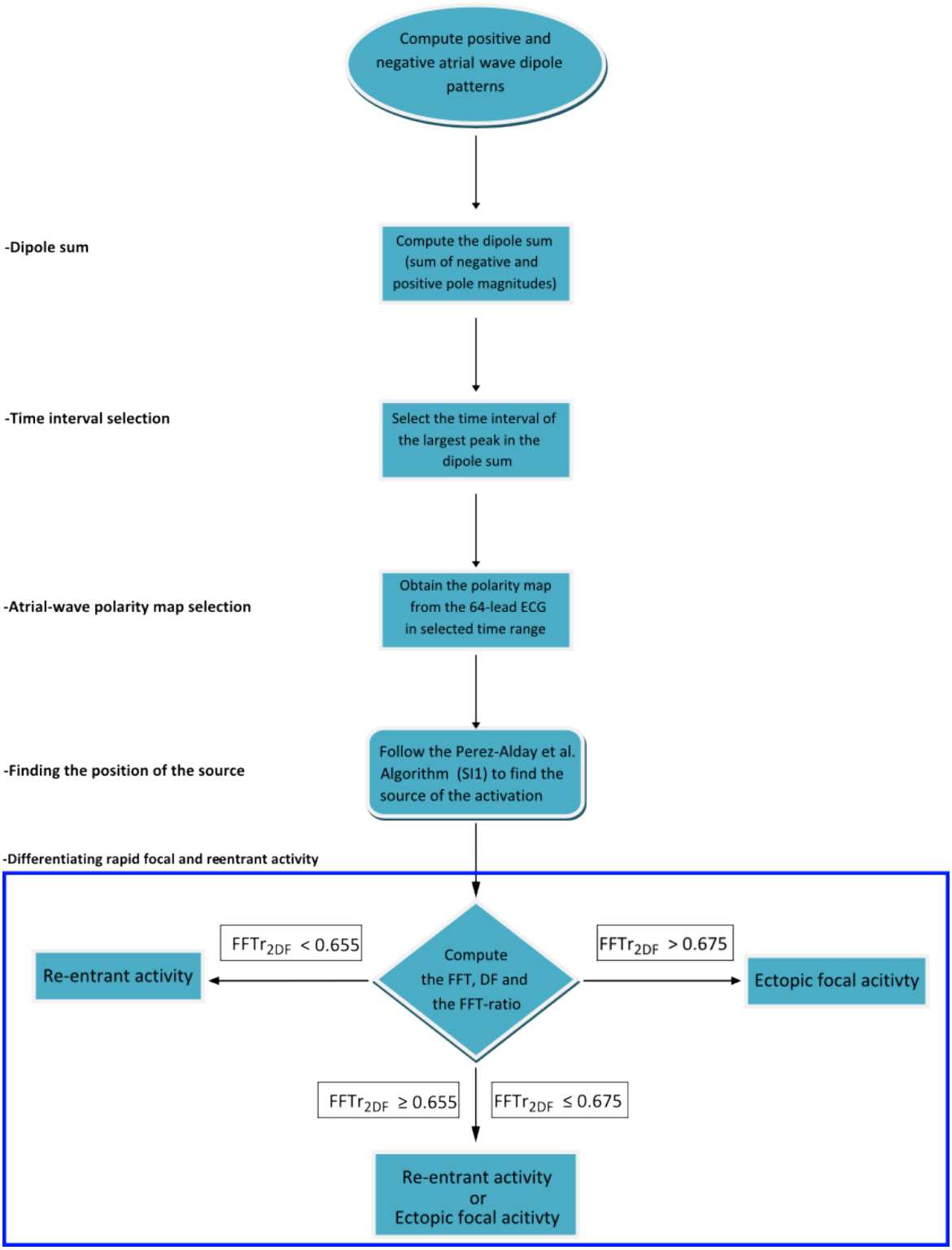

Figure 6.6: Schematic illustration of the algorithm to identify the location of atrial focal origin or re-entry from atrial wave polarity maps.

Results

Success rate of algorithm

Location

The algorithm (Figure 6.6) was developed based on simulated data of re-entrant excitation waves and ectopic focal activities with their origins located at 10 different sites across the atria. The algorithm was then tested with 20 further simulations to determine its success rate.

In the test for re-entrant excitation, the success rate of determining the atrial quadrant containing the tip of the scroll wave was 75%. In the cases which the origin of the scroll wave was not identified by the algorithm, it was due to the tip of the scroll wave being close to the boundary of two nearby quadrants (i.e., within 0.5 cm). The direction of the rotation of the scroll wave played an important role as well.

In the test for ectopic focal excitation the success rate for detecting the atrial quadrant where the rapid focal activity was located was 92%. This is comparable with the success rate of our previous algorithm [18] for slow ectopic foci (93%). The consistency between the present and the previous algorithm suggests the newly devised tool for identifying the polarity of the f-wave is valid.

Focal vs Re-entry

The success rate to differentiate ectopic activity from re-entrant activation with the same frequency was 88%. Note that the algorithm never produced a false positive, because in the remaining 12% of the cases the $AFFTr_{2DF}$ was within the overlapping area where ectopic and re-entrant activity could not be distinguished (Figure 6.5D, magenta shaded area).

Further test

The algorithm was tested with random noise added to ECG signals. During this test, a dipole sum was obtained with the same characteristics as previously described. The $AFFTr_{2DF}$ values were affected by the addition of noise, however, the changes did not produce large differences. Further information can be found in supporting information text S4.

The algorithm was also tested with a different torso geometry. During this test, dipole sum and $AFFTr_{2DF}$ values were obtained and the algorithm successfully iden-

tified the quadrant where the origin of the arrhythmia was located. Further information can be found in supporting information text S5.

Determining the time-dependent location of meandering re-entry

The algorithm showed good feasibility for tracking the tip of scroll waves with a significant degree of meander. This was done by selecting the time intervals when the tip of the rotor was in two different positions across the atria (Figure 6.7).

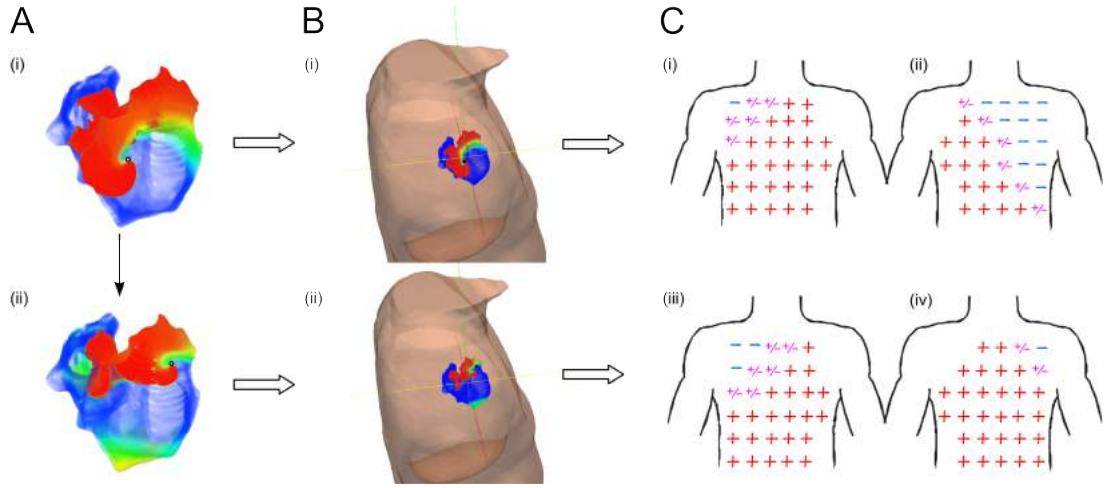

Figure 6.7: Comparison of quadrants position and atrial-waves polarity maps in meandering re-entrant activation. (A) Snapshot at two different instant of re-entrant activation in the atria. (B) Snapshot at two different instant of re-entrant activation of the atria-torso model from a posterior superior right view. (C) Simulated 64-lead ECG atrial-waves polarity map at two different instant of re-entrant activation. We observed the polarity pattern of the atrial waves of the experimental and simulation, in the anterior (i), (iii) and posterior (ii), (iv) part of the body. The red positive sign represents a positive atrial-wave, the blue negative sign represents negative atrial-wave, and the purple positive/negative sign represents a biphasic atrial-wave.

Discussion

Major contribution

By using a biophysically detailed computer model of human atria-torso and identifying the correct polarity of the f-waves, we have developed a novel algorithm to locate the origin of atrial fibrillation in association with both of ectopic focal and re-entrant activity. The success rate of the algorithm was 92% and 75% for focal and re-entry activation, respectively. The properties of the FFT allowed re-entry and focal activation to be distinguished with a success rate of 88%.

Comparison to previous/other algorithms

Previous studies have been focused on differentiating ectopic activity against re-entry [29, 30, 31, 32]. Most use atria-electrocardiograms to detect and characterize complex fractionated signals, FFT and DF atria maps [29, 30, 33]. The success rate of these algorithms is in the range of 60-80% [29, 30, 34], however, as it is an invasive method, it might unduly lengthen the ablation procedure [35]. By using a 12-lead ECG system, algorithms to detect ectopic activity have been developed [16, 36], however, the success rates range within 55-78% [15, 16, 18] and it has been proved that the 12-lead ECG system does not produce enough information to identify the origins when f-waves are presented or under re-entrant activity [15, 18, 32]. Other attempts have used multi-lead ECG systems and body surface mapping [31, 32, 37], to correlate to atrial DF or add extra information like phase mapping [32]. However, it has been difficult to validate the time interval, location and the source of the atrial activation when f-waves are presented. Nevertheless, they are promising methods that can add extra useful information. Ours is the first attempt to distinguish the main activity and find the position of the focus and tip of the re-entry from a multi-lead ECG.

Comparison with reconstruction of the atrial surface potentials from body surface potentials.

In order to demonstrate the advantage of the developed algorithm for detecting AF origins from 64-lead ECG over that of inverse problem solutions, the epicardial excitation pattern of the atria was reconstructed during the time course of re-entrant excitation based on the computed BSP from the atria-torso model. To solve the inverse problem, the transfer matrix, which relates the BSP to the electrical potential in the atrial epicardio-surface, was calculated using Greens Theorem and a boundary element discretization [38, 39]. A common zero order Tikhonov regularization was implemented to find the potentials in the surface of the atria [40]. This method has been suggested as a feasible method for reconstruction cardiac electrical excitation [12, 14]. In numerical implementation, the L-curve was used to find the best regularization parameter for each case [41]. Mathematical details of the reconstruction method used can be found in Supporting information 2 (S6).

The body surface potentials at different lead densities were simulated. The effects of lead density on the accuracy of the inverse-solution were investigated.

Figure 6.8 presents the snapshot of reconstructed atrial epi-cardial excitation patterns at different timings using lead densities of 64 (Figure 6.8A), 256 (Figure 6.8B) and 2024 (Figure 6.8C) electrodes. These are compared to the actual activation pattern shown in Figure 6.8D. It demonstrates that a high number of electrodes is

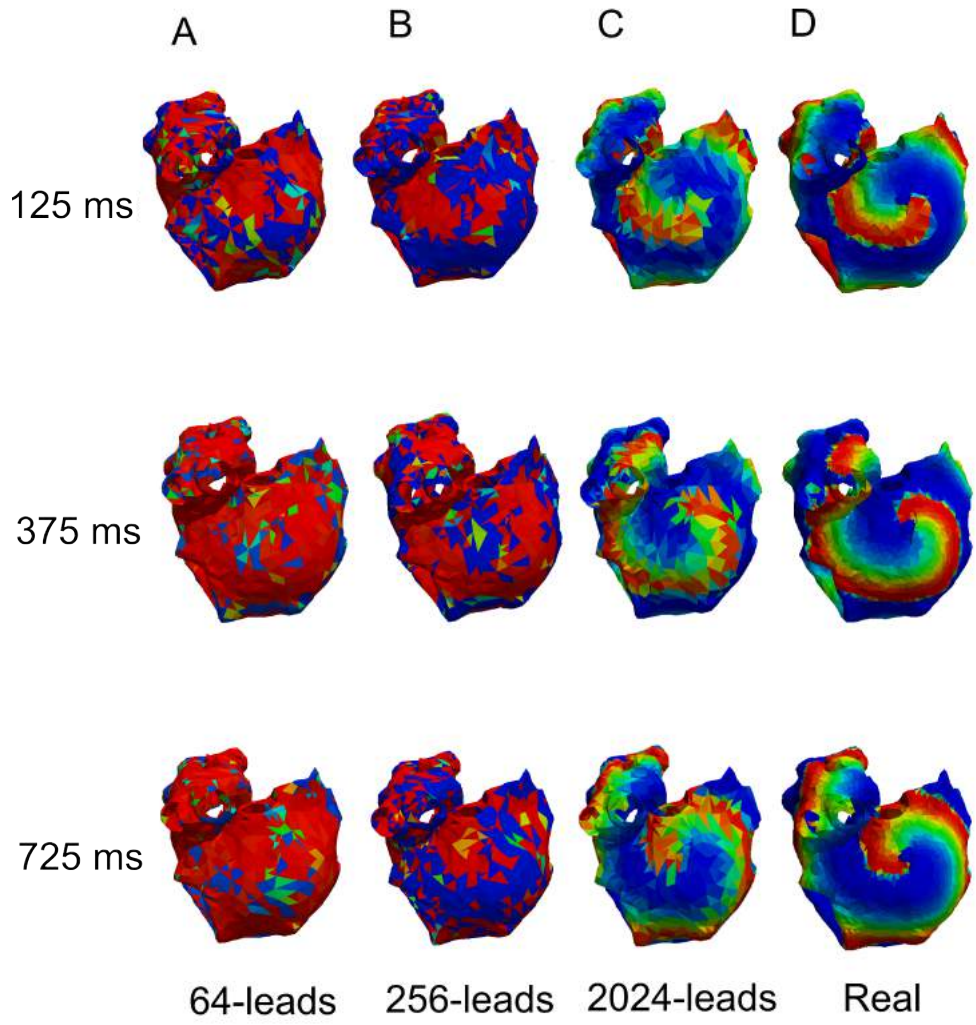

Figure 6.8: Snapshot of epi-cardial reconstruction of a rotor wave. Snapshot of epi-cardial reconstruction of a rotor wave with its origin located in the sino-atrial node region at different timings (125, 375 and 725 ms). Reconstructed pattern with variant numbers of electrodes of 64 (A), 256 (B) and 2024 (C) were compared to the real activation pattern (D).

needed to reliably reconstruct the atrial excitation patterns, and subsequently locate the atrial activation source. Specifically, in the case of 64-lead ECG, the constructed atrial activation pattern was not sufficient to locate the AF origin by inverse solution, whereas our algorithm using 64-lead ECG performed very well.

The number of body surface potential leads can be artificially increased using different types of interpolation [42, 43]. However, the minimum required distance between electrodes and therefore the spatial resolution is still an open question [42].

The algorithm developed in the present study using 64-lead ECG provided sufficient information to locate the origin of the atrial activation, demonstrating the superiority of the developed algorithm over the inverse-problem solution.

Further work to improve the reconstruction and therefore a comparison of the accuracy of different inverse problem reconstruction with different spatial resolution and different interpolation methods in all the different cases presented needs to be performed. Also, the cases where the tip of the spiral wave is inside the atria and not on its surface are not possible to be identified with the inverse solution, whereas the algorithm presented in this study can still produce good results.

Limitations

The torso model lacks considerations of some other tissue types or organs (such as muscles, fat tissue, bowel, kidneys and spleen) that may affect the amplitude of simulated surface potentials. However, the absence of those tissues does not have a large effect on the polarity of the atrial-waves, which is the characteristic used in the present algorithm, as demonstrated previously [18]. In the algorithm, two-sets of quadrants were defined to cover the torso. The spatial resolution of the quadrant may require further refinement. For example, each quadrant can be split into four sub-quadrants, though; the success rate of the algorithm may decrease.

Future work

In the present study, we only tested the effectiveness of the algorithm for detecting single atrial focal activity and a single centre of a rotor activity. However, a possible extension is to identify multiple wavelets, using the dipole evolution patterns. For that purpose, consideration of combined use of the present algorithm with vecto-cardiograms, phase relationships, correlation analysis and inverse problem reconstruction may be necessary, warranting further investigation.

Conclusion

A novel algorithm has been developed to locate the origins of rapid and irregular atrial excitation waves, associated with both ectopic focal and re-entrant activity. This represents a significant progress to previously developed algorithms to predict AF origins in association with focal activities.

Supporting Information

Figure S1

Comparison of p-waves and dipole evolution between the simulated and experimental data.

Figure S2

Schematic illustration of the algorithm to identify the quadrant of atrial focal origin based on 64-lead ECG P-wave values. Fig adapted from [18].

Text S3

AFFTr frequency ratios dependency on the dominant frequency (DF).

Text S4

Testing the algorithm with random noise added to ECG signals.

Text S5

Testing the algorithm with a female torso geometry.

Text S6

Reconstruction of the atrial surface activation from the electric potential measured in the surface of the body performed using a Zero order Tikhonov regularization.

Acknowledgments

CONACYT

Bibliography

[1] E. Anter, M. Jessup, and D. J. Callans, "Atrial fibrillation and heart failure treatment considerations for a dual epidemic," *Circulation*, vol. 119, no. 18, pp. 2516–2525, 2009.

[2] E. J. Benjamin, P. A. Wolf, R. B. DAgostino, H. Silbershatz, W. B. Kannel, and D. Levy, "Impact of atrial fibrillation on the risk of death the framingham heart study," *Circulation*, vol. 98, no. 10, pp. 946–952, 1998.

[3] K. T. Konings, J. L. Smeets, O. C. Penn, H. J. Wellens, and M. A. Allessie, "Configuration of unipolar atrial electrograms during electrically induced atrial fibrillation in humans," *Circulation*, vol. 95, no. 5, pp. 1231–1241, 1997.

[4] S. M. Narayan, D. E. Krummen, and W. J. Rappel, "Clinical mapping approach to diagnose electrical rotors and focal impulse sources for human atrial fibrillation," *Journal of cardiovascular electrophysiology*, vol. 23, no. 5, pp. 447–454, 2012.

[5] J. Jalife, O. Berenfeld, A. Skanes, and R. Mandapati, "Mechanisms of atrial fibrillation: mother rotors or multiple daughter wavelets, or both?," *Journal of cardiovascular electrophysiology*, vol. 9, no. 8 Suppl, pp. S2–12, 1998.

[6] I. Graham, D. Atar, K. Borch-Johnsen, G. Boysen, G. Burell, R. Cifkova, J. Dallongeville, G. De Backer, S. Ebrahim, B. Gjelsvik, *et al.*, "European guidelines on cardiovascular disease prevention in clinical practice: executive summary," *European heart journal*, 2007.

[7] F. Rahman, G. F. Kwan, and E. J. Benjamin, "Global epidemiology of atrial fibrillation," *Nature Reviews Cardiology*, vol. 11, no. 11, pp. 639–654, 2014.

[8] P. Jais, D. Shah, M. Hocini, L. Macle, K. J. Choi, M. Haïssaguerre, and J. Clémenty, "Radiofrequency ablation for atrial fibrillation," *European Heart Journal Supplements*, vol. 5, no. suppl H, pp. H34–H39, 2003.

[9] O. M. Wazni, N. F. Marrouche, D. O. Martin, A. Verma, M. Bhargava, W. Saliba, D. Bash, R. Schweikert, J. Brachmann, J. Gunther, *et al.*, "Radiofrequency ablation vs antiarrhythmic drugs as first-line treatment of symptomatic atrial fibrillation: a randomized trial," *Jama*, vol. 293, no. 21, pp. 2634–2640, 2005.

[10] A. N. Ganesan, N. J. Shipp, A. G. Brooks, P. Kuklik, D. H. Lau, H. S. Lim, T. Sullivan, K. C. Roberts-Thomson, and P. Sanders, "Long-term outcomes of catheter ablation of atrial fibrillation: A systematic review and meta-analysis," *Journal of the American Heart Association*, vol. 2, no. 2, p. e004549, 2013.

[11] C. Schmitt, G. Ndrepepa, S. Weber, S. Schmieder, S. Weyerbrock, M. Schneider, M. R. Karch, I. Deisenhofer, J. Schreieck, B. Zrenner, *et al.*, "Biatrial multisite mapping of atrial premature complexes triggering onset of atrial fibrillation," *The American journal of cardiology*, vol. 89, no. 12, pp. 1381–1387, 2002.

[12] Y. Rudy and J. E. Burnes, "Noninvasive electrocardiographic imaging," *Annals of noninvasive electrocardiology*, vol. 4, no. 3, pp. 340–359, 1999.

[13] W. Anné, H. Van Rensburg, J. Adams, H. Ector, F. Van de Werf, and H. Heidbüchel, "Ablation of post-surgical intra-atrial reentrant tachycardia. predilection target sites and mapping approach," *European heart journal*, vol. 23, no. 20, pp. 1609–1616, 2002.

[14] H. S. Oster and Y. Rudy, "The use of temporal information in the regularization of the inverse problem of electrocardiography," *Biomedical Engineering, IEEE Transactions on*, vol. 39, no. 1, pp. 65–75, 1992.

[15] J.-S. Uhm, J. Shim, J. Wi, H.-S. Mun, H.-N. Pak, M.-H. Lee, and B. Joung, "An electrocardiography algorithm combined with clinical features could localize the origins of focal atrial tachycardias in adjacent structures," *Europace*, vol. 16, no. 7, pp. 1061–1068, 2014.

[16] Z. Y. Qian, X. F. Hou, D. J. Xu, B. Yang, M. L. Chen, C. Chen, F. X. Zhang, Q. J. Shan, K. J. Cao, and J. G. Zou, "An algorithm to predict the site of origin of focal atrial tachycardia," *Pacing and Clinical Electrophysiology*, vol. 34, no. 4, pp. 414–421, 2011.

[17] M. A. Colman, O. V. Aslanidi, J. Stott, A. V. Holden, and H. Zhang, "Correlation between p-wave morphology and origin of atrial focal tachycardiainsights from realistic models of the human atria and torso," *Biomedical Engineering, IEEE Transactions on*, vol. 58, no. 10, pp. 2952–2955, 2011.

[18] E. A. P. Alday, M. A. Colman, P. Langley, T. D. Butters, J. Higham, A. J. Workman, J. C. Hancox, and H. Zhang, "A new algorithm to diagnose atrial ectopic origin from multi lead ecg systems-insights from 3D virtual human atria and torso," *PLoS computational biology*, vol. 11, no. 1, 2015.

[19] E. A. Perez Alday, M. A. Colman, P. Langley, and H. Zhang, "Spatial refinement of a new algorithm to identify focus of atrial ectopic activity from 64-lead ecgs," in *Computing in Cardiology Conference (CinC), 2014*, pp. 501–504, IEEE, 2014.

[20] E. A. Perez Alday, M. A. Colman, T. D. Butters, J. Higham, D. Giacopelli, P. Langley, and H. Zhang, "Diagnosis of atrial ectopic origin from the body surface ecg: Insights from 3D virtual human atria and torso," in *Computing in Cardiology Conference (CinC), 2013*, pp. 1075–1078, IEEE, 2013.

[21] O. V. Aslanidi, M. A. Colman, J. Stott, H. Dobrzynski, M. R. Boyett, A. V. Holden, and H. Zhang, "3D virtual human atria: a computational platform

for studying clinical atrial fibrillation," *Progress in biophysics and molecular biology*, vol. 107, no. 1, pp. 156–168, 2011.

[22] M. A. Colman, O. V. Aslanidi, S. Kharche, M. R. Boyett, C. Garratt, J. C. Hancox, and H. Zhang, "Pro-arrhythmogenic effects of atrial fibrillation-induced electrical remodelling: insights from the three-dimensional virtual human atria," *The Journal of physiology*, vol. 591, no. 17, pp. 4249–4272, 2013.

[23] N.-W. Hsu, Y.-J. Lin, C.-T. Tai, T. Kao, S.-L. Chang, W. Wongcharoen, L.-W. Lo, A. R. Udyavar, Y.-F. Hu, H.-W. Tso, *et al.*, "Frequency analysis of the fibrillatory activity from surface ecg lead v1 and intracardiac recordings: implications for mapping of af," *Europace*, vol. 10, no. 4, pp. 438–443, 2008.

[24] V. Biktashev and A. Holden, "Reentrant waves and their elimination in a model of mammalian ventricular tissue," *Chaos: An Interdisciplinary Journal of Nonlinear Science*, vol. 8, no. 1, pp. 48–56, 1998.

[25] S. R. Kharche, T. Stary, M. A. Colman, I. V. Biktasheva, A. J. Workman, A. C. Rankin, A. V. Holden, and H. Zhang, "Effects of human atrial ionic remodelling by β-blocker therapy on mechanisms of atrial fibrillation: a computer simulation," *Europace*, p. euu084, 2014.

[26] Y. Salu, "Implementing a consistency criterion in numerical solution of the bioelectric forward problem," *Biomedical Engineering, IEEE Transactions on*, no. 6, pp. 338–341, 1980.

[27] D. Giacopelli, J. P. Bourke, A. Murray, and P. Langley, "Spatial pattern of p waves in paroxysmal atrial fibrillation patients in sinus rhythm and controls," *Pacing and Clinical Electrophysiology*, vol. 35, no. 7, pp. 819–826, 2012.

[28] A. Bollmann, D. Husser, M. Stridh, L. Soernmo, M. Majic, H. U. Klein, and S. B. Olsson, "Frequency measures obtained from the surface electrocardiogram in atrial fibrillation research and clinical decision-making," *Journal of cardiovascular electrophysiology*, vol. 14, no. s10, pp. S154–S161, 2003.

[29] D. Scherr, D. Dalal, A. Cheema, A. Cheng, C. A. Henrikson, D. Spragg, J. E. Marine, R. D. Berger, H. Calkins, and J. Dong, "Automated detection and characterization of complex fractionated atrial electrograms in human left atrium during atrial fibrillation," *Heart Rhythm*, vol. 4, no. 8, pp. 1013–1020, 2007.

[30] B. Ghoraani, R. Dalvi, S. Gizurarson, M. Das, A. Ha, A. Suszko, S. Krishnan, and V. Chauhan, "Localized rotational activation in the left atrium during human atrial fibrillation: relationship to complex fractionated atrial electrograms and low-voltage zones," *Heart Rhythm*, vol. 10, no. 12, pp. 1830–1838, 2013.

[31] M. Bojarnejad, J. R. Blake, J. Bourke, E. Shepherd, A. Murray, and P. Langley, "Non-invasive estimation of left atrial dominant frequency in atrial fibrillation from different electrode sites: Insight from body surface potential mapping," *JAFIB: Journal of Atrial Fibrillation*, vol. 7, no. 3, 2014.

[32] M. Rodrigo, M. S. Guillem, A. M. Climent, J. Pedrón-Torrecilla, A. Liberos, J. Millet, F. Fernández-Avilés, F. Atienza, and O. Berenfeld, "Body surface localization of left and right atrial high-frequency rotors in atrial fibrillation patients: A clinical-computational study," *Heart Rhythm*, vol. 11, no. 9, pp. 1584–1591, 2014.

[33] F. Ravelli and M. Masè, "Computational mapping in atrial fibrillation: how the integration of signal-derived maps may guide the localization of critical sources," *Europace*, vol. 16, no. 5, pp. 714–723, 2014.

[34] D. H. Lau, B. Maesen, S. Zeemering, S. Verheule, H. J. Crijns, and U. Schotten, "Stability of complex fractionated atrial electrograms: a systematic review," *Journal of cardiovascular electrophysiology*, vol. 23, no. 9, pp. 980–987, 2012.

[35] M. K. Stiles, A. G. Brooks, B. John, L. Wilson, P. Kuklik, H. Dimitri, D. H. LAU, R. L. Roberts Thomson, L. Mackenzie, S. Willoughby, *et al.*, "The effect of electrogram duration on quantification of complex fractionated atrial electrograms and dominant frequency," *Journal of cardiovascular electrophysiology*, vol. 19, no. 3, pp. 252–258, 2008.

[36] P. M. Kistler, S. P. Fynn, H. Haqqani, I. H. Stevenson, J. K. Vohra, J. B. Morton, P. B. Sparks, and J. M. Kalman, "Focal atrial tachycardia from the ostium of the coronary sinus: electrocardiographic and electrophysiological characterization and radiofrequency ablation," *Journal of the American College of Cardiology*, vol. 45, no. 9, pp. 1488–1493, 2005.

[37] M. S. Guillem, A. M. Climent, F. Castells, D. Husser, J. Millet, A. Arya, C. Piorkowski, and A. Bollmann, "Noninvasive mapping of human atrial fibrillation," *Journal of cardiovascular electrophysiology*, vol. 20, no. 5, pp. 507–513, 2009.

[38] M. Stenroos and J. Haueisen, "Boundary element computations in the forward and inverse problems of electrocardiography: comparison of collocation and galerkin weightings," *Biomedical Engineering, IEEE Transactions on*, vol. 55, no. 9, pp. 2124–2133, 2008.

[39] R. C. Barr, M. Ramsey III, and M. S. Spach, "Relating epicardial to body surface potential distributions by means of transfer coefficients based on geometry measurements," *Biomedical Engineering, IEEE Transactions on*, no. 1, pp. 1–11, 1977.

[40] A. Tikhonov, *Solutions of ill-posed problems.*

[41] P. C. Hansen, *Rank-deficient and discrete ill-posed problems: numerical aspects of linear inversion*, vol. 4. Siam, 1998.

[42] P. W. Macfarlane, A. van Oosterom, and M. Janse, *Comprehensive electrocardiology*, vol. 4. Springer Science & Business Media, 2010.

[43] C. F. Pieper and A. Pacifico, "The epicardial field potential in dog: Implications for recording site density during epicardial mapping," *Pacing and Clinical Electrophysiology*, vol. 16, no. 6, pp. 1263–1274, 1993.

Chapter 7

Third Manuscript

Comparison of Electric- and Magnetic-cardiograms Produced by Myocardial Ischemia in Models of the Human Ventricle and Torso.

Erick A. Perez Alday[1], Haibo Ni[1], Chen Zhang[2], Michael A. Colman[1], Zizhao Gan[2], Henggui Zhang[1]

1 Biological Physics Group, Department of Physics and Astronomy, University of Manchester, Manchester, United Kingdom,
2 Peking University, Beijing, China.

Comparison of Electric- and Magnetic-cardiograms Produced by Myocardial Ischemia in Models of the Human Ventricle and Torso.

Erick A. Perez Alday[1], Haibo Ni[1], Chen Zhang[2], Michael A. Colman[1], Zizhao Gan[2], Henggui Zhang[1]

1 Biological Physics Group, Department of Physics and Astronomy, University of Manchester, Manchester, United Kingdom,
2 Peking University, Beijing, China.

Abstract

Myocardial ventricular ischemia arises from a lack of blood supply to the heart, which may cause abnormal repolarization and excitation wave conduction patterns in the tissue, leading to cardiac arrhythmias and even sudden death. Current diagnosis of cardiac ischemia by the 12-lead electrocardiogram (ECG) has limitations as they are insensitive in many cases and may show unnoticeable differences compared to normal patterns. As the magnetic field provides extra information on cardiac excitation and is more sensitive to tangential currents to the surface of the chest, whereas the electric field is more sensitive to radial currents, it has been hypothesized that the magnetocardiogram (MCG) may provide a complementary method to the ECG in ischemic diagnosis. However, it is unclear yet about the differences in sensitivity regions of body surface ECG and MCG signals to ischemic conditions. The aim of this study was to investigate such differences by using 12-, 36- ECG and 36-MCG computed from multi-scale biophysically detailed computational models of the human ventricles and torso in both control and ischemic conditions. It was shown that ischemia produced changes in the ECG and MCG signals in the QRS complex, T-wave and ST-segment, with greater relative differences seen in the 36-lead ECG and MCG as compared to the 12-leads ECG. The 36-lead ECG showed more averaged sensitivity than the MCG in the change of T-wave due to ischemia, whereas the MCG showed greater sensitivity than the ECG in the change of the ST-segment. In addition, both MCG and ECG showed regional-dependent changes to ischemia, but with MCG showing a stronger correlation between ischemic region in the heart and the maximal difference map on the body surface. In conclusion, MCG shows more sensitivity than ECG in response to ischemia, which may provide an alternative method for the diagnosis of ischemia.

Introduction

Ischemic heart disease is one of the leading causes of death in developed countries and worldwide [1, 2, 3]. Coronary artery occlusion can cause, within hours, cell death in ischemic myocardium [1]. This results from a lack of blood flow to the heart which decreases partially or completely the oxygen supply to the cell, damaging the muscle [1]. Significant ischemic regions within the heart can promote abnormal excitation wave conduction and repolarization patterns, leading to ventricular arrhythmias and even sudden cardiac death [4, 5]. Therefore, being able to detect, quantify and locate the site of acute transient ischemic regions in the heart by non-invasive techniques is a clinically important challenge [3, 6].

The 12-lead electrocardiogram (ECG) has been implemented as a standard bedside evaluation procedure for cardiac condition diagnosis for multiple decades [3, 7]. Unfortunately, the standard 12-lead ECG has been shown to be insensitive to cardiac ischemia; the ECG waveforms of patients with ischemia may only differ by 15-30% compared to none-ischemic patients [3, 4, 6, 8]. This suggests that the 12-lead ECG provides insufficient information for satisfactory diagnosis of ischemia. Other non-invasive techniques, including radionuclide methods [9], magnetic resonance imaging [10] and positron computed tomography [11], are far more sensitive to the detection of ischemia. However, they are highly expensive and time consuming, and therefore not practical for day-to-day, bedside monitoring and detection of silent ischemia (i.e. asymptomatic ischemia which does not present as an arrhythmia) [12, 13, 14].

Previous studies have shown that multi-lead ECG configurations provide more information for the diagnosis of irregular cardiac conduction and repolarization patterns than the standard 12-lead ECG [8, 12, 15]. Moreover, the magnetic field produced by the electrical activity of the heart may provide a greater level of detail of cardiac excitation compared to the body surface potential (BSP), because magnetocardiograms (MCG) are more sensitive to currents tangential to the surface of the chest than ECGs. Combined with its high independence to inhomogeneities in electrical resistivity inside the tissues of the body and on the skin [12, 16, 17], the MCG therefore provides a potential practical alternative to the ECG for monitoring the cardiac conditions. However, detailed correlation between the presence of ischemia and the characteristics of the MCG has yet to be established.

In this study, we aim to compare and quantify the effects of the presence of ventricular ischemia on BSP and MCG maps and the 36-lead ECG and MCG recordings derived from these maps, in order to compare the most sensitive regions of the body related to the presence of ischemia. This was achieved through application of a

multi-scale computational model of the human ventricles to simulate the effects of ischemic zones on electrical wave propagation throughout the heart. Then, using the simulation data of the human ventricles, the electric and magnetic forward problems were solved in a torso model to obtain the BSP and MCG maps, respectively.

Methods

Experimental ECG and MCG equipment and data acquisition

A self-developed 4-channel (HTc-rf-SQUID) Bio-magnetometer (Peking University, China) [18] was used to detect the cardiac magnetic field. The multichannel system (36-lead MCG) was arranged in a squared structure and was placed on the front of the chest and recorded the vertical component of the MCG signal, which is, the normal component of the magnetic field to the chest surface of the subject [18]. The sensor array covered a square area of 80x80 mm, and the distance between adjacent channels was 40 mm. The system was operated inside a magnetically shielded room after inserting the system in a resin rod of identical epoxy-reinforced nonmagnetic glass fiber crystals containing liquid helium [18]. The noise spectral density of the fabricated magnetometers was less than in the white noise region [18, 19]. A 36-lead ECG was also obtained placing the electrodes on the surface of the body, in a similar position of the MCG sensors, in order to compare the measurements [18]. The MCG and ECG experimental data was obtained from a 25 years old healthy (no cardiac disease presented) subject.

Description of mathematical models

A three dimensional (3D) biophysically detailed computational model of the human ventricles was incorporated into a heart-torso model to simulate normal and ischemic conditions (Figure 7.1). The 3D ventricular anatomical model was previously developed and is segmented into the major distinctive electrically heterogeneous regions [20] (Figure 7.1A). All of the models incorporated anatomical structures and detailed electrophysiological heterogeneity with cellular electrophysiology being described by the Ten Tusscher et al. single cell model of human ventricular action potentials (TNNP) [21].

Single cell model

The human ventricular cell model proposed by Ten Tusscher, Noble, Noble and Panfilov (TNNP) [21] was employed to simulate the action potential (AP) of the

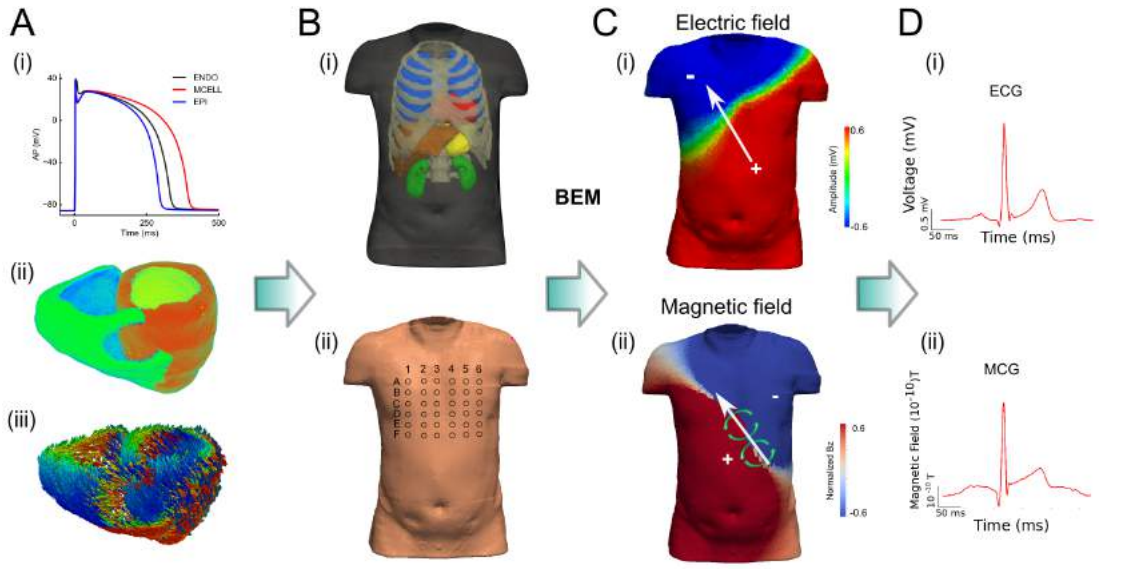

Figure 7.1: Multi-scale computer models of the human ventricles and torso. (A) Computational model of the human ventricles showing (i) AP, (ii) anatomically accurate structure, and (iii) myofibre orientations derived from DT-MRI scanning. (B) Heart-torso model (i), and positions of the electrodes/sensors on the surface of the body (ii). (C) simulated body-field maps and (D) example single electrode signals, for the ECG (i) and MCG (ii). The white arrows show the direction of the electric potential, while the green circled arrows show the direction of the magnetic field, consistent with the right hand rule.

myocytes. The formulation of the rapid delayed rectified potassium current (I_{Kr}) was replaced by a Markov-chain formulation [20]. The membrane potential can be evaluated by:

$$\frac{dV}{dt} = -\frac{I_{ion} + I_{stim}}{C_m} \tag{7.1}$$

where V is the voltage across the membrane, t is time, I_{ion} is the total transmembrane current, I_{stim} is the stimulus current applied externally, and C_m is the capacitance of the cell. Also, the late component of the sodium current (I_{NaL}) was incorporated by adapting the model of I_{NaL} from the Ohara et al. model [22]. The TNNP model is capable of simulating three types of action potential representing endocardial (ENDO), midcardial (MCELL) and epicardial (EPI) cells (Figure 7.1A (i)).

Tissue model

The excitation and wave propagation in the tissue was abstracted to be a diffusion-reaction problem, and modelled with the monodomain equation:

$$C_m \frac{\partial V}{\partial t} = -I_{ion} + I_{stim} + \nabla \cdot (D \nabla V) \tag{7.2}$$

where D is the diffusion tensor describing the conductivities of the tissue along different directions. D was set at 0.18 mm^2/ms along the fibre direction and 0.06 mm^2/ms across the fibre direction, giving a planar conduction velocity of 71.9 cm/s along fibre direction and 42.5 cm/s across fibre direction. These values are close to the 70 cm/s conduction velocity along the fibre direction found in human ventricles [23].

The activation and wave propagation of excitation was simulated on an anatomically accurate human ventricular geometry reconstructed from DT-MRI scanned data. The derived fibre orientation was incorporated to account for the anisotropy in the material property. In order to simulate the transmural electrical heterogeneity of the ventricle walls, the tissue was segmented into ENDO, EPI and MCELL regions. Specifically, the MCELL region was considered to be isolated islands within the endocardium [24, 25]. Apico-basal heterogeneities in the electrophysiological properties of the myocardium were considered by adding gradients to I_{Ks} (slow rectified delayed current) [24, 26]. A linear scaling function based on the distance to the base of ventricles was applied to the channel conductance of I_{Ks}. As such, the conductance of I_{Ks} in the myocytes in the apex was 2.67-fold larger than that of the basal cells [26]. Empirically determined activation sites across the endo-surface of ventricular walls were used to mimic the Purkinje conduction network, as a detailed structure of such conduction system is not available. These activation sites were validated by reproducing the excitation wave propagation pattern in human ventricles and QRS complex of measured 64-channel ECG [20, 27].

Modelling ventricular ischemia

Acute ischemia can be considered in two phases: phase A (first 2-10 minutes post-occlusion) and B (15-45 minutes after coronary occlusion) [28, 29]. These two phases were modeled separately by mimicking ischemia induced changes on cardiac electrophysiology [30, 30] at 10 and 45 minutes post-occlusion, respectively. In phase A, we considered: (i) hyperkalemia: an increase in extracellular potassium concentration; (ii) acidosis: decrease in the maximum conductivity of sodium and L-type calcium currents, and; (iii) hypoxia: activation of ATP dependent potassium current, I_{KATP} [31, 32]. In phase B, changes to sodium-calcium exchanger, sodium-potassium pump and intracellular calcium handling system were introduced in addition to the alterations seen in phase A. The conductivity of tissue was also reduced in phase B but not in phase A [30]. A detailed summary of the changes is given in Appendix 1. The

resulting changes to ENDO, MCELL and EPI action potentials are shown in Figure 7.2.

I_{KATP} was modelled using the formula from Kazbanov et al. 2014 [31], given by:

$$I_{KATP} = G_{KATP} \cdot f_{ATP} \cdot (\frac{[K^+]_0}{5.4})^{0.3}(V - E_K) \tag{7.3}$$

where G_{KATP} is the maximum channel conductance, f_{ATP} the fraction of open gate, $[K^+]_o$ the extracellular potassium concentration, V the membrane potential, E_K the Nernst reversal potential for potassium. The parameters of I_{KATP} were kept the same with Kazbanov et al. 2014 [31].

To perform a thorough comparison of ischemia induced changes in ECG and MCG, a number of ischemic lesion conditions with a single lesion but in 20 different locations and different sizes were created. To simplify the problem, spherical ischemic regions were used with randomly selected centres throughout the ventricular myocardium. Both small and large lesions (18 mm and 27 mm in radius respectively) were considered. Similar to previous studies [30, 30], the lesions are composed of central zones (CZ) and border zones (BZ), with CZ occupying myocardium within 80% of the lesion radius to the centre. In the BZ, the ischemic parameters were assumed to vary linearly from CZ ischemic parameter to normal.

Simulating ECG and MCG

To simulate ECG and MCG, the ventricle models were placed within a previously developed torso model [33], which considers the presence of lungs, liver, stomach, kidneys, blood masses, spinal cord and ribs, each with different electrical conductivities (Figure 7.1 B). The boundary element method (BEM) was used to compute the electric potentials on the surface of the body (Figure 7.1 C), resulting from an applied current density, J_i, obtained from the electrical activity of the ventricular tissue-models. Details can be found in previous studies [33, 34]. Once the electric potential ϕ is known, the magnetic field, B, was obtained by discretizing the volume into m homogenous elements and using a BEM of the Biot-Savart law [35, 36]:

$$\vec{B}(r) = \vec{B}_0 - \frac{\mu_0}{4\pi}\sum_{k=1}^{m}(\sigma_k^- - \sigma_k^+)\int_{S_k}\phi(r)\vec{n}(r) \times \frac{\vec{r} - \vec{r'}}{|\vec{r} - \vec{r'}|^3}dS_j \tag{7.4}$$

where B_0 is the magnetic field produced by the current source J_i, σ and σ are the inside and outside conductivities of the element k, respectively, and r and r are the distance to the observation point and the distance to a volume element dV, respectively. Then, the z-component of the magnetic field was selected in order to compare simulated and experimental data.

Elements of the torso mesh corresponding to the locations of the electrodes and magnetic sensors were selected to simulate 12- and 36- lead ECGs and 36-lead MCG (Figure 7.1B). The simulated 12- and 36-lead ECG and MCG was compared with experimental data.

The QRS complex, ST-segment and T-wave were analyzed to compare control with the two different ischemic stages. In order to evaluate the functional effects of ischemia on the spatial distribution pattern of BSP and MCG maps, relative differences in the amplitude of BSP and MCG signals between control and ischemic conditions were calculated during each segment duration of the cardiac excitation rhythm for variant ischemic cases, i.e. the amplitude difference between the control and ischemic cases divided by the amplitude of the control signal at each specific point. This is similar to the discriminant index [37], which has been suggested to indicate the capability of each sensor site to distinguish between patients and control [37, 38].

Results

Figure 7.2 shows the simulated ventricular action potentials of endocardium (ENDO), mid-layer (MCELL) and epicardium (EPI) cells in the control and Phase A & B of ischemic conditions. It was shown that ischemia caused an elevation in the resting potential, reduced amplitude of AP and shortened action potential durations (APDs). These effects became more pronounced with time course of ischemia. These simulation results well matched to experimental [29, 30] and previous simulation studies [31, 21].

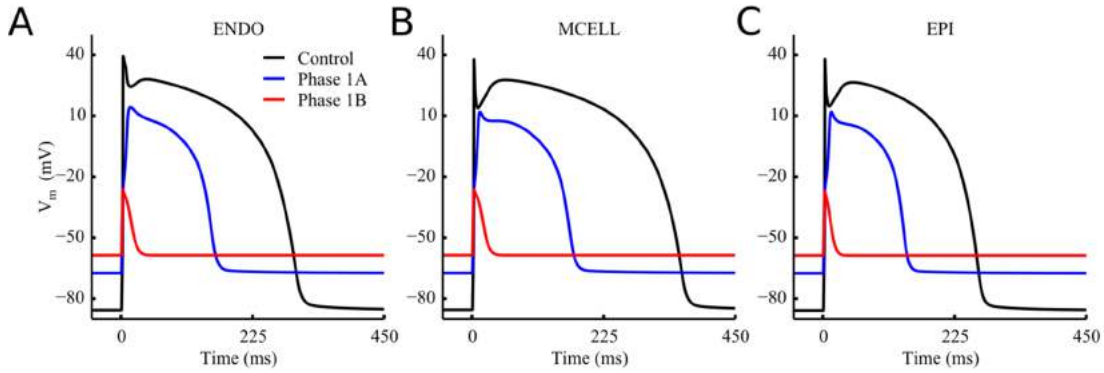

Figure 7.2: Simulated action potentials (APs) under control conditions (Black line), phase A (blue line) and phase B (red line) of ischemia. (A) Endocardium. (B) Myocardium cell. (C) Epicardium.

Effects of ischemia on ECG and MCG

First, we investigated the effects of ischemia on 12-lead ECGs, as well as MCGs computed from the leads close to the chest leads for conventional 12-lead ECGs (i.e., leads D3 to D6 in Figure 7.1). The features of the time courses of the computed 12-lead ECGs during the control condition were within the range of previous experimental studies [1, 3, 39, 40] and also matched to experimental recordings (Figure 7.3-ECG). The simulated MCG time courses from leads D3 to D6 also matched to the experimental data (Figure 7.3-MCG). This validated the developed models and algorithms for simulating ECGs and MCGs.

With the validated model, further simulations were performed to investigate the effects of ischemia on the 12-leads ECG and MCGs. Results are shown in Figure 7.4. It was shown that the presence of ischemic condition (Phase A with variant ischemic locations) resulted in noticeable changes to the profiles of the 12-lead ECGs as compared to control (normal) condition (Figure 7.3ECG). In simulations, ischemia primarily affected the ST-segment (depending on the ischemic location, it either elevated or depressed the ST-segment) and T-wave amplitude (dependent on the ischemic location, it either increased or decreased the amplitude of the T-wave), and also had a smaller effect on the QRS complex. These simulation results were consistent with previous studies [40, 37, 30, 3]. Similar changes were also observed in the simulated MCGs (Figure 7.3-MCG), which were consistent with previous studies [12, 13, 15, 16].

Figure 7.4 shows the simulated 36-lead ECG and MCG under control and ischemic conditions. In the control condition, the simulated QRS complex and T-waves of the 36-lead ECG and MCG showed strong agreement to experimental data [18] (Figure 7.4) for all of the 36-leads, which validated the multi-scale models of the ventricle.

In both experimental and simulation data, the polarity of the QRS and T-wave of ECG and MCG signals showed similar spatial distribution patterns. For ECG, the QRS complex was mainly positive in the left-inferior part of the body, negative in the superior right part of the body, and biphasic or flat in intermediary locations (Figure 7.4-ECG). The T-wave was positive in most of the leads, except for the superior right part of the body. In contrast, for MCG, the polarity of the QRS complex was mainly positive in the right-inferior part of the body, negative in the superior left part of the body, and biphasic or flat in intermediary locations (Figure 7.4-MCG). The T-wave was positive in most of the leads, except for the superior left part of the body. These simulated spatial distributions patterns of QRS and T-wave of ECG and MCG matched to experimental data. The slight differences in the traces

between simulated ECG and MCG signals might reflect the difference between the two measurement methods.

The effects of ischemia in the 36-leads are also shown in Figure 7.4. As the 36-leads covered much wider area of the body surface compared to the 12-lead system, simulation data showed more pronounced changes in BSP and MCG signals in some specific regions of the body compared to the 12-lead system. For example, T-wave inversion was seen in some of the 36-leads of both ECG (lead B5) and MCG (lead C4), which was not seen in any of the 12-lead ECGs. Therefore, an analysis of sensitivity regions through the calculation of the relative differences was performed in both ECG and MCG data to quantify the regions with more pronounced changes in signal due to ischemia conditions.

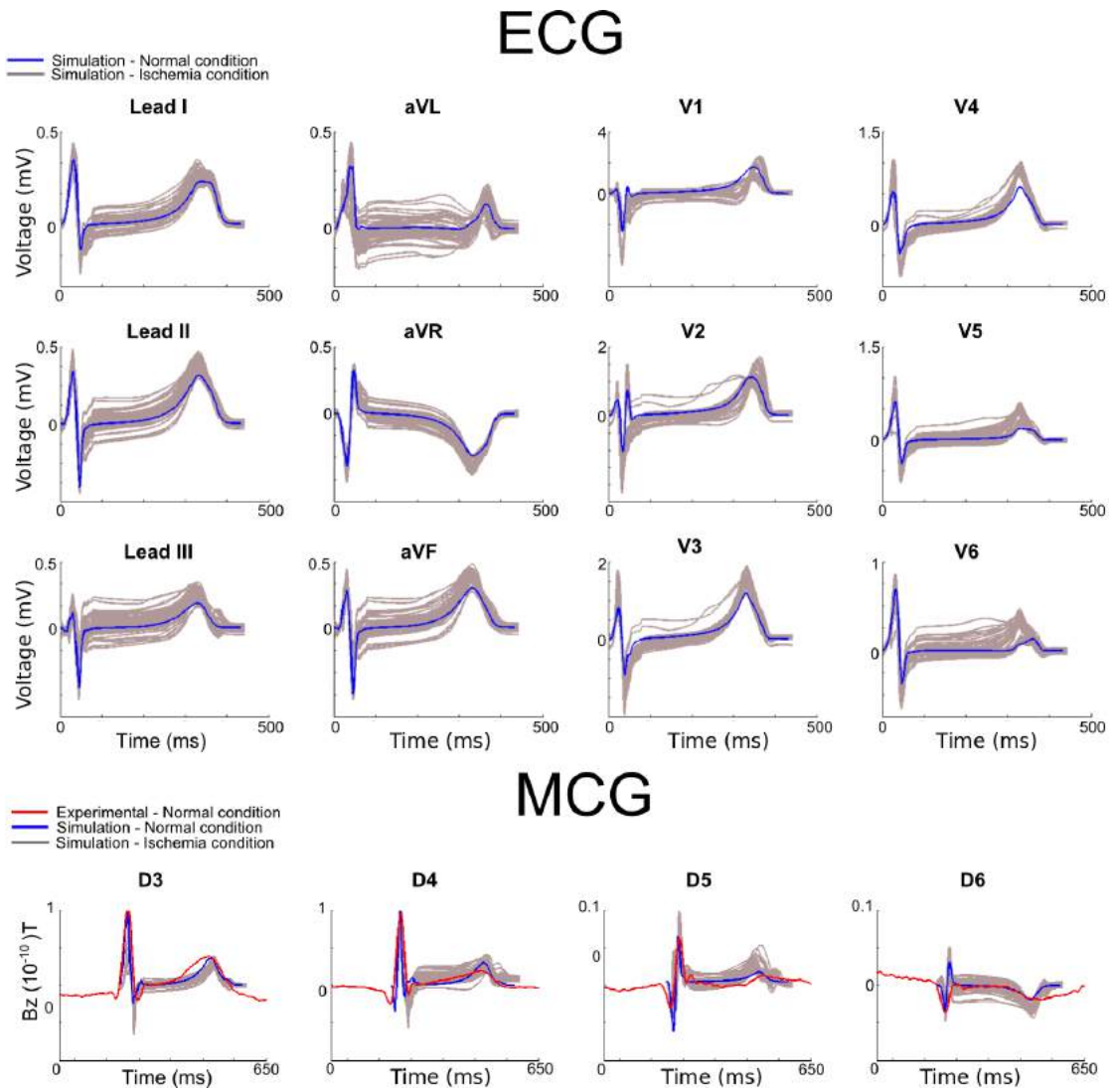

Figure 7.3: Simulated time courses of 12-lead ECGs (superior), MCGs (from leads D3 to D6; bottom) under control (blue line) and ischemic conditions (Phase A with variant locations; gray lines). Experimental data (red) was included in the MCG for comparison purposes. Simulated 12-lead ECG and MCG were normalized to the maximum amplitude of each lead, and superimposed over normalized experimental recordings from a healthy subject.

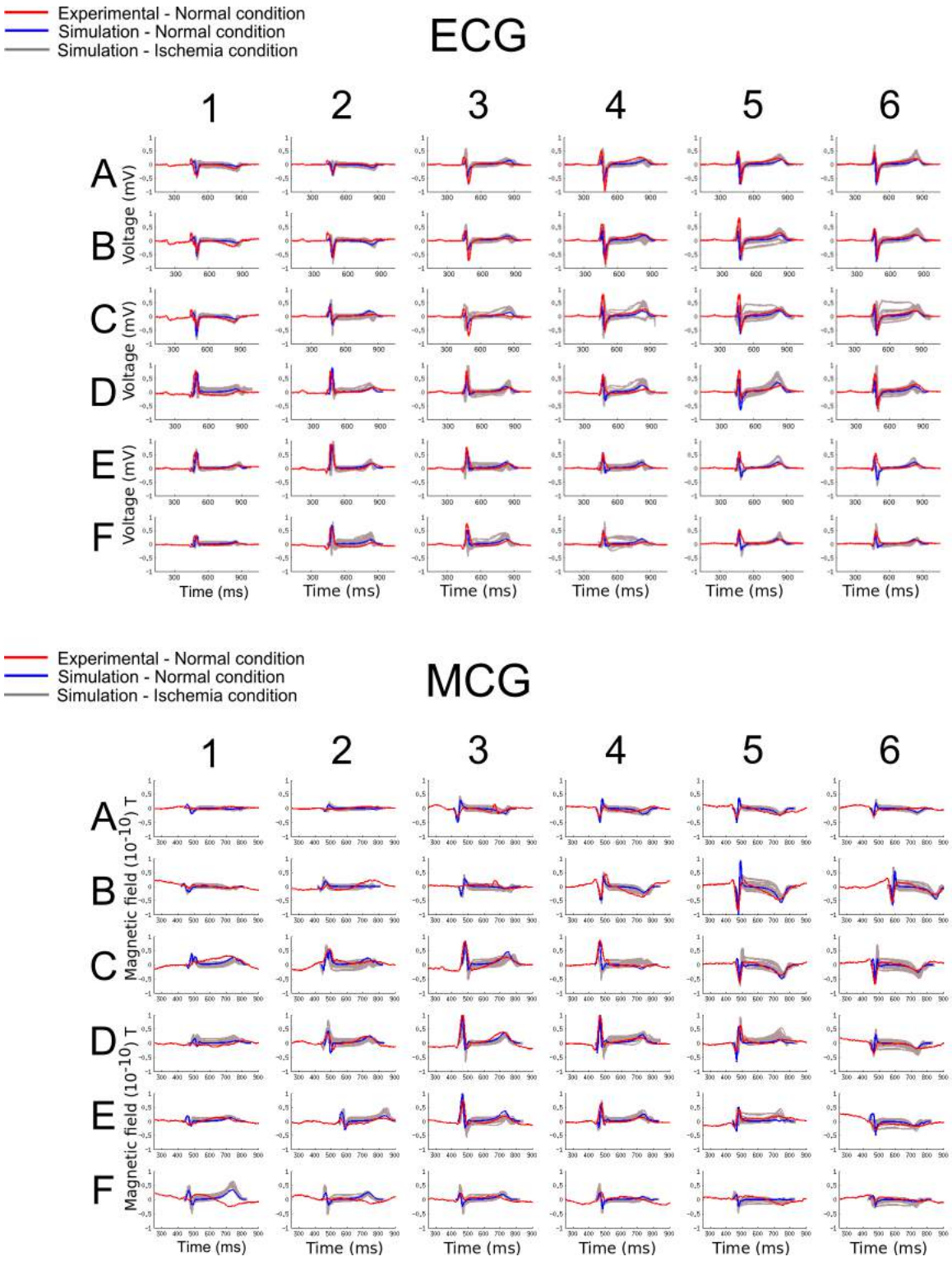

Figure 7.4: Simulated 36-lead ECG (top panels) and MCG (bottom panels) in control (blue line) and ischemic (grey line) conditions. In control conditions, ECG and MCG were normalized and superimposed with experimental data [18] (red line), simulated data (blue line) during control and ischemic conditions (Phase A with variant locations; grey lines). The numbers and letters represent the electrode/sensor position (Figure 7.1B-ii). Simulated 36-lead ECG and MCG were normalized to the maximum amplitude of each lead, and superimposed over normalized experimental recordings from a healthy subject.

Sensitivity of ECG and MCG to ischemia.

To analyse the sensitivity of ECG and MCG to ischemia conditions (Phase A & B with variant locations), averaged relative differences were calculated for the 12-lead ECG, 36-lead ECG and 36-lead MCG, for the QRS complex (during the time period of 410-460 ms), ST-segment (550-650ms) and T-wave (700-400ms) time intervals. Results are shown in Figure 7.5.

For the QRS complex, ischemia induced small differences between ECG and MCG signals. The computed relative differences between ischemia and control conditions were similar for both ECG and MCG, which were 21% for 12-lead ECG, 25% for 36-lead ECG and 29% for the 36-lead MCG respectively (Figure 7.5, QRS complex).

For the ST-segment, ischemia induced marked changes in both ECG and MCG as compared to control conditions. However, the MCG showed greater sensitivity to ischemia than the ECG. The computed relative differences were 29% for the 12-lead ECG, 40% for 36-lead ECG and 50% for the 36-lead MCG respectively (Figure 7.5, ST-segment).

For the T-wave, the presence of ischemia produced greater changes in ECG than MCG. The computed relative differences between control and ischemia were 28% for 12-lead ECG, 37% for 36-lead ECG and 32% for 36-lead MCG respectively (Figure 7.5, T-wave).

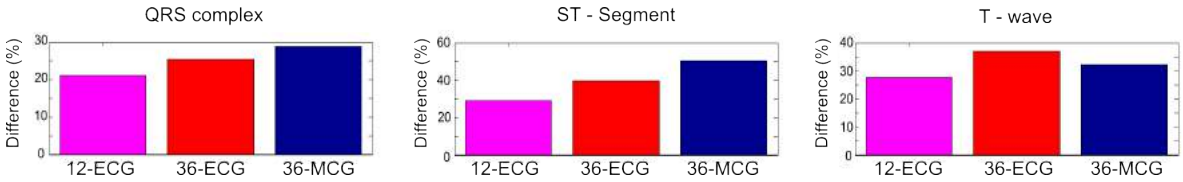

Figure 7.5: Averaged relative differences of the QRS complex, ST- segment and T-wave of the 12-lead ECG (pink bar), 36-lead ECG (red bar) and MCG (blue bar) between the ischemic (Phase A & B with variant locations) and control condition.

Regional differences in the sensitivity of ECG and MCG to ischemia.

Next, possible regional differences in the sensitivity of ECG and MCG to ischemia were investigated. As the 36-lead ECG and MCG provide more spatial information of the torso, analysis was conducted in the 36-lead data. Results are presented in

Figure 7.6, showing computed relative differences of ECG and MCG between control and ischemia (during both phases) for each of the 36 leads during the ST-segment and T-wave time intervals. It was shown that the relative difference for both of the ECG and MCG was region-dependent, and was different between the ST-segment and T-wave period. Such differences in the regional dependence between the ST-segment and the T-wave period may account for the discrepancy shown by the averaged relative differences between MCG and ECG regarding their sensitivity to ischemic QRS and T-wave.

Figure 7.7 shows quantified regional relative differences of ECG and MCG for the QRS complex, ST-segment and T-wave in Phase A & B ischemic conditions.

The spatial distribution of the relative difference map of the BSP and MCG between ischemia and control did not show great changes between the two ischemia phases (Figure 7.7). However, the map of the ST-segment differences showed pronounced changes as compared to control (Figure 7.7 ST-segment), with more pronounced changes in the MCG maps.

Further investigations were performed to study the effects of variant ischemic locations on profiles of ECG and MCGs. Ischemic region in four sub-sections of the ventricles were considered: the superior left ventricle, inferior left ventricle, superior right ventricle and inferior right ventricle. For each case the relative difference between control and ischemia was computed.

Figure 7.8 plots the relative difference map of ECG and MCG signals, showing a correlation between the ischemic region of the heart and the torso region with maximal relative changes in the ST-segment of MCG, but not ECG. Our simulation data showed that an ischemic region located in the superior left ventricle produced a maximal relative change of MCG signals in the superior part of the torso (Figure 7.8A). An ischemic region located in the inferior part of the left ventricle produced a maximal change of MCG signals in the superior and inferior right of the torso (Figure 7.8B). Similarly, an ischemic region located in the superior part of the right ventricle produced a maximal relative change of MCG signals in the superior-left part of the torso (Figure 7.8C), and an ischemic region in the inferior right ventricle produced a maximal relative change of MCG signals in the left-mid part of the torso (Figure 7.8D). However, there was no such correlation observed from the ECG map.

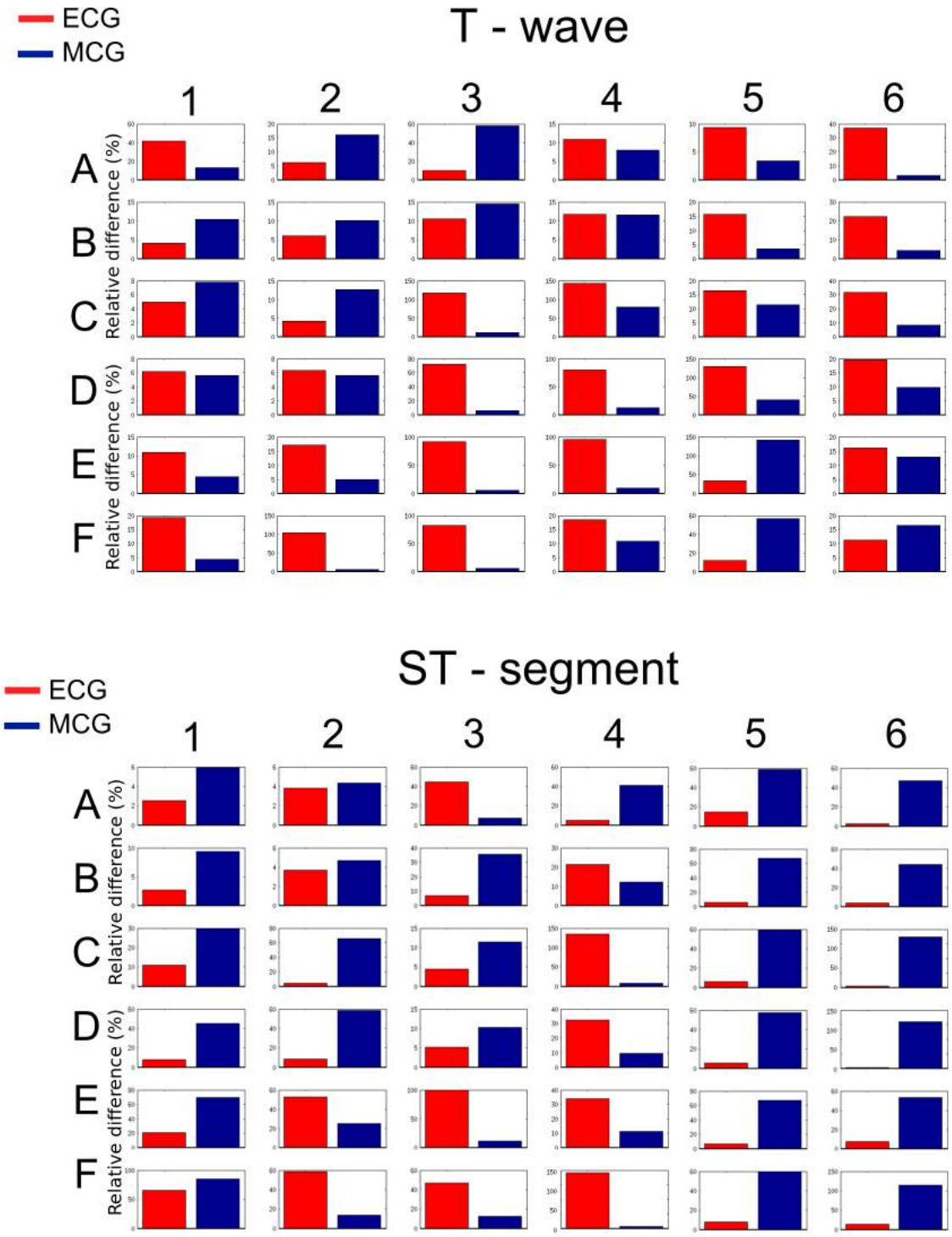

Figure 7.6: Relative differences for each of the 36 leads ECG (red) and MCG (blue) with control conditions for the QRS complex, ST-segment, and T-wave.

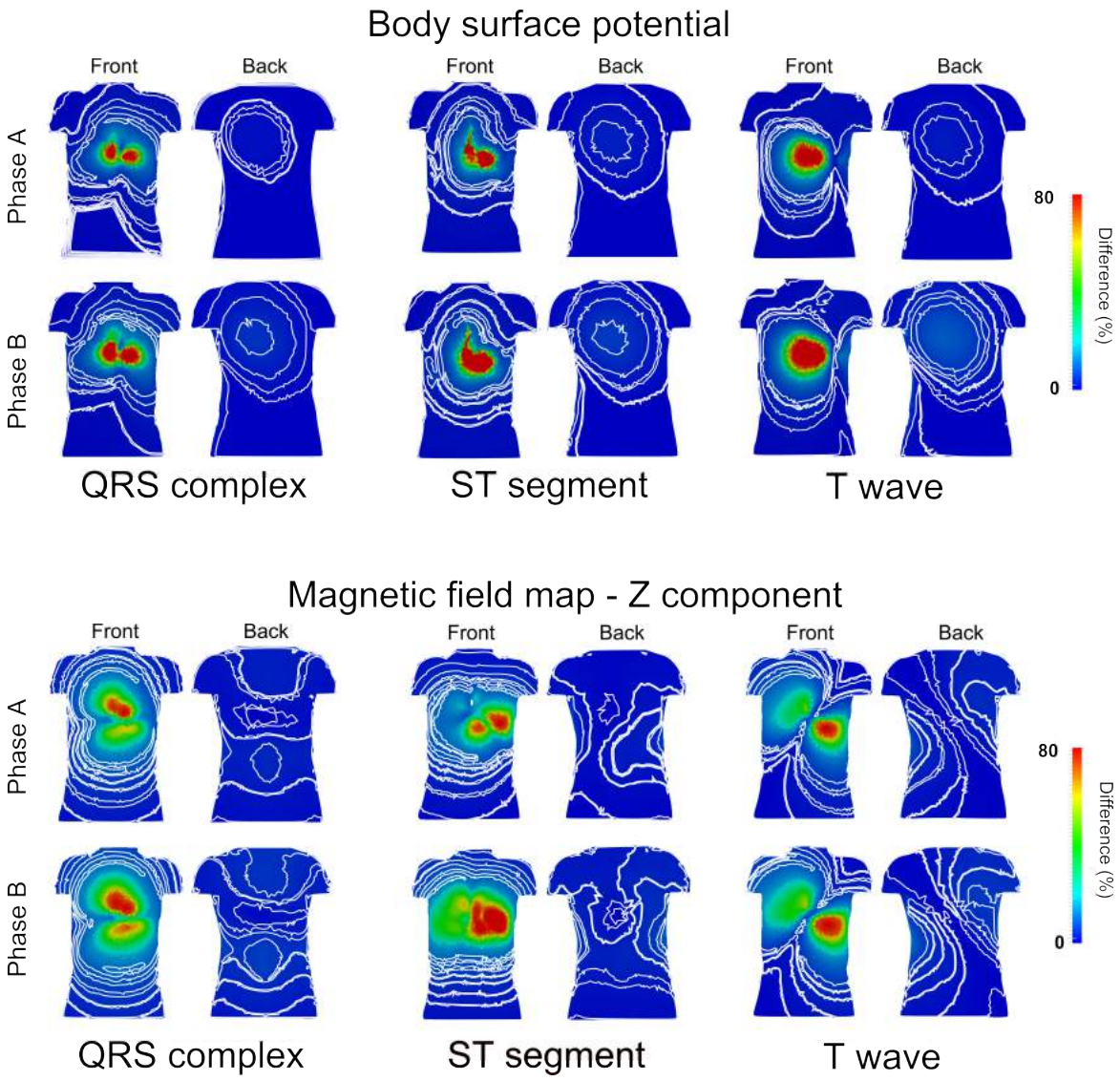

Figure 7.7: Maps of major differences of BSP (top panels) and MCG (bottom panels) between ischemia and control conditions for the QRS complex, ST-segment, and T-wave, during both early (Phase A) and late (Phase B) ischemic phases. The contour lines correspond to small variations in the small difference range, in both frontal (front) and posterior (back) part of the torso.

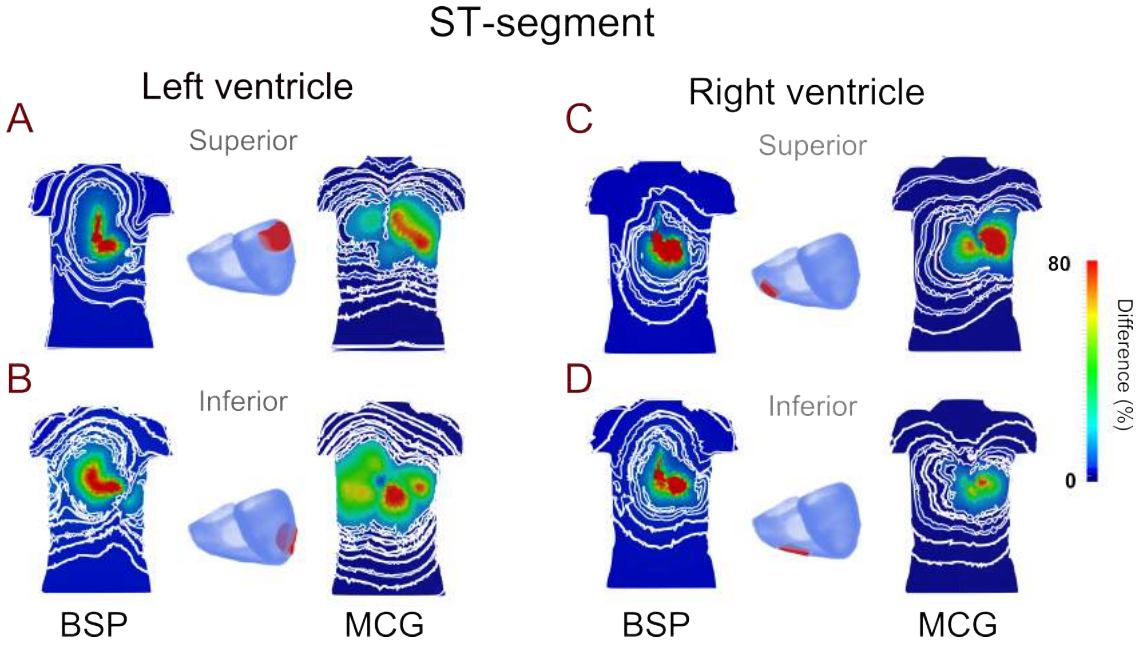

Figure 7.8: Maps of the major difference of BSP and MCG between control and varied localized ischemic condition during the ST-segment. Ischemic region was considered in four different ventricular locations (labeled in red): Superior left ventricle (A), inferior left ventricle (B), superior right ventricle (C), inferior right ventricle (D). The contour lines correspond to small variations in the small difference range.

Discussion

Major contribution

It remains controversial if MCG signals can provide useful extra information which increases diagnose and characterization of cardiac diseases, mainly the one asymptomatic to the ECG [23, 31, 41]. Previous studies have shown that both ECG and MCG can produce similar results during specific silent ischemia [41], while other studies have suggested that circular vortex currents can be detected by MCG but not by ECG [16, 42, 43]. Moreover, the ischemic injury might increase the tangential current flow through the ventricular tissue, producing the repolarization abnormalities, which are detected differently by MCG and ECG [36, 42, 43]. In this study, by using a biophysically detailed computer model of human ventricles-torso, we investigated the different features of 12-, 36-lead ECG and MCG, BSP and MCG maps during normal and variant ischemic conditions. We also investigated the regional dependence of the measured relative difference and how the area with maximal relative difference on the body surface varied due to altered stage and location of the ischemic region.

Our major findings are: (i) both the 36-lead ECG and MCG showed greater averaged relative difference in the QRS complex, T-wave and ST-segment than the 12-lead ECG, indicating the advantages of implementing multi-lead ECG/MCG systems than the conventional 12-lead ECG in diagnosing the ischemic condition; (ii) ECG and MCG showed a different sensitivity to ischemia in producing changes in the T-wave and ST-segment. Our results showed that the 36-leads ECG was more sensitive than the 36-leads MCG in detecting changes in the T-wave by producing a greater averaged relative difference in the T-wave. However, for detecting changes in the ST-segment the MCG showed greater sensitivity by producing a greater relative difference; (iii) both ECG and MCG showed regional-dependent changes to ischemic condition on the body surface of the torso, but with MCG showing a stronger correlation between ischemic region in the heart and the maximal difference map on the body surface. Such difference in the sensitivity between ECG and MCG may be due to the different effects produced by the ischemia to the AP (an elevation in the resting potential, reduced amplitude of AP and shorter APDs), which mainly affects the repolarization propagation that is associated with ST-segment and T-wave. Such a cellular effect maps to electrical wave propagation, producing different tangential and normal currents leading to altered electrical and magnetic fields; and (iv) the correlation between ischemic region in the heart and the maximal relative differences of MCG during QRS complex, ST-segment and T-wave provides a theoretical basis for non-invasively diagnosing ischemic region.

Limitations

The limitations of used cellular models for human ventricular action potentials have been discussed in previous studies [20, 21], and such limitations were inherited in the present study. In addition, the torso model lacks considerations of some tissue types or organs (such as muscles, fat tissue) that may affect the amplitude of simulated surface potentials. Nevertheless, the absence of those tissues does not have a significant effect on the polarity of the ventricular-waves [33, 44], and produces less effect in the MCG measurements [42, 12].

In the present study, by comparing the regional-dependence of the averaged relative difference map between control and ischemic ECG/MCG signals, we were able to show a strong correlation between the ischemic region in the heart and maximal relative difference in the MCG. However, it should be pointed out that for both experimentally recorded and simulated MCG its amplitude decreases significantly in the areas far from the heart position, i.e. back of the torso or close to the limbs. This causes smaller changes in the MCG as compared to ECG in these areas of the body, which may limit the accuracy to detect ischemic region by using the whole body MCG map. A possible solution to overcome such technique limitations is to use combined high spatial resolution BSP and MCG maps, which provide a feasible tool to diagnose cardiac ischemic in clinical environments.

Conclusion

Computer modelling provides a useful tool to compare the electric and magnetic field produced by the electrical activity of the heart during normal and ischemic conditions, which is a challenging task in clinical settings. Using biophysically detailed models of human ventricles and torso, we have compared the sensitivity regions of the ECG and MCG in response to ischemic conditions. Our results suggest that the 12-lead ECG is less effective to provide diagnosis of the ischemia, whereas the 36-lead ECG and in particular MCG offer advantages in the identification of ischemic conditions. By comparing the relative differences in the BSP and MCG maps, our results shows that MCG has greater sensitivity than ECG in response to ischemia, which may provide an alternative method for the diagnosis of ischemia.

Supporting Information

S1 Table

Table 1 Summary of ischemia induced changes to the electrophysiological properties of the human ventricles.

Acknowledgments

CONACYT

Bibliography

[1] A. M. Katz, *Physiology of the Heart*. Lippincott Williams & Wilkins, 2010.

[2] N. J. Pagidipati and T. A. Gaziano, "Estimating deaths from cardiovascular disease: a review of global methodologies of mortality measurement," *Circulation*, vol. 127, no. 6, pp. 749–756, 2013.

[3] C. W. Hamm, J.-P. Bassand, S. Agewall, J. Bax, E. Boersma, H. Bueno, P. Caso, D. Dudek, S. Gielen, K. Huber, *et al.*, "Esc guidelines for the management of acute coronary syndromes in patients presenting without persistent st-segment elevation," *European heart journal*, vol. 32, no. 23, pp. 2999–3054, 2011.

[4] P. Taggart, P. M. Sutton, M. R. Boyett, H. Swanton, *et al.*, "Human ventricular action potential duration during short and long cycles rapid modulation by ischemia," *Circulation*, vol. 94, no. 10, pp. 2526–2534, 1996.

[5] A. Ghuran and A. Camm, "Ischaemic heart disease presenting as arrhythmias," *British medical bulletin*, vol. 59, no. 1, pp. 193–210, 2001.

[6] J. L. Cohen, K. L. Chan, W. Jaarsma, D. S. Bach, D. W. Muller, M. R. Starling, and W. F. Armstrong, "Arbutamine echocardiography: efficacy and safety of a new pharmacologic stress agent to induce myocardial ischemia and detect coronary artery disease," *Journal of the American College of Cardiology*, vol. 26, no. 5, pp. 1168–1175, 1995.

[7] P. Klootwijk, S. Meij, G. v. Es, E. Müller, V. Umans, T. Lenderink, and M. Simoons, "Comparison of usefulness of computer assisted continuous 48-h 3-lead with 12-lead ecg ischaemia monitoring for detection and quantitation of ischaemia in patients with unstable angina," *European heart journal*, vol. 18, no. 6, pp. 931–940, 1997.

[8] D. Stilli, E. Musso, E. Macchi, C. Manca, L. Dei Cas, P. Vasini, and B. Taccardi, "Body surface potential mapping in ischemic patients with normal resting ecg.," *The Canadian journal of cardiology*, pp. 107A–112A, 1986.

[9] A. Kapetanopoulos, A. W. Ahlberg, C. C. Taub, D. M. Katten, and G. V. Heller, "Regional wall-motion abnormalities on post-stress electrocardiographic-gated technetium-99m sestamibi single-photon emission computed tomography imaging predict cardiac events," *Journal of Nuclear Cardiology*, vol. 14, no. 6, pp. 810–817, 2007.

[10] C. Hamilton-Craig, W. E. Strugnell, O. C. Raffel, I. Porto, D. L. Walters, and R. E. Slaughter, "Ct angiography with cardiac mri: non-invasive functional and anatomical assessment for the etiology in newly diagnosed heart failure," *The international journal of cardiovascular imaging*, vol. 28, no. 5, pp. 1111–1122, 2012.

[11] K. C. Siontis and P. Chareonthaitawee, "Prognostic value of positron emission tomography myocardial perfusion imaging beyond traditional cardiovascular risk factors: Systematic review and meta-analysis," *IJC Heart & Vasculature*, vol. 6, pp. 54–59, 2015.

[12] B. Hailer, I. Chaikovsky, S. Auth Eisernitz, H. Schäfer, and P. Van Leeuwen, "The value of magnetocardiography in patients with and without relevant stenoses of the coronary arteries using an unshielded system," *Pacing and clinical electrophysiology*, vol. 28, no. 1, pp. 8–16, 2005.

[13] K. Tolstrup, B. E. Madsen, J. A. Ruiz, S. D. Greenwood, J. Camacho, R. J. Siegel, H. C. Gertzen, J.-W. Park, and P. A. Smars, "Non-invasive resting magnetocardiographic imaging for the rapid detection of ischemia in subjects presenting with chest pain," *Cardiology*, vol. 106, no. 4, pp. 270–276, 2006.

[14] T. M. Helle-Valle, W.-C. Yu, V. R. Fernandes, B. D. Rosen, and J. A. Lima, "Usefulness of radial strain mapping by multidetector computer tomography to quantify regional myocardial function in patients with healed myocardial infarction," *The American journal of cardiology*, vol. 106, no. 4, pp. 483–491, 2010.

[15] O. Kittnar, J. Slavicek, M. Vavrova, M. Barna, A. Dohnalová, A. Málková, M. Aschermann, J. Humhal, J. Hradec, and J. Král, "Repolarization pattern of body surface potential maps (bspm) in coronary artery disease.," *Physiological research/Academia Scientiarum Bohemoslovaca*, vol. 42, no. 2, pp. 123–130, 1992.

[16] J. S. Kwong, B. Leithäuser, J.-W. Park, and C.-M. Yu, "Diagnostic value of magnetocardiography in coronary artery disease and cardiac arrhythmias: A review of clinical data," *International journal of cardiology*, vol. 167, no. 5, pp. 1835–1842, 2013.

[17] D. B. Geselowitz, "Electric and magnetic field of the heart," *Annual review of biophysics and bioengineering*, vol. 2, no. 1, pp. 37–64, 1973.

[18] C. Zhang, F. Tang, P. Ma, and Z. Gan, "A simplified htc rf squid to analyze the human cardiac magnetic field," *AIP Advances*, vol. 4, no. 12, p. 127131, 2014.

[19] D. Robbes, "Highly sensitive magnetometersa review," *Sensors and Actuators A: Physical*, vol. 129, no. 1, pp. 86–93, 2006.

[20] I. Adeniran, M. J. McPate, H. J. Witchel, J. C. Hancox, and H. Zhang, "Increased vulnerability of human ventricle to re-entrant excitation in herg-linked variant 1 short qt syndrome," *PLoS Comput Biol*, vol. 7, no. 12, pp. e1002313–e1002313, 2011.

[21] K. Ten Tusscher, D. Noble, P. Noble, and A. Panfilov, "A model for human ventricular tissue," *American Journal of Physiology-Heart and Circulatory Physiology*, vol. 286, no. 4, pp. H1573–H1589, 2004.

[22] T. O'Hara, L. Virág, A. Varró, and Y. Rudy, "Simulation of the undiseased human cardiac ventricular action potential: model formulation and experimental validation," *PLoS Comput Biol*, vol. 7, no. 5, p. e1002061, 2011.

[23] P. Taggart, P. M. Sutton, T. Opthof, R. Coronel, R. Trimlett, W. Pugsley, and P. Kallis, "Inhomogeneous transmural conduction during early ischaemia in patients with coronary artery disease," *Journal of molecular and cellular cardiology*, vol. 32, no. 4, pp. 621–630, 2000.

[24] D. U. Keller, D. L. Weiss, O. Dössel, and G. Seemann, "Influence of heterogeneities on the genesis of the t-wave: A computational evaluation," *Biomedical Engineering, IEEE Transactions on*, vol. 59, no. 2, pp. 311–322, 2012.

[25] A. V. Glukhov, V. V. Fedorov, Q. Lou, V. K. Ravikumar, P. W. Kalish, R. B. Schuessler, N. Moazami, and I. R. Efimov, "Transmural dispersion of repolarization in failing and nonfailing human ventricle," *Circulation research*, vol. 106, no. 5, pp. 981–991, 2010.

[26] M. Perazzolo Marra, A. Zorzi, F. Corbetti, M. De Lazzari, F. Migliore, F. Tona, G. Tarantini, S. Iliceto, and D. Corrado, "Apico-basal gradient of left ventricular

myocardial edema underlies transient t-wave inversion and qt interval prolongation (wellens' ecg pattern) in tako-tsubo cardiomyopathy," *Circulation*, vol. 126, no. 21 Supplement, p. A17302, 2012.

[27] D. Keller, R. Kalayciyan, O. Dössel, and G. Seemann, "Fast creation of endocardial stimulation profiles for the realistic simulation of body surface ecgs," in *World Congress on Medical Physics and Biomedical Engineering, September 7-12, 2009, Munich, Germany*, pp. 145–148, Springer, 2009.

[28] X. Jie, B. Rodríguez, J. R. de Groot, R. Coronel, and N. Trayanova, "Reentry in survived subepicardium coupled to depolarized and inexcitable midmyocardium: insights into arrhythmogenesis in ischemia phase 1b," *Heart Rhythm*, vol. 5, no. 7, pp. 1036–1044, 2008.

[29] E. Kaplinsky, S. Ogawa, C. W. Balke, and L. S. Dreifus, "Two periods of early ventricular arrhythmia in the canine acute myocardial infarction model.," *Circulation*, vol. 60, no. 2, pp. 397–403, 1979.

[30] X. Jie, V. Gurev, and N. Trayanova, "Mechanisms of mechanically induced spontaneous arrhythmias in acute regional ischemia," *Circulation research*, vol. 106, no. 1, pp. 185–192, 2010.

[31] I. V. Kazbanov, R. H. Clayton, M. P. Nash, C. P. Bradley, D. J. Paterson, M. P. Hayward, P. Taggart, and A. V. Panfilov, "Effect of global cardiac ischemia on human ventricular fibrillation: insights from a multi-scale mechanistic model of the human heart," *PLOS Comput Biol*, vol. 10, no. 11, p. e1003891, 2014.

[32] J. M. Ferrero, B. Trenor, and L. Romero, "Multiscale computational analysis of the bioelectric consequences of myocardial ischaemia and infarction," *Europace*, vol. 16, no. 3, pp. 405–415, 2014.

[33] E. A. P. Alday, M. A. Colman, P. Langley, T. D. Butters, J. Higham, A. J. Workman, J. C. Hancox, and H. Zhang, "A new algorithm to diagnose atrial ectopic origin from multi lead ecg systems-insights from 3D virtual human atria and torso," *PLoS computational biology*, vol. 11, no. 1, 2015.

[34] E. A. Perez Alday, M. A. Colman, T. D. Butters, J. Higham, D. Giacopelli, P. Langley, and H. Zhang, "Diagnosis of atrial ectopic origin from the body surface ecg: Insights from 3D virtual human atria and torso," in *Computing in Cardiology Conference (CinC), 2013*, pp. 1075–1078, IEEE, 2013.

[35] J. Nenonen, C. J. Purcell, B. M. Horacek, G. Stroink, and T. Katila, "Magnetocardiographic functional localization using a current dipole in a realistic torso,"

Biomedical Engineering, IEEE Transactions on, vol. 38, no. 7, pp. 658–664, 1991.

[36] D. B. Geselowitz, "On the magnetic field generated outside an inhomogeneous volume conductor by internal current sources," *Magnetics, IEEE Transactions on*, vol. 6, no. 2, pp. 346–347, 1970.

[37] F. Kornreich, T. J. Montague, and P. M. Rautaharju, "Body surface potential mapping of st segment changes in acute myocardial infarction. implications for ecg enrollment criteria for thrombolytic therapy.," *Circulation*, vol. 87, no. 3, pp. 773–782, 1993.

[38] H. Hänninen, P. Takala, M. Mäkijärvi, J. Montonen, P. Korhonen, L. Oikarinen, K. Simelius, J. Nenonen, T. Katila, and L. Toivonen, "Recording locations in multichannel magnetocardiography and body surface potential mapping sensitive for regional exercise-induced myocardial ischemia," *Basic research in cardiology*, vol. 96, no. 4, pp. 405–414, 2001.

[39] B. Acar, G. Yi, K. Hnatkova, and M. Malik, "Spatial, temporal and wavefront direction characteristics of 12-lead t-wave morphology," *Medical & biological engineering & computing*, vol. 37, no. 5, pp. 574–584, 1999.

[40] J. R. Hampton, *The ECG made easy*. Elsevier Health Sciences, 2013.

[41] D. Potyagaylo, G. Seemann, W. Schulze, and O. Doessel, "Magnetocardiography did not uncover electrically silent ischemia in an in-silico study case," in *Computing in Cardiology Conference (CinC), 2015*, pp. 1145–1148, IEEE, 2015.

[42] J. Lant, G. Stroink, B. ten Voorde, B. M. Horacek, and T. J. Montague, "Complementary nature of electrocardiographic and magnetocardiographic data in patients with ischemic heart disease," *Journal of electrocardiology*, vol. 23, no. 4, pp. 315–322, 1990.

[43] V. Mäntynen, T. Konttila, and M. Stenroos, "Investigations of sensitivity and resolution of ecg and mcg in a realistically shaped thorax model," *Physics in medicine and biology*, vol. 59, no. 23, p. 7141, 2014.

[44] D. U. Keller, F. M. Weber, G. Seemann, and O. Doessel, "Ranking the influence of tissue conductivities on forward-calculated ecgs," *Biomedical Engineering, IEEE Transactions on*, vol. 57, no. 7, pp. 1568–1576, 2010.

Chapter 8

Fourth Manuscript

Reconstruction of atrial ectopic focal and re-entrant excitations from body surface potentials. Insights from 3D virtual human atria and torso.

Erick A. Perez Alday[1,], Michael A. Colman[2], Henggui Zhang[1]

1 Biological Physics Group, Department of Physics and Astronomy, University of Manchester, Manchester, United Kingdom
1 Theoretical Physics Division, Department of Physics and Astronomy, University of Manchester, Manchester, United Kingdom

Reconstruction of atrial ectopic focal and re-entrant excitations from body surface potentials. Insights from 3D virtual human atria and torso.

Erick A. Perez Alday[1], Michael A. Colman[2], Henggui Zhang[1]

1 Biological Physics Group, Department of Physics and Astronomy, University of Manchester, Manchester, United Kingdom
1 Theoretical Physics Division, Department of Physics and Astronomy, University of Manchester, Manchester, United Kingdom

Abstract

Non-invasive electrocardiographic imaging has been seen as a painless and ideally economic method to map the electrical functions of the heart, showing advantages over prevailing invasive imagining methods, which are usually expensive and/or provide the potential of complications. However, it is still a great challenge to obtain accurate reconstruction of cardiac electrical activity from recorded body surface potentials due to the ill-posed nature of the cardiac inverse-problem. Though some advances have been made in solving the ventricular inverse-problem, few studies have been conducted for the atria, which have dramatic differences to the ventricles in the anatomical structures (such as tissue size and wall thickness) and electrophysiological properties (such as the morphology of the action potentials (AP)). It is unclear either how the spatial resolution of electrodes on the body surface and rapid excitation rates of atrial activation during atrial fibrillation (AF) affect the accuracy of the atrial inverse-problem.

In this study, we used a biophysically detailed model of the human atria and torso to investigate the reliability of the three different Tikhonov regularization methods and variant electrode spatial resolutions (corresponding to 64-, 256- and 512-lead ECG vest) in reconstructing both simple and rapid and irregular epicardial activation patterns, in the absence and presence of electrophysiological heterogeneity and AF-induced electrical remodelling.

It was shown that the solution of the atrial inverse-problem was dependent on the spatial resolution of electrodes on the body surface, with 512-lead producing the best and most reliable solution; however, in some specific cases 256-lead also produced a reliable solution. Different regularization methods produced the most reliable reconstructions in different conditions, being particularly influenced by excitation rate

and AP morphology.

In conclusion, an efficient method was determined to reconstruct atrial epi-cardiac electrical excitation patterns non-invasively from a multi-lead ECG system, which may provide a powerful method to diagnose AF. Novel insight is provided into the effectiveness of different methods under varying underlying atrial electrophysiology and activation patterns.

Introduction

The electrocardiographic imaging, based on the cardiac inverse problem solution [1], provides a promising method for non-invasive diagnosis of cardiac arrhythmias. The approach attempts to reconstruct the epicardial electrical potentials and the activation time isochrones from the body surface potentials (BSP) by solving the inverse problem with the Tikhonov regularization method [1, 2, 3]. However, due to the ill-posed nature of the problem, some prior empiric information is required to provide constraints in order to achieve a reliable solution [4, 2]. Therefore, due to the limited number (i.e., the spatial resolution) of electrodes on the body surface and unavoidable noise of the measured signals, it is still a challenge to obtain a reliable and accurate solution of the problem.

Previous studies on the ventricular inverse-problem have shown that the number of electrodes on the body surface has dramatic effects on the solution [5, 6, 7]. For achieving a reliable reconstruction of the electrical activity on the ventricular epicardial surface, a minimal number of electrodes was required [8, 9, 10, 4]. As few studies have been conducted to investigate the atrial inverse-problem [3, 11, 12], it is unclear if the findings in ventricular inverse-problem are applicable to the atria-inverse problem, given the dramatic differences in their electrophysiology and anatomical structures [13].

However, there is a pressing need to develop new non-invasive methods to improve the diagnosis of atrial fibrillation (AF), which is the most common cardiac arrhythmia causing an increased risk of morbidity and mortality [14, 15]. Notably, AF has a high incidence (> 2 % of population with ageing over 65), and such an incidence is expected to be increased due to the ageing society in the next decade [16].

The primary differences between the atria and ventricles chambers are in (i) the anatomic structures - the ventricles are almost twice the size and have thicker walls than the atria [13]; and (ii) electrophysiological heterogeneity - there are greater extents of electrophysiological heterogeneity in the atria than in the ven-

tricles [17, 18, 19]. The unique features in both of the anatomical and electrophysiological complexities in the atria may impose different requirements to the number of electrodes on the body surface to obtain a reliable reconstruction of atrial epicardial potentials as compared to the ventricles. In addition, the morphology of the atrial action potential (AP) varies regionally from almost a triangular to almost squared shape [20], which differs to the ventricular epicardial APs. As AF is normally associated with combinations of rapid focal pacing (spontaneous rapid firing of non-pacemaker cells) [21, 22], fibrillatory conduction of multiple wavelets [23], and re-entrant excitation scroll waves (i.e., rotors) [22, 23], its electrical activity is characterised by rapid and irregular activation of the atria, which may be confounded by complex anatomical structure. All of these may impose a challenge to obtain a reliable solution to the atrial inverse-problem.

Implementation of variant Tikhonov regularization methods may also affect the solution of the cardiac inverse-problem. However, it is still unclear how variant orders of the Tikhonov regularization method determine optimal solutions for cardiac excitation waves with different rates and dynamical behaviours during AF.

The aim of this study was to use a biophysically detailed model of the human atria and torso to investigate reliability of three different Tikhonov regularization methods using variant electrode spatial resolutions (corresponding to 64-, 256-, 512-lead ECG vest) in reconstructing atrial epicardial activation patterns, during slow and rapid ectopic pacing and rapid re-entry. Effects of the intrinsic electrophysiological heterogeneity of the atria and atrial fibrillation induced electrical remodelling were also considered.

Methods

Atrial-torso model

A previously validated biophysically detailed computational model of the three-dimensional (3D) human atria and torso [24, 25, 26] was used to simulate ectopic focal and re-entry conditions (Figure 8.1A). Details of the atrial-torso model (Figure 8.1C), which accounts for major anatomical structures (Figure 8.1D), electrophysiological heterogeneity in different the atrial regions [27] and the respective electrical conductivities within the internal body structures (Figure 8.1C) [24, 25], have been considered in the model following the same method as described in the previous publication [24]. The atrial model has been shown to be suitable for studying atrial

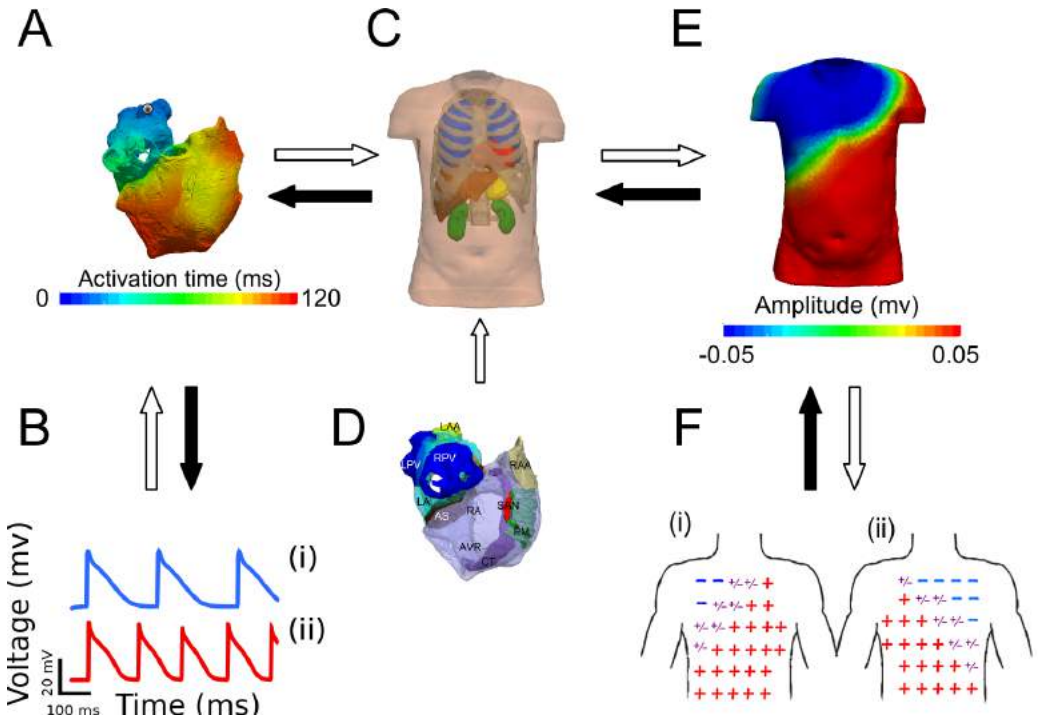

Figure 8.1: Scheme of solving atrial forward (open arrow) and inverse (solid arrow) problem pathway. (A) Atria activation pattern during ectopic activity; (B) Recorded epicardial potential in slow (i) and fast (ii) rates; (C) the integrated torso model; (D) trha atria model; (E) body surface potential (BSP); (F) Body surface polarity pattern reconstructed from a multi-lead ECG system.

arrhythmia mechanisms (Figure 8.1B) [20, 26]. The atria-torso has been validated and used to develop an algorithm to diagnose atrial ectopic origin from multi-lead ECG systems (Figure 8.1E) in our previous study [24]. Details of the atrial cell models and 3D simulation protocols can be found in Colman et al [20]; details of the torso model development, validation and simulation protocols can be found in Perez Alday et al [24].

Simulating atrial rapid ectopic foci and re-entry

Atrial ectopic foci and re-entry were initiated in different regions of the atria (Figure 8.2Ai-ii) following the same protocols that have been described previously [20, 24]. In order to allow rapid excitation waves with rates at frequencies typical of atrial fibrillation, atrial tachycardial and atrial flutter (i.e. 2.5-8 HZ [20, 28]) (Figure 8.2Aiii) to be sustained in the atrial model, parameters of the Colman et al. model of single human atrial myocytes were modified to incorporate experimentally observed AF-induced electrical remodelling of ion channels [20], which resulted in a reduction of the AP duration (APD) (Figure 8.2B). This reduction modified the morphology of

AP, which, in some cases, changed from a squared AP (Figure 8.2Bi-RAA) to triangular AP (Figure 8.2Bii-RAA). To simulate ectopic focal activity, a sequence of external supra-threshold electrical pulses (with amplitude of 2nA and duration of 2-3ms) was applied to various locations across different regions of the atria (Figure 8.2Ai). Re-entrant excitation waves were initiated by a phase distribution method [29, 30]. Although this is an artificial method for initiating re-entrant excitation, it allows the location of the centre of the rotor wave to be easily controlled in a specific location (Figure 8.2Aii).

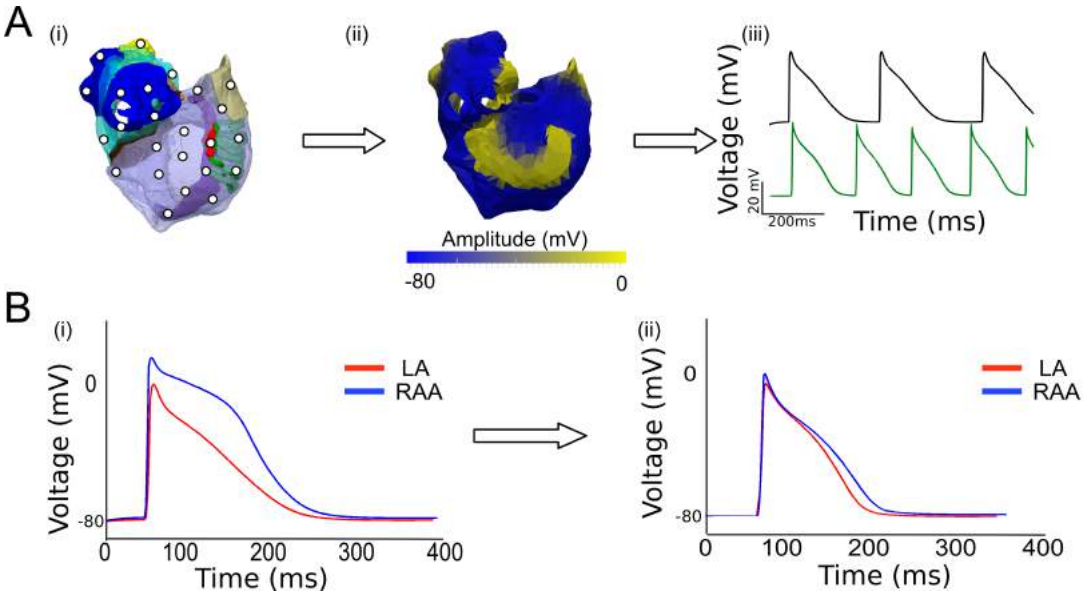

Figure 8.2: Illustration of the atrial ectopic and re-entrant simulation protocols. (A) Illustration of position of the ectopic and re-entrant origins on the atria (A-i) and a re-entry activation centred on the sino-atrial node (SAN) (A-ii), with excitation waves at different rates (A-iii). (B) Illustration of the effects of electrical remodelling in the AP of a cell/node located in the left atria (LA-red line) and right atria appendage (blue line- RAA). (i) Control and (ii) remodelling conditions.

Simulating body surface potential by solving the forward problem

To solve the atrial forward problem, a boundary element method (BEM) was used to calculate the potential on the surface of the torso [31, 24]. From the body surface potential (BSP), 64-,256- and 512-lead ECG (Figure 8.3) signals were obtained by selecting elements of the torso mesh corresponding to the position of the electrodes as described in previous studies [24, 25]. The P-wave of the 64-lead ECG during control conditions matched the experimental data of multiple patients [24, 32] (Figure 8.3B), validating the development of the heart-torso model. Details of the model

development and its validation can be found in [24, 25].

Inverse reconstruction of the atrial surface electrical excitation

Based on the computed BSP from the atria-torso model, the epicardial excitation pattern of the atria was reconstructed during the time course of ectopic focal and re-entrant excitation. The transfer matrix, Z_{BH}, which relates the electric potentials measured on the surface of the body, Φ_B, with the electric potentials on the atrial surface, Φ_H, was calculated using Greens Theorem and a boundary element discretization method described in [33, 34] for triangular meshes:

$$\Phi_B = Z_{BH}\Phi_H \tag{8.1}$$

As the inverted solution is an ill-posed problem, Tikhonov regularization method was used to find the best inverse solution [35]. The epicardial regularized solution, x_λ, is computed by finding the minimum argument that best solved equation 8.2

$$x_\lambda = \min_x\{||Z_{BH}\Phi_H - \Phi_B||^2 + \lambda^2||R||\}, \tag{8.2}$$

where λ is the regularization parameter and R is the regularization operator, which constraints the solution in the spatial domain. The zero order Tikhonov regularization uses the identity matrix as the regularization matrix, i.e. $R = I$. The first order Tikhonov regularization uses the gradient matrix as regularization matrix, i.e., $R = \nabla$. The second order Tikhonov regularization uses the Laplacian matrix as regularization matrix, i.e. $R = \Delta$. The regularization parameter, λ, was found using the L-curve method [36] together with the triangle method for each case [37]. The inverse solution was validated by comparing the reconstructed atria surface with the simulated one with the same resolution.

In numerical implementation, the effects of spatial resolution of ECG electrodes (i.e., the number of electrodes on the body surface) on the accuracy of the inverse-solution were investigated. Atrial epicardial excitation patterns were reconstructed at different densities using 64, 256 and 512 electrodes, which were compared to the actual activation pattern. A linear interpolation was used in each case to increase the number of input in the implementation, as described in previous studies [38, 39].

In order to compare the different Tikhonov regularization methods and lead systems, whole atrial time activation maps were computed. Then, real and reconstructed epicardial potentials from different points on the epicardial surface were

obtained (the positions were selected due to their difference in electrophysiology (Figure 8.2B)). From those epicardial potential, relative errors (RE) as a function of time were calculated in order to quantify the specific differences.

REs were obtained by dividing the absolute error (absolute difference between real and approximated data) by the magnitude of the real value:

$$RE = \frac{|real\ data - reconstructed\ data|}{real\ data} \tag{8.3}$$

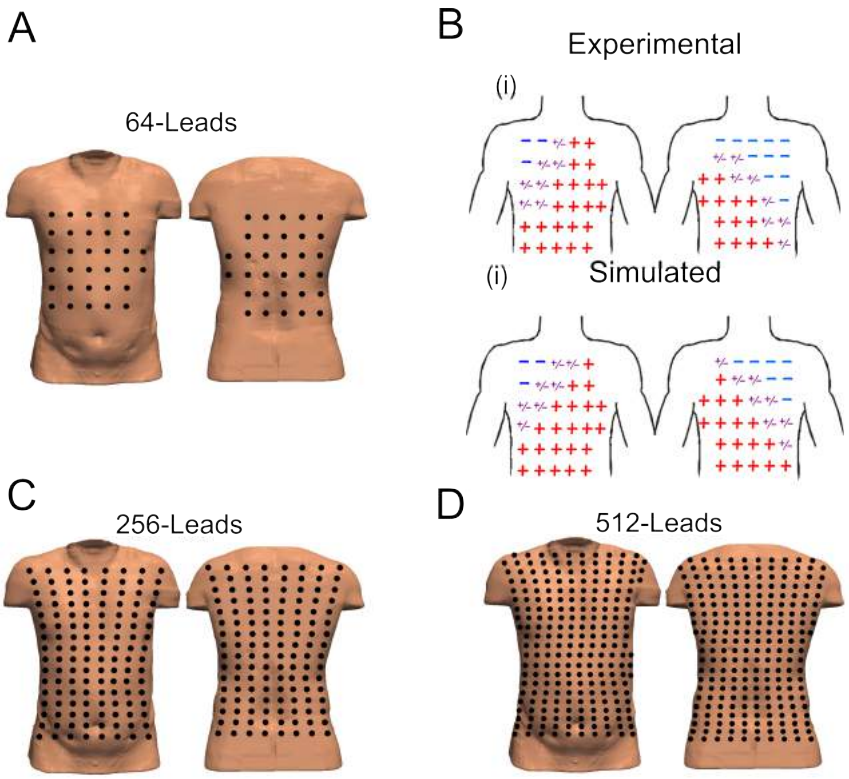

Figure 8.3: Illustration of the Multi-lead ECG systems. Illustration of electrode position used to simulate the 64-lead ECG (A). Experimental and simulated anterior and posterior polarity map in the 64-lead ECG (B) validating the forward and 3D atria-torso models. Illustration of the electrode position used to simulate the 256-lead (C) and 512-lead (D) ECG.

Results

Comparison of the atrial surface reconstruction with ectopic focus.

Potential maps, RE and isochrones were analysed for all datasets produced. For illustrative purposes, the results from individual simulations are presented.

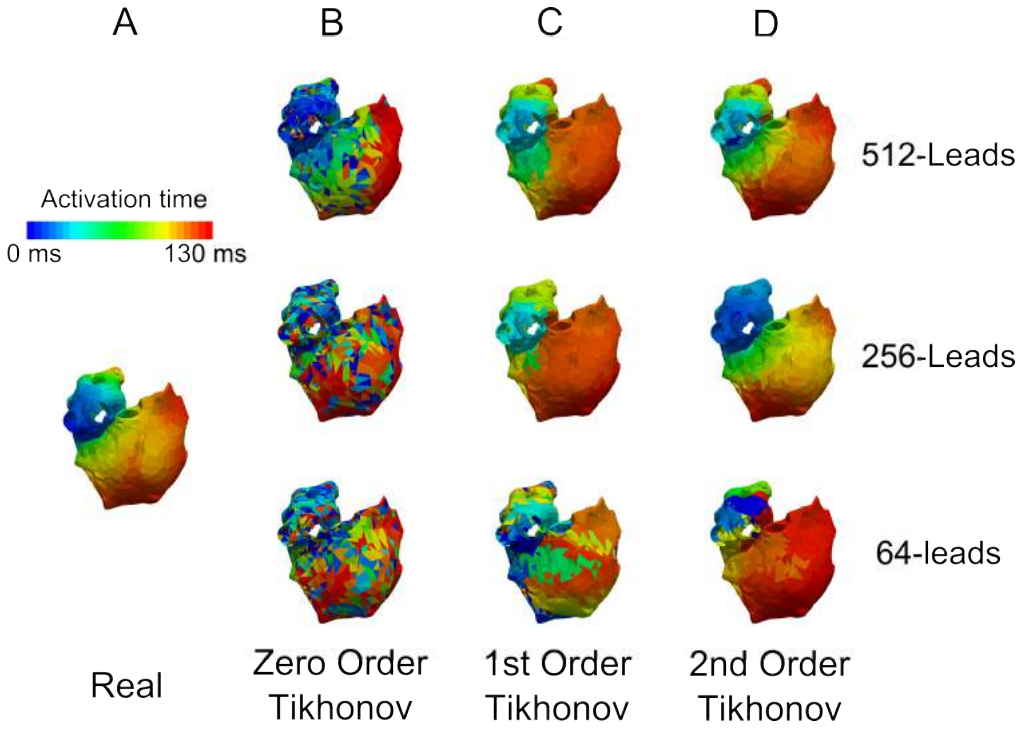

Figure 8.4: Isochrones maps of real and reconstructed ectopic activity with its origin located in the pulmonary veins. Isochrones maps of epicardial reconstruction of an ectopic focus atrial activity with its origin located in the pulmonary veins region. Real activation pattern (A) was compared with reconstructed patterns with variant numbers of electrodes of 64, 256 and 512, using zero (B), first (C) and second (D) order Tikhonov regularization.

Surface isochrones maps were obtained for real atrial activation and epicardial reconstruction using zero, first and second (Figure 8.4A-D) order Tikhonov regularization and 64-, 256- and 512-lead ECG systems (Figure 8.4bottom-top). Smooth and reliable time activation maps were produced with the second order Tikhonov regularization with 512- and 256-leads systems (Figure 8.4D). A closed solution in the case of first order (Figure 8.4C) was also obtained, although 512-leads were necessary. In the case of zero order, similar solutions were obtained, but with a significantly larger degree of noise (Figure 8.4B).

APs and RE were computed from single nodes located on the right atrial ap-

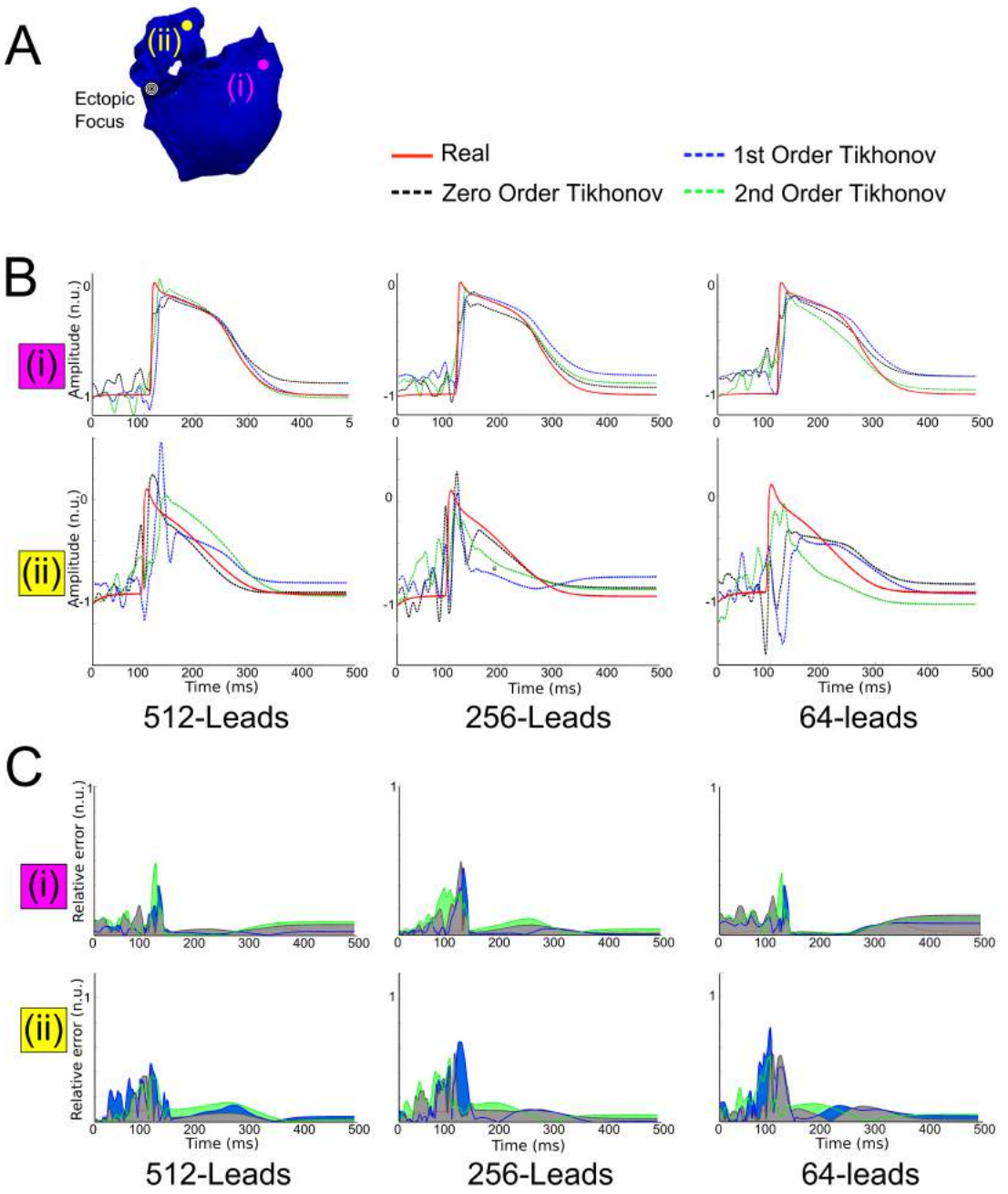

Figure 8.5: Epicardial potential and Relative error of epi-cardial reconstruction of an ectopic atrial activity focus on pulmonary veins. Epicardial potential and Relative error (RE) of epi-cardial reconstruction of an ectopic atrial activity with its origin located in the pulmonary veins region using 512-, 256- and 64-lead ECG. The ectopic focus can be observed in A (black and white spot). Left (i) and right atria appendage (ii) epicardial potentials are observed in each case. The epicardial potentials of real activation (red line), zero (black line), first (blue line), second (green line) order Tikhonov regularization method can be observed in B. RE between real and reconstructed patterns using zero (black line), first (blue line) and second (green line) order Tikhonov regularization method can be observed in B.

pendage (Figure 8.5Ai) and left atria (Figure 8.5Aii) for each activation pattern. Here, both square (Figure 8.5Bi) and triangular (Figure 8.5Bii) epicardial potentials were observed in different regions due to electrophysiological heterogeneity. For each case, RE were calculated between the real atrial activation and the atrial epicardial reconstruction for all lead systems and regularization methods (Figure 8.5).

As expected, the RE signal decreased when the number of electrodes increased (Figure 8.5C) and thus, the solution which matched best the AP (i.e., have lower RE signal) was produced with 512-lead system in all cases (Figure 8.5C). However, the 256-lead ECG displayed a reliable atrial reconstruction in some cases (Figure 8.5C-i). On the comparison of the different Tikhonov regularizations, different peaks were observed in the RE signals close to the depolarization phase (upstroke) with all methods. Second and first order showed similar results (Figure 8.5C) with larger RE signal around this area compared to zero order. In general, a higher RE signal was observed for the first order in almost any case.

Note: If a peak was seen in the RE signal after or before (but close to) the upstroke of the AP (depolarization phase), it usually meant the reconstructed epicardial signal showed a delay or an advance in comparison with the real one, respectively (Figure 8.5C).

Comparison of homogenous and heterogeneous cases

For theoretical comparison, epicardial potentials (Figure 8.6) and RE (Figure 8.7) were also computed for all lead systems and regularization methods under three different electrphysiological conditions: regionally-homogeneous with a square AP-morphology (Figure 8.6A); regionally-homogeneous with a triangular and shorted AP morphology (as is observed in chronic AF remodelling - Figure 8.6B); regionally-heterogeneous with both square (Figure 8.6Ci) and triangular (Figure 8.6Cii) morphologies in different atrial locations. For all cases, the activation maps showed similar results than the one in Figure 8.4.

A significant increase was observed in the RE signals when the electrophysiology was modified from a squared to a triangular morphology, even though the tissue was homogeneous in both cases (Figure 8.7 A and B). Furthermore, the RE signals, when heterogeneous electrophysiology was included (Figure 8.7 C-i and C-ii), were considerably larger compared to homogeneous square case but not as much as the homogeneous triangular case. In addition, the increment in the RE signals when comparing triangular and squared APs within the same heterogeneous electrophysi-

ology atrial activation (Figure 8.7 C-i and C-ii) was also observed.

The 512-lead ECG system presented the lower RE signals, however, the 256-lead ECG showed a close solution in each case. Furthermore, the 64-lead ECG showed low RE signals in the case of squared and homogeneous electrophysiology. In addition, the first order Tikhonov regularization showed the largest RE signals in most of the cases (Figure 8.7 blue line). For homogeneous APs, second and first order showed similar results. However, a smaller RE signal was seen in the second order case with square APs (Figure 8.7A), and in zero order for triangular APs case (Figure 8.7B), demonstrating the most reliable reconstruction in each case.

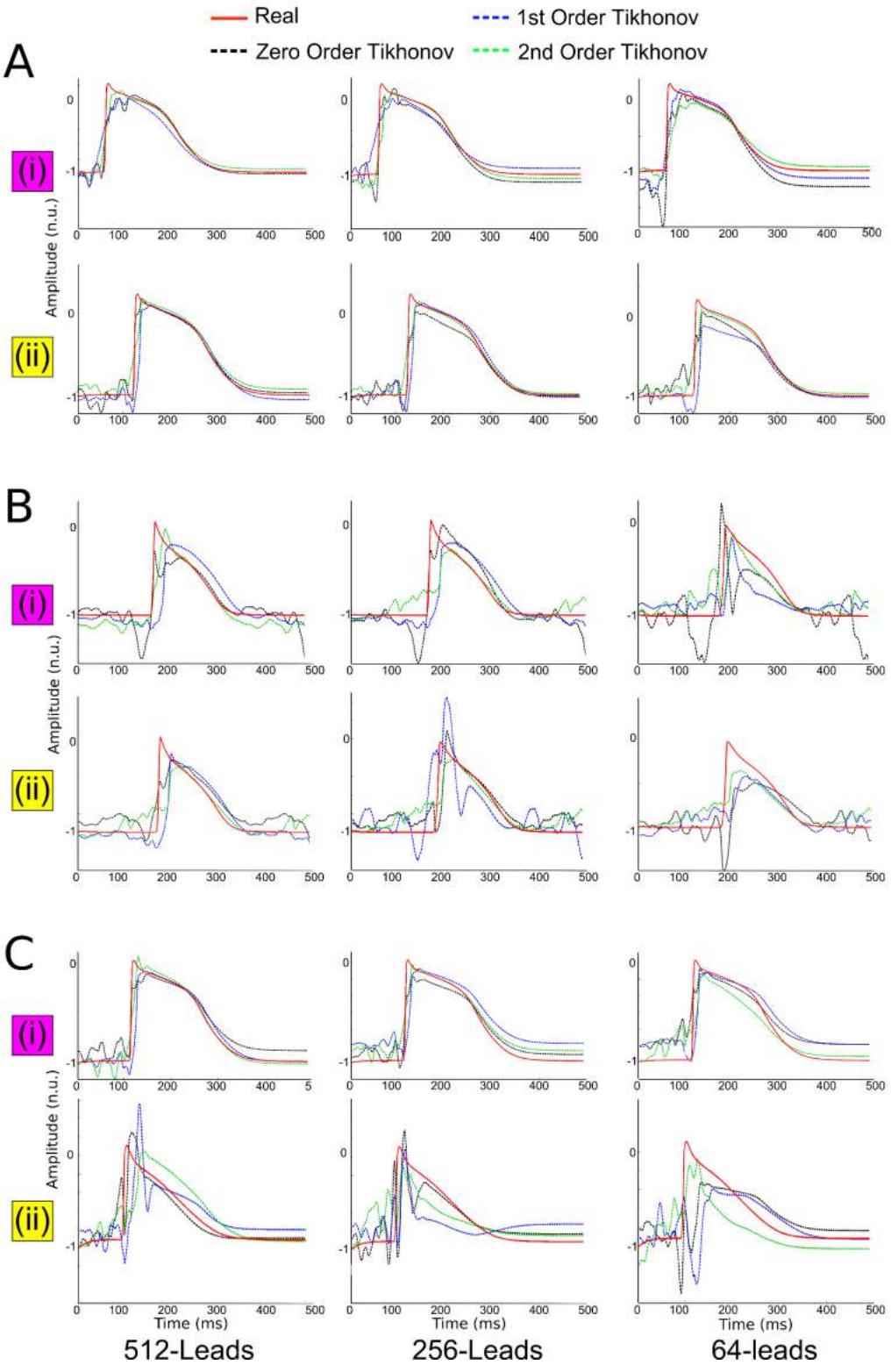

Figure 8.6: Reconstructed epicardial potential of an ectopic atrial activity focus on pulmonary veins. Epicardial potential reconstruction of an ectopic atrial activity with its origin located in the pulmonary veins region using 512-, 256- and 64-lead ECG. Real activation (red line) patterns were compared with reconstructed pattern using zero (black line), first (blue line) and second (green line) order Tikhonov regularization method. The reconstructions were obtained for homogeneous squared (A), homogeneous triangular (remodelling) (B) and heterogeneous (C) cases. Left (i) and right atria appendage (ii) epicardial potentials are presented in each case.

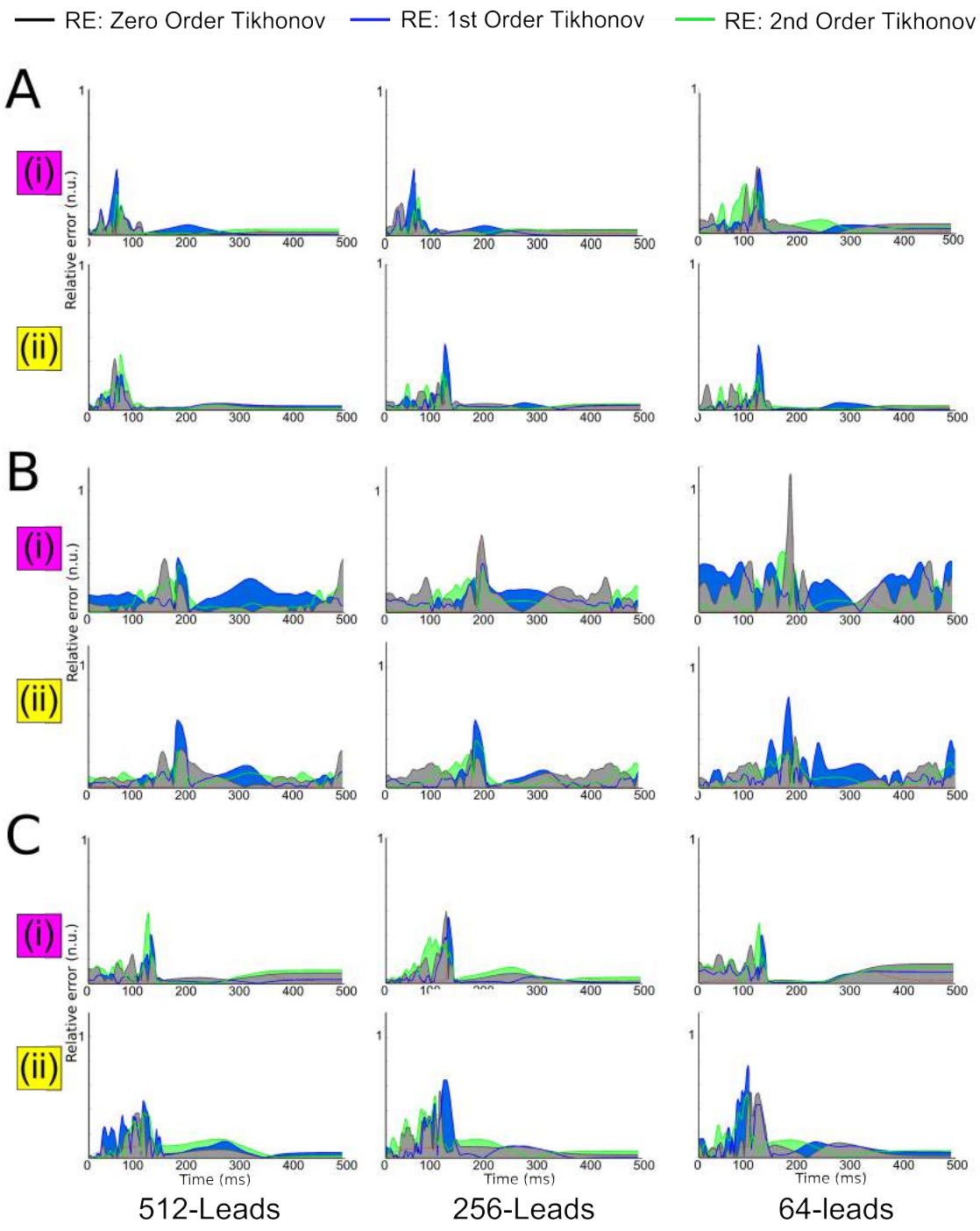

Figure 8.7: Relative error of reconstructed epicardial potential of an ectopic atrial activity focus on pulmonary veins. Relative errors of reconstruction of an ectopic atrial activity with its origin located in the pulmonary veins region using 512-, 256- and 64-lead ECG. Real activation patterns were compared with reconstructed pattern using zero (black line), first (blue line) and second (green line) order Tikhonov regularization method. The reconstructions were obtained for homogeneous squared (A), homogeneous triangular (remodelling) (B) and heterogeneous (C) cases. Left (i) and right atria appendage (ii) epicardial potentials are presented in each case.

Comparison of fast and slow ectopic activation rates

Different rates of focal ectopic activation were analysed (3, 4 and 5 Hz). In each case, a heterogeneous electrophysiology was used. However, remodelling was included to allow the faster rates to be sustained, which reduced the AP duration and its variability, and resulted in mostly triangular APs [20].

Figure 8.8 shows epicardial activation maps of an ectopic focus located in right atrial appendage. The maps were obtained at different timings for real (Figure 8.8A) and reconstructed signal using zero, first and second (Figure 8.8B-D) order Tikhonov regularization with 512-leads ECG at 3Hz and 5Hz (Figure 8.8i,ii). It was observed that the solution which matched best the original slow (3Hz) ectopic activation was obtained with the second order Tikhonov regularization (Figure 8.8D). However, when the rate was increased to 5Hz, the first and second order Tikhonov regularization highly smoothed the solution, and therefore, the zero order method produced the most reliable reconstruction (Figure 8.8B).

Figure 8.9 shows epicardial potentials (Figure 8.9-i) and RE signals (Figure 8.9-ii) of reconstructed AP from a cell/node located on the left atria during an ectopic focus located in right atrial appendage at different rates: 3Hz (Figure 8.9A), 4Hz (Figure 8.9B) and 5Hz (Figure 8.9C). The RE grew with increasing pacing rate in all the cases, except the 64-lead ECG at 4Hz case (Figure 8.9-left). The 512-lead ECG system produced the lowest RE (Figure 8.9 left). At slower rates, the 256-leads ECG showed similar results to the 512-lead system (Figure 8.9 middle). The difference between those two ECG systems increased when the rate was increased (Figure 8.9 B and C). When comparing the different Tikhonov orders, it was observed that a small RE was obtained with the second order at a slow rate, i.e., 3 Hz (Figure 8.9Aii). However, at the fastest rate, i.e., 5 Hz (Figure 8.9Cii), the smallest RE was obtained with the zero order. These results were consistent with the activation maps (Figure 8.8), where the smoothing effects were more pronounced. In most of the cases, the first order showed a delay in the reconstructed epicardial potential (blue peaks observed in all the sets of Figure 8.9-ii), which may explain the results observed in Figure 8.8.

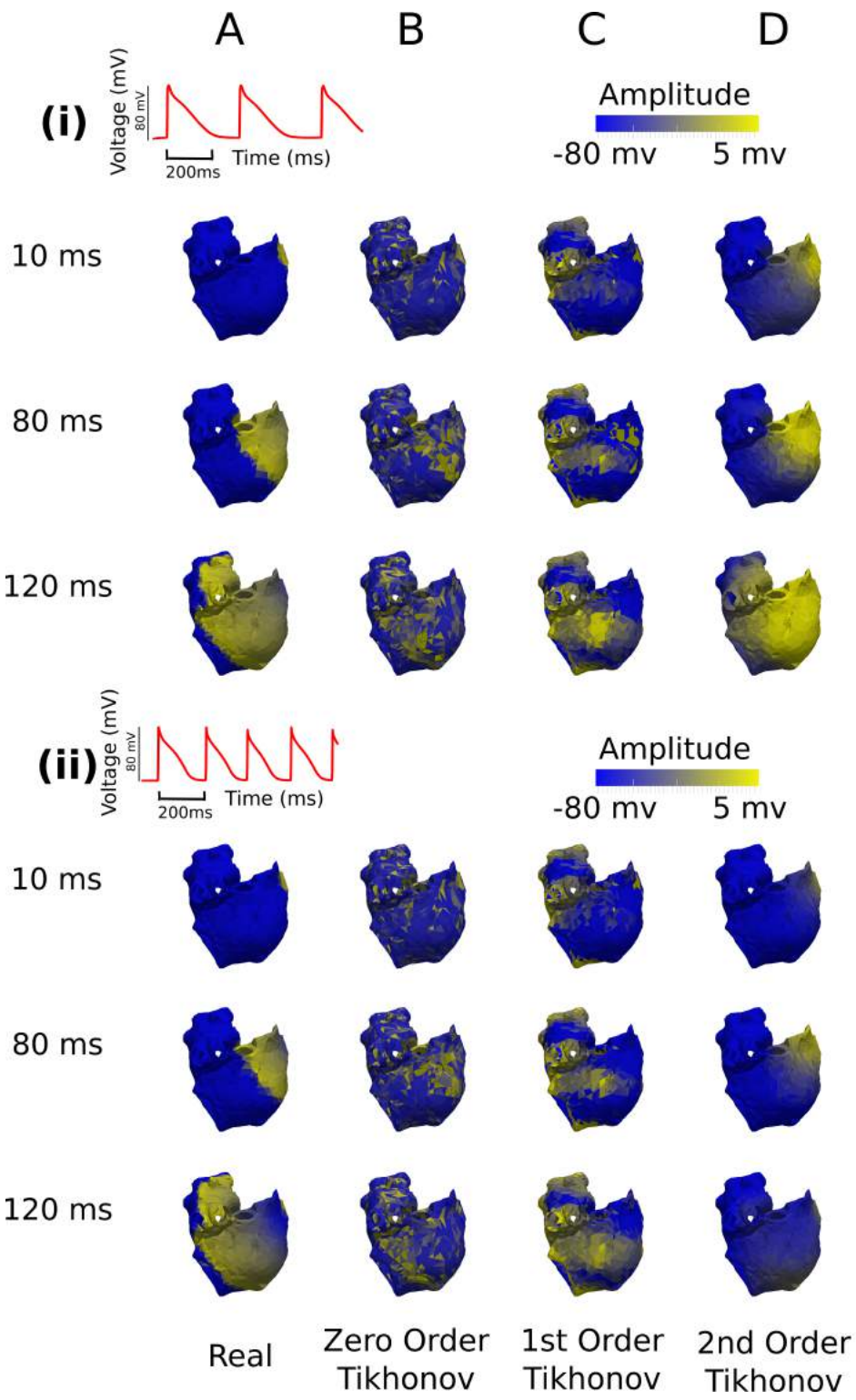

Figure 8.8: Snapshot of epicardial reconstruction of an ectopic atrial activity focus on the Right atria appendage. Snapshot of epicardial reconstruction of an ectopic atrial activity with its origin located in right atrial appendage region at different timings (10, 80 and 120 ms) at a slow (i) and fast (ii) rate. Real activation patterns (A) were compared with reconstructed pattern using zero (B), first (C) and second (D) order Tikhonov regularization method with 512-lead ECG.

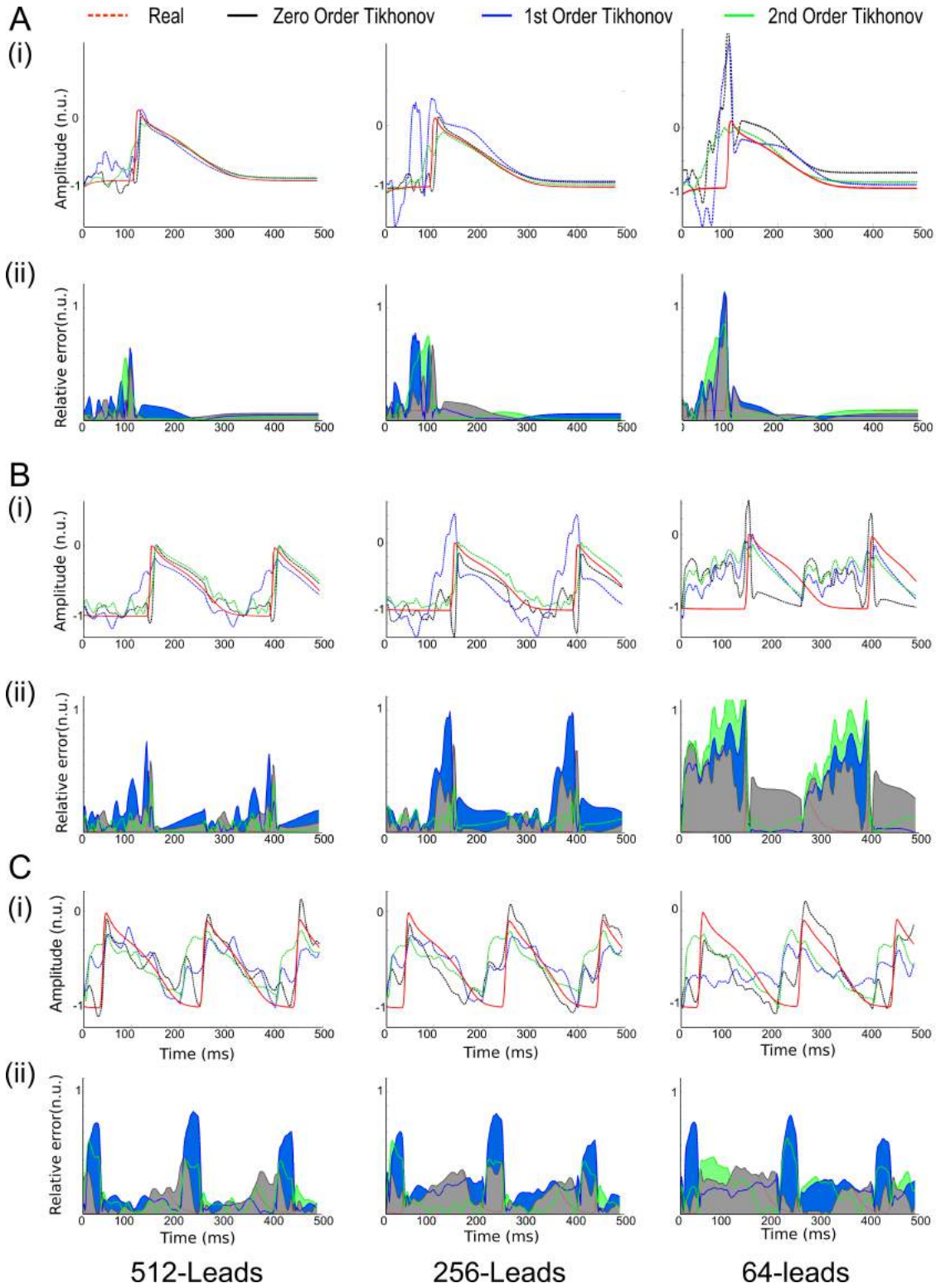

Figure 8.9: Epicardial potential and relative error of epicardial reconstruction of an ectopic atrial activity focus on the Right atria appendage. Epicardial potential and relative error of epicardial reconstruction of an ectopic atrial activity with its origin located in right atrial appendage region at different timings at increasing rates (A-C) from a cell/node located on the left atria, using 512-, 256- and 64-lead ECG. The epicardial potentials of real activation (red line), zero (black line), first (blue line), second (green line) order Tikhonov regularization method can be observed in (i). RE between real and reconstructed patterns using zero (black line), first (blue line) and second (green line) order Tikhonov regularization method can be observed in (ii).

Comparison of the atrial surface reconstruction of Re-entry activation.

Different re-entry atrial activation patterns were analysed. Heterogeneous electrophysiology with remodelling was used, as with the analysis of fast and slow rates.

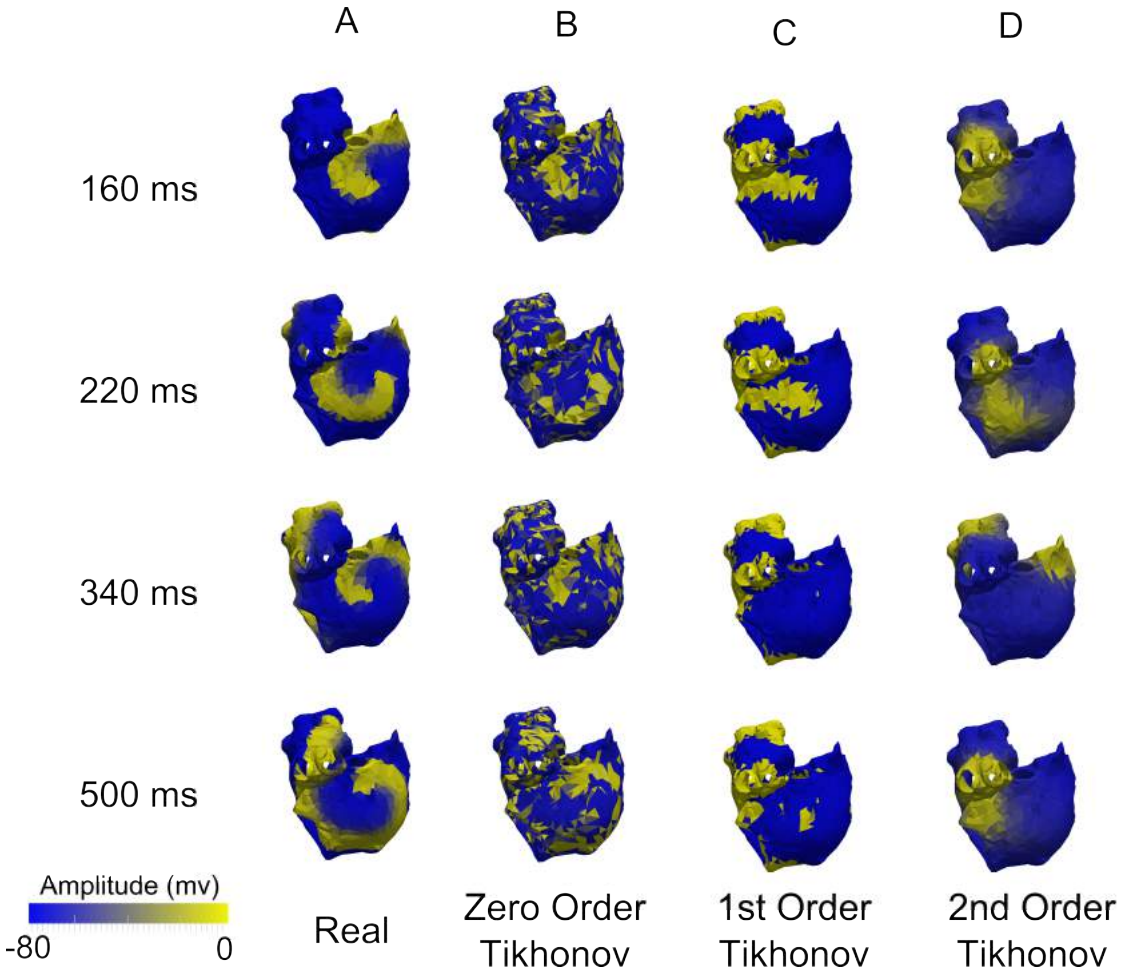

Figure 8.10: Snapshot of epicardial reconstruction of a rotor wave with its origin located at the sino-atrial node region. Snapshot of epicardial reconstruction of a rotor wave with its origin located in the sino-atrial node region at different timings (160, 220, 340 and 500 ms). Real activation pattern (A) were compared with reconstructed pattern using zero (B), first (C) and second (D) order Tikohonov regularization with 512-lead ECGs.

Figure 8.10 shows epicardial activation maps of a re-entrant atrial activation centred on the sino-atrial node (SAN). The maps were obtained at different timings for real (Figure 8.10A) and reconstructed signal using all three Tikhonov regularization methods with 512-leads ECG (Figure 8.10B-C). Figure 8.11 shows epicardial potentials (Figure 8.11 top) and RE signals (Figure 8.11 bottom) of the same atrial activation.

When comparing the different activation maps, the zero order reconstruction showed good feasibility for reconstructing the scroll waves with certain degree of noise (Figure 8.10B). Despite the noise, the key features of the location of the scroll-wave tip and gross atrial activation were captured. The first and second order Tikhonov approaches did not result in reliable reconstructions because the signal was smoothed and thus failed to capture the spatially complex pattern (Figure 8.10 C and D). For the case of epicardial potentials, the 512- and 256-lead systems showed similar results when comparing the RE (Figure 8.11). The RE calculations showed a peak at the beginning of the rising phase mainly for first and second order Tikhonov regularization (Figure 8.11); this meant a delay in the reconstructed signal. This delay may affect the reconstructed map and explains the reason of being unable to track the re-entry wave, and was consistent with the results at fast ectopic rates.

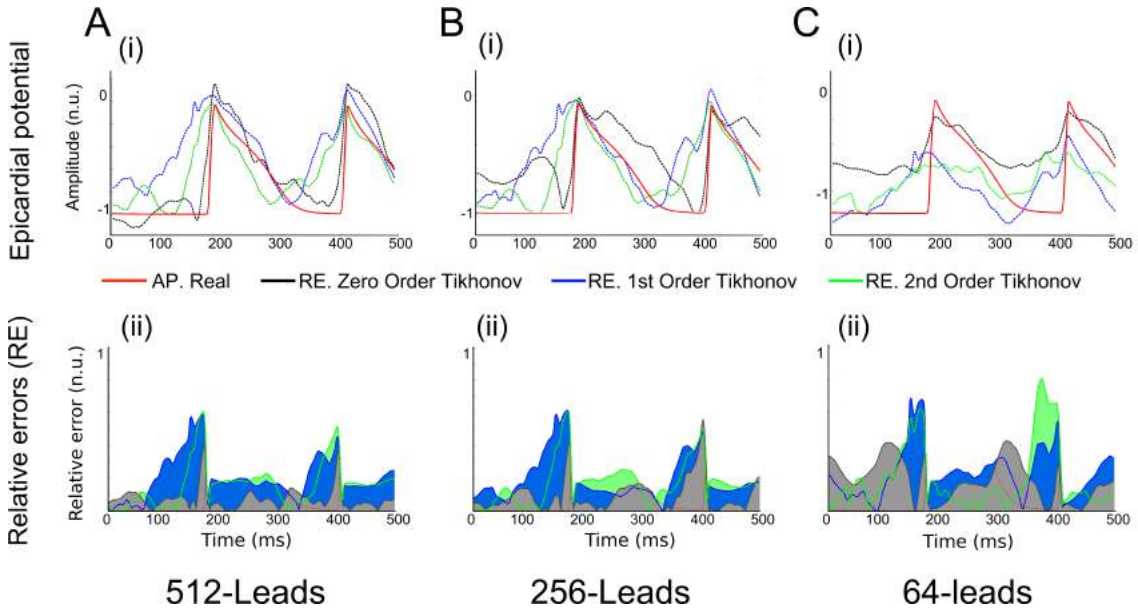

Figure 8.11: Epicardial potentials and relative error of epicardial reconstruction of a rotor wave with its origin located at the sino-atrial node region. Epicardial potentials and relative error of epicardial reconstruction of a rotor wave with its origin located at the sino-atrial node region from a cell/node located on the left atria, using (A) 512-, (B) 256- and (C) 64-lead ECG. The epicardial potentials of real activation (red line), zero (black line), first (blue line), second (green line) order Tikhonov regularization method can be observed in (i). RE between real and reconstructed patterns using zero (black line), first (blue line) and second (green line) order Tikhonov regularization method can be observed in (ii).

Discussion

Major contribution

By using a biophysically detailed computer model of human atria-torso and different Tikhonov regularization methods we have reconstructed the epicardial atria activation of arrhythmic rapid excitation in association with both of ectopic focal and re-entrant activity. Our results provide novel insight into the effectiveness of different methods under varying underlying atrial electrophysiology and activation patterns.

Specifically, we have demonstrated that the Tikhonov regularization methods which produces the most reliable reconstruction is dependent on AP morphology and activation rate. The second order regularization method provided better reconstructed atrial activation during ectopic atrial pacing with more squared action potentials and slow rates with homogeneous and heterogeneous electrophysiology, compared with first and zero order. However, zero order performed better under reentry and fast ectopic atrial activation, wherein short and frequent action potentials are observed. These results showed how the smoothing properties of the different order Tikhonov regularization affect the reconstructed epicardial solution.

The number of body surface potential leads were artificially increased using simple interpolation [38, 39], which improved the reconstructed solution. The minimum number of electrodes varied depending on the type of epicardial potential to reconstruct. However, reliable time activation patterns (isochrones) were possible to obtain with 512- and 256- lead ECG systems, for ectopic activation cases. Unfortunately, in none of the cases the 64-lead ECG system produced a reliable solution.

The RE showed the delay or advance produced in the reconstructed potentials which may affect the diagnosis of the disease, mostly due to the smoothing properties. In some cases (slow pacing) this does not affect the activation maps obtained, which plays an important role in the location of the origins of the ectopic foci activation. However, in cases where rapid pacing was observed (rapid ectopic or re-entrant), this effect was increased and influenced the computation of the atrial activation map.

limitations

The torso model lacks considerations of some other tissue types or organs (such as muscles, fat tissue, bowel, kidneys and spleen) that may affect the amplitude of simulated surface potentials. However, the absence of those tissues does not have a large effect on the polarity of the atrial-waves as demonstrated previously [24].

Different types of interpolation can be used to improve the inverse problem input [38, 39], however, the best interpolation method, the position and the minimal distance between electrodes are still open questions [40, 41].

No noise was added in the any regularized solution which may produce important differences. However, most of the ECG signals are highly filtered in order to be used by diagnosis algorithms.

Future work

In the present study, we only tested the effectiveness of the inverse solution during single atrial focal activity and a single centre of a rotor activity. However, a possible extension is to test the effectiveness of the inverse solution during multiple wavelets, using different constraints. For that purpose, consideration of combined use of inverse solution with multi-leads algorithms, vecto-cardiograms, phase relationships and/or correlation analysis may be necessary, warranting further investigation. Further work to improve the reconstruction and therefore a comparison of the accuracy of different inverse problem reconstruction with different spatial resolution and different interpolation methods in all the different cases presented needs to be performed.

Conclusion

Different Tikhonov regularization methods with different ECG lead systems were developed to reconstruct the epicardial atrial activation during rapid and irregular atrial excitation waves, associated with both ectopic focal and re-entrant activity. Activation maps, isochrones and RE showed how the reliability of the different reconstruction methods depended on the morphology of the epicardial potentials and the rate of the activation.

Supporting information

Bibliography

[1] Y. Rudy, "Noninvasive electrocardiographic imaging of arrhythmogenic substrates in humans," *Circulation research*, vol. 112, no. 5, pp. 863–874, 2013.

[2] H. S. Oster and Y. Rudy, "The use of temporal information in the regularization

of the inverse problem of electrocardiography," *Biomedical Engineering, IEEE Transactions on*, vol. 39, no. 1, pp. 65–75, 1992.

[3] P. S. Cuculich, Y. Wang, B. D. Lindsay, M. N. Faddis, R. B. Schuessler, R. J. Damiano, L. Li, and Y. Rudy, "Noninvasive characterization of epicardial activation in humans with diverse atrial fibrillation patterns," *Circulation*, vol. 122, no. 14, pp. 1364–1372, 2010.

[4] C. Ramanathan, R. N. Ghanem, P. Jia, K. Ryu, and Y. Rudy, "Noninvasive electrocardiographic imaging for cardiac electrophysiology and arrhythmia," *Nature medicine*, vol. 10, no. 4, pp. 422–428, 2004.

[5] R. N. Ghanem, C. Ramanathan, P. Jia, and Y. Rudy, "Heart-surface reconstruction and ecg electrodes localization using fluoroscopy, epipolar geometry and stereovision: application to noninvasive imaging of cardiac electrical activity," *Medical Imaging, IEEE Transactions on*, vol. 22, no. 10, pp. 1307–1318, 2003.

[6] Y. Jiang, C. Qian, R. Hanna, D. Farina, and O. Dössel, "Optimization of the electrode positions of multichannel ecg for the reconstruction of ischemic areas by solving the inverse electrocardiographic problem," *International Journal of Bioelectromagnetism*, vol. 11, no. 1, pp. 27–37, 2009.

[7] A. Ghodrati, D. H. Brooks, and R. S. MacLeod, "Methods of solving reduced lead systems for inverse electrocardiography," *Biomedical Engineering, IEEE Transactions on*, vol. 54, no. 2, pp. 339–343, 2007.

[8] T. Helle-Valle, J. Crosby, T. Edvardsen, E. Lyseggen, B. H. Amundsen, H.-J. Smith, B. D. Rosen, J. A. Lima, H. Torp, H. Ihlen, *et al.*, "New noninvasive method for assessment of left ventricular rotation speckle tracking echocardiography," *Circulation*, vol. 112, no. 20, pp. 3149–3156, 2005.

[9] A. M. van der Graaf, P. Bhagirath, J. de Hooge, H. Ramanna, V. J. van Driel, N. M. de Groot, and M. J. Götte, "Non-invasive focus localization, right ventricular epicardial potential mapping in patients with an mri-conditional pacemaker system-a pilot study," *Journal of Interventional Cardiac Electrophysiology*, vol. 44, no. 3, pp. 227–234, 2015.

[10] H. S. Oster, B. Taccardi, R. L. Lux, P. R. Ershler, and Y. Rudy, "Noninvasive electrocardiographic imaging reconstruction of epicardial potentials, electrograms, and isochrones and localization of single and multiple electrocardiac events," *Circulation*, vol. 96, no. 3, pp. 1012–1024, 1997.

[11] R. Dubois, A. J. Shah, M. Hocini, A. Denis, N. Derval, H. Cochet, F. Sacher, L. Bear, J. Duchateau, P. Jais, *et al.*, "Non-invasive cardiac mapping in clinical practice: Application to the ablation of cardiac arrhythmias," *Journal of Electrocardiology*, vol. 48, no. 6, pp. 966–974, 2015.

[12] M. S. Guillem, A. M. Climent, F. Castells, D. Husser, J. Millet, A. Arya, C. Piorkowski, and A. Bollmann, "Noninvasive mapping of human atrial fibrillation," *Journal of cardiovascular electrophysiology*, vol. 20, no. 5, pp. 507–513, 2009.

[13] A. M. Katz, *Physiology of the Heart*. Lippincott Williams & Wilkins, 2010.

[14] S. Nattel, A. Shiroshita-Takeshita, B. J. Brundel, and L. Rivard, "Mechanisms of atrial fibrillation: lessons from animal models," *Progress in cardiovascular diseases*, vol. 48, no. 1, pp. 9–28, 2005.

[15] E. J. Benjamin, P. A. Wolf, R. B. DAgostino, H. Silbershatz, W. B. Kannel, and D. Levy, "Impact of atrial fibrillation on the risk of death the framingham heart study," *Circulation*, vol. 98, no. 10, pp. 946–952, 1998.

[16] F. Rahman, G. F. Kwan, and E. J. Benjamin, "Global epidemiology of atrial fibrillation," *Nature Reviews Cardiology*, vol. 11, no. 11, pp. 639–654, 2014.

[17] D. Li, L. Zhang, J. Kneller, and S. Nattel, "Potential ionic mechanism for repolarization differences between canine right and left atrium," *Circulation research*, vol. 88, no. 11, pp. 1168–1175, 2001.

[18] D. Gong, Y. Zhang, B. Cai, Q. Meng, S. Jiang, X. Li, L. Shan, Y. Liu, G. Qiao, Y. Lu, *et al.*, "Characterization and comparison of Na+, K+ and Ca2+ currents between myocytes from human atrial right appendage and atrial septum," *Cellular Physiology and Biochemistry*, vol. 21, no. 5-6, pp. 385–394, 2008.

[19] A. V. Glukhov, V. V. Fedorov, Q. Lou, V. K. Ravikumar, P. W. Kalish, R. B. Schuessler, N. Moazami, and I. R. Efimov, "Transmural dispersion of repolarization in failing and nonfailing human ventricle," *Circulation research*, vol. 106, no. 5, pp. 981–991, 2010.

[20] M. A. Colman, O. V. Aslanidi, S. Kharche, M. R. Boyett, C. Garratt, J. C. Hancox, and H. Zhang, "Pro-arrhythmogenic effects of atrial fibrillation-induced electrical remodelling: insights from the three-dimensional virtual human atria," *The Journal of physiology*, vol. 591, no. 17, pp. 4249–4272, 2013.

[21] K. T. Konings, J. L. Smeets, O. C. Penn, H. J. Wellens, and M. A. Allessie, "Configuration of unipolar atrial electrograms during electrically induced atrial fibrillation in humans," *Circulation*, vol. 95, no. 5, pp. 1231–1241, 1997.

[22] S. M. Narayan, D. E. Krummen, and W. J. Rappel, "Clinical mapping approach to diagnose electrical rotors and focal impulse sources for human atrial fibrillation," *Journal of cardiovascular electrophysiology*, vol. 23, no. 5, pp. 447–454, 2012.

[23] J. Jalife, O. Berenfeld, A. Skanes, and R. Mandapati, "Mechanisms of atrial fibrillation: mother rotors or multiple daughter wavelets, or both?," *Journal of cardiovascular electrophysiology*, vol. 9, no. 8 Suppl, pp. S2–12, 1998.

[24] E. A. P. Alday, M. A. Colman, P. Langley, T. D. Butters, J. Higham, A. J. Workman, J. C. Hancox, and H. Zhang, "A new algorithm to diagnose atrial ectopic origin from multi lead ecg systems-insights from 3D virtual human atria and torso," *PLoS computational biology*, vol. 11, no. 1, 2015.

[25] E. A. Perez Alday, M. A. Colman, T. D. Butters, J. Higham, D. Giacopelli, P. Langley, and H. Zhang, "Diagnosis of atrial ectopic origin from the body surface ecg: Insights from 3D virtual human atria and torso," in *Computing in Cardiology Conference (CinC), 2013*, pp. 1075–1078, IEEE, 2013.

[26] M. A. Colman, O. V. Aslanidi, J. Stott, A. V. Holden, and H. Zhang, "Correlation between p-wave morphology and origin of atrial focal tachycardiainsights from realistic models of the human atria and torso," *Biomedical Engineering, IEEE Transactions on*, vol. 58, no. 10, pp. 2952–2955, 2011.

[27] O. V. Aslanidi, M. A. Colman, J. Stott, H. Dobrzynski, M. R. Boyett, A. V. Holden, and H. Zhang, "3D virtual human atria: a computational platform for studying clinical atrial fibrillation," *Progress in biophysics and molecular biology*, vol. 107, no. 1, pp. 156–168, 2011.

[28] N.-W. Hsu, Y.-J. Lin, C.-T. Tai, T. Kao, S.-L. Chang, W. Wongcharoen, L.-W. Lo, A. R. Udyavar, Y.-F. Hu, H.-W. Tso, *et al.*, "Frequency analysis of the fibrillatory activity from surface ecg lead v1 and intracardiac recordings: implications for mapping of af," *Europace*, vol. 10, no. 4, pp. 438–443, 2008.

[29] V. Biktashev and A. Holden, "Reentrant waves and their elimination in a model of mammalian ventricular tissue," *Chaos: An Interdisciplinary Journal of Nonlinear Science*, vol. 8, no. 1, pp. 48–56, 1998.

[30] S. R. Kharche, T. Stary, M. A. Colman, I. V. Biktasheva, A. J. Workman, A. C. Rankin, A. V. Holden, and H. Zhang, "Effects of human atrial ionic remodelling by β-blocker therapy on mechanisms of atrial fibrillation: a computer simulation," *Europace*, p. 084, 2014.

[31] Y. Salu, "Implementing a consistency criterion in numerical solution of the bioelectric forward problem," *Biomedical Engineering, IEEE Transactions on*, no. 6, pp. 338–341, 1980.

[32] D. Giacopelli, J. P. Bourke, A. Murray, and P. Langley, "Spatial pattern of p waves in paroxysmal atrial fibrillation patients in sinus rhythm and controls," *Pacing and Clinical Electrophysiology*, vol. 35, no. 7, pp. 819–826, 2012.

[33] M. Stenroos and J. Haueisen, "Boundary element computations in the forward and inverse problems of electrocardiography: comparison of collocation and galerkin weightings," *Biomedical Engineering, IEEE Transactions on*, vol. 55, no. 9, pp. 2124–2133, 2008.

[34] R. C. Barr, M. Ramsey III, and M. S. Spach, "Relating epicardial to body surface potential distributions by means of transfer coefficients based on geometry measurements," *Biomedical Engineering, IEEE Transactions on*, no. 1, pp. 1–11, 1977.

[35] A. N. Tikhonov, A. Goncharsky, V. Stepanov, and A. G. Yagola, *Numerical methods for the solution of ill-posed problems*, vol. 328. Springer Science & Business Media, 2013.

[36] P. C. Hansen, "Analysis of discrete ill-posed problems by means of the l-curve," *SIAM review*, vol. 34, no. 4, pp. 561–580, 1992.

[37] J. L. Castellanos, S. Gómez, and V. Guerra, "The triangle method for finding the corner of the l-curve," *Applied Numerical Mathematics*, vol. 43, no. 4, pp. 359–373, 2002.

[38] B. J. Schijvenaars, J. A. Kors, G. van Herpen, F. Kornreich, and J. Van Bemmel, "Interpolation of body surface potential maps," *Journal of electrocardiology*, vol. 28, pp. 104–109, 1995.

[39] T. F. Oostendorp, A. van Oosterom, and G. Huiskamp, "Interpolation on a triangulated 3D surface," *Journal of Computational Physics*, vol. 80, no. 2, pp. 331–343, 1989.

[40] P. W. Macfarlane, A. van Oosterom, and M. Janse, *Comprehensive electrocardiology*, vol. 4. Springer Science & Business Media, 2010.

[41] C. F. Pieper and A. Pacifico, "The epicardial field potential in dog: Implications for recording site density during epicardial mapping," *Pacing and Clinical Electrophysiology*, vol. 16, no. 6, pp. 1263–1274, 1993.

Chapter 9

Summary and Further work

This chapter summarises the research work, main contributions and future directions of the presented Thesis, which are detailed below.

The major contributions of the Thesis can be summarized as:

- The improvement of the BSP model which include different internal organs and soft/hard tissues with electrical conductivity inhomogeneities.
- The segmentation of two torso models based on male and female visible human project data, in each of which tissue electrical conduction inhomogeneities were included.
- The development of a novel and well validated model of human atria-torso, with consideration of different positions of the atria inside the body. The model was used to investigate possible effects of heart positioning on 64-lead ECG.
- A computational program to calculate the magnetic field and MCGs was created which include different internal organs and soft/hard tissues with electrical conductivity inhomogeneities.
- A novel human ventricle-torso model with simulated 36-lead ECG and MCG matching experimental data was developed.
- The development of a computational program to solve the cardiac inverse problem by using the Tikhonov regularization method.
- A new algorithm was created to detect atrial ectopic foci from multi-lead ECG systems.
- A new algorithm was created to identify atrial re-entry and fast ectopic foci from multi-lead ECG systems.

- A sensitivity analysis of 36-lead ECG and MCG under ischemic conditions, from which the correlation between ischemic regions and characteristics of ECG and MCG was established.

- A comparison of atrial surface reconstruction using different multi-lead systems and different order Tikhonov regularization during ectopic foci and re-entry.

All these represent a substantial improvement to the available models and a significant advancement in the studies of detecting cardiac arrhythmias non-invasively. It was shown that there were some differences in the sensitivity of ECG and MCG signals in response to ventricular ischemia; it is therefore interesting to investigate possible sensitivity difference of ECG and MCG signals to other cardiac diseases to establish if MCG can provide useful extra information compared to ECG.

In addition, the algorithm for detecting atrial ectopic foci and re-entry from multi-lead systems has been developed by using new features of ECG signal analysis (such as dipole evolution, quadrant division). To the author's best knowledge, these new features of ECG signals have not been proposed or applied for detecting cardiac arrhythmias before. Furthermore, the study in Chapter 8 demonstrates for the first time, the effects of epicardial potential morphology, heterogeneity and excitation rates on different Tikhonov regularization with different multi-lead systems during ectopic and re-entry atrial activation.

9.1 Computational heart-torso models

In this Thesis, a powerful set of computational tools for modelling the electrical and magnetic fields produced by cardiac activity were developed. The model used to calculate the forward problem and to solve the cardiac inverse problem forms a significant advancement to the cardiac modelling field.

The BSP model consisted of: (i) a parallelised C++ program which computes the forward problem using BEM; (ii) two realistic torso meshes; (iii) fine detail on internal structures, such as the spine, ribs, kidneys, stomach and liver as well as blood-masses and lungs; (iv) multiple, experimentally justified orientations of the atria and ventricles. All the torso geometries and their inhomogeneities were segmented solely as part of this Thesis.

Major contribution

The present model has the following advantages over previously published models [1, 2] in the following ways: (i) realistic geometries were used rather than idealised ones, (ii) different organs were segmented and included rather than only idealised lungs used in the previous study, (iii) only one atrial orientation was previously used, whereas the present study uses two atria/ventricles orientations. In addition, the model was validated (and applied in two studies (Chapter 5 and Chapter 7) by considering BSP patterns, dipole evolutions and different multi-lead ECG systems (see Chapter 4). These are substantially improvements compared to the previous studies, which were only validated through the 12-lead ECG [1, 2]. The additions made to the model significantly improve its clinical relevance and provide a powerful in silico tool for theoretical investigation of non-invasive approaches to detect cardiac arrhythmias.

The MCG model consisted of: (i) a parallelised C++ program which computes the forward problem using BEM; (ii) and the same realistic torso geometries and their inhomogeneities used in the BSP model. Furthermore, the MCG model offers a comparable, if not better, level of validation compared to other published models (see Chapter 4), which allowed investigation into the diagnostic potential of MCG compared to ECG for different cardiac diseases (see Chapter 7).

The computational model used to calculate the cardiac inverse problem solution consisted of: i) a parallelised C++ program which computes the inverse problem using BEM; (ii) and the same realistic torso geometries and their inhomogeneities used in the BSP model. Furthermore, the inverse problem model offers comparable, if not better, results than other published models in the sense that the computing time is no more than the BSP method used and a comparison/validation with the real atria simulation was also obtained. This allowed investigation of different heart surface reconstruction techniques under different configurations (see Chapter 8).

Further work

In the future, further different tissue types and organs can be segmented and included in the torso model to improve the accuracy of simulated ECG and MCG signal, as well as their respective surface reconstruction. Also, the motion of the body and internal organs, such as respiration or cardiac contraction, can be incorporated into the model to increase the accuracy of the present model. Further clinical MCG signals and atrial epicardial measurements are also needed to validate the accuracy of the

MCG and inverse problem model; unfortunately, these measurements are difficult to obtain under experimental settings [3]. Nevertheless, the models presented provide a powerful in silico tool for theoretically investigating cardiac arrhythmias through non-invasive approaches.

9.2 Multi-lead ECG algorithm

In this Thesis, a new algorithm was developed to locate the origin of rapid and irregular atrial excitation waves, associated with both ectopic focal and re-entrant activity, by using a multi-lead ECG system. This represents a significant improvement over previously developed algorithms to predict AF origins associated with focal and re-entry activities [4]. Therefore, the methods/algorithm presented in this thesis may become a vital part in the early diagnosis for the onset of AF, helping in the global effort to manage this epidemic more effectively and improve the quality of patients' lives.

Briefly, the algorithm can be divided in two parts: (i) a study described in Chapter 5, which locates the origins of ectopic activity; and (ii) a follow-up study presented in Chapter 6, which extended the algorithm to be used during fast pacing and re-entry. This second part is a vital step in the process, because of the similarities in the 12-lead ECG signals which makes it difficult, if not impossible, to distinguish them.

Major contribution

The first part of the algorithm presented, i.e. Chapter 5, demonstrated a success rate of 93%. The developed algorithm is, to the author's best knowledge, the first to be based on such a multi-lead ECG system. Simulation results indicate that the extra level of detail provided by such a system is useful in accurately locating focal activity. The multi-lead ECG systems are not as clinically available as the 12-lead ECG (as there is one of these at every hospital bed) and one of the aims of this study was to indicate whether the extra level of detail provided by a multi-lead system provides benefits over the 12-lead ECG.

The first part of the algorithm has two key advantages: (i) splitting the torso into two sets of quadrants means that the algorithm is not specific to an electrode array set-up; in other words, any array which covers the front and back of the torso may be used, and the algorithm need not be adjusted. This is certainly important if it is to be used in the clinic, where the 64 lead vest may not be available; (ii) the algorithm

is based on polarity patterns of the P-waves, rather than the detailed morphology itself. Whereas this does not provide the level of detail that PWM does, it helps in the following ways: (a) not basing the algorithm on fine details that may vary from case to case; (b) the effect of noise is reduced, in other words, whereas noise may affect PWM, it will not affect the polarity, unless noise is higher than signal, in which case the data is not suitable for any data analysis; (c) not basing any decisions on bifidity, which can be affected by noise and has caused problems in other algorithms [5, 6].

The second part of the algorithm, i.e. Chapter 6, identifies the correct polarity of the f-waves, and subsequently locates the origin of atrial fibrillation in association with both ectopic focal and re-entrant activity. The success rate of the algorithm was 92% and 75% for focal and re-entry activation respectively. Re-entry and focal activation were distinguished with a success rate of 88%.

The second part of the algorithm has two key advantages: (i) It can locate the time interval and (ii) the source of the atrial activation when f-waves are presented. The time interval was obtained through the calculation of the atrial dipole from a multi-lead system, whereas the source of the atrial activation was obtained through the use of FFT properties. These two aspects are, to the author's best knowledge, these results represent the first effort to distinguish the main activity and find the position of the focus and tip of the re-entry from a multi-lead ECG. The algorithm developed in the present study using 64-lead ECG provided sufficient information to locate the origin of the atrial activation (see Chapter 6).

Further work

The algorithm was developed using simulation data, where it is more straight-forward to correlate BSP patterns with atrial activation sequences than in an experimental setting. Therefore, further tests involving real ECG data from experimental models with known atrial activation
origins are required.

A spatial refinement of the first part of the algorithm can be performed, a previous attempt can be found in [7]. However, the improvement in the spatial resolution produced a decrease in the accuracy of diagnosis. Additionally, the minimum number of electrodes that can produce the same results can be further investigated.

The algorithm was proved to be effective for detecting a single atrial focal activity and a single centre of a reentry activation. However, a possible extension

is to identify multiple wavelets, using the dipole evolution patterns. For that purpose, consideration of combined use of the present algorithm with vectorcardiograms, phase relationships, correlation analysis and inverse problem reconstruction may be necessary, warranting further investigation.

9.3 MCG and ECG comparison

The results presented in this study provide insight into the discussion around the potential of MCG in cardiac monitoring, suggesting that it can provide extra, useful information which improves diagnose and characterization of cardiac diseases, mainly those that are asymptomatic to the ECG. Therefore in this Thesis, the different features of 12-, 36-lead ECG and MCG, BSP and MCG maps during normal and variant ischemic conditions were investigated, especially their relative differences between the normal and ischemic conditions. Also, the regional dependence of the measured relative difference and how the area with maximal relative difference on the body surface varied due to altered stage and location of the ischemic region was investigated.

Major contribution

The major contributions were: (i) the comparison of 12-, 36-lead ECG and MCG averaged relative difference in the QRS complex, T-wave and ST-segment, to indicate the advantages of implementing multi-lead ECG/MCG systems than the conventional 12-lead ECG in diagnosing the ischemic condition. In addition, by comparing averaged relative difference it was found that the 36-leads ECG was more sensitive than the 36-leads MCG in detecting changes in the T-wave, however, for detecting changes in the ST-segment the MCG showed greater sensitivity by producing a greater relative difference; (ii) The calculation of relative differences in both ECG and MCG body map signals, which showed regional-dependent changes to ischemic condition on the body surface of the torso, but with MCG showing a stronger correlation between ischemic region in the heart and the maximal difference map on the body surface. Finally, (iii) a correlation between ischemic region in the heart and the maximal relative differences of MCG during ST-segment was obtained which provided a theoretical basis for non-invasively diagnosing ischemic region, which to the author's best knowledge is the first attempt to directly correlate both particularities. Such correlation was not seen from the ECG maps.

Therefore, results suggested that the 12-lead ECG is less effective to provide diagnosis of the ischemia, whereas the 36-lead ECG and in particular MCG offer

advantages in the identification of ischemic conditions. By comparing the relative differences in the BSP and MCG maps, the results showed that MCG has greater sensitivity than ECG in response to ischemia, which may provide an alternative method for the diagnosis of ischemia.

Further work

A possible extension of this study is to produce an algorithm to detect and locate the ischemia regions with high resolution using MCG maps, BSP map or specific electrodes/sensors based on the correlation found in the study. In the same sense, different ECG and MCG signals during cardiac arrhythmias can be compared to test further differences between these two signals. In addition, inverse solutions can be calculated and compared for both ECG and MCG signals, during different cardiac arrhythmias.

9.4 Atrial surface reconstruction

The inverse problem in electrocardiography clearly offers advantages over prevailing imagining methods [3], which are usually invasive or expensive. Unfortunately, further research is still needed in order to make it clinically practical. In the study described in Chapter 8, a biophysically detailed computer model of human atria-torso and different order Tikhonov regularization method were used to reconstruct the epicardial atria activation during ectopic focal and re-entrant activity. Activation maps, isochrones and relative errors (RE) were used to compare real atrial simulation and reconstructed ones, in order to investigate how the different multi-lead ECG and the different regularization methods affect the epicardial reconstruction.

Major contribution

The major contributions were: (i) a good activation pattern was possible to obtain with any 512- and 256-lead ECG, but not with a 64-lead ECG system. (ii) Activation maps, isochrones and RE showed that the surface reconstruction depends on the morphology of the epicardial potentials and the rate of the activation. (iii) Second order Tikhonov regularization method provided a better reconstructed atrial activation, and slow ectopic atrial activation compared with first and zero order. However, zero order worked better under re-entry and fast ectopic atrial activation. (iv) The smoothing properties of the first and second order Tikhonov regularization produced a slight delay or advance in the reconstructed potentials which may affect

the diagnosis of the disease, which was showed through the RE calculation.

Therefore, the results showed that ectopic focus and re-entry atrial activation can be reconstructed through a simple Tikhonov regularization method, however, the minimum number of electrodes and the order of Tikhonov regularization significantly depend on the morphology of the epicardial potential and the rate of the activation.

Further work

In the present study, the effectiveness of the inverse solution during single atrial focal activity and a single centre of rotor activity were tested. However, a possible extension is to test the effectiveness of the inverse solution during multiple wavelets, using different constraints. In addition, consideration of combined use of inverse solution with multi-lead algorithms, vecto-cardiograms, phase relationships and/or correlation analysis can also be tested, warranting further investigation.

Different regularization or inverse reconstruction methods, which have been proposed but not tested, can be further performed. In addition, ventricular surface reconstruction during different ventricular arrhythmias can also be tested.

No noise was added in any reconstruction, therefore a future study should include how the epicardial reconstructions are affected by the addition of it.

Bibliography

[1] J. D. Stott, *Developing realistic models of the atrium and the p-wave*. PhD thesis, The University of Manchester, 2009.

[2] M. A. Colman, O. V. Aslanidi, J. Stott, A. V. Holden, and H. Zhang, "Correlation between p-wave morphology and origin of atrial focal tachycardiainsights from realistic models of the human atria and torso," *Biomedical Engineering, IEEE Transactions on*, vol. 58, no. 10, pp. 2952–2955, 2011.

[3] P. W. Macfarlane, A. van Oosterom, and M. Janse, *Comprehensive electrocardiology*, vol. 4. Springer Science & Business Media, 2010.

[4] O. V. Aslanidi, M. A. Colman, J. Stott, H. Dobrzynski, M. R. Boyett, A. V. Holden, and H. Zhang, "3d virtual human atria: a computational platform for

studying clinical atrial fibrillation," *Progress in biophysics and molecular biology*, vol. 107, no. 1, pp. 156–168, 2011.

[5] P. M. Kistler, K. C. Roberts-Thomson, H. M. Haqqani, S. P. Fynn, S. Singarayar, J. K. Vohra, J. B. Morton, P. B. Sparks, and J. M. Kalman, "P-wave morphology in focal atrial tachycardia: development of an algorithm to predict the anatomic site of origin," *Journal of the American College of Cardiology*, vol. 48, no. 5, pp. 1010–1017, 2006.

[6] Z. Y. Qian, X. F. Hou, D. J. Xu, B. Yang, M. L. Chen, C. Chen, F. X. Zhang, Q. J. Shan, K. J. Cao, and J. G. Zou, "An algorithm to predict the site of origin of focal atrial tachycardia," *Pacing and Clinical Electrophysiology*, vol. 34, no. 4, pp. 414–421, 2011.

[7] E. A. Perez Alday, M. A. Colman, P. Langley, and H. Zhang, "Spatial refinement of a new algorithm to identify focus of atrial ectopic activity from 64-lead ecgs," in *Computing in Cardiology Conference (CinC), 2014*, pp. 501–504, IEEE, 2014.

Appendix A

Supporting Information MS2

Supporting Text S3

The overlapping area, region where re-entrant and ectopic activation cannot be distinguished (magenta regions in Figure A.11DF, 2DF, 3DF), depends on the frequency used to calculate the AFFTr ratios, this frequency depends on the dominant frequency (DF) of each activation:

$$AFFTr_{1DF} = \frac{Area\ under\ the\ FFT\ curve\ between\ 0\ and\ the\ DF\ in\ Hz}{Area\ under\ the\ FFT\ curve\ between\ 0\ and\ 50\ Hz}$$

$$AFFTr_{2DF} = \frac{Area\ under\ the\ FFT\ curve\ between\ 0\ and\ 2\ times\ the\ DF\ in\ Hz}{Area\ under\ the\ FFT\ curve\ between\ 0\ and\ 50\ Hz}$$

$$AFFTr_{3DF} = \frac{Area\ under\ the\ FFT\ curve\ between\ 0\ and\ 3\ times\ the\ DF\ in\ Hz}{Area\ under\ the\ FFT\ curve\ between\ 0\ and\ 50\ Hz}$$

Once the ratios are calculated, scatter plots of the ratio values against the DF are created to find the ratio at which the overlapping area is minimized.

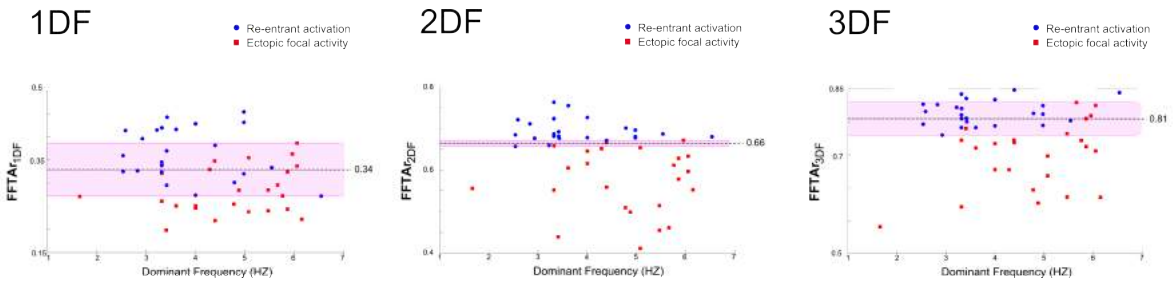

Figure A.1: Scatter plots of different (AFFTr) against the DF, the magenta area is the overlapping area where both activities can occur. 1DF is (AFFTr1DF) against the DF. 2DF is (AFFTr2DF) against the DF. 3DF is (AFFTr3DF) against the DF.

The properties of the scatter plots of different (AFFTr) against DF are displayed. Figure A.2A, shows the width of the overlapping area against the DF. Figure A.2B, shows the number of cases (re-entrant and focal ectopic activation) inside the overlapping area against the DF. Figure A.2C, shows the number of focal ectopic activation inside the overlapping area against the DF. Figure A.2D, shows the number of re-entrant activation in the overlapping area against the DF.

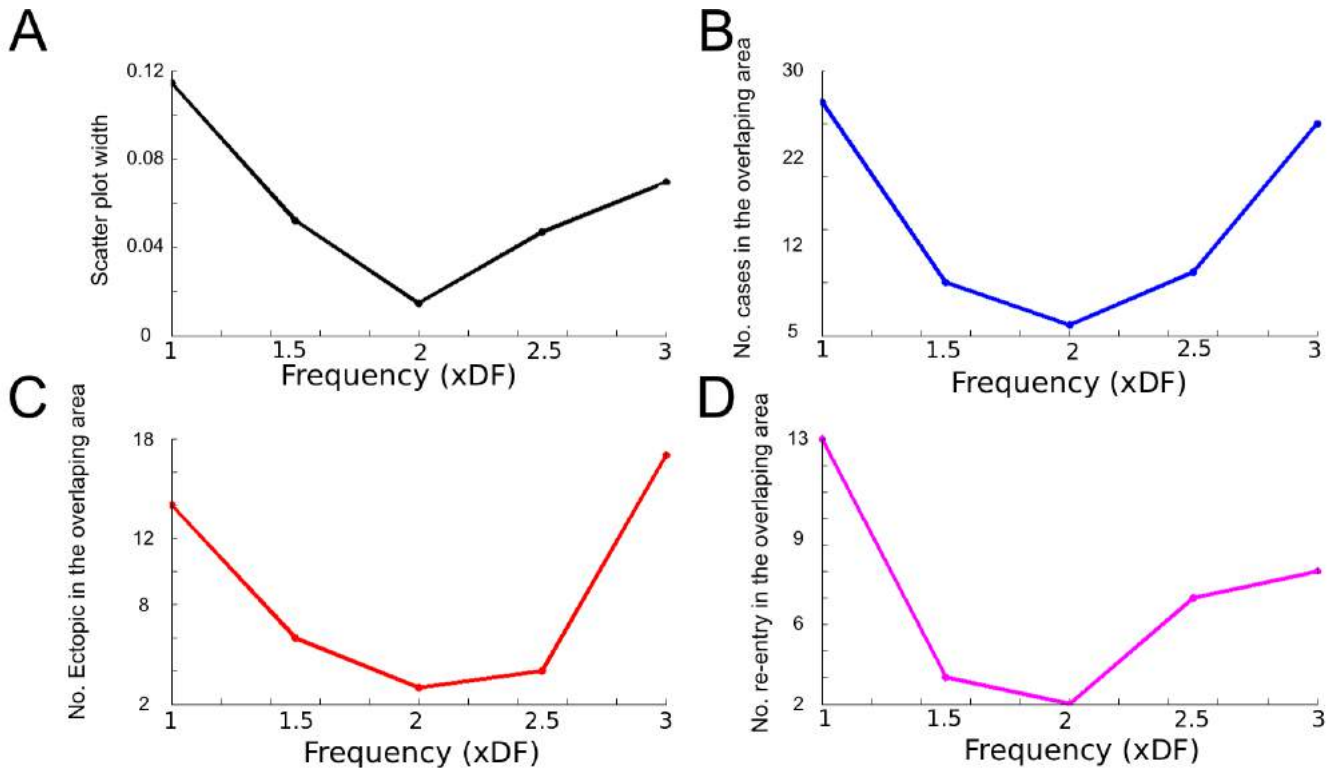

Figure A.2: Properties of the overlapping area from scatter plots against different values of the dominant frequency (DF). (A) Width of the overlapping area from scatter plot vs values of DF. (B) All simulation cases (Ectopic focal and re-entrant activity) that are inside the overlapping area vs values of DF. (C) Number of Ectopic focal activity simulations inside the overlapping area vs values of DF. (D) Number of Re-entrant activity simulations inside the overlapping area vs values of DF.

Supporting Text S4

White noise was added to re-entrant and ectopic focus ECG signals with origins in the right atria appendage (Figure A.3). A dipole sum was obtained in each case (Figure A.3Ai and Bi), and the time interval of the main activation was selected (Figure A.3A and B). Subsequently, $\mathrm{AFFTr_{2DF}}$ signals of original and noise signals were computed to differentiate ectopic and re-entrant activation (Figure A.3C and D).

20% and 40% white noise () was added to simulated ECG signals using the formula:

$$\sigma = Rnd \times RMS \times f \tag{A.1}$$

Where Rnd are random numbers, RMS is the root mean square value of the body surface potentials over the entire time period to be analyzed, and f is the percentage of noise to be added, i.e. f=.2 for 20% noise level, with a signal to noise ratio (SNR) of 10.

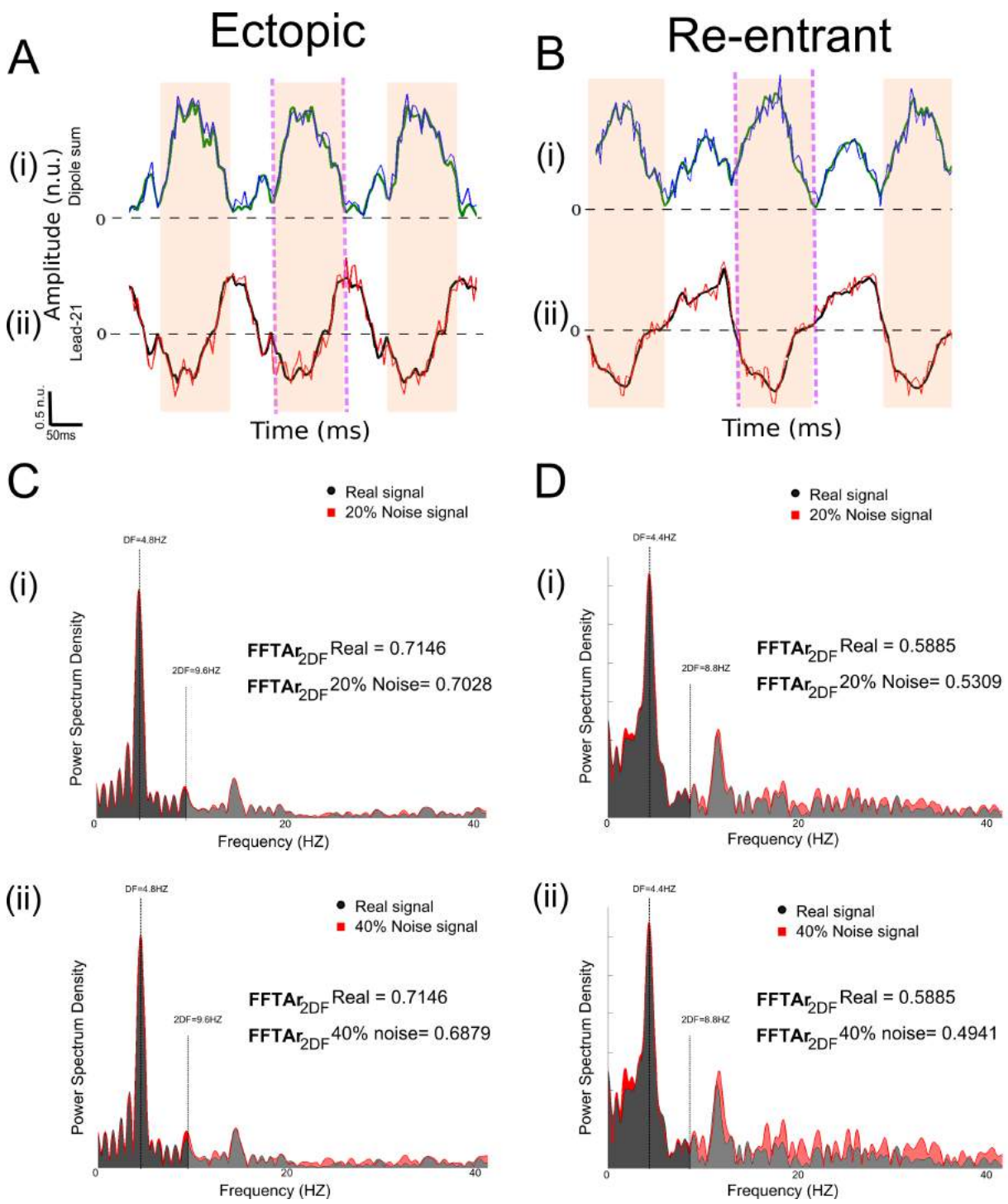

Figure A.3: Illustration of dipole sum and $AFFTr_{2DF}$ signals of ectopic and re-entrant activation focused on the right atrial appendage with added white noise. Dipole sum (green line) with 20% added white noise (blue line) (i) and lead 15 (black line) with 20% added white noise (red line) (ii). Time interval (section in magenta shadow) of ectopic (A) or re-entrant (B) patterns. Power spectral density for ectopic focal (C) and re-entrant (D) activation without (gray shadow) and with added noise (red shadow) at 20% (C-i and D-i) and 40% (C-ii and D-ii) noise level. The darker shadow corresponds to the area between 0 2 x Dominant frequency (DF). $AFFTr_{2DF}$ is the ratio of the area under the power spectrum density in the ranges 0 (2 x DF) Hz and (2 x DF) 50 Hz: $AFFTr_{2DF}$ = Area (0 - 2DF) / Area (0 - 50 Hz).

Supporting Text S5

Re-entrant and ectopic focus activations with origins in the inferior vena cava (IVC) (Figure A.4Ai) were tested within a female torso model. The position of the atria can be observed in Figure A.4Aii-iii. $AFFTr_{2DF}$ values of Lead-15 were obtained to differentiate ectopic and re-entrant activation (Figure A.4B). Subsequently, the dipole sum was calculated and the time interval of the main activation in each case was selected (Figure A.4C). Polarity maps were then obtained in each case (Figure A.4D). The algorithm correctly identifies the correct quadrant in each case.

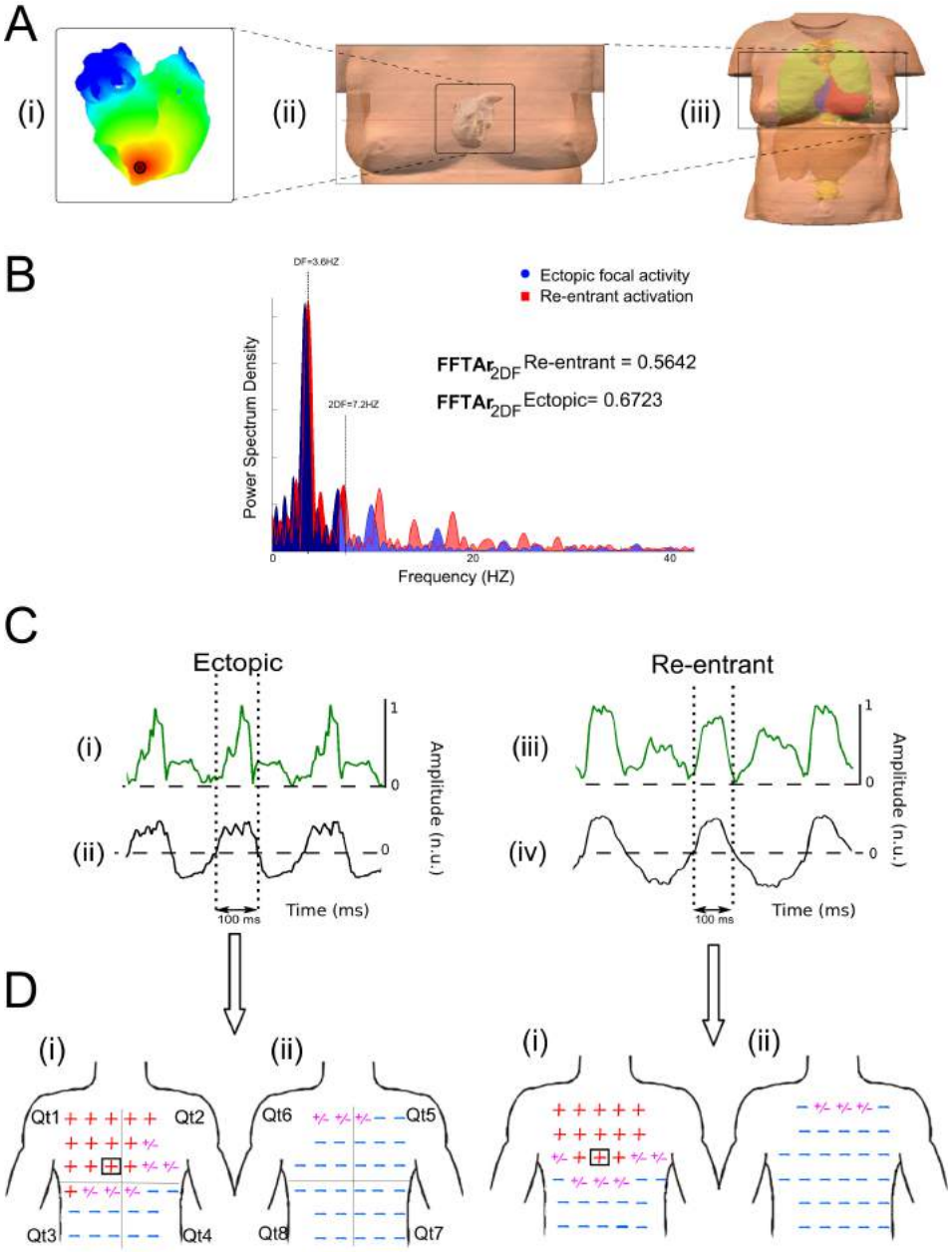

Figure A.4: Illustration of algorithm implementation in a female torso geometry. (A): Illustration of atria ectopic activation focused on the inferior vena cava (i) placed inside a female torso geometry (ii). (B): Power spectral density for ectopic focal (blue) and re-entrant (red) activity located in the IVC. The darker shadow corresponds to the area between 0 2 x Dominant frequency (DF). $AFFTr_{2DF}$ is the ratio of the area under the power spectrum density in the ranges 0 (2 x DF) Hz and (2 x DF) 50 Hz: $AFFTr_{2DF}$ = Area (0-2DF) / Area (0-50Hz). (C): Dipole sum (green line) (i) and lead 15 (black line) (ii), (i) used to identify the time interval (section between dotted lines) of the main atrial activation. (D): Atrial-wave polarity maps in the anterior (i) and posterior (ii) part of the torso. A red sign represents a positive polarity in the atrial-wave, the blue sign is a negative polarity and a purple sign represents a biphasic atrial-wave. The black square represents the electrode position of lead 15. In each case the algorithm correctly identifies the correct quadrant.